Photoinduced Phase Transitions Studied by Femtosecond Single-shot Spectroscopy

by

Taeho Shin

M.S. Chemistry, Pohang University of Science and Technology, 1999
B.S. Chemical Technology, Seoul National University, 1997

Submitted to the Department of Chemistry
in partial fulfillment of the requirements for the degree of

Doctor of Philosophy

at the

MASSACHUSETTS INSTITUTE OF TECHNOLOGY

September 2010

Author .....
Department of Chemistry
August 25, 2010

Certified by .....
Keith A. Nelson
Professor of Chemistry
Thesis Supervisor

Accepted by .....
Robert W. Field
Chairman, Department Committee on Graduate Students

This doctoral thesis has been examined by a committee of the Department of Chemistry as follows:

Professor Robert W. Field ... .

Committee Chair

Professor Keith A. Nelson .. ..

Thesis Supervisor

Professor Robert G. Griffin ....

Committee Member

Photoinduced Phase Transitions Studied by Femtosecond Single-shot Spectroscopy

by

Taeho Shin

Submitted to the Department of Chemistry
on August 25, 2010, in partial fulfillment of the
requirements for the degree of
Doctor of Philosophy

Abstract

Single-shot femtosecond spectroscopy has been developed and employed for the study of phase transitions of solid-state materials. Using two crossed echelons, a two dimensional spatial delay gradient was generated across a single probe pulse profile. This novel scheme enables us to monitor irreversible change in solids by acquiring many time-resolved data points with a single laser pulse. With the integration with a noncollinear optical parametric amplifier (NOPA) and a conventional pump-probe instrument, ultrafast dynamics of coherent lattice vibrations and photoinduced phase transitions were examined in two different systems.

Ultrafast dynamics such as coherent lattice vibrations and bond softening were investigated for Bi thin films and bulk single crystals. Depending on the thickness, transient reflectivity was changed significantly. The variations are ascribed to different electronic structures possibly originating from quantum confinement. Bond softening exhibits a strong thickness dependence due to hot carrier dynamics as well as to the different electronic structures. At high pump fluences, no phonon oscillations were observed suggesting a phase transition to liquid or to a higher symmetry crystalline phase (reverse Peierls distortion). Together with thermal modeling, double pump measurements reveal nonthermal melting occurring in bulk and thin Bi films. A higher threshold fluence for nonthermal melting is observed in bulk bismuth as compared to thin films, suggesting ultrafast carrier dynamics such as ballistic transport. In addition to nonthermal effects, thermal effects such as inelastic electron-phonon scattering and nonradiative recombination play a crucial role in melting and cooling at later times after nonthermal melting takes place.

A quasi one-dimensional platinum iodide complex showed strong oscillations in reflectivity which are attributed to oscillatory motions of wave packets on a self-trapped exciton (STE) potential surface. As optical excitation increased, electron transfer from Pt^{2+} to an adjacent Pt^{4+} occurred over a wider range of lattice sites and weakened the oscillations. Above a certain pump fluence, oscillations disappeared completely indicating that the mixed valence, charge density wave state changed to monovalent, Mott-Hubbard phase. The reverse phase transition, i.e., from the Mott-

Hubbard phase to the charge density wave state began within 3 ps of the optical pump.

Thesis Supervisor: Keith A. Nelson
Title: Professor of Chemistry

Acknowledgments

Wow! Almost fourteen years have passed since I decided to pursue Ph.D. study in the States when I was a senior college student in Korea. After earning the M.S. degree and completing the five-year mandatory service afterwards, I was lucky enough to have an opportunity to study at MIT. This would be an unforgettable and invaluable experience in my life.

Living in single-shot territory for the past several years in the Nelson group, I felt often that I am wandering through an absolutely dark tunnel without even knowing whether or not it has an exit. Now I am glad to be on the verge of getting out of it. It would have been impossible without the support of family, friends, and colleagues.

First of all, I would like to thank my research advisor, Professor Keith Nelson. I greatly appreciate his advice and the support he provided. I was always impressed with his energy and enthusiasm in science, considering him to be an ideal advisor and scientist. It is my honor to have Professor Bob Field and Professor Bob Griffin as my thesis committee members. They encouraged me and suggested many ideas during my oral exam and annual meetings.

I cannot thank Johanna enough. I have enjoyed working with such an agreeable and talented friend. She and I shared the difficulties in the single-shot measurements and tried to get through them together. Without her devoted efforts, I might be still in the dark tunnel. I would also like to express my appreciation to former members Maria and Peter. Their endeavors on the single-shot project made my work possible as well. It was a great opportunity to collaborate with Ikufumi and Taro. Even though it was a short period, discussion with them broadened my knowledge and stimulated me intellectually. I was lucky to have smart and nice Kit in the same lab space. I have enjoyed discussing many things with him. Owing to his expertise in optics and his logical approach, I was able to solve many problems. Some of the most cherishable moments were chatting about anything with Kit and Johanna in the dark lab. Christoph Klieber was always willing to help me with anything. Thanks to him, life in the group was much easier.

I have had the distinct pleasure of interacting with other former and current group members: Josh, Kenan, Kathy, Duffy, Dylan, and Patrick in four wave-mixing; Ka-Lo, Matthias, Janos, Harold, Zhao, Nate, Cassie, Brad, Sharly, and Xibin in THz; Emmanuel, Thomas, Darius, Kung-Hsuan, Gagan, Jeremy, Kara, Vasily, Alex, and David in acoustics; Eric, Qiang, Ryan, and Stephanie in polaritonics. I would like to express my gratitude to Gloria, Li, and Nancy. As one of my best friends in another group, I am happy to acknowledge Gautham Nair. I was able to get through the tough first year thanks to him.

Life would have been tough without the support and friendship from the Korean community at MIT. I owe numerous Korean friends from the ChemE and Chemistry Department: Rilla (Dae Kun) and his wife Diane, Jongnam, Sang Hwal, Yoon Sung, Chang Hoon, Seung Woo, Bong, Su Kyung, Jung Ah, Seok Joon, Hoi Sung, Jae-Gook, and Jeewoo. Drinking and chatting with them, especially Rilla, at S&P, the Muddy Charles, Thirsty Ear, Characters, and Miracle of Science were most relaxing at MIT. I am also grateful to Won Yong, Sangwon, Jaemyung, Jin-Oh, Sangjin, Kang Hyun, Yeon Woo, Joonwoo, and Soohan. I will miss the days in Cambridge that I spent having fun, cooking, and drinking with them. I wish to acknowledge also the support from friends in Korea: Kiyeo, Junghwan, Sunyong, and the lovely Hye Ryung—Thank you very much!

Lastly but most importantly, I wish to thank my parents, brother, and sister for their endless and unconditional support and love. I love you! This thesis I would like to dedicate to my family.

Contents

List of Figures

Chapter 1

Introduction

Chemical reactions, phase transitions and surface processes involve rearrangement of atoms via bond breaking and reforming on timescales comparable to characteristic oscillation periods of atoms or molecules. Theses processes occur typically on femtosecond to picosecond timescales. Since the advent of the femtosecond laser, ultrafast dynamics of small gas molecules, complex biological materials such as proteins, and condensed matter have been unveiled. Experimental variations for time-resolved spectroscopy have been invented over the past decades [Rul05]. The common scheme behind these variations involves excitation or perturbation of the equilibrium state followed by measurement of the time-dependent response. This is a widespread technique called pump-probe spectroscopy. In order to study photodissociation of gas molecules on femtosecond timescales, for example, we first need an ultrashort light pulse (the pump) as a stimulus which promotes electrons from a ground potential energy surface to an excited potential energy surface. This leads to the dissociation of the molecule. Then we need another light pulse (the probe) which arrives a certain time after the first pulse and interacts with the dissociating molecule. The interaction may result in emission, absorption, or scattering of light which eventually provides dynamical information. By changing the arrival time of the second light pulse and acquiring many data points, the time evolution of the dissociation event is recovered.

In spite of the success of conventional pump-probe spectroscopy, it imposes a restriction on samples. Because of the repetitions of pump and probe pair, it is nec-

essary that the sample return or relax back to its original state between pump probe sequences. If the pump induces a permanent change of the sample, then fresh sample needs to be supplied for every pump shot. In the case of gas or liquid samples, flowing guarantees fresh sample for each laser shot. For solids, fresh sample is supplied by translating the sample in a plane perpendicular to the direction of pulse propagation. This method requires caution and is labor-intense. It is also limited to samples with a large area and good optical quality. For small crystals or novel samples, it is impractical or impossible to investigate ultrafast "irreversible" dynamics using the conventional pump-probe method. However, most photochemical or photophysical events in solids are irreversible at high excitation fluences. Photodissociation, phase transitions, solid-state polymerization, and explosive detonation are such processes. The limitations of the conventional pump-probe technique prevent observation of these processes on ultrafast timescales. This failure led to the development of dual echelon single-shot spectroscopy a decade ago in our group [Wak01, Pou05]. This novel method was recently used to study the dynamics of truly irreversible chemistry in organic crystals [Pou06].

Among many ultrafast phenomena that have been examined, ultrafast phase transitions are the most challenging due to their irreversible nature and to complex dynamics such as carrier-lattice interactions. Recently, time-resolved X-ray or electron diffraction techniques have been successfully employed to capture transient structural change of atoms directly, providing the most convincing picture of the transitions [SBB+03, FRA+07, SHK+09]. Despite their great capabilities, such techniques are not commonly implemented for the study of irreversible phase transitions. But the optical single-shot technique, while unable to capture atomic motion directly, offers a detailed view of electron or carrier dynamics as well as indirect information on atomic rearrangement during the phase transition. Moreover, it provides a better time resolution and more versatility in terms of wavelength of probe than the diffraction method. The topic of this thesis is the study of photoinduced phase transitions using dual echelon single-shot spectroscopy. Two different Peierls distorted solids were employed: Bismuth and a novel inorganic crystal consisting of one-dimensional

platinum-iodide bonds.

Organization of the Thesis

Chapter 2 describes the motivation, scheme, and optical setup of the dual echelon single-shot technique. The temporal and spatial beam profiles are analyzed when the beam propagates through the echelon, sample and imaging optics. The most limiting obstacle in the single-shot pump-probe measurement is signal to noise level. The current signal to noise level and intrinsic systematic noise are discussed. The conventional pump-probe set-up and noncollinear optical parametric amplifier (NOPA) are integrated into the single-shot setup for versatility and flexibility of the whole system. The descriptions of these optical set-up is also included in this chapter.

Chapter 3 presents femtosecond time-resolved measurements of the reflectivity of bismuth thin films and single crystals upon photoexcitation. The mechanism of displacive excitation of coherent phonons is introduced. Coherent lattice vibrations, bond softening, vibrational dephasing, and carrier relaxation are discussed. Continuum probe measurements are also presented and interpreted using the Fermi distribution function, which may reveal different energy gaps for the samples with different thickness. At higher pump fluences, bismuth undergoes a phase transition supported by the disappearance of the lattice vibrations. In order to understand the nature of the transition, double pump measurements were conducted and the two-temperature model in semimetals was used for interpretation.

Chapter 4 presents femtosecond reflectivity measurements of a platinum iodide complex. Coherent phonons or oscillatory motions of wave packets on the self-trapped exciton states, are discussed. Different responses to variable wavelengths may reflect ultrafast vibrational cooling of the wave packet and annihilation of the self-trapped exciton states. Increasing pump fluence leads to the disappearance of the oscillations suggesting a phase transition from a charge density wave state to a Mott-Hubbard phase. Double pump measurements were conducted to elucidate the nature of the transition and its reverse transition.

Finally, chapter 5 summarizes the works of the thesis and emphasizes their im-

portance. Possible future works using the unique single-shot technique are discussed briefly.

Chapter 2

Dual Echelon Single-shot Ultrafast Spectroscopy

Dual echelon single-shot spectroscopy is a unique and novel method. The details of the optical layout and software for this method are presented in this chapter. In spite of using the single-shot measurement without averaging, high signal-to-noise level is demonstrated. Noise sources are examined as important limitations of the single-shot technique. The temporal and spatial beam profiles of ultrashort pulses are analyzed along the beam path as well.

2.1 10 Hz Amplified Laser System

The laser system consists of an oscillator, a 1 kHz regenerative amplifier, a 10 Hz pulse selector, and a second stage amplifier. The master oscillator is a commercially available modelocked Ti:sapphire laser (Vitesse from Coherent). The CW output from a Coherent Verdi Nd:YVO_4 intracavity second harmonic pumps the Ti:sapphire crystal and produces 800 nm CW. Modelocking is obtained using the Kerr-Lens modelocking (KLM) technique with an automatic starter, which triggers the initiation of modelocking by introducing power fluctuations. The oscillator uses two pairs of negative dispersion mirrors instead of a prism compressor in order to compensate for the positive dispersion of pulses by the thick gain medium (Ti:sapphire). The

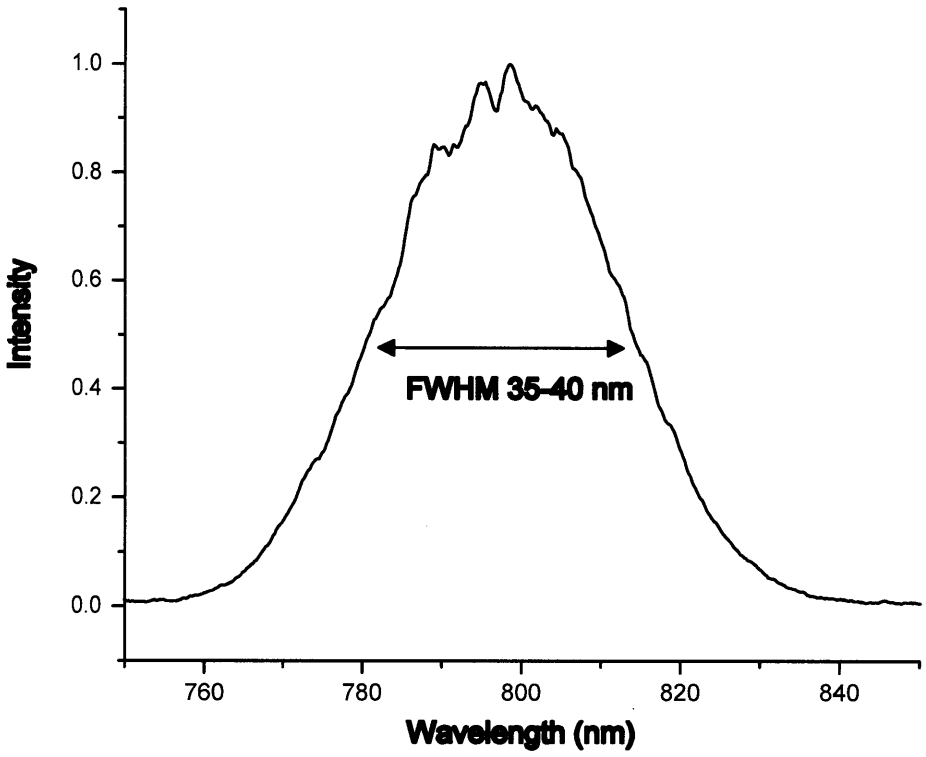

Figure 2-1: Spectrum of the output from the oscillator. Spectral measurements reveal a full-width half-maximum spectral bandwidth of 35-40 nm at a central wavelength of 800 nm.

repetition rate is 80 MHz and the corresponding effective cavity length is estimated to be ~1.9 m. The TTL electronic signal of 80 MHz is connected to the 1 kHz regenerative amplifier controller, and synchronization between them is achieved. The 1 kHz TTL signal enables further synchronization with subsequent electronics. The average output power of the oscillator is 320–400 mW, and the corresponding pulse energy is approximately 4–5 nJ. The output beam is about 2 mm wide in diameter and well-collimated over a long distance so that the divergence is negligible for the long optical path through the regenerative amplifier. In particular, the collimation is essential in the stretcher. If the seed beam is diverging or focusing over the stretcher, nonlinear chirp is introduced, which cannot easily be compensated by the compressor.

The output spectrum is presented in figure 2-1. The spectrum shows a full-width

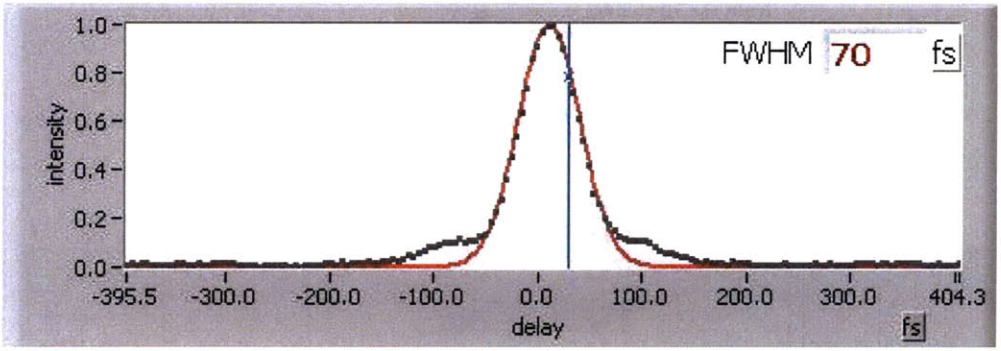

Figure 2-2: Intensity autocorrelation trace of the output from the oscillator via second-harmonic generation. A FWHM of 70 fs in the autocorrelation trace indicates a pulse duration of 50 fs.

half-maximum (FWHM) spectral bandwidth of 35–40 nm at a central wavelength of 800 nm. Autocorrelation measurements via second-harmonic generation in a 100 μm thick BBO crystal yield a FWHM of 70 fs. The deconvolution of the autocorrelation gives a FWHM of 50 fs. Figure 2-2 illustrates the second-order intensity autocorrelation and a Gaussian curve fitting.

The regenerative amplifier is seeded by the pulses from the oscillator. The regenerative amplifier is comprised of a Faraday isolator, stretcher, cavity, and grating compressor. The Faraday isolator prevents undesired back propagation of light from disrupting the oscillator and affecting the regenerative amplifier. It transmits the incoming seed pulses forward and rotates their polarization by 45° through a magneto-optic effect. The back-reflected beam from the cavity optics experiences another 45° rotation. The resulting polarization is then perpendicular to that of the incoming beam and the polarizer blocks the back-reflected beam.

The seed pulses are stretched before they are amplified in the cavity. They can be amplified by 5-6 orders of magnitude to yield the energy of 2.5–3 mJ/pulse. If the pulses are not stretched, then such strong amplified pulses create high instantaneous power and can destroy several optics such as the Ti:sapphire crystal and Pockels cells inside the cavity. The seed pulses propagate back and forth between a grating and two retro-reflectors, and temporal delays are generated between shorter and longer wavelength sides within the pulse. The optical pathlength difference between shorter

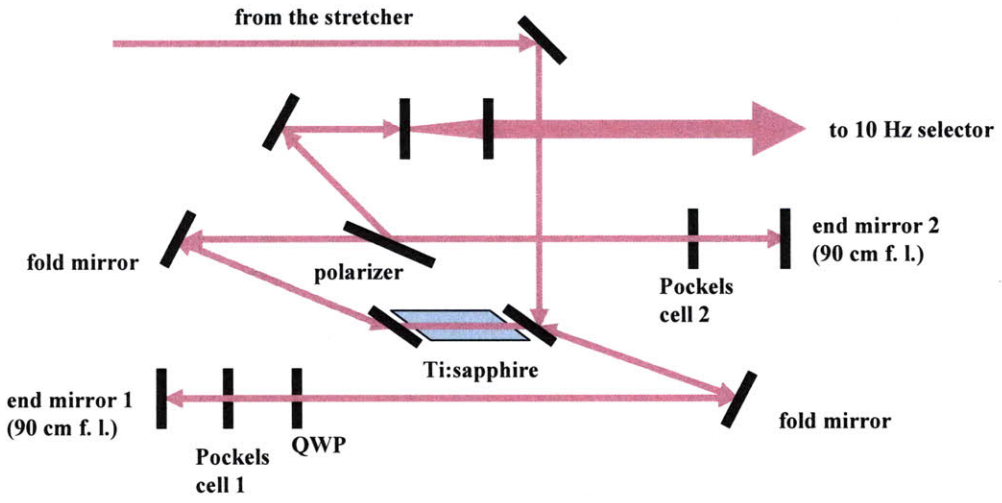

Figure 2-3: Schematic illustration of the cavity in the Ti:Sapphire regenerative amplifier.

and longer wavelength sides is observed to be several centimeters. The corresponding temporal delay, which is the pulse duration, is a few hundred picoseconds.

Long pulses are directed into the cavity which contains the Ti:sapphire crystal, two Pockels cells, a quarter-wave plate, a thin film polarizer, two fold mirrors, and two end mirrors. The crystal is Brewster-angle cut and its length is about 2 cm. It is pumped by a 1 kHz Nd:YLF diode laser (Evolution from Coherent). Every pump pulse is split into two pieces (6:4 ratio) which are counter-propagating through the crystal. The total pump power of both arms is 17–19 W. For higher amplification efficiency and better thermal stability, the crystal temperature is kept at 0°C by an electric cooler unit. Dry air is circulating through a box which contains the crystal to prevent water condensation on the crystal. Figure 2-3 illustrates the cavity.

The seed pulses enter the cavity with a vertical polarization and are reflected off the Brewster-cut window. With both Pockels cells off, the polarization is rotated by 180° after two round trips across the quarter-wave plate. Because of the Brewster angle of the window and the crystal, most of the light pulse is rejected by them and amplification does not occur. In order to be amplified, the polarization of the pulse should be horizontal throughout the cavity. The unchanged horizontal polarization is achieved by firing Pockels cell 1 immediately after the pulse leaves Pockels cell 1

towards the quarter-wave plate or the gain medium. The Pockels cell behaves like a quarter wave plate when a high voltage is applied across it. Therefore, the combination of Pockels cell 1 and the quarter-wave plate does not affect the polarization during the round trip through them. When the amplified pulse reaches its maximum intensity and right before it enters Pockels cell 2 towards the end mirror 2, Pockels cell 2 should be fired to rotate the polarization by 45° for each trip across it. Finally, the thin film polarizer rejects the vertically polarized beam. The time required for a single round trip in the cavity is approximately 10 ns (measured by a scope) and the corresponding effective cavity length is about 1.5 m. The total number of round trips for the gain maximum is determined by the difference between firing times of Pockels cells 1 and 2. Under normal conditions which produce a power of 2.5–2.9 W (before the compression), the interval is around 250 ns and the corresponding number of round trips is 25.

After being amplified, the beam is directed to a 10 Hz selector. 90° rotation of the polarization is made by a periscope before the 10 Hz selector. Because of the slow data acquisition process for a single-shot measurement, determined by slow shutters, CCD camera, and a commanding procedure, the repetition rate should be decreased. The repetition rate is adjustable and 10 Hz is used most of time. The 10 Hz pulse selector is described in figure 2-4. A Pockels cell is fired every 100 ms via a high voltage supplier whose action is synchronized with the 1 kHz system. The Pockels cell behaves as an ideal half wave plate when 5.3 kV is applied across it. The thin film polarizer then reflects off the vertically polarized beam to the 10 Hz single-shot instrument. The remaining pulses, i.e., 99 pulses out of every 100 pulses for 100 ms, pass through the thin film polarizer and subsequent optics and then finally are compressed. The extinction ratio is higher than 200–300:1 on the 10 Hz side. Sometimes, a 1 kHz repetition rate is necessary for purposes other than a single-shot measurement such as a conventional pump-probe measurement. In this case, the 1 kHz rate offers much higher signal to noise. In addition, using the 1 kHz pulses is much more convenient for the alignment of the optics in the single-shot apparatus, especially in the NOPA. By placing a half-wave plate behind the Pockels cell and changing the angle, a small

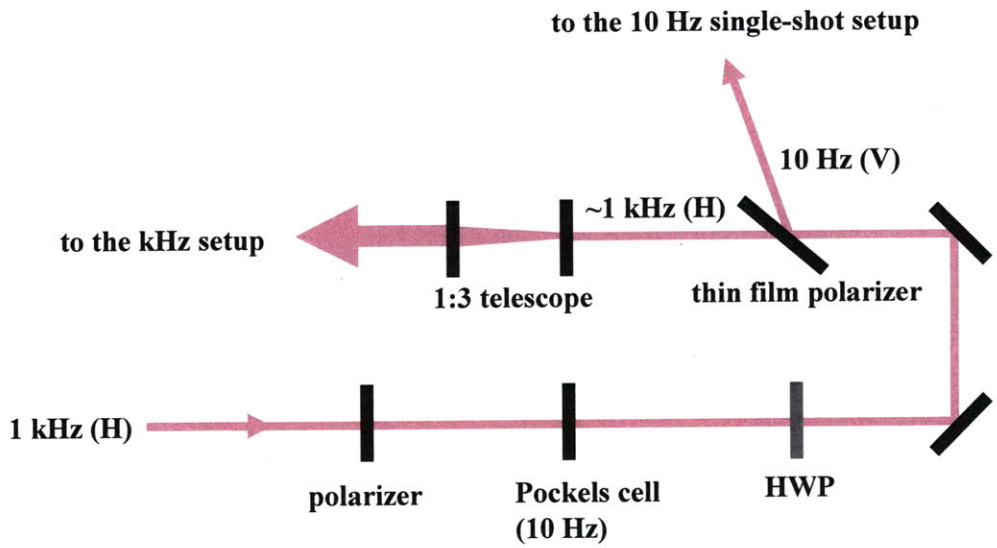

Figure 2-4: Schematic diagram of the 10 Hz selector. A combination of the Pockels cell and thin film polarizer picks one pulse out of 100 pulses every 100 ms and sends it to the single-shot apparatus.

or full fraction of the 1 kHz beam can be taken.

In most cases, the beam is directly introduced to the single-shot instrument without being amplified further. Out of the 10 Hz selector, the pulse energy is about 2.3–2.5 mJ which is sufficient for most experiments. However, future experiments such as a THz-driven irreversible phase transition would require even higher pulse energies. For those measurements, it is necessary to amplify each pulse further in a second stage amplifier. The second stage amplifier was built [Wak01]. The amplifier adopts a bow-tie configuration in which the beam makes four round trips in the cavity. In this amplifier, a perpendicular-cut Ti:sapphire crystal ($\alpha = 2.85/\text{cm}$) is pumped by a 10 Hz Nd:YAG green laser (Continuum Surelite I) which is also synchronized with the 1 kHz signal. The pump energy is adjustable by using a half-wave plate-polarizer attenuator. The beam waist of the seed is 2.5–3 mm in diameter at the crystal. With a 50 cm f.l. lens, the pump beam is focused well before the crystal (5–7 cm) such that its spot size is comparable to that of the seed at the crystal. The final pulse energy can rise up to 8 mJ or even higher using the second stage amplifier.

At this point, the pulse remains temporally stretched and needs to be compressed

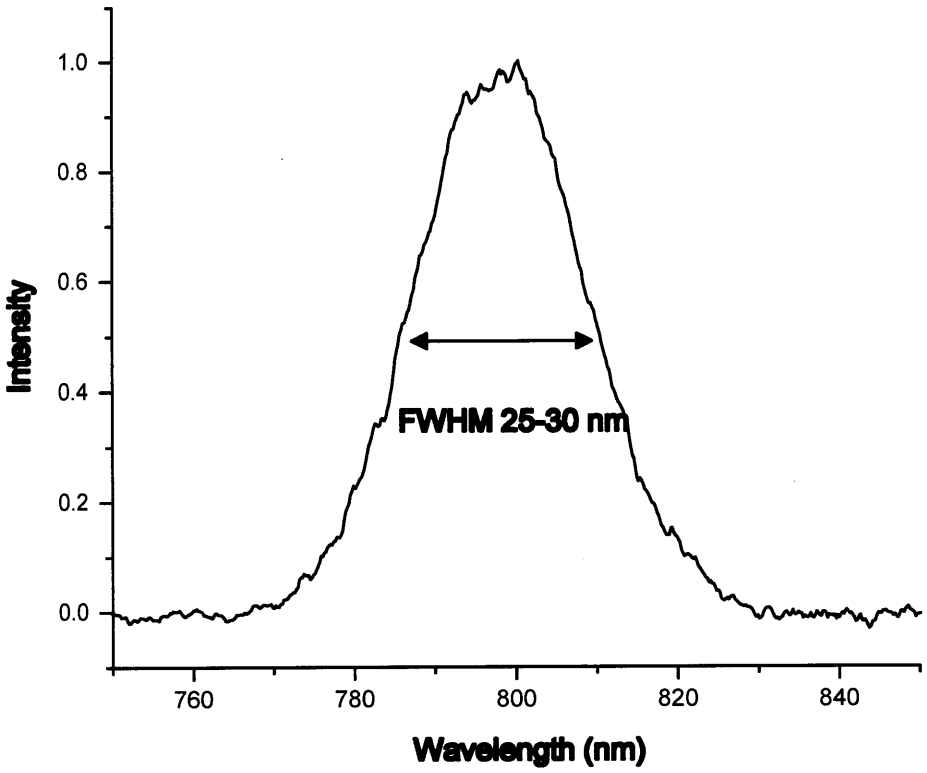

Figure 2-5: Spectrum of the output from the regenerative amplifier. A spectral width (FWHM) is 25–30 nm. Band-narrowing results from preferential amplification at the central wavelength of 800 nm in the cavity.

for ultrafast measurements. A compressor was built. The compressor consists of a grating (1400 lines/mm, Spectragon), a horizontal retro-reflector, and a vertical retro-reflector. In order to avoid damaging the grating, the amplified beam was magnified 3 times using a 1:3 telescope where a spatial filter (50 μm) is in place at the focal point of the first lens. The grating shows reflectivity higher than 90% for a p-polarized beam. The overall throughput is approximately 70-75% after reflecting off the grating four times. By adjusting the distance between the horizontal retro-reflector and the grating, the pulse duration is optimized. The average distance between them is about 20 cm. In figure 2-5, spectral measurement after the compressor reveals an amplified pulse bandwidth of 25–30 nm. The amplification process usually narrows the overall bandwidth of each pulse because wavelengths nearer to the center wavelength are

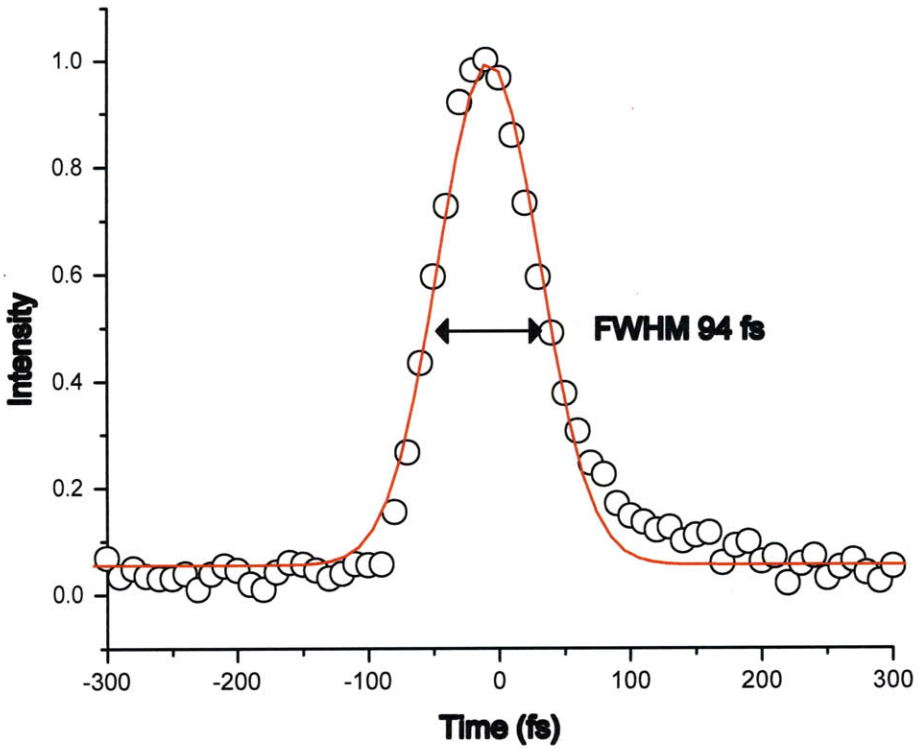

Figure 2-6: Intensity autocorrelation trace of the output from the regenerative amplifier using second harmonic generation. A pulse duration of 70 fs is obtained by a home-built multi-pass grating compressor (10 Hz).

amplified more effectively. In figure 2-6, the intensity autocorrelation trace is fitted to a Gaussian function and the resulting FWHM is 94 fs. The band-narrowing can explain the longer pulse duration. The pulses from the oscillator and the amplifier are not transform-limited due to the higher-order chirp terms which are not readily compensated by the current grating compressor. The deconvolution of the autocorrelation yields a pulse duration of 65 fs. This is short enough for most studies, including structural phase transition studies.

2.2 Dual Echelon Single-shot Technique

2.2.1 Motivation

As described in the previous chapter, the potential utility for a single-shot spectroscopic method is great. The contingency that materials under investigation should return to their original state between pump-probe sequences prohibits extension of the pump-probe technique to the study of ultrafast irreversible processes in the solid state. Photodissociation, photo-induced phase transitions, photochemistry, and photophysics under shock loading are all among these processes. Such dynamic events have attracted much attention but have been left unexplored because of experimental limitations. Several versions of the single-shot measurement have been attempted using different schemes of generating and measuring time delays from a single probe piece. For example, time-to-space mapping [DFN94, FDNT95, WLGS97, MFIT06] and time-to-wavelength correspondence [LM02] have been demonstrated. There are disadvantages to each method. For the time-to-space mapping scheme, a temporal gradient is obtained by tilting the wavefront or by changing the incidence angle of either pump or probe on the sample. In this method, both are focused linearly using cylindrical lenses. After passing through or being reflected from the sample, the probe beam is imaged onto a CCD. The temporal signal is converted from the image using the one-to-one time-space correspondence. However, because of the experimental geometry, some limitations are imposed on samples and the pump beam. For a longer time window, the pumped region must be longer accordingly. At a given probe incidence angle of 45° (0° for pump), for instance, the sample should be excited simultaneously over a 1 cm long range at the same time in order to acquire about 20 ps of data time window. This means the sample must have great homogeneity over the pumped region. The pump beam must also be uniform over the region. Alternatively, the pump profile should be well-defined over the pump region and the corresponding intensity-dependent response should be also well-characterized for extraction of the time signal. These constraints make the implementation of the method very difficult. The time-to-wavelength mapping methods use a probe pulse

with a well-characterized frequency chirp [LM02]. The different wavelength components arrive at the pumped region with different delay times, and these intensities are measured by a spectrometer. With knowledge of instantaneous frequency in time, the temporal signal is extracted from a one-to-one correspondence between time and wavelength. However, if the excitation affects the spectrum of the probe through wavelength-dependent absorption, it is difficult to extract the time evolution. Also, the long chirped pulse limits the temporal resolution.

2.2.2 Concept

The scheme described in this thesis is to create a temporal gradient using echelons. The concept of the echelon in spectroscopy was introduced by Topp *et al.* for the first time in [TRJ71, TO75]. Topp *et al.* invented the echelon in order to divide the cross-sectional profile of the probe beam into variably delayed probe pieces. Each probe piece is focused onto the same sample spot and spatially resolved to produce temporal information. The concept of the dual echelon single-shot spectroscopy presented in this thesis is exactly the same. As an extended form, we use two crossed echelons to gain femtosecond time resolution. Accordingly, the temporal gradient has a two dimensional structure.

Figure 2-7 illustrates the structure of a transmissive echelon. The concept of generating delay times is straightforward. The speed of light traveling through the optic is slower than through the air. Consequently, light travels the same distance faster through less steps than through more steps. The time delay introduced by unit step thickness d and index of refraction n is

$$\Delta t = (n-1)\frac{d}{c}. \tag{2.1}$$

Figure 2-8 illustrates the scheme of generating time delay in one dimension. We have used two pairs of echelons which differed in their compositions and fabrication methods. The former version was made by coating the hypotenuse of a right-angled prism with an index matched epoxy, and then carefully machining a stepped struc-

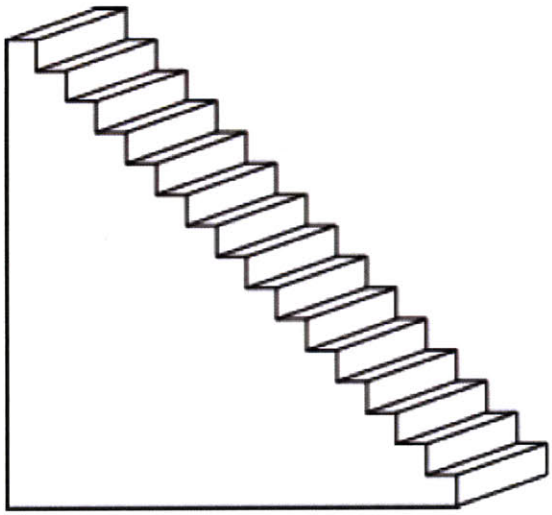

Figure 2-7: Schematic drawing of the echelon. 20 steps are fabricated along the diagonal direction. The crossectional area is about 1 cm×1 cm.

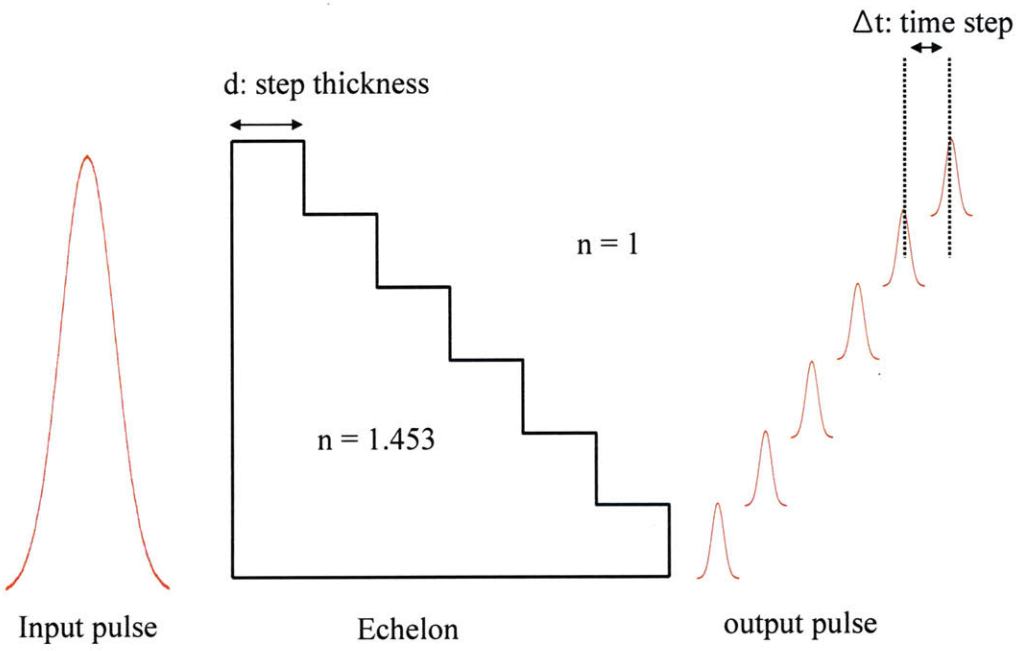

Figure 2-8: Concept for generating time-delayed probe pulses through an echelon. A probe piece that passes through a thinner region arrives at the sample earlier than a probe piece that passes through a thicker region.

ture. The disadvantage of the epoxy-based echelon is that it includes some bubbles and other imperfections, and deteriorates over a long time period by deformation or warpage, especially near the edges. The present version was constructed by chemically

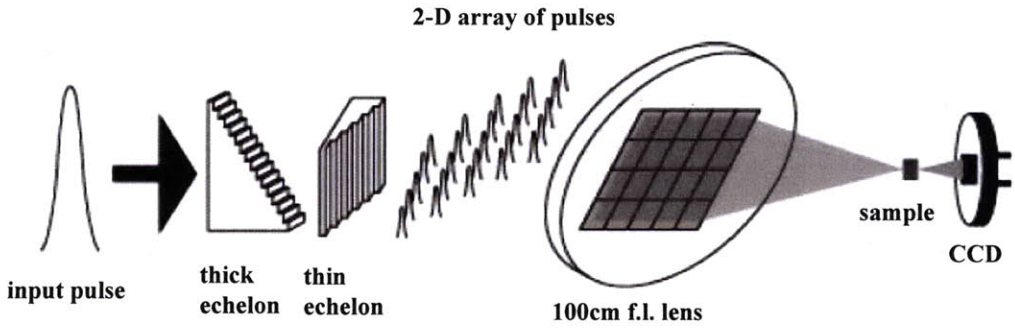

Figure 2-9: Simplified view for dual echelon single-shot measurement. A two dimensional spatially- and temporally separated probe array is generated by the crossed echelons. All of the probe pieces are focused to the same spot which is excited by a pump pulse. The probe array is reconstructed at the CCD.

stacking 20 thin layers of fused silica such that a lateral side of each layer is shifted by an equal distance with respect to the adjacent layer. All of the opposite lateral sides are cut such that their ends coincide and form a flat plane. The lateral sides are well polished to a good optical level. The presently-used echelons have a very high resistance to deformation. Since the two types have different indices of refraction and structural dimensions, hereafter only the present version will be referenced, unless otherwise specified. (figure 2-8)

The echelons' refractive index, n is 1.453 for 800 nm and d is 300 μm for the thick echelon and 15 μm for the thin echelon. The corresponding time steps of the thick and the thin echelon are 453 fs and 22.65 fs, respectively (figure 2-8). A simplified schematic of the dual echelon single-shot apparatus is presented in figure 2-9.

A probe pulse is divided into 20 pieces by the thick echelon along its stepped direction. Each probe piece is further divided into 20 pieces by the crossed thin echelon. This geometry yields the two-dimensional temporal gradient. The phase difference between two adjacent pieces is given by

$$\Delta\phi = (n-1)\frac{d}{\lambda}. \tag{2.2}$$

Unlike the time and phase for each probe piece, the wave vector and wavefront are unchanged by the action of echelons. Therefore, all of them can be focused by

a lens onto the same small spot of a sample. This behavior makes it possible to use a fairly small sample for the study of ultrafast dynamics. After propagating through or being reflected from the sample, the two-dimensional array or crossed echelon pattern is reconstructed at the image plane using a CCD camera. Strictly speaking, the image on the CCD should be considered a three-dimensional intensity array rather than a two-dimensional one because each square formed by the two crossed echelons represents intensity at a different time. The time signal is extracted from the three-dimensional intensity array using a sophisticated analysis code that is described subsequently.

2.2.3 Optical Layout

The entire layout of the single-shot instrument is illustrated in figures 2-10 and 2-11. Figure 2-10 shows transmission mode, allowing measurements for transmission or absorption change. Transient reflectivity measurements can be made in the reflection mode as described in figure 2-11.

The transition between one and the other mode is easily achieved by using several flip mirrors and replacing one lens in front of the CCD camera. All three image planes of the reference, the transmitted signal, and the reflected signal are collapsed to the same plane. This plane is also the location of the CCD camera.

An amplified 800 nm pulse is admitted by a shutter which is triggered by a TTL signal. An electronic 5 V signal is originally created in the DAQ card of the computer via a Labview code and sent to a delay generator. The delay generator synchronized with the 1 kHz (and 10 Hz) sends the TTL signal to the shutter and the CCD camera. The amplified beam is compressed to 70 fs. Some portion of it can be reflected into the noncollinear optical parametric amplifier (NOPA) setup if a wavelength other than 800 nm is needed for pump or probe. The beamsplitter (R:T = 1:1) is mounted on a magnetic plate so that it is detached when the NOPA is not in use. Another beamsplitter divides the beam into a pump and a probe arm. The pump arm is quite simple. There are two delay lines which vary the arrival time of the pump relative to the probe. The first one translates the beam using a finely tunable micrometer.

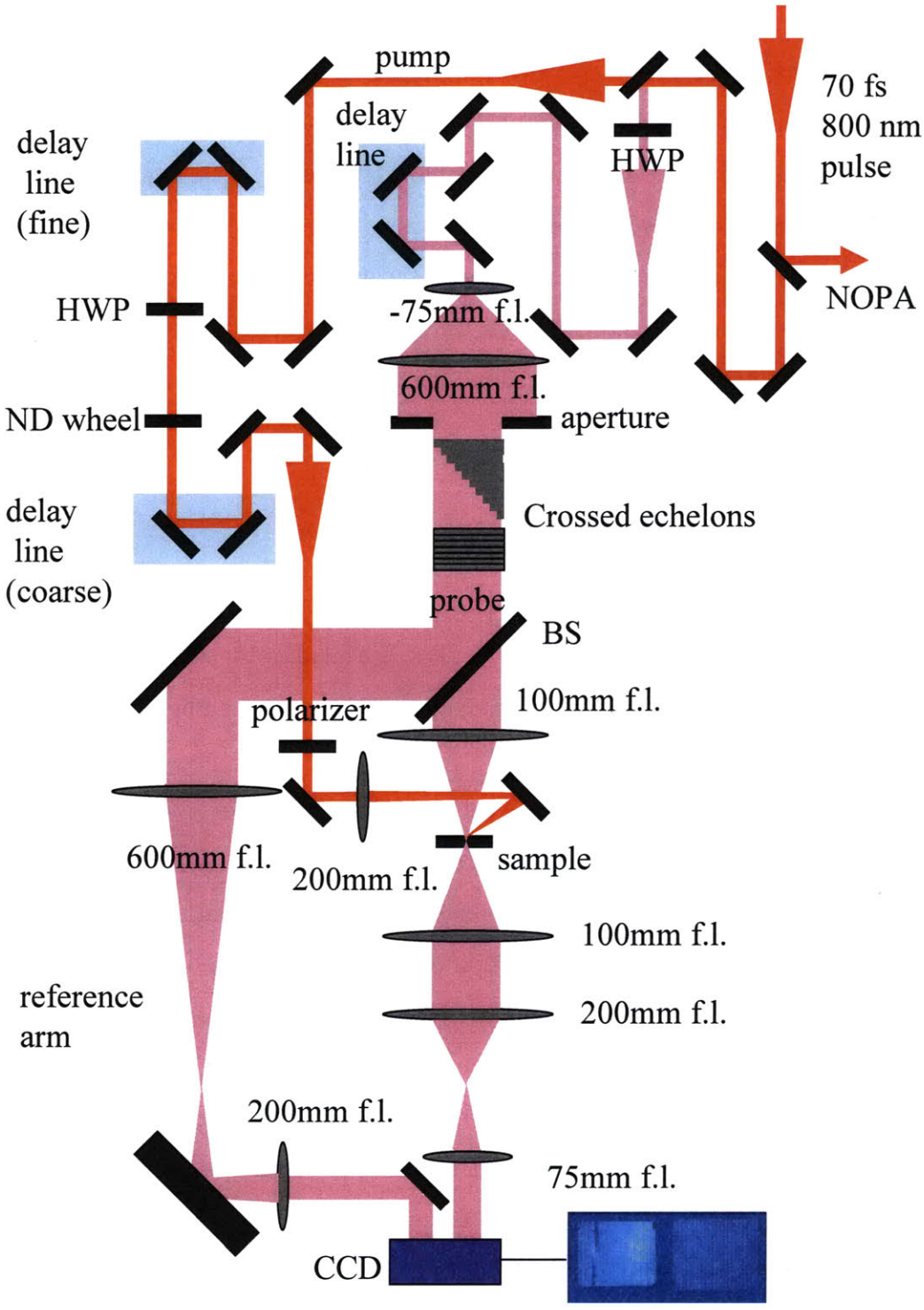

Figure 2-10: Optical layout of the dual echelon single-shot instrument. The diagram depicts the transmission (or absorption) detection mode.

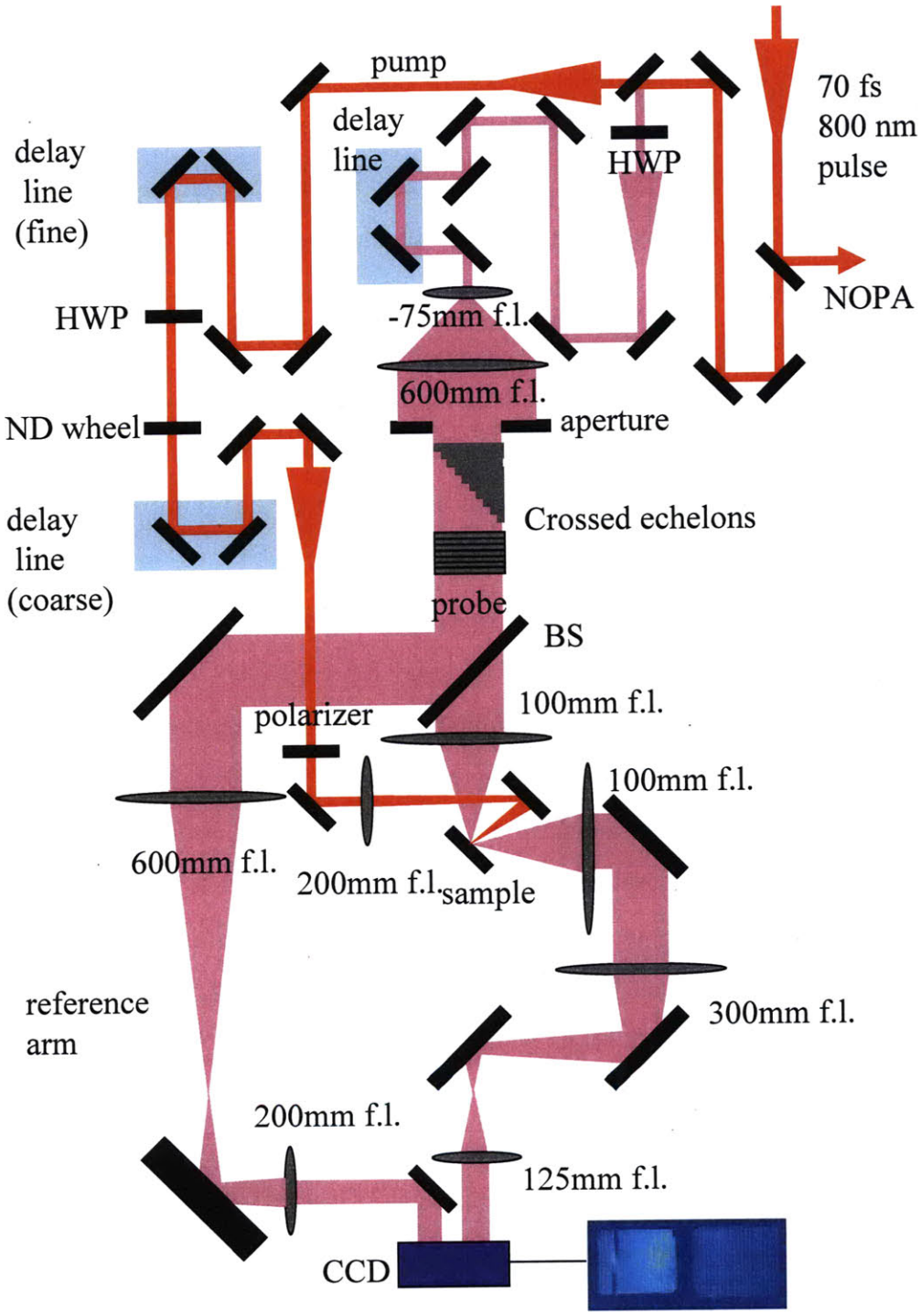

Figure 2-11: Optical layout of the dual echelon single-shot instrument. The diagram describes the reflection detection scheme.

The second one moves the beam up to 10 inches by a coarse moving stage. This delay line, when the pump is combined with the probe from the NOPA, needs to be moved further by several meters to compensate the long path length difference. The pump power is varied by an attenuator with a half wave plate and a polarizer. Neutral density filters on a rotating wheel can also reduce the power, but the rotation of the wheel sometimes changes the pointing of the beam so caution is needed. The pump is focused behind the sample rather than on the sample surface for uniform excitation over the probing spot. The focusing lens with 200 mm f.l. is mounted on a translational stage so that the pump spot size can be varied by moving it. The overlap between the pump and probe is confirmed by a camera with a telescope. The location and angle of the final mirror guarantees about 22.5° pump incidence angle for both transmission and reflection modes.

The probe beam path is complicated optically. The probe beam can be delayed by a translational stage as well. This is unnecessary for single-shot measurements but is used for standard pump-probe measurements. The beam diameter is about 7–8 mm at present, while the cross section of the echelons is 10 mm x 10 mm. The cross section of the beam must be larger than the echelon cross section. Also, the beam needs to be fairly uniform over the cross section of the echelon to take advantage of the limited number of bits in the CCD. If the beam is gaussian and barely larger than the echelons, the intensity could be several times higher at the center than near the edge in the echelon image. This would limit the capability of the CCD, because the intensity near the edge would need to be very low to prevent saturation at the center. To avoid this unfavorable situation, the beam is magnified significantly with a telescope before the echelons. The focal length of the first lens of the telescope is variable and that of the second one is 600 mm. For current measurements, the focal length of the first lens is set to 75 mm, and the corresponding magnification ratio is 8 (=600/75). The overall beam profile is fairly flat and uniform over the entire cross section of the echelons. After being magnified, the unneeded part of the beam is truncated by an aperture and only the central part of it passes through the echelons.

The thick echelon is followed by the thin echelon, though the order does not

make any difference. Every step runs vertically in the thick echelon and every step runs horizontally in the thin echelon. Thus, a two-dimensional array of temporally delayed probe pieces is generated. The stepped sides of the echelons are facing inward toward each other, which better defines the object plane and accordingly produces a better image at the CCD. The spatially and temporally structured beam is focused at the sample by a best form lens (100 mm f.l.). The best form lens is a singlet lens which is optimized to have diffraction-limited wavefront distortion. In other words, it minimizes or eliminates the spherical aberrations resulting from the large diameter of the beam array (10 mm x 10 mm). Accurate focusing of the probe array as well as strong overlap between pump and probe are essential for the single-shot measurement. Small deviations from either ideal would lead to considerable systematic noise. Using the best form lens is one effort that reduces the noise.

In transmission mode, the array is recollimated on the other side of the sample by a 100 mm f.l. achromatic lens. The locations of the echelons, the focusing lens, sample, and the recollimating lens are determined by the 4f imaging technique. All of the distances from one optic to the next one are fixed to f = 100 mm. Following the 4f imaging optics, a standard Keplerian telescope reduces the size of the array by a factor of 2.67 (= f1/f2 = 200/75). Finally, the array image is reconstructed by the CCD. Since each telescope inverts the image once, inverting the image twice yields the same configuration. A portion of the two dimensional probe array is partially reflected from a beamsplitter instead of being directed to the sample. This array forms a "reference image" which will be discussed in detail in the next section. The reference array is reduced by a factor of three in a telescope and then reconstructed next to the signal array image on the CCD. The reference image is inverted only once.

In reflection mode (figure 2-11), the reference arm does not change and the CCD is located at the same spot for an easy transition. The sample is rotated by 45° and the resulting incidence angle of the probe is 45°. The angle between the pump and probe is approximately 22.5° as in transmission mode. After being reflected from the sample, probe signal beam array is recollimated by a 100 mm f.l. achromatic lens. Afterwards, the reducing telescope is designed such that the image is reconstructed at

the same place as that of the transmission mode. The telescope consists of a 300 mm f.l. and a 125 mm f.l. achromatic lens and reduces the actual array size by a factor of 2.4.

Technical tips for the alignment

A He-Ne laser facilitates the alignment because it is easily visible but has weak power. The laser is integrated to the single-shot instrument and two flip mirrors guarantee that the He-Ne beam travels the same optical path as that of the real 800 nm beam. All of the imaging lenses are originally aligned by the He-Ne beam and a shear plate which allows determination of beam collimation.

The need for exact overlap between the sample location and the probe focal plane cannot be exaggerated. It is evident that every probe piece should hit the same spot excited by the pump. If probe pieces hit different spots, the heterogeneity of the sample or inhomogeneity of the pump strength tends to distort the temporal signal and lead to characteristic noise. The location of the focal plane is confirmed while viewing the echelon image reconstructed at the CCD by translating a razor blade near the plane in a direction perpendicular to the beam propagation. If the razor blade is translated and partially blocks the beam out of the focal plane (Fourier plane), one side of the echelon image starts getting dark first. However, if the razor blade moves in the Fourier plane and blocks the beam, the image fades away uniformly over the entire area. In this manner, the Fourier plane of the beam can be found. A camera with a telescope recognizes the focusing point exactly by imaging the point source of scattered light of the blade onto the camera. The focusing point is displayed by a screen. Adjustment of the pump path can be made until the pump and probe spots coincide with each other on the screen to overlap spatially. Marking the spot on the screen provides a guide for a later step. The next procedure is to block the pump, replace the razor blade with the sample, and translate the sample in the z-direction (probe beam propagation direction) until the scattered light of the probe from the sample coincides with the marked spot on the screen. Now the pump and probe are well-overlapped on the sample.

Switching of the probe wavelength from 800 nm to visible wavelengths (NOPA output) may necessitate slight realignment of the optics. In transmission mode, relocation of the sample to a new focal plane can be done either by moving the sample or the focusing lens on a translational stage following the described procedure. A final slight adjustment of the CCD in the z-direction may be needed to achieve a better echelon image. In reflection mode, movement of the sample to a new focal plane would give rise to a gross misalignment of the subsequent optics because of the different outgoing angle of the probe beam from the sample. Instead of moving the sample in reflection mode, translation (in the z-direction) of the focusing lens maintains the focal plane regardless of the wavelength. This prevents the outgoing angle from changing and thus avoids gross misalignment. A final little adjustment of the CCD may produce a better echelon image and thus better signal to noise.

2.2.4 Echelon Images and Extraction of Temporal Signal

Signal, background and their reference images

Figure 2-12 displays the echelon images reconstructed by the CCD.
The left and right sides correspond to the signal image and its reference image, respectively. The signal image was obtained from an antimony thin film (85 nm) on a glass substrate. The polymer-based echelons are configured such that the relative time delay from step to step increases in 25 fs increments down each row and the step-delay increment from column to column is 500 fs. It will be convenient to use matrix notation to refer to specific square elements which represent specific time elements. For example, the earliest time element is represented by (1,1) which is located at the upper left corner. The coordinate (20,20) indicates the latest time point. Since the reference is inverted, the coordinates (20,20) and (1,1) in the reference image correspond to the element (1,1) and (20,20) in the signal image, respectively. The temporal signal is not obvious from the signal image at this moment. The temporal signal is hidden over variations produced by large beam fluctuations. The following section describes how to remove the variations and convert the images to a real

temporal signal.

In order to image an object at its image plane, a well-defined object plane is required. Also, intact reconstruction of the zeroth and higher order diffracted light at the image plane demands a high numerical aperture of the imaging optics. However, due to the finite thickness of the echelons and the distance between them, the object plane is not defined perfectly. The total thickness of the object is approximately 1 cm, which implies that any location of the CCD is not able to reconstruct the echelon perfectly. In addition, transmissive optics such as the beamsplitter and polarizer hamper good image reconstruction by inducing phase differences between collimated zeroth order and diverging higher order diffraction light. The optical quality of samples also affects the image quality in the signal and background images. The zeroth order beam is diffracted further from sample defects creating higher order contributions which make the signal image blurry. The size of the sample matters

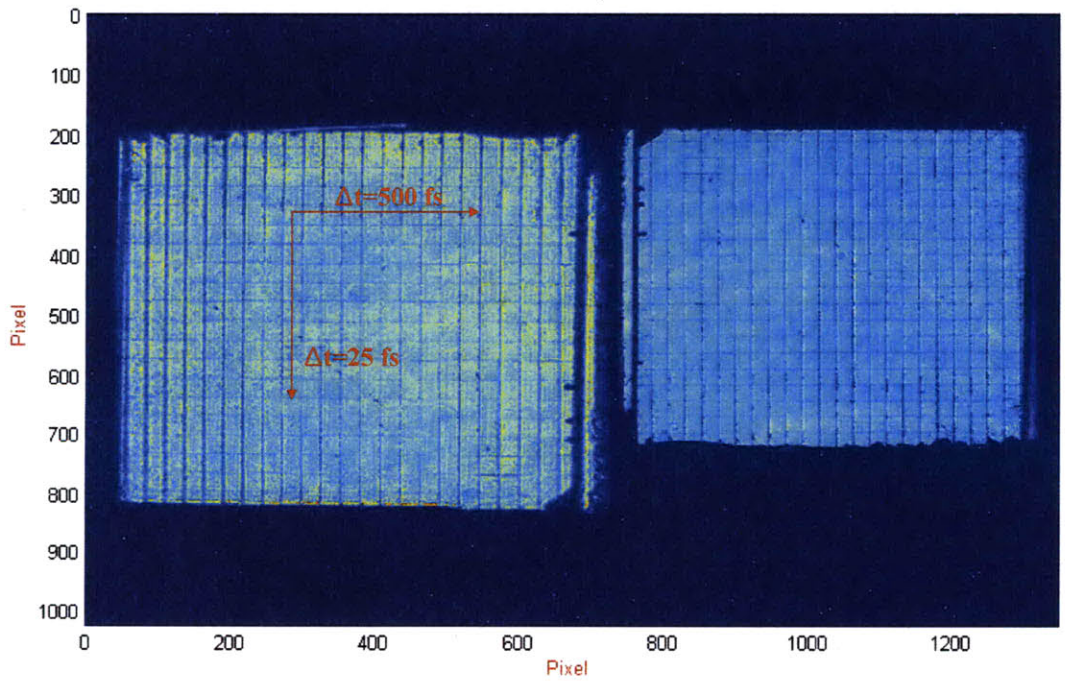

Figure 2-12: Raw echelon images reconstructed in the CCD (1024 pixel x 1344 pixel x 12 bit). The probe array forms the left-side image after interacting with the sample via reflection or absorption. It generates the right-side image by bypassing the sample. Each square is clearly visible, formed by two crossed echelons. There is one-to-one correspondence between the squares and time delays.

as well. If the sample size is comparable to the spot size of the zeroth order, other higher order diffraction light can be lost further hampering the reconstruction. This is especially true in reflection mode. Due to all of the above effects, diffracted light from echelon step edges does not form its own step edges at the image plane. Instead, it smears out to the neighboring square cells making the whole echelon image blurry. This can deteriorate the temporal signal during the decoding process. Much caution is necessary to avoid this artifact.

An automatic algorithm recognizes the coordinates of 21 strong diffraction lines along both directions by finding local minima, and generates 20 x 20 grids. The grids are overlayed on the raw images as shown in figure 2-13. The grids are used for assigning each square and extracting the temporal signal. Each grid consists of approximately 25 x 25 pixels, but only a fraction (60–80%) of them is used for conversion to the time signal in order to avoid the effects of diffracted light smearing

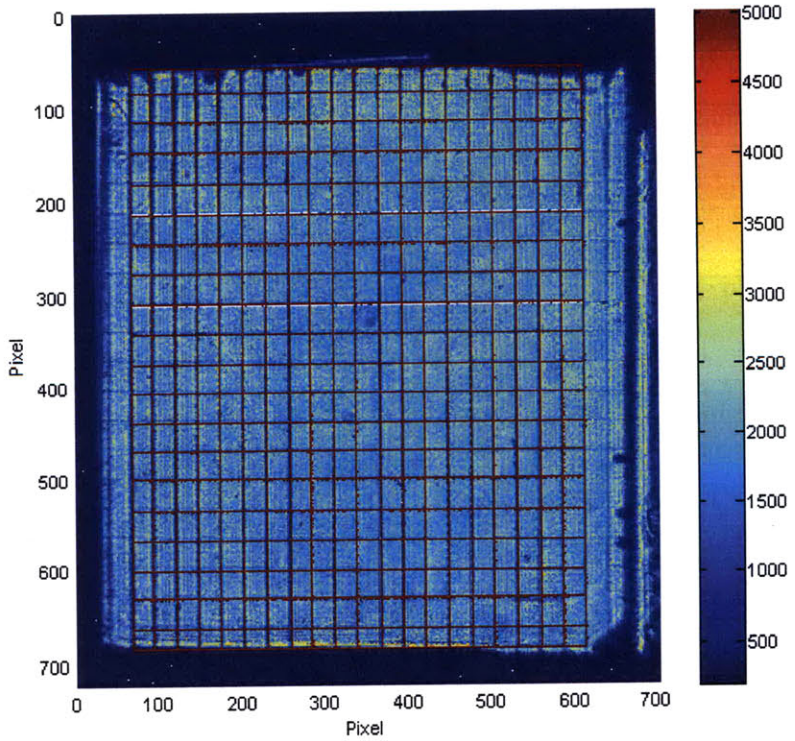

Figure 2-13: Partitioned echelon image. The (20×20) spatial elements are divided for the space-to-time conversion. The boundary lines are created based on the coordinates of diffraction peaks from step edges in the thick and thin echelons.

into adjacent cells.

Extraction of time-dependent signal

Every single-shot measurement involves two laser shots. The first shot generates the probe array or the echelon image in the absence of the pump and the second shot yields the array in the presence of the pump. Of course, the array by the second shot exhibits the optical change by the excitation. If the beam profile over the cross section of the echelon is perfectly flat or uniform, then only the array with the pump yields the temporal signal without the need for the first shot. However, it is impossible to obtain such a perfect beam profile. Even though the profile is fairly flat, there are fast-varying intensity variations which are mostly ascribed to diffraction from optics defects. When mapping the image intensity to the temporal signal, such spatial variations would superimpose on the real temporal signal. If the temporal signal is small, the variations dominate and hide the real signal. A three-dimensional view of the signal image in figure 2-13 is illustrated in figure 2-14 in which average intensities over each grid are represented. Even though the beam profile is fairly flat, identification of the temporal signal is impossible due to large beam variations.

The fluctuating beam profile or the spatial variations can be corrected if they are known, however. This supports the need for the first shot without pump excitation. Simple division of one by the other smooths out the beam profile as the spatial variations disappear. Now only the real signal created by the pump is encoded as spatial deviations from the flat array. The array or the echelon image obtained in the absence of pump is called a "background image". The image with pump excitation is called a "signal image". The pixel-to-pixel division of the signal image by the background image yields the "normalized signal image" (equation 2.3):

$$\frac{\Delta I + I}{I} = \frac{signal}{background}. \tag{2.3}$$

The division produces a beautifully normalized signal image, as shown in figure 2-15. The spatial beam fluctuations disappear significantly and the temporal signal is

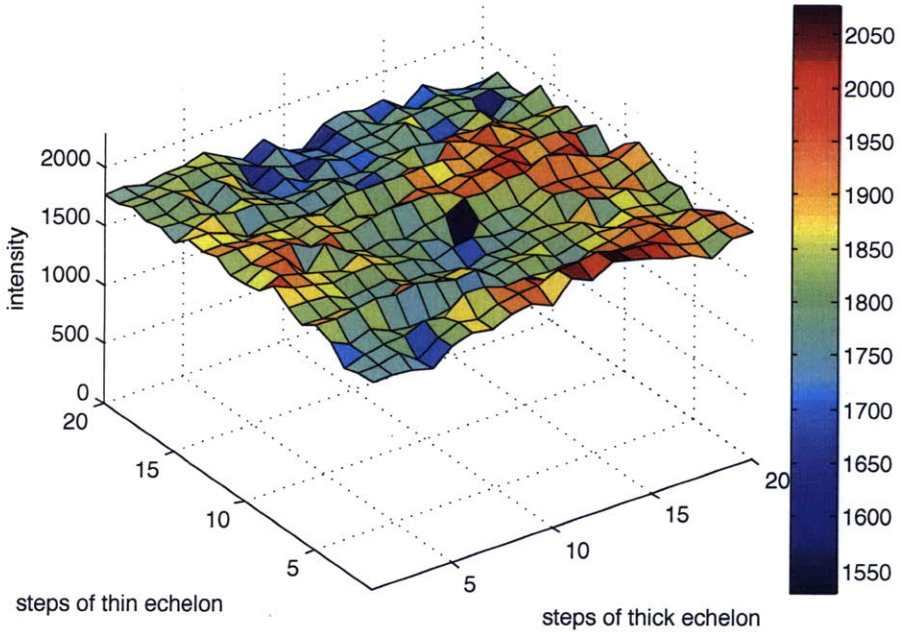

Figure 2-14: Three-dimensional view of the probe beam profile over the crossed echelons. The beam is fairly flat over the cross-section but there are spatial intensity fluctuations originating from optics defects.

pronounced. A three-dimensional view reveals the temporal information in figure 2-16. The color of each point represents the average intensity over pixels forming the inner part of the square. The temporal signal is clearly identified. A sharp increase in the reflectivity is induced upon the pump excitation and then the reflectivity decays gradually. Note how greatly the image is flattened before the time origin.

Even the division, however, would not produce a perfectly flat array because two laser shots are not identical. Corrugations (noise) are obvious in figure 2-16. There is always shot-to-shot noise in laser intensity which is attributed to thermal fluctuations and air current. At a given shot-to-shot noise level, there is an efficient way to compensate for the noise in the single-shot measurement. That is to use the "reference images". The background and signal images have their own reference images in the CCD. As mentioned earlier, the background and signal arrays pass through or are reflected from the sample, while their reference arrays are directed to the CCD without interacting with the sample. Division of the "reference image of the signal" by the "reference of the background" yields a "normalized reference

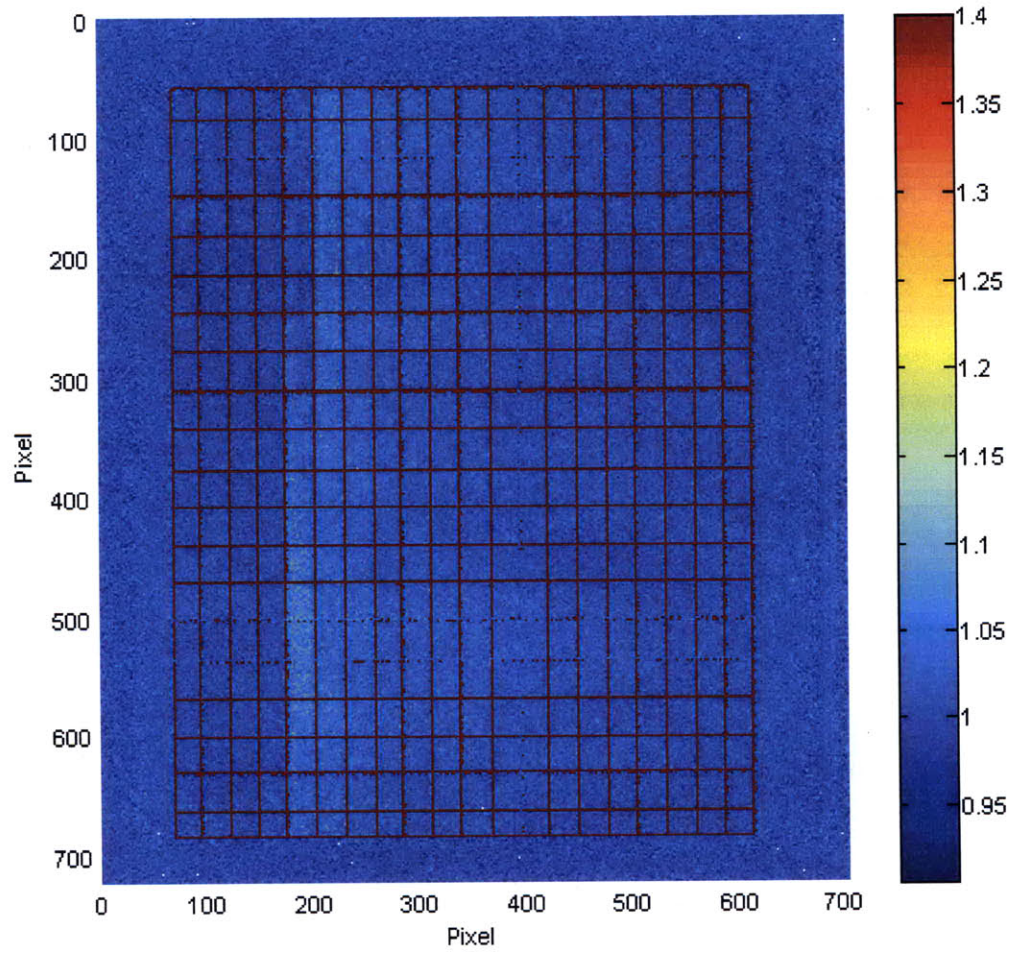

Figure 2-15: Normalized signal image. A pixel-to-pixel division of the signal image by the background image yields a pronounced time-dependent signal. The division flattens the signal image except for the actual temporal signal because the signal and background beam are derived from the same beam, recorded on different laser shots, so fluctuations due to imperfections encountered in the beam path are eliminated. The only difference between them is whether or not they are obtained in the presence of the pump pulse.

image", but shot-to-shot fluctuations prevent the normalized reference image from being perfectly flat. However, imperfect flatness or small variations due to the shot-to-shot noise appear commonly in the "normalized signal image" as well as in the "normalized reference image". This suggests another division as a way to compensate for the shot-to-shot noise:

$$\frac{\Delta I + I}{I} = \frac{signal}{background} \div \frac{reference^{signal}}{reference^{background}}. \tag{2.4}$$

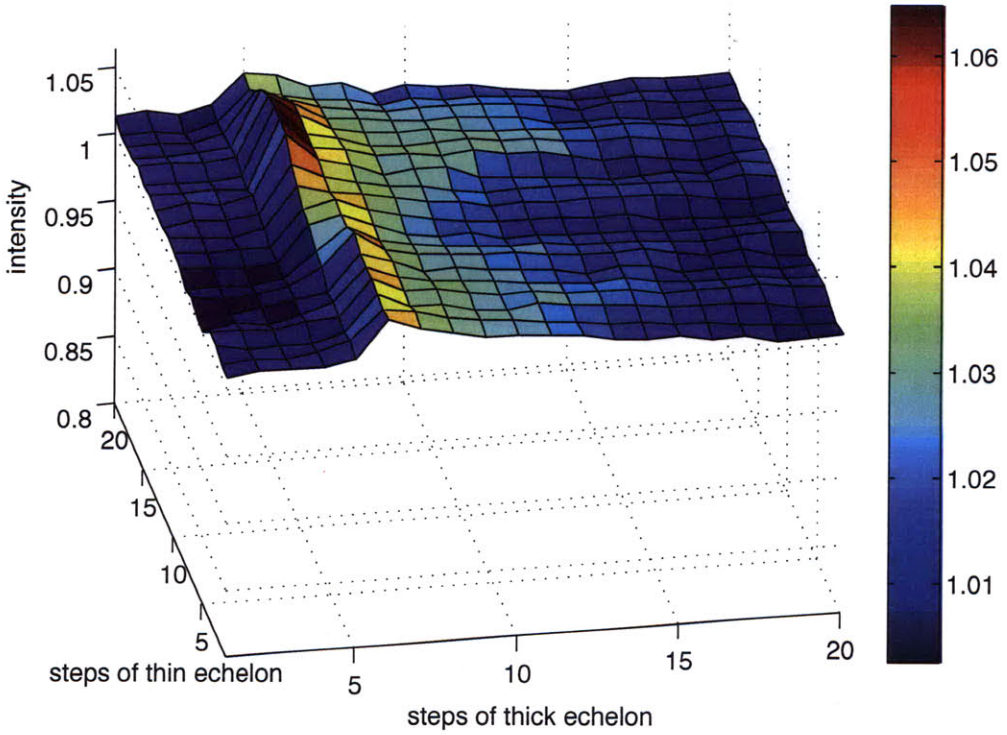

Figure 2-16: Three-dimensional view of the normalized signal image after the averaging process. Each data point represents an average intensity over a fraction (60–80%) of pixels inside each square in the normalized signal image. The pump arrival time is clearly visible and reflectivity exhibits a positive change within the time window. Corrugations originate from shot-to-shot laser fluctuations between the signal and background shot.

Pixel-to-pixel division between the normalized signal image and the normalized reference image is not possible because of different image sizes (Note the different magnification ratio in the signal and the reference images). Pixel-to-pixel division is possible only for the signal-background image pair and the reference image pair. Instead, grid-to-grid (not pixel-to-pixel) division can be used after retrieving the average intensity of every square and generating 20 x 20 grids. Division of the normalized signal image by the normalized reference image yields another 20 x 20 data points as shown in figure 2-17. Noticeable changes are visible. It appears that the reflectivity oscillates near time zero. In addition, the background fluctuation level before the time origin seems smaller. It is trivial to display the temporal signal by unfolding the 2-dimensional spatial signal to the 1-dimensional signal using equation 2.5 and 2.6.

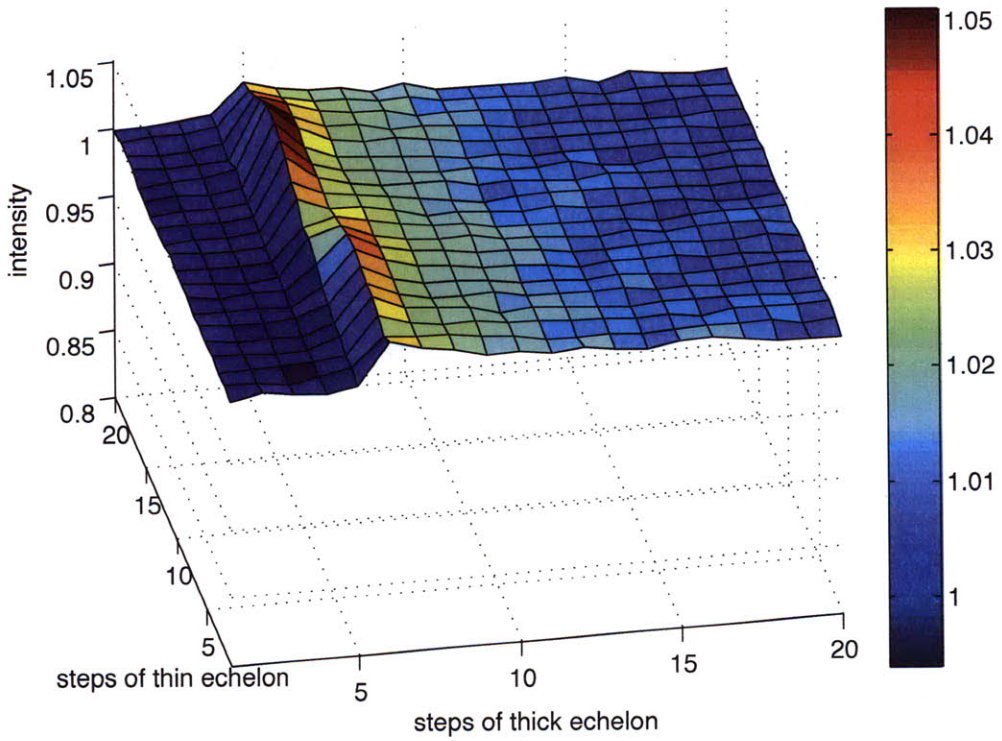

Figure 2-17: Three dimensional view of the actual temporal signal. The actual signal is more pronounced and wavy corrugations are more suppressed after compensating the shot-to-shot laser fluctuations between the signal and background shots using two reference images. Oscillations due to lattice vibrations are evident in the reflectivity change as small modulations along the thin echelon dimension.

The indices i and j indicate i^{th} row and j^{th} column in the image, respectively:

$$\frac{\Delta I + I}{I}(t) = \frac{signal}{background}(i,j) \div \frac{reference^{signal}}{reference^{background}}(i,j), \tag{2.5}$$

$$\text{where } t \text{ (in fs)} = 25 \times (i-1) + 500 \times (j-1), \quad (i \text{ and } j = 1-20). \tag{2.6}$$

A series of temporal signals are recovered to reveal such dramatic effects of the calibration by the background and reference images as shown in figure 2-18. Graph (a) represents the time trace of the original signal image corresponding to figure 2-14. As inspected earlier, the real temporal signal is not distinguishable because of large amplitude (10–15%) spatial fluctuations. A black line in graph (b) shows the time trace of the normalized signal image (figure 2-16), which was obtained by

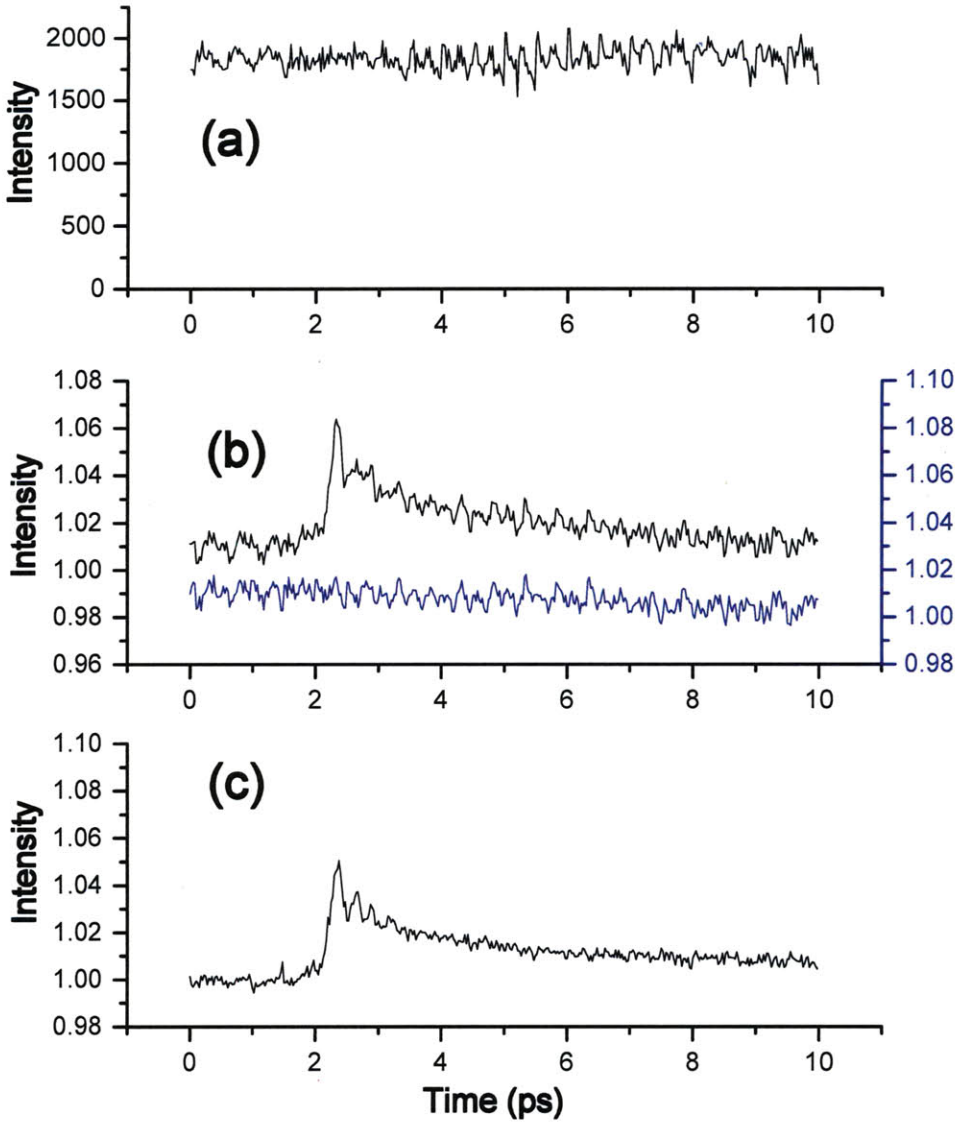

Figure 2-18: Three different time traces. (a) represents just intensity variations along the 400 time points in the raw signal image. The actual signal is hidden by the large spatial beam fluctuations. In (b), the black line corresponds to the temporal signal extracted from the normalized signal image (signal image divided by the background). The blue line indicates the time series obtained from the normalized reference (the reference image of the signal divided by the reference image of the background). There is a strongly correlated noise pattern between them which results mainly from shot-to-shot noise. (c) shows the time-dependent signal of Sb decoded finally via background (flattening beam profile) and reference (removal of shot-to-shot noise) calibration.

dividing the signal image by the background image. As seen before, the background calibration removes the spatial variations substantially and makes the temporal signal pronounced. At this point, the noise level (1–2%) is still significant. The blue line describes the time trace of the normalized reference image which was recovered by dividing the reference of the signal image by the reference of the background image. As mentioned earlier, the purpose of the reference images is to compensate the shot-to-shot noise between the background and signal shots. Common features are obvious between the two time traces (black and blue), implying that the shot-to-shot noise can be eliminated by division between them. Finally, the division yields a clear time signal (c) which is equivalent to the time trace of figure 2-17. The signal becomes much cleaner through calibration using the reference images, and the noise level reduces down to a few tenths of a percent. The signal demonstrated here agrees with other experimental results by Zeiger *et al* [ZVC+92]. The oscillations in the reflectivity are attributed to lattice vibrations which are launched by the excitation pulse discussed in detail in chapter 3.

2.3 Beam Propagation through Echelons

2.3.1 Temporal Dispersion of Probe Pulses

An ultrashort pulse requires more caution in dealing with optics than does a cw beam because of dispersion of the ultrashort pulse which has a broad spectral width. It is important to examine the propagation of a light pulse in a transparent medium and to keep the results in mind during the course of experiments.

An ultrashort pulse undergoes a phase distortion causing an increase of its pulse width due to its wide spectral range and due to group velocity dispersion in transparent media [Rul05]. The Fourier transform of a Gaussian pulse is given as

$$E_0(w) = exp(\frac{-(w - w_0)^2}{4\Delta}). \tag{2.7}$$

After the pulse propagates a distance l, the spectrum is changed to

$$E_0(w,l) = E_0(w)exp(-ik(w)l), \quad k(w) = nw/c, \tag{2.8}$$

where $k(w)$ is a frequency-dependent wave vector and expressed in a power series by a Taylor expansion:

$$k(w) = k(w_0) \; + \; k'(w - w_0) \; + \; \frac{1}{2}k''(w - w_0)^2 \; + \cdots, \tag{2.9}$$

where

$$\begin{aligned} k' &= (\frac{dk(w)}{dw})_{w=w_0}, \\ k'' &= (\frac{d^2k(w)}{dw^2})_{w=w_0}. \end{aligned} \tag{2.10}$$

The pulse spectrum by equation 2.8 can be rearranged into

$$E_0(w,l) = E_0(w)exp[-ik(w_0)l - ik'l(w - w_0) - (\frac{1}{4\Delta} + \frac{i}{2}k'')(w - w_0)^2]. \tag{2.11}$$

In order to derive the time evolution of the electric field in the pulse, we need to take the inverse Fourier transform of equation 2.11:

$$\varepsilon(t,l) = \int_{-\infty}^{\infty} E(w,l)e^{iwt}\mathrm{d}w, \tag{2.12}$$

so that

$$\varepsilon(t,l) = \sqrt{\frac{\Delta(l)}{\pi}}exp[iw_0(t - \frac{l}{v_\phi(w_0)})] \times exp[-\Delta(l)(t - \frac{l}{v_g(w_0)})^2], \tag{2.13}$$

where

$$v_\phi(w_0) = (\frac{w}{k})_{w_0}\,, \quad v_g(w_0) = (\frac{dw}{dk})_{w_0}\,, \quad \frac{1}{\Delta(l)} = \frac{1}{\Delta} + 2ik''l. \tag{2.14}$$

The first exponential term of equation 2.13 says that the phase of the center frequency w_0 is delayed by an amount of l/v_ϕ after propagation over the distance l.

Here, v_ϕ is the phase velocity, w/k. In the second exponential term of equation 2.13, it is observed that the pulse keeps a Gaussian envelope through the distance l with the envelope being delayed by an amount of l/v_g where v_g represents the group velocity dw/dk. By rewriting Δ(l) as

$$\Delta(l) = \frac{\Delta}{1+\xi^2 l^2} - i\frac{\Delta\xi l}{1+\xi^2 l^2}, \qquad \xi = 2\Delta k'', \tag{2.15}$$

and substituting equation 2.15 into the second exponential term of equation 2.13, it can be rearranged into

$$exp[-\frac{\Delta}{1+\xi^2 l^2}(t-\frac{l}{v_g})^2 + i\frac{\Delta\xi l}{1+\xi^2 l^2}(t-\frac{l}{v_g})^2]. \tag{2.16}$$

The real part of equation 2.16 indicates that the pulse is still a Gaussian envelope, while the pulse duration changes. The pulse widths (FWHM) before and after the propagation are given by

$$\tau_0 = \sqrt{\frac{4ln2}{\Delta}}, \tag{2.17}$$

$$\tau = \sqrt{\frac{4ln2}{\frac{\Delta}{1+\xi^2 l^2}}} = \tau_0\sqrt{1+\xi^2 l^2} = \tau_0\sqrt{1+4\Delta^2 k''^2 l^2}, \tag{2.18}$$

where k'' is called the "group velocity dispersion (GVD)". Since the factor $\sqrt{1+4\Delta^2 k''^2 l^2}$ is always larger than one, the pulse duration is always broadened after the propagation. For a large propagation distance l, $\tau/\tau_0 \simeq \Delta k'' l \simeq \tau_0^{-2} k'' l$. This states that pulse broadening is more pronounced for an initially shorter pulse. This is the natural consequence of larger dispersion of the pulse with a spectrally broader width.

The imaginary part of equation 2.16, i.e., the phase, contains a quadratic term in time, which tells that the frequency gets linearly chirped as $w(t) = \partial\phi/\partial t = w_0 + \beta t$. According to equation 2.16, a positive k'' yields a positive β. When $k'' > 0$, the frequency is said to be positively chirped meaning that the instantaneous frequency is more red in the leading part of the pulse, and more blue in the trailing part.

As mentioned previously, the group velocity dispersion k'' is responsible for the

broadening of the pulse width. Since k is $n(w)w/c$, taking the second derivative of k with respect to w eventually yields the following equation:

$$k'' = \frac{\lambda^3}{2\pi c^2}\frac{d^2n}{d\lambda^2}. \tag{2.19}$$

For a variety of transparent materials, the index of refraction can be estimated precisely using the empirical Sellmeier's formula. Sellmeier's formula describes the variation of the index with wavelength and has the following functional form:

$$n^2 - 1 = \lambda^2[\frac{B_1}{\lambda^2 - C_1} + \frac{B_2}{\lambda^2 - C_2} + \frac{B_3}{\lambda^2 - C_3}], \tag{2.20}$$

where B and C have been measured for many materials and are available in the literature. Equations 2.18, 2.19, and 2.20 make it possible to determine how much the pulse is broadened after the propagation over a distance l of materials. Since the echelons have different step thickness, it is expected that the pulse durations will be different for every probe piece. It is worth estimating pulse durations for each step using the above equations. The Sellmeier's equation with proper coefficients yields the refractive index of fused silica from which the new echelons are made (figure 2-19). The second derivative of the index, $d^2n/d\lambda^2$ is estimated as 0.03988 μm^{-2} at 800 nm and 0.14622 μm^{-2} at 600 nm from figure 2-19. Subsequently equation 2.19 yields the GVD of 0.01083 $fs^2/\mu m$ at 800 nm and 0.01676 $fs^2/\mu m$ at 600 nm, respectively.

Figure 2-20 illustrates the increase in the pulse duration ($\Delta\tau$, not an absolute width τ) at different time delays which are created by the different step thickness. The compressor is assumed to be optimized for the earliest probe pulse. As expected, it is revealed that an originally shorter pulse undergoes more severe pulse broadening. The pulse broadening by the GVD imposes limitations on the application of the transmissive echelons to attosecond spectroscopy. Reflective echelons must replace the transmissive ones for the application. At a given same pulse width, the pulse broadening is more pronounced at 600 nm than at 800 nm because the GVD of fused silica exhibits a higher value at 600 nm.

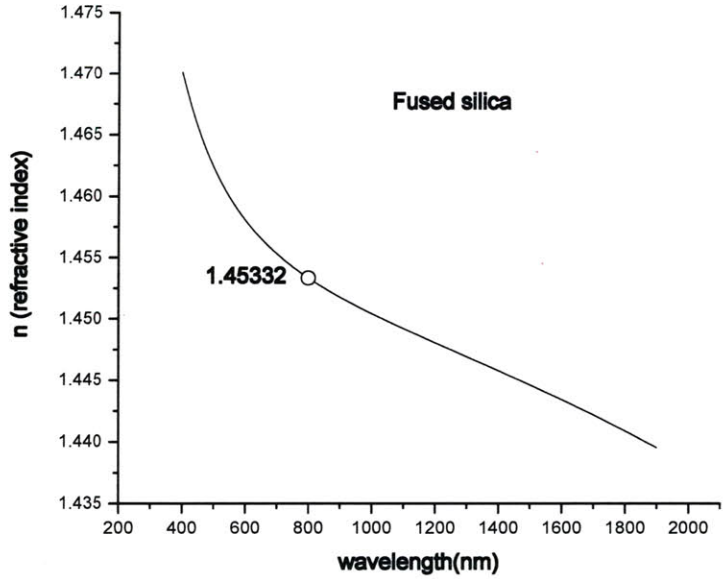

Figure 2-19: Refractive index change of fused silica as a function of wavelength. The curve was obtained from Sellmeier's equation.

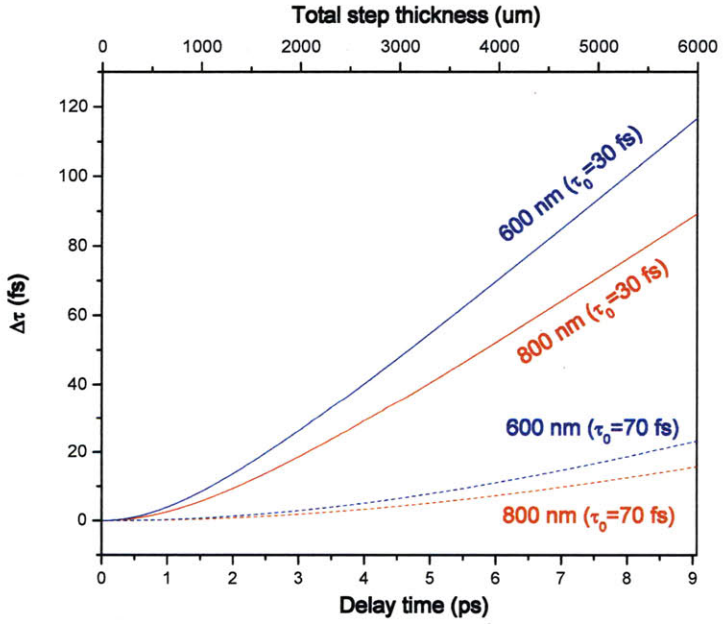

Figure 2-20: Temporal broadening of probe piece as a function of delay time through echelons due to group velocity dispersion. Initially shorter pulses experience more severe pulse broadening through the echelons because of their wider bandwidth.

2.3.2 Spatial Beam Profile at the Fourier Plane

In the dual echelon single-shot method, a temporally divided 2-D probe array is focused and interacts with the pump beam via materials at the focal plane. If an incoming beam is Gaussian, then its intensity profile is also Gaussian at the focal plane. This is the case for most conventional pump-probe techniques. However, the intensity distribution of the 2-D array at the Fourier plane may not form a Gaussian profile in the current dual echelon technique because of diffraction from step edges. The echelon single-shot method uses the imaging technique. No matter how the beam profile looks at the Fourier plane, the original image of the 2-D array is reconstructed at the image plane. However, sometimes the system is not ideal. For example, the sample might have defects over the probe spot or the pump beam may be structured over the sample spot because of optics defects. The inhomogeneity would distort the image quality during the reconstruction process as described by the inverse Fourier transform. Eventually, the image would affect the sensitivity of the temporal signal or create unusual noise. Therefore, it is important to examine the beam profile of the 2-D array at the Fourier plane and to gain insight into the effect of the profile on the temporal signal.

Fourier methods in Fraunhofer diffraction

According to Fraunhofer diffraction theory [Hec02], a far field diffracted field by an aperture is given as

$$E(X,Y) = \frac{\varepsilon_A e^{i(\omega t - kR)}}{R} \int\int_{Aperture} e^{ik(Yy+Zz)/R} dydz. \tag{2.21}$$

This formula depicts an arbitrary diffracting aperture in the yz plane upon which is incident a monochromatic plane wave. R is the distance from the center of the aperture to the output point where the field is $E(Y,Z)$. ε_A denotes the source strength per unit area of the aperture. The time-varying term $e^{i(\omega t - kR)}$ connects the phase relation between the net disturbance at the point (X,Y) and that at the center of the aperture. This phase term is not important since we are interested in the relative

amplitude distribution of the field. The factor $1/R$ represents the attenuation of field amplitude with distance from the aperture. The factor ε_A is assumed to be invarient over the aperture, but this is not the general case. The variations in ε_A, which originate from irregular optical properties over the aperture, can be described by a single complex quantity

$$A(y,z) = A_0(y,z)e^{i\phi(y,z)}, \tag{2.22}$$

which is called the "aperture function". The amplitude of the field over the aperture is represented by $A_0(y,z)$ and the phase fluctuation by $e^{i\phi(y,z)}$. Accordingly, $A(y,z)dydz$ is proportional to the diffracted field emitting from the infinitesimal source element $dydz$. Considering all of these, equation 2.21 can be rewritten as

$$E(Y,Z) = \int_{-\infty}^{+\infty}\int_{-\infty}^{+\infty} A(y,z)e^{ik(Yy+Zz)/R}dydz. \tag{2.23}$$

It is helpful to envision $dE(Y,Z)$ at a given point P as if it were a plane wave propagating in the direction of $\vec{k}$ (figure 2-21) and having an amplitude determined by $A(y,z)dydz$. It is convenient to introduce the spatial frequency k_Y and k_Z as

$$k_Y = kY/R \quad \text{and} \quad k_Z = kZ/R. \tag{2.24}$$

For each point on the image plane, there is a corresponding spatial frequency. The diffracted field can now be expressed as follows:

$$E(k_Y,k_Z) = \int_{-\infty}^{+\infty}\int_{-\infty}^{+\infty} A(y,z)e^{i(k_Yy+k_Zz)}dydz. \tag{2.25}$$

This states that the field distribution in the Fraunhofer diffraction pattern is the Fourier transform of the field distribution across the aperture. Conversely, the aperture function is reconstructured by the inverse Fourier transform:

$$A(y,z) = \frac{1}{(2\pi)^2}\int_{-\infty}^{+\infty}\int_{-\infty}^{+\infty} E(k_Y,k_Z)e^{-i(k_Yy+k_Zz)}dk_Ydk_Z. \tag{2.26}$$

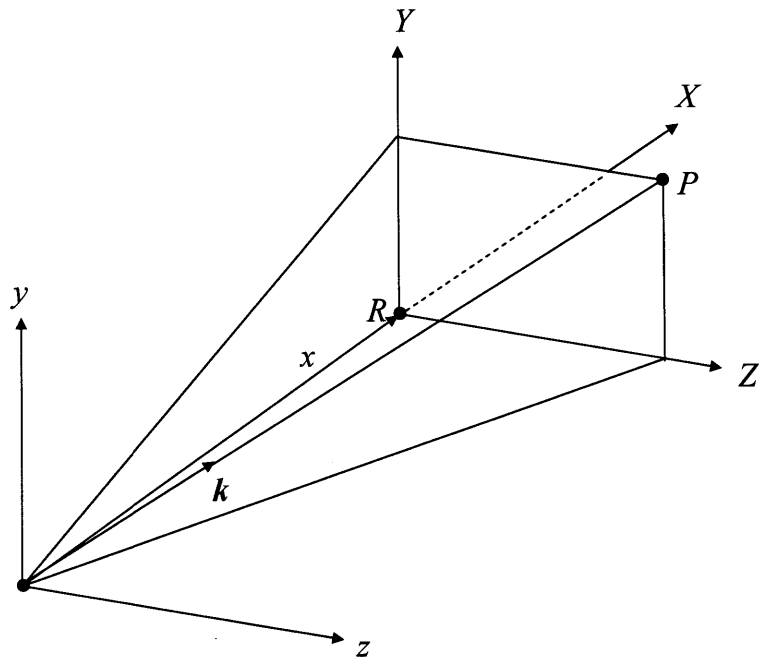

Figure 2-21: The field distribution in the Fraunhofer diffraction pattern is the Fourier transform of the field distribution across the aperture.

Array theorem

The Fraunhofer diffraction field $E(Y, Z)$ at the point P on the image plane will be a superposition of the individual fields at P arising from each separate aperture. If the aperture is the array of a repeating basis A_I, the Fourier transform of the entire aperture function is simplified by the Fourier transform of the basis:

$$E(k_Y, k_Z) = \sum_{j=1}^{N} \int_{-\infty}^{+\infty} \int_{-\infty}^{+\infty} A_I(y', z') e^{ik(Y(y_j+y')+Z(z_j+z'))/R} dy' dz' \quad (2.27)$$

$$= \int_{-\infty}^{+\infty} \int_{-\infty}^{+\infty} A_I(y', z') e^{ik(Yy'+Zz')/R} dy' dz' \sum_{j=1}^{N} e^{ik(Yy_j+Zz_j)/R} \quad (2.28)$$

$$= \int_{-\infty}^{+\infty} \int_{-\infty}^{+\infty} A_I(y', z') e^{i(k_Y y'+k_Z z')} dy' dz' \sum_{j=1}^{N} e^{i(k_Y y_j+k_Z z_j)}, \quad (2.29)$$

or

$$\mathcal{F}\{A(y, z)\} = \mathcal{F}\{A_I(y, z)\} \cdot \mathcal{F}\{A_\delta\}. \quad (2.30)$$

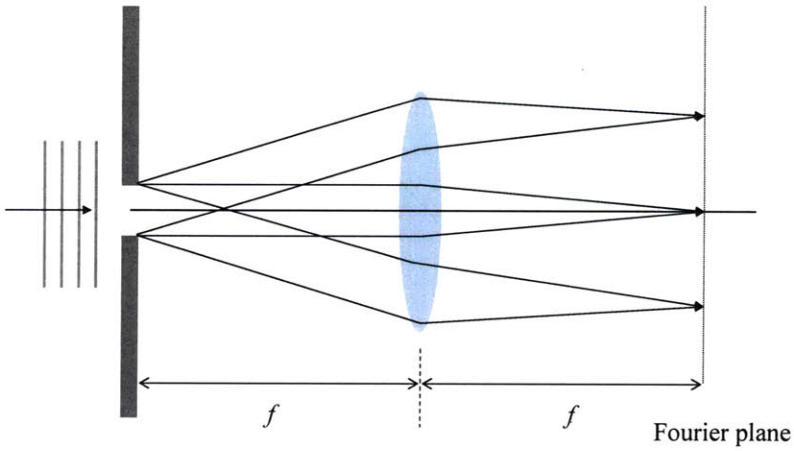

Figure 2-22: Lens as a Fourier transformer. The light diffracted by an object at the front focal point of a lens converges to form the far-field diffraction pattern at the back focal point of the lens.

In equation 2.29, the integral is the Fourier transform of a basis aperture, while the sum is the transform of an array of delta functions which denote the coordinates of the individual apertures as follows:

$$A_\delta = \sum_j \delta(y - y_j)\delta(z - z_j). \tag{2.31}$$

Equation 2.30 is a statement of the array theorem, which says that the field distribution in the Fraunhofer diffraction pattern of an array of identical apertures equals the Fourier transform of an individual aperture function multiplied by the pattern that would result from a set of point sources arrayed in the same configuration (which is the transform of A_δ). In fact, the array theorem is also a mathematical outcome of the convolution theorem. The entire aperture function is built by convolving the basis aperture with the array of delta function A_δ and the Fourier transform of the convolved function is represented by the product of each of the Fourier transforms of the constituents (convolution theorem).

Lens as a Fourier transformer

Figure 2-22 shows a slit, located in the front of focal plane of a converging lens, illuminated by plane waves. This object scatters the plane waves, which are collected

by the lens, and parallel rays converge at the other focal plane. If a screen were placed there, we would see the far-field diffraction pattern of the slit spread across it. In other words, the electric field distribution across the slit is transformed by the lens into the far-field diffraction pattern. As shown already, the Fraunhofer electric field pattern corresponds to the exact Fourier transform of the aperture function. Accordingly, the diffraction pattern of the aperture at the focal plane is represented by the Fourier transform of the aperture function. For this reason, the focal plane is called the Fourier or transform plane. When describing the diffraction pattern by the lens in terms of the Fourier transform 2.25, the wave vectors in equation 2.24 are rewritten as equation 2.32 by replacing the R by the focal length f of the lens:

$$k_Y = kY/f \quad \text{and} \quad k_Z = kZ/f. \tag{2.32}$$

The lens as the Fourier transformer can be described mathematically using Fresnel-Kirchhoff diffraction theory and the derivation is found in [Hau84].

Example 1: a square aperture

As an illustration of the Fourier method, let's examine the diffraction pattern of a square aperture. The 2-D array formed by two crossed echelons can be considered as a collection of the square apertures with a different phase factor. It will be shown that the diffraction pattern of the square aperture serves as an envelope function of the diffraction pattern for the entire 2-D echelon array:

$$A(y,\ z) = \begin{cases} A_0 & \text{when} - b/2 \leq y, z \leq b/2, \\ 0 & \text{otherwise.} \end{cases} \tag{2.33}$$

The Fourier transform of the aperture function yield a 2-D sinc function:

$$\begin{aligned} E(k_Y, k_Z) &= \int_{-\infty}^{+\infty}\int_{-\infty}^{+\infty} A(y,z)e^{i(k_Y y + k_Z z)}dydz \\ &= \int_{-b/2}^{+b/2}\int_{-b/2}^{+b/2} A_0 e^{i(k_Y y + k_Z z)}dydz \end{aligned}$$

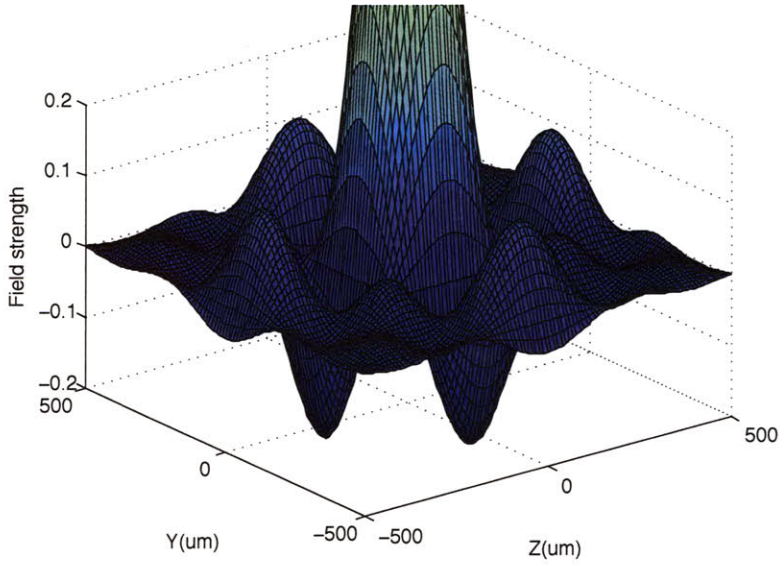

Figure 2-23: Field distribution of the square aperture at the Fourier plane. The central peak is normalized to have an amplitude of 1. Here it is truncated to emphasize the small side peaks.

$$\begin{aligned} &= A_0 b^2 \mathrm{sinc}(\frac{bkY}{2f})\mathrm{sinc}(\frac{bkZ}{2f}) \\ &= A_0 b^2 \mathrm{sinc}(\frac{\pi bY}{f\lambda})\mathrm{sinc}(\frac{\pi bZ}{f\lambda}). \end{aligned} \tag{2.34}$$

Figure 2-23 shows the field distribution at the Fourier plane of the aperture. The parameters used to generate the distribution are $b = 500$ µm, $f = 10$ cm, and $\lambda = 800$ nm. The square of the field strength yields the diffraction pattern and local intensity maxima occur at $\frac{\pi bY}{f\lambda} = 0, \pm\frac{3}{2}\pi, \pm\frac{5}{2}\pi, \pm\frac{7}{2}\pi \cdots$. For the above parameters for b, f, and λ, maxima appear at $Y = 0, \pm\frac{3}{2}160$ µm, $\pm\frac{5}{2}160$ µm, $\pm\frac{7}{2}160$ µm$\cdots$ in the Y direction.

Example 2: an array of N slits without phase difference

We have examined the beam profile of a square-shape incoming beam at the focal plane. How does the diffraction pattern change after adding apertures? The array theorem answers the question immediately. It would be easy to consider the slit instead of the aperture. First let's use two slits and suppose that they are contacting each other and their widths b are identical. Then, the aperture function A_I of the

basis (a single slit) and the array function A_δ are written as follows:

$$A_I(y) = \begin{cases} 1 & \text{when} - b/2 \leq y \leq b/2, \\ 0 & \text{otherwise,} \end{cases} \tag{2.35}$$

and

$$A_\delta = \delta(y + b/2) + \delta(y - b/2). \tag{2.36}$$

The Fourier transform of the aperture function yields $b\ \mathrm{sinc}(\frac{k_Y b}{2})$. The transform of array function produces $e^{ik_Y b/2} + e^{-ik_Z b/2} = 2\cos(k_Y b/2)$. Therefore the beam profile is given by the product $2b\ \mathrm{sinc}(\frac{k_Y b}{2}) \cdot \cos(k_Y b/2)$. The cosine term is additional, originating from the array function. The general form of the array function's Fourier transform is easily derived:

$$\mathcal{F}\{A_\delta\} = 2\Sigma_{j=1}^{N/2} \cos\frac{(2j-1)k_Y b}{2}, \quad \text{for even number of } N, \tag{2.37}$$

$$\mathcal{F}\{A_\delta\} = 1 + 2\Sigma_{j=1}^{\frac{N-1}{2}} \cos\frac{jk_Y b}{2}, \quad \text{for odd number of } N. \tag{2.38}$$

For several N's (for $f = 10$ cm and $\lambda = 800$ nm), the beam profiles are revealed in figure 2-24. The array functions were normalized by the number of the slits so that the maximum intensity always yields 1. It is apparent the spot size is inversely proportional to the number of slits. It has been assumed that there is no phase variation over the aperture function. However, there are spatial phase variations over the echelons because of the different step thickness.

Example 3: an array of N slits with phase difference

The introduction of phase variations over the aperture function would simulate the actual beam profile of the echelon array at the sample plane more accurately. The method to include the phase variations was briefly mentioned in equation 2.22. It would not be difficult to consider all of the probe pieces ($20 \times 20 = 400$) in order to

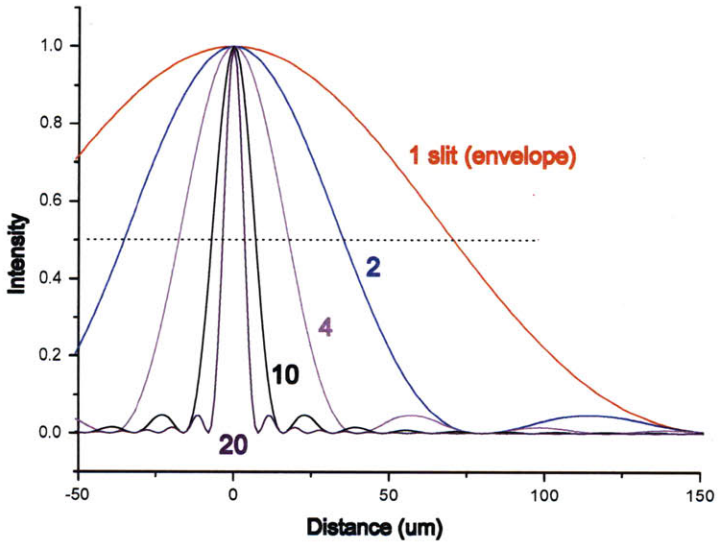

Figure 2-24: Beam intensity profile at the Fourier plane (focal plane or sample plane) resulted from N slits with no phase difference between them. The beam diameter decreases with increasing numbers of slits. The beam profile from a single slit is referred to as an envelope function.

produce the diffraction pattern at the Fourier plane, but it is more intuitive to have 20 pieces (or less) which are divided by the 20 steps of the thin echelon. The array is here viewed as slits rather than square apertures for simplicity. The phase difference between two adjacent steps is given by equation 2.2. The refractive index n of the echelon is assumed as 1.453 for all wavelengths under investigation (540, 720, and 800 nm). The aperture function A_I is unchanged and is given in equation 2.35. The array function must be modified due to the phase factor. The amplitude term is the same, while the phase term needs to be introduced carefully. Figure 2-25 illustrates how to construct the array function. The arrows represent delta functions at $y = \frac{\pm(2j-1)}{2}b$. Below the notation of the delta functions, relative phases are described with respect to the origin. The array function for the 20 slits is represented as follows:

$$\begin{aligned} A_\delta &= \Sigma_{j=1}^{10}[\delta(y - \frac{2j-1}{2}) \exp\{id\frac{(n-1)}{\lambda}\frac{2j-1}{2}\} \\ &+ \delta(y + \frac{2j-1}{2}) \exp\{-id\frac{(n-1)}{\lambda}\frac{2j-1}{2}\}] \end{aligned}$$

$$= \Sigma_{j=1}^{10}[\delta(y - \frac{2j-1}{2}) \exp\{i\phi\frac{2j-1}{2}\}$$
$$+ \delta(y + \frac{2j-1}{2}) \exp\{-i\phi\frac{2j-1}{2}\}], \tag{2.39}$$

where

$$\phi = \frac{n-1}{\lambda}d. \tag{2.40}$$

Finally, the Fourier transform of the array function A_δ yields the following equation:

$$\mathcal{F}\{A_\delta\} = 2\Sigma_{j=1}^{10} \cos[\frac{(2j-1)(k_Y d + \phi)}{2}], \tag{2.41}$$

where k_Y is given by equation 2.32. Based on equations 2.39 and 2.40 together with the sinc function, which is the Fourier transform of the aperture function, the intensity distribution at the sample plane was recovered. For several different numbers of slits, the beam profile is represented in figure 2-26 where the beam wavelength and focal length are 800 nm and 10 cm, respectively. The phase change by the step thickness corresponds to about 2.7π. Since the phase difference is not a multiple of 2π, it causes a strong destructive interference at the center and two big constructive interference peaks out of the center. The beam profile constructed by a single slit serves as an envelope function for other beam profiles. Within the envelope function, the gap

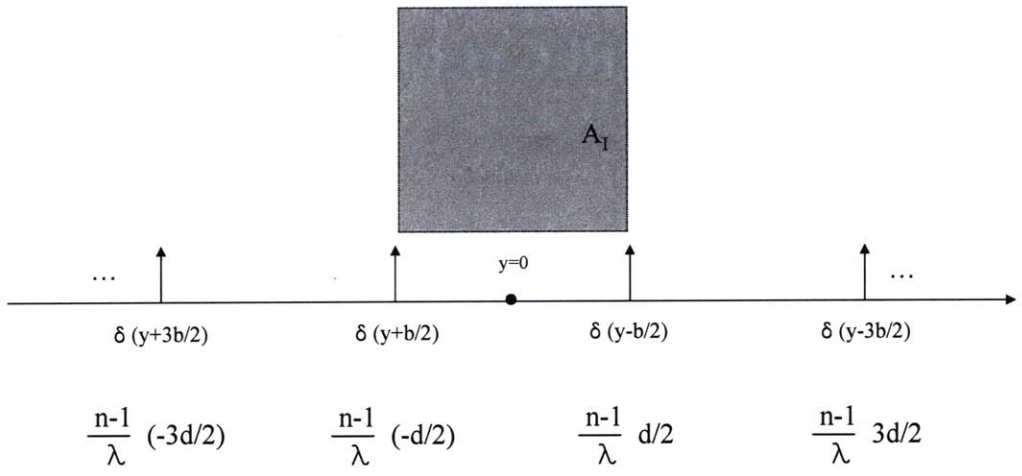

Figure 2-25: Schematic representation of array function for N slits with a phase difference. The aperture function A_I of the basis (a slit) is represented by the square.

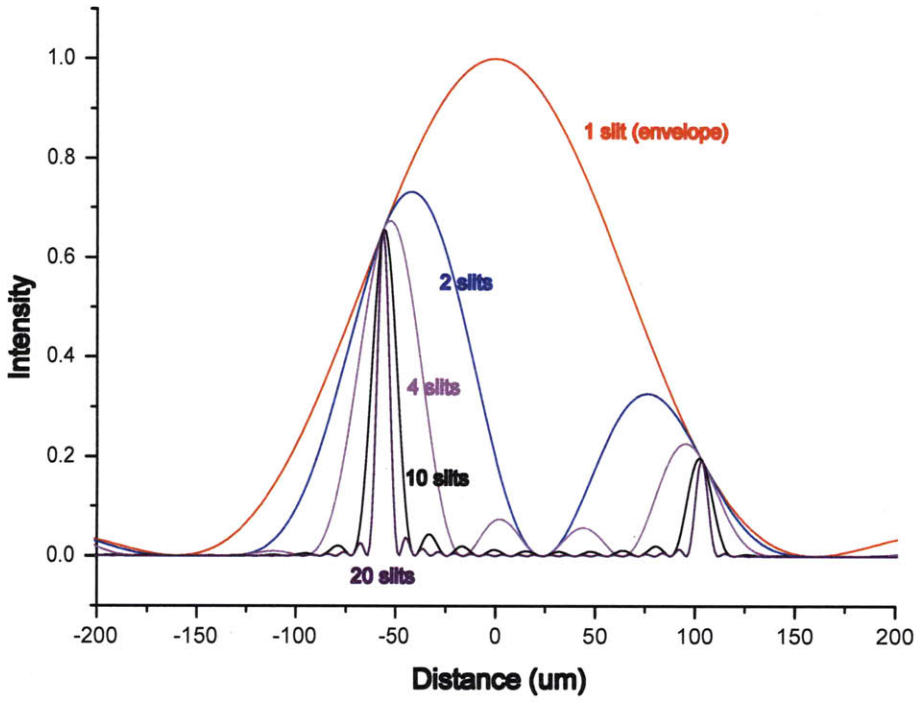

Figure 2-26: Beam profile at the Fourier plane resulting from the phase-shifted N slits. Strong destructive interference is observed at the center, while two constructive peaks appear in both sides of the center.

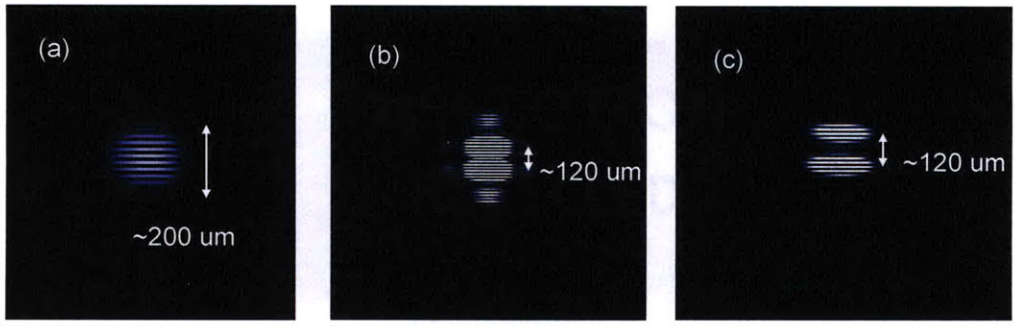

Figure 2-27: Actual 800 nm probe beam profile through the crossed echelons measured by a CCD. (a) represents the beam profile created by a single square aperture (0.5 mm×0.5 mm). (b) shows a sinc function-like beam profile. The CCD was saturated at the center to show multiple side peaks. (c) exhibits two strong constructive interference peaks near the center, and their relative intensity ratio is about 1:0.8. The fringes are not real—they originate from a camera artifact.

between two big interference peaks increases and their width reduces with the number of the slits.

For the comparison between the calculated and real beam profiles, the measured beam profiles are presented in figure 2-27. In figure 2-27, (a) was measured using a square aperture of 500 μm×500 μm instead of using the thin echelon. The cross sectional profile corresponds to the envelope function in figure 2-26. There is excellent agreement between them. (b) in figure 2-27 was obtained using crossed echelons (20 × 20), whose vertical cross section can be compared to the profile created by the 20 slits. However, there is a large difference between them. The measured images reproduces the double constructive peaks and the distance between them, but their width is much broader than the calculation predicts. This is attributed to the ultrashort pulse duration. The diffraction theory reviewed here assumes that the beam is a continuous wave. This assumption leads to the big discrepancy. In the case of a CW beam, all of the beam pieces from the 20 slits are strongly interacting with each other at all times and yield characteristic interference patterns due to a firm phase relation. However, in the case of an ultrashort pulse, the spatial and temporal overlap is significant only for several neighboring pieces. As an extreme example, if the pulse duration is shorter than the time step (25 fs), then no piece overlaps with another temporally at the focal plane. Accordingly, ultrashort pulses shorter than 25 fs produce the envelope-like profile in figure 2-26.

The pulse duration was measured as 70 fs which corresponds to triple the unit time step. This implies that approximately 2 or 3 pieces which are next to each other in time can form a group, interact strongly and give a characteristic diffraction pattern. If we compare the real profile (b) in figure 2-27 with the profile from 2 slits in figure 2-26, we can notice good agreement. (c) was obtained by allowing the beam to pass through only 2 or 3 steps. There was no significant difference from (b) except decreased intensity. Likewise, the overall profile is quite similar to the calculated beam profile of 2 slits. Interestingly, the diffraction pattern may allow an approximate estimation for the pulse duration.

The diffraction pattern is dependent on the incoming wavelength. For 540 nm, a

very strong constructive interference peak is observed at the center((a) in figure 2-28). This is due to the phase difference which is a multiple of 2π. If the phase difference is an odd multiple of π, then completely destructive interference is observed at the center and two symmetric constructive peaks about the center appear. The wavelength of

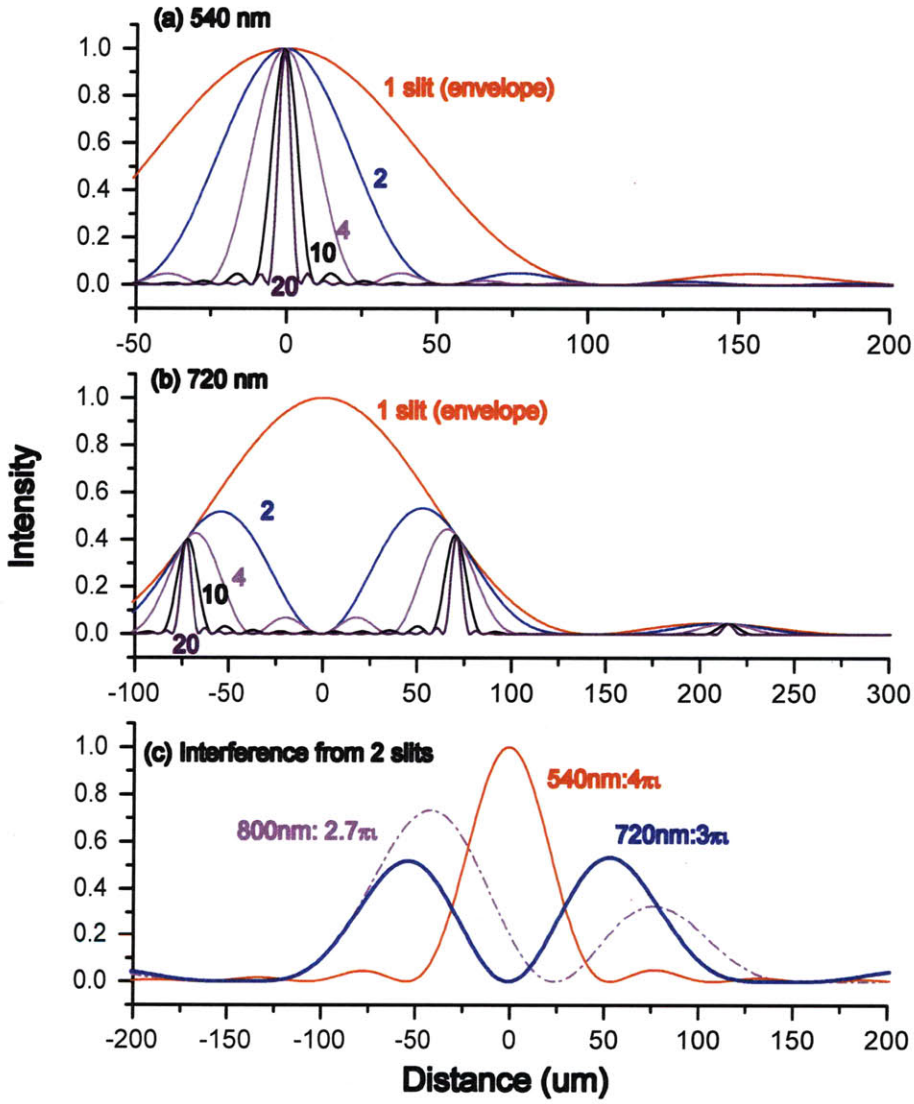

Figure 2-28: Simulated beam profiles at the Fourier plane. (a) shows the beam profile of 540 nm probe wavelength as a function of number of slits. The phase difference between adjacent slits is 4π so the strong constructive interference peak is observed at the center. The beam profile of (b) results from a wavelength of 720 nm (3π phase shift) which gives rise to a completely destructive interference peak at the center. (c) simulates plausible beam profiles for three different wavelengths (540 nm, 720 nm, and 800 nm) through the echelons, assuming that the effective number of slits is 2.

720 nm is very close to this category((b) in figure 2-28). Caution is needed to overlap the pump and probe pieces and to enhance the sensitivity. As mentioned before, the beam profile is affected by the pulse duration. Assuming that the pulse duration is about 50–80 fs such that two adjacent pulses (corresponding to two slits here) interact strongly, a plausible beam profile is reproduced for three wavelengths ((c) in figure 2-28).

2.4 Noise Sources

Generally speaking, the most challenging part in every single-shot technique is achieving a high signal-to-noise level. The current dual echelon single-shot technique is not completely free of the problem. Since the noise level sets the limitation of measurements, noise sources are discussed in this section.

Shot-to-shot beam fluctuation and multishot average

A single-shot measurement involves two laser shots. One leads to the background image and the other one to the signal image. The background is necessary to flatten the image, leaving only the real time-dependent signal. The normalized signal image, obtained by dividing a signal image by a background image, shows clear temporal information as shown in figure 2-16 and (b) in 2-18. However, this procedure was not enough because of the shot-to-shot fluctuations. Compensation of the shot-to-shot noise by a pair of reference images enhances the signal-to-noise greatly, as shown in figure 2-17 and (c) figure 2-18. The noise floor is less than 1% which limits the capability of the single-shot measurements eventually. A signal smaller than the floor level is hardly detectable. As seen, the reference compensation does not eliminate the shot-to-shot fluctuations completely. The fluctuations are ascribed to the thermal instability and air current in the laser head or in the room. In order to provide stable operation of the laser, all of the chillers and electronic controllers are isolated by an insulating box. All optics are isolated by boxes as another effort to remove the thermal instabilities and air currents. These enhance long-term stability but not short-term

stability. A time correlation measurement of the laser output shows a decay time of 0.5 sec, meaning that two pulses within 0.5 sec are correlated more closely. It is inferred that a shorter time interval between the background and signal produces a more efficient reference correction scheme (and background correction as well). For example, if the signal shot follows 100 ms after the background (the shortest time interval in the 10 Hz system), then the reference correction scheme works better due to the strongly correlated pair. On the contrary, if the time interval is much longer than 0.5 sec, then the reference correction scheme does not work well. The current time interval between the background and signal shots is set as $\sim$1 sec. This time cannot be shorter at present due to the slow data acquisition time.

Since the beam fluctuations are random, taking an average over many shots enhances the signal-to-noise level. Figure 2-29 shows the transient reflectivity of a bismuth sample, representing the enhancement of the signal-to-noise level with the repeated shots. The signal-to-noise level increases with $\sqrt{N}$, where N is number of shots. The noise floor level is 0.5% for the single-shot data, while it decreases considerably for the 100-shot data. The 9-shot average produces a fairly small noise level which is comparable to 0.1%. For the single-shot data, wavy noise is observed. The time period corresponds to the unit time step of the thick echelon (453 fs). The origin of the noise is the space-to-time correlation in the 2-D probe beam profile. As shown, the noise is eliminated by the multishot average indicating that the wavy noise is not systematic but random.

The averages in figure 2-29 were taken for the same sample spot. To take a multishot average, a series of probe and pump pulses are admitted continuously every 1 sec, but a shutter in the pump arm blocks the pump pulse alternatively to generate background and signal pairs. Instead of producing every image for every shot, the CCD updates the background and signal image in real time by adding up to the latest shots and by averaging over them, which keeps the size of the image unchanged (about 5 MB). If every CCD image is produced after every shot, then the total size of the images can be tremendous. For example, the 100 multishots would generate 1 GB data (a hundred of 5 MB background and 5 MB signal). In addition, the

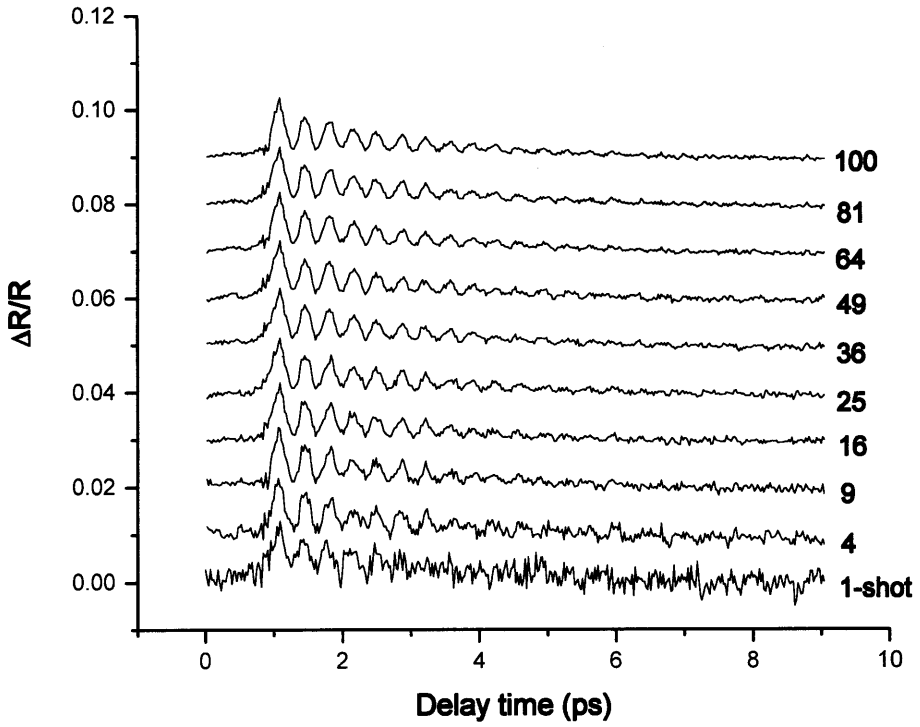

Figure 2-29: Enhancement of signal-to-noise level by increasing the number of shots. The background noise level for one shot is about 0.5% which originates mainly from laser fluctuations. Since fluctuations are random, the multi-shot average washes them out.

task of extracting the time signal from every image prolongs the data processing time significantly. In that sense, the average in figure 2-29 does not represent the "true" average (of each time signal) because the signal and background images are first averaged over the shots. The time signal is recovered from the images later. This averaging scheme fails when the beam fluctuation is large over the shots. In that circumstance, the time signal should be averaged over the individual signal after recovering each time signal from background-signal image pairs.

The purpose of the single-shot method is to study the irreversible change of the sample with one shot. However, in many cases, the irreversible change or damage process is accumulative with multiple laser shots. This suggests that the above multishot average scheme (for the same spot) is available, yielding valid results when the damage by a single shot is negligible. Of course, the multishot average over different sample spots is always possible as long as the sample size permits it, but it would

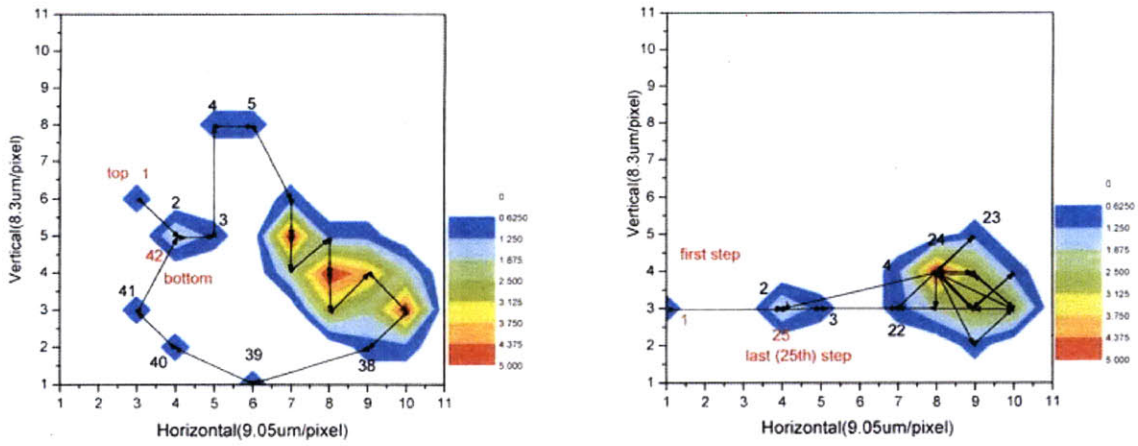

Figure 2-30: Spatial distribution of probe pieces at the Fourier plane. The left side exhibits the coordinates of 41 pieces which pass through a single step in the thick echelon. The pieces are indexed with a number from the top (1) to the bottom (41) along the step. The right side shows the spatial distribution of 25 probe pieces across all of the steps in the thick echelon. The color bar indicates the frequency with which the pieces hit the specific location on the CCD.

take much more time due to the data processing as well as re-alignment of optics while changing the sample spots.

Deformation of echelons

One of the requirements for a successful measurement of the single-shot method is that every probe piece should hit the same spot. The only reason for using different probe pieces to reach the pumped region is different delay times. But if the sample is out of the focal plane, then all probe pulses reach different spots, which are also excited with different strengths of the pump. This creates undesirable intensity variations over the echelon image and distorts the time signal in the end. Therefore, it is extremely important to locate the sample at the focal plane. However, it was observed that all of the probe pieces were not focused at the same spot for the previously used echelons. Some of the probe pieces, especially, those from near the edges of the thick echelon, deviated from the focusing point.

Figure 2-30 represents the spatial variations of the probe pieces at the focal plane. The variations are measured using a He-Ne laser. A He-Ne ray with a small diameter (300 µm) passed through the thick echelon (or thin echelon) and was focused. Its

intensity profile was captured at the CCD located at the focal plane. By translating the thick echelon (or thin echelon) carefully along the 13^{th} step (left side in figure 2-30) or across the all steps (right side in figure 2-30), the coordinates yielding the highest intensity were recorded and plotted. If the plane of the echelon were perfectly flat, then the coordinate should not move no matter where the ray passes through the echelon. However, if the plane is not flat so that it tilts the beam direction (or wave vector), then the beam is focused at other spots. The deviations are more pronounced near the edges of the thick echelon and the maximum deviation is observed to be 100 μm. This means that the probe pieces from the edges and those near the center reach different regions of the sample and feel different pump strengths, which leads to systematic noise in temporal signal. In order to compensate for the deviations, the optical quality of the sample must be uniform over the entire probe spot and the pump spot size needs to be far larger than the probe spot. The thin echelon exhibited a fairly flat surface over the entire cross section so the centers of all the probe pieces were distributed within 30 μm. For the new echelons made from fused silica, both the thick and thin echelons showed very flat surfaces such that the maximum deviation was measured to be less than 30 μm.

Crosstalk: pump as a window function

What happens if a pump spot is smaller than the probe in the conventional pump probe technique? Only a central fraction of the probe will interact with the pump and the sensitivity becomes low. The overall time-dependent signal will not be changed. However, in the current single-shot method, the smaller size causes more complicated problems and may distort the temporal signal due to the space-to-time correlation in the array. Let's consider an incoming beam as a square and denote $I(x, y)$ as the beam profile at the focal plane. $I(x, y)$ is a two dimensional sinc function, which is the Fourier transform of the square function. The sinc function yields the square function at the image plane (via the inverse Fourier transform). Now, let's put a pinhole at the focal plane so that the sinc function is overlapped at the center of pinhole. It is evident that if the size of the pinhole is infinitely large, it will not affect

the reconstruction of the square function at the image plane. On the contrary, if the pinhole size is comparable to the central peak of the sinc function, the image will not be the square function anymore. Mathematically speaking, the inverse Fourier transform of the product between the sinc function $I(x, y)$ and the window function $W(x, y)$ representing the pinhole does not yield the exact square function:

$$\begin{aligned} image &= \mathcal{F}^{-1}\{I(x,y) \times W(x,y)\} \\ &= \mathcal{F}^{-1}\{I(x,y)\} * \mathcal{F}^{-1}\{W(x,y)\}. \end{aligned} \tag{2.42}$$

Equation 2.42 describes the effect of the window function representing the pinhole mathematically. If the size of the pinhole is infinitely large, then its inverse Fourier transform will be a delta function. The convolution between the square function and the delta function results in the square function intact (at the image plane). On the other hand, if the size of the pinhole is infinitely small, then its inverse Fourier transform will be a constant over the entire space. Accordingly, the convolution between the square function and the constant yields a constant value over the space. In this case, the image of the square disappears completely. If the size of the pinhole is comparable to the sinc function, then the convolution of the square function and the inverse transform of the window function would lead to a large and blurry square image. The smaller the pinhole is, the larger and more blurry the image is.

In reality, the pinhole represents a pump and the window function corresponds to the pump beam profile. Now, let's suppose a probe piece originating from a square of the 2-D probe array (20×20 squares) and a pump is overlapped with the probe at the focal plane temporally. Let's also assume that the pump induces an impulsive change in the transmissivity of the sample. In the same vein as the above argument, if the pump spot is big enough, then the probe piece will form exactly the same square image with increased intensity due to the increased transmissivity. If the pump spot is the same as the probe spot at the focal plane, then the convolution results in a $\sqrt{2}$ times larger square image. The intensity smears out into neighboring squares. This crosstalk is an artifact attributed to the small pump size. It is very likely that

the artifact can be conveyed in the temporal signal and can distort the real temporal signal. This may happen for all probe pieces if they interact with the pump via the sample. Since a grid is usually surrounded by 8 neighboring squares, crosstalk from all 8 neighbors can contribute to the intensity of the center square. By contrast, if the square is located at the edge, only five of the neighboring squares can contribute to the intensity of the square. This is the edge effect in the single-shot method, and it causes systematic noise. Equation 2.42 also implies that a strange noise pattern might result from a spatially structured pump or an inhomogeneous sample over the probe spot. When the pump energy is increased, the artifact is more pronounced. The noise could get much worse when the pump induces a nonlinear response, by reducing the effective size of the window function further (from its physical spot size).

In order to eliminate the crosstalk and systematic noise, the spot size of the pump must be bigger than that of probe. Also the pump and the sample should exhibit homogeneity over the probe spot. For measurements, the diameter of the pump is set normally 2-3 times bigger than that of the probe.

Other noise sources

In addition to the sources mentioned so far, there are some minor sources. One of them is spherical aberration of the focusing lens. Since the echelon size is big, the resulting spherical aberration of the lens may be significant. The spherical aberration prevents probe pieces from being focused at the same plane as shown in figure 2-31 [Fow89].

The distance between two focal planes Δ can be expressed by

$$\Delta = 0.5Kh^2, \tag{2.43}$$

where

$$K = \frac{f^2(n-1)}{n^2}[\frac{1}{r_1^3} + (\frac{1}{f} + \frac{1}{r_2})(\frac{n+1}{f} + \frac{1}{r_2})]. \tag{2.44}$$

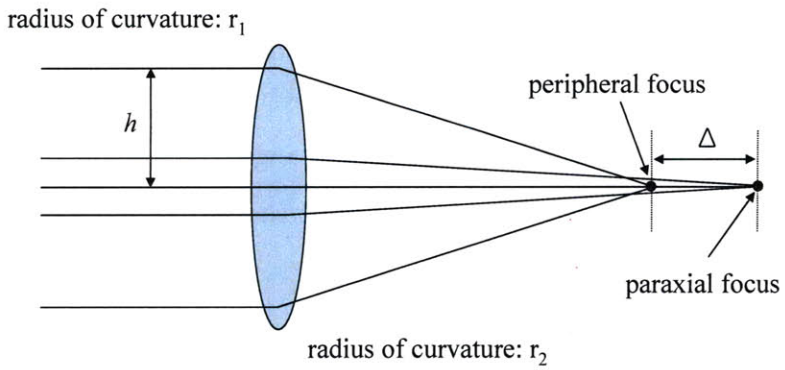

Figure 2-31: Spherical abberation caused by a spherical lens.

This is minimum when the ratio of the radii is

$$\frac{r_1}{r_2} = \frac{n + 4 - 2n^2}{n + 2n^2}. \tag{2.45}$$

The best form lens used in the current setup is designed to give minimum abberation and thus minimum K based on equation 2.45. According to equations 2.43 and 2.44, a bigger h and a shorter focal length f result in an increase in Δ, but the probe spot size at the focal plane would then be smaller. On the contrary, a smaller h and a longer focal length f decrease Δ but lead to a larger probe spot size at the focal plane. Practically, a smaller size of the probe at the focal plane is more desirable because it allows a smaller size of sample and pump spot. There is a trade−off between the spot size and Δ. For a given echelon size (h), Δ is made small by using a 10 cm focal length lens.

The incident angle of the probe is another noise source. The angle of incidence is different for all probe pulses. The reflectivity and transmissivity are dependent on the angle of incidence. When the beam is s-polarized, they are given by the following equations:

$$r = \frac{\cos\theta - \sqrt{\epsilon - \sin^2\theta}}{\cos\theta + \sqrt{\epsilon - \sin^2\theta}}, \tag{2.46}$$

$$t = \frac{2\cos\theta}{\cos\theta + \sqrt{\epsilon - \sin^2\theta}}. \tag{2.47}$$

A pump induces a change in dielectric function ϵ and probe pieces recognize the corresponding change $\Delta\epsilon$ resulting in a change in R or T.

$$\frac{(R+\Delta R)-R}{R} = \frac{(r+\Delta r)^2-r^2}{r^2} = \frac{2r\Delta r+(\Delta r)^2}{r^2}, \tag{2.48}$$

and

$$\Delta r = \frac{\cos\theta-\sqrt{\epsilon+\Delta\epsilon-\sin^2\theta}}{\cos\theta+\sqrt{\epsilon+\Delta\epsilon-\sin^2\theta}} - \frac{\cos\theta-\sqrt{\epsilon-\sin^2\theta}}{\cos\theta+\sqrt{\epsilon-\sin^2\theta}} \tag{2.49}$$

$$= \Delta r\,(\Delta\epsilon,\ \theta). \tag{2.50}$$

The change in reflectance (ΔR) or reflectivity (Δr) are not influenced only by $\Delta\epsilon$, but also by θ. Therefore, the temporal signal might be distorted by the angular dependence. The maximum angle θ in the current geometry is $\tan^{-1}(h/f) \cong h/f =$ 0.5 cm/10 cm = 0.05 (rad). Calculations reveal that $\Delta R/R$ is approximately +12% when the refractive indices ($n^2 = \epsilon$) change from ($n_r = 3.3,\ n_i = 4.0$) to ($n_r = 2.7,\ n_i = 5.0$). In this case, the variation originating from the angular dependence was estimated as 0.2%. The calculation also indicates that the variation could be suppressed by the superposition of s- and p- polarizations using a half wave plate. For the above case, a linear combination of 57% s- and 43% p-polarized light can suppress the variation below 10^{-4}%.

We have examined several possible noise sources but there may be additional noise sources. Since noise is the biggest concern in single-shot spectroscopy, caution is necessary.

2.5 Accessory Apparatus

We have discussed the single-shot instrument in the previous sections. In order to provide versatility and convenience, it is integrated with a conventional pump-probe setup and with a noncollinear optical parametric amplifier for tunable wavelength. Both are extremely useful. They are introduced briefly in following sections.

2.5.1 Standard Pump-probe setup

For a standard pump-probe setup, it is most convenient to take advantage of the same optics used in the single-shot instrument. This allows better reliability in comparing single-shot data and conventional pump-probe data by using the common pump line and fluence. For operation of the standard pump-probe instrument, 1 kHz repetition rate is used instead of 10 Hz. To achieve this, the 10 Hz pockels cell is turned off and some amount of 1 kHz power is taken using the half-wave plate and thin film polarizer in figure 2-4.

The pump beam is chopped at 500 Hz with a chopper and focused on the sample by the same optics as in the 10 Hz single-shot apparatus. In the probe arm, the echelons are simply removed. Probe pulses are focused on the sample which is excited by the pump. The time delay between the pump and probe is varied by a translational stage in the probe arm. The signal modulated at 500 Hz is recorded by a lock-in amplifier and sent to a computer through a DAQ card.

Different pump-probe combinations such as an 800 nm pump and a visible wavelength probe are also possible using a continuum source from sapphire. Focusing weak 800 nm pulses in a 1 mm thick sapphire crystal generates a broadband continuum. Self-focusing in the crystal leads to nonlinear self-phase modulation, which in turn modulates the optical phase of the driving field, yielding new frequency components as shown in figure 2-32. Wavelengths from 500 nm to 1000 nm are strong enough to be used as a probe without being further amplified, but not strong enough for use in the single-shot measurements, which require a NOPA setup.

Figure 2-33 illustrates the continuum generation setup. 800 nm pulses are focused at the rear side of the sapphire crystal in order to minimize dispersion and pulse broadening of white light. Nonetheless, the pulse width is not as short as that of the incoming 800 nm beam. The power of 800 nm is controlled by opening an iris, and set below the threshold for a multi-filament process. The point continuum source is imaged onto the sample with an achromatic lens by translating the stage on which both the focusing lens and the sapphire are placed. After being reflected from the

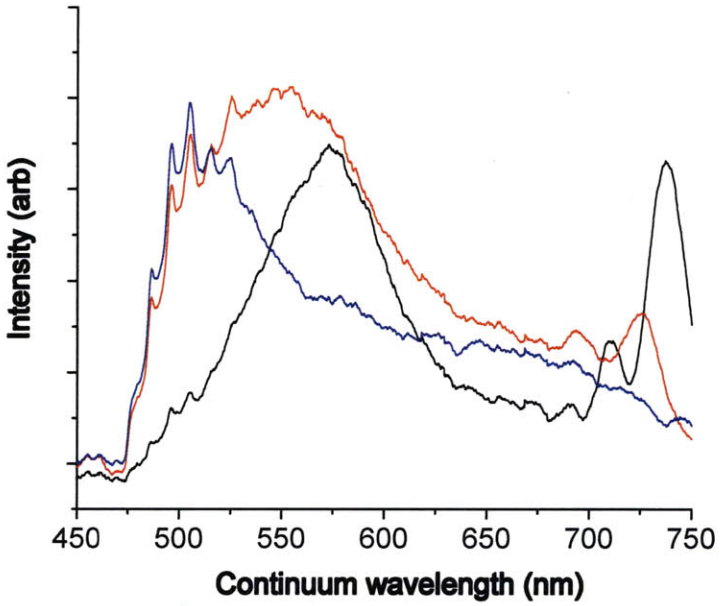

Figure 2-32: Spectra of continuum white light source from a sapphire plate. The spectrum changes from a blue to red to black with increasing 800 nm pump power. All are obtained below the threshold for a multi-filament process.

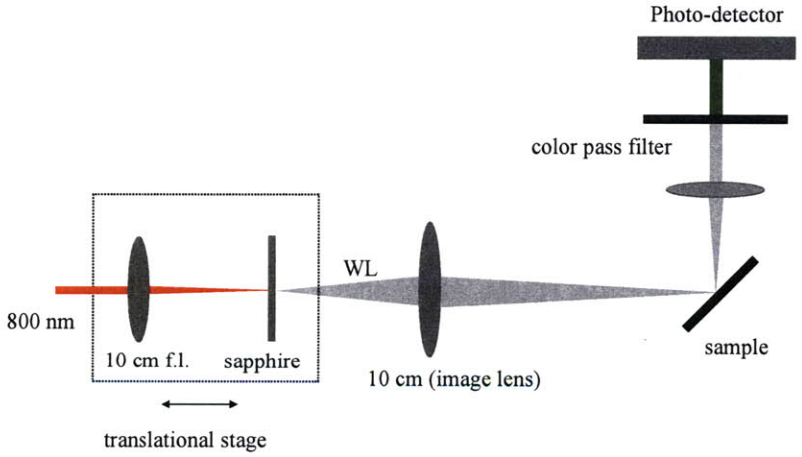

Figure 2-33: Schematic illustration of regular pump-continuum probe measurements. Focusing weak 800 nm pulses in a sapphire plate generates a broadband continuum (WL). The continuum point source is imaged onto the sample which is excited by a pump pulse. A specific probe wavelength is selected by a color pass filter and its intensity is detected via photodetector.

sample or transmitted through it, the beam is collimated. Then a specific wavelength passes through a color pass filter and its intensity is recorded by a photodetector.

2.5.2 Non-collinear Optical Parametric Amplifier

Introduction

It is desirable to provide the single-shot system with tunability for pump and probe wavelengths. Tunability makes it possible to investigate wavelength-sensitive dynamics such as resonance-enhanced Raman scattering, transient electronic absorption, and femtosecond photochemistry. Practically, non-degenerate pump-probe separates the scattered pump light spectrally and removes the relevant noise in the CCD. The continuum source from sapphire is not strong enough for single-shot measurements because the beam is expanded over the entire area of the echelons. The continuum source needs to be amplified for the application to single-shot measurements.

A non-collinear optical parametric amplifier (NOPA) is widely used to amplify the continuum source. Gale *et al.* reported that by utilizing a noncollinear geometry in crystal β-barium borate (BBO), it was possible to simultaneously phase-match wavelengths over a broad bandwidth including a significant portion of the visible region [GCH98]. De Silvestri and co-workers examined the influence of continuum chirp on the efficiency of white-light seeded OPAs [CNS97, CNSS98, CNS$^+$99, CS03]. Kobayashi and coworkers have built a NOPA which generates pulses compressible to 4.7 fs by employing a pulse-front tilting scheme to maximize the three-wave interaction volume [SK98, SSTK99]. E. Riedle has successfully showed wavelength tunability of the signal output over the visible region from a NOPA and has also seeded the NOPA along the idler phase-matching direction to create tunable pulses from 1–7 μm for vibrational spectroscopy [WPR97, PBR00].

Experimental setup and results

Theoretical details on the noncolliner OPA are described in [Pou05] so only experimental details are presented in this section. A schematic diagram of the OPA is illustrated in figure 2-34.

A single ultrashort pulse (70 fs) is admitted by a shutter which is triggered by a computer. A 1:1 (R:T) beamsplitter divides the pulse into two pieces. One is

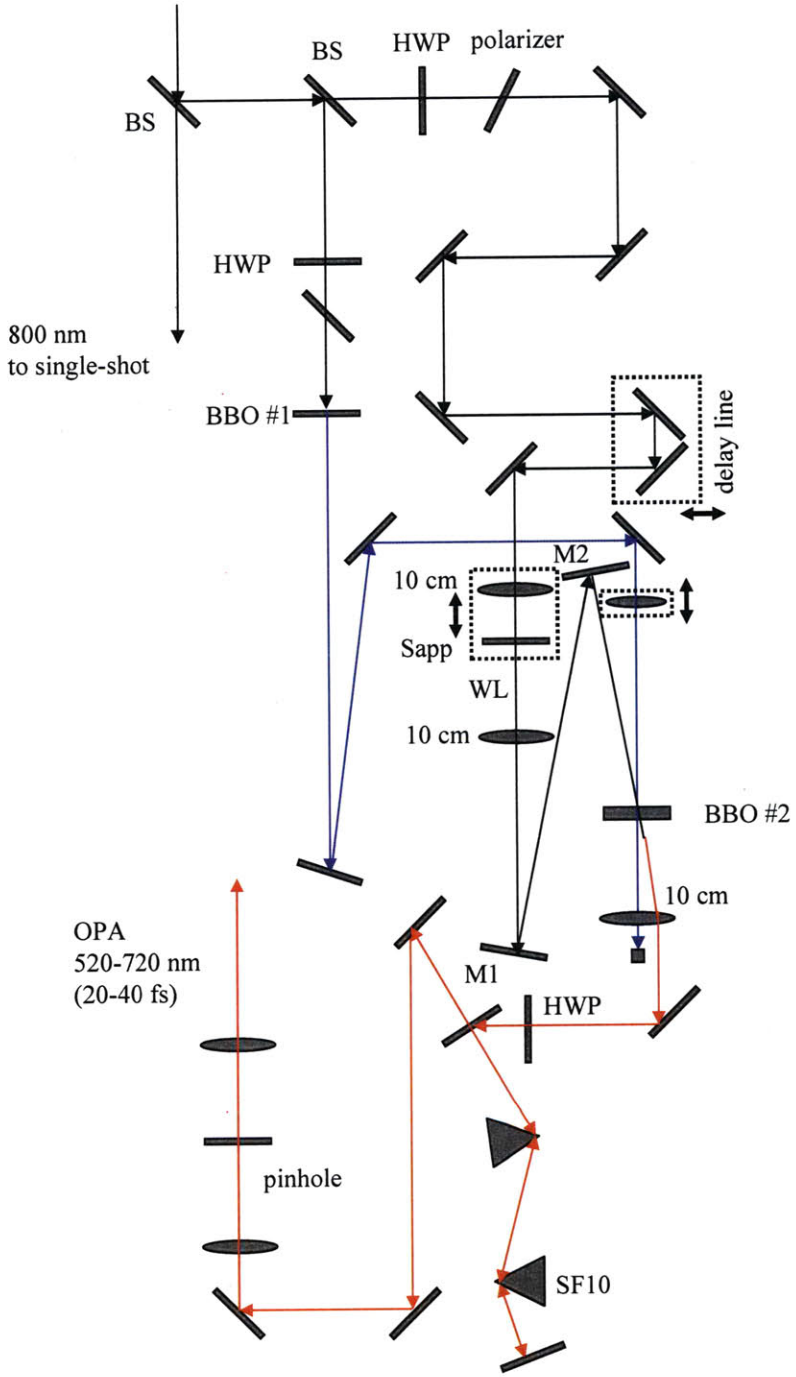

Figure 2-34: Schematic view of the single-shot noncollinear optical parametric amplifier. Single pulses gated out of the Ti:sapphire amplifier are divided and used to generate both pump and seed pulses for the parametric interaction. The center wavelength is varied by adjusting the seed pulse delay line. The M1 and M2 are used to align the seed for the phase matching condition. Following amplification, the output is compressed by a double-pass prism compressor.

directed to the sample for a pump or probe at 800 nm. The other is directed to the OPA setep. On entering the setup, the beam is divided into two arms again by a 8:2 (R:T) beamsplitter. The reflected beam passes through a half-waveplate and polarizer pair which control beam intensity. The beam is converted to the second harmonic with about 15% efficiency via type-I phase-matching in a 1.5 mm BBO crystal (BBO #1). The efficiency can be increased by reducing the beam diameter, but the spot size is not reduced. The second harmonic is roughly 100 fs in duration and about 15 µJ in power. This is the pump for the NOPA. The beam is focused a little before the second BBO crystal (BBO #2) by a 25 cm focusing lens mounted on a translational stage. The pump intensity at the BBO is controlled by translating the lens. Tight focusing leads to the formation of multiple filaments and thus causes instability and incoherence between photons. Thus, the BBO cannot be pumped very strongly and the maximum output energy is thereby limited.

The second BBO crystal (BBO #2) is cut at 31.5° to the z-axis. The polarization of the pump (the second harmonic) is parallel to the plane which is defined by its wave vector and the crystalline z-axis. The crystal is oriented such that the second harmonic is horizontally polarized. This is the type-I phase-matching NOPA: the pump is *e*-polarized and both signal and idler are *o*-polarized.

The second harmonic pump creates a many-colored ring pattern which emerges at the rear of the crystal. This phenomenon is known as *parametric superfluorescence.* The broad bandwidth of the superfluorescence results from parametric conversion of pump photons to signal and idler photons. The visible ring is formed by the signal photons. Another bigger ring is created by idler photons, but it is not visible because of its longer wavelength. Both signal and idler photons propagate in a cone geometry which appears as a ring in transverse cross-section. The angle of the visible cone is 3.7° which satisfies a broadband phase-matching condition at the given polar angle (31.5°). The visible ring serves as a guide for aligning the seed beam. It is apparent that for a given superfluorescence pattern, the amplifier must be arranged such that the seed beam passes through the pump spot at the front surface of the crystal, and propagates along the direction of the cone. This guarantees that the parametric

conversion process is phase-matched properly over a broad bandwidth.

The remaining 20% of the 800 nm incoming beam is used to generate the broadband seed employed in the parametric conversion process. After passing through a waveplate-polarizer attenuator and a delay line, it is focused at the rear side of a 1 mm sapphire plate by a 10 cm focusing lens and produces a white light source. Its spectrum is shown in fig 2-32. Generally, it is important that chirp from dispersion be minimized. Otherwise the frequency mixing with the 100 fs pump would be inefficient, leading to a narrow bandwidth and a longer pulse duration. Therefore, it is desirable to use reflective optics to avoid this effect. By doing so, even a single-digit-femtosecond pulse can be produced from the OPA. However, it is not trivial to maintain a good beam shape, particularly due to reflective lenses. Moreover in our single-shot experiments, such an ultrashort pulse may result in worse temporal resolution because of the dispersion by the transmissive echelons afterwards. In fact, a certain amount of chirp is necessary. The subsequent transmissive optics including a low pass filter ($\leq$ 750 nm) and an imaging lens may be enough to fulfill this need. It will be shown that the pulse can be compressed to about 20 fs after a double-pass prism compressor. The generated continuum source diverges as it propagates. A 10 cm achromatic lens is used as an imaging lens such that the continuum point source is imaged onto the pumped spot at the BBO (#2). To image precisely, it is much easier to translate the point source (sapphire plate and focusing lens on the same stage) than to move the imaging lens (fig 2-34). Two mirrors, M1 and M2 provide the degree of freedom needed to steer the continuum source such that the parametric conversion process is phase-matched. The output wavelength is tuned by adjusting the delay line. The typical energy of the amplified pulse is about 0.5–1.0 µJ. This is more than enough for the probe in single-shot measurements. However, it may not be enough for strong excitation pumps. In this case, a subsequent amplification stage is necessary.

Following parametric interaction within the crystal, the pulse is positively chirped due to dispersion and needs to be compressed. A double-pass prism is used to compensate the positive chirp by introducing negative group velocity dispersion. A pair

of SF10 ($n = 1.711$) or SF11 ($n = 1.779$) prisms is used for the compressor. Before entering the compressor, the polarization (V) needs to be rotated by 90° (H) in order to minimize loss due to reflection by the prims. The incident angle at both sides of the prism should be set as its Brewster angle for the double pass. To satisfy the requirement, the apex angle of SF10 and SF11 prisms should be 59.7° and 60.6°, respectively. However, the actual angle is 60° in both materials. This small error results in only a very small loss due to reflection. The spacing between the SF10 prisms is about 20 cm for almost all visible wavelengths, while the spacing between the SF11 prisms is about 13 cm. By translating the first or second prism in a transverse direction, the pulse duration is optimized. Figure 2-35 shows the output spectrum (a), autocorrelation intensity (b), and FROG trace (c), respectively.

In the more general case, both pump and probe pulses employ different wavelengths from the fundamental wavelength 800 nm of Ti:sapphire amplifier. Another OPA output can be combined with the existing OPA output for either the pump or probe. It was reported that a dual beam phase-locked NOPA was produced by using two independent but phase-coherent continuum seed pulses and a common crystal for the seed pulses [Pou05]. Another continuum generation step was added to the previously existing NOPA layout by dividing the photons from the beam transmitted through the first beamsplitter. A schematic diagram of the dual beam layout is shown in figure 2-36. The additional optics for the second arm are almost the same as the first arm. The geometry is almost symmetric with respect to the BBO crystal (#2). Adjustment of either delay line shifts the center wavelength of the corresponding amplified beam without changing the other beam. The combined process is slightly power-reducing, but the effect is not large. The second output is directed to a separate compressor. Finally, one output is sent to the pump arm and the other to the probe arm. Figure 2-37 illustrates several combinations of different colors for both arms.

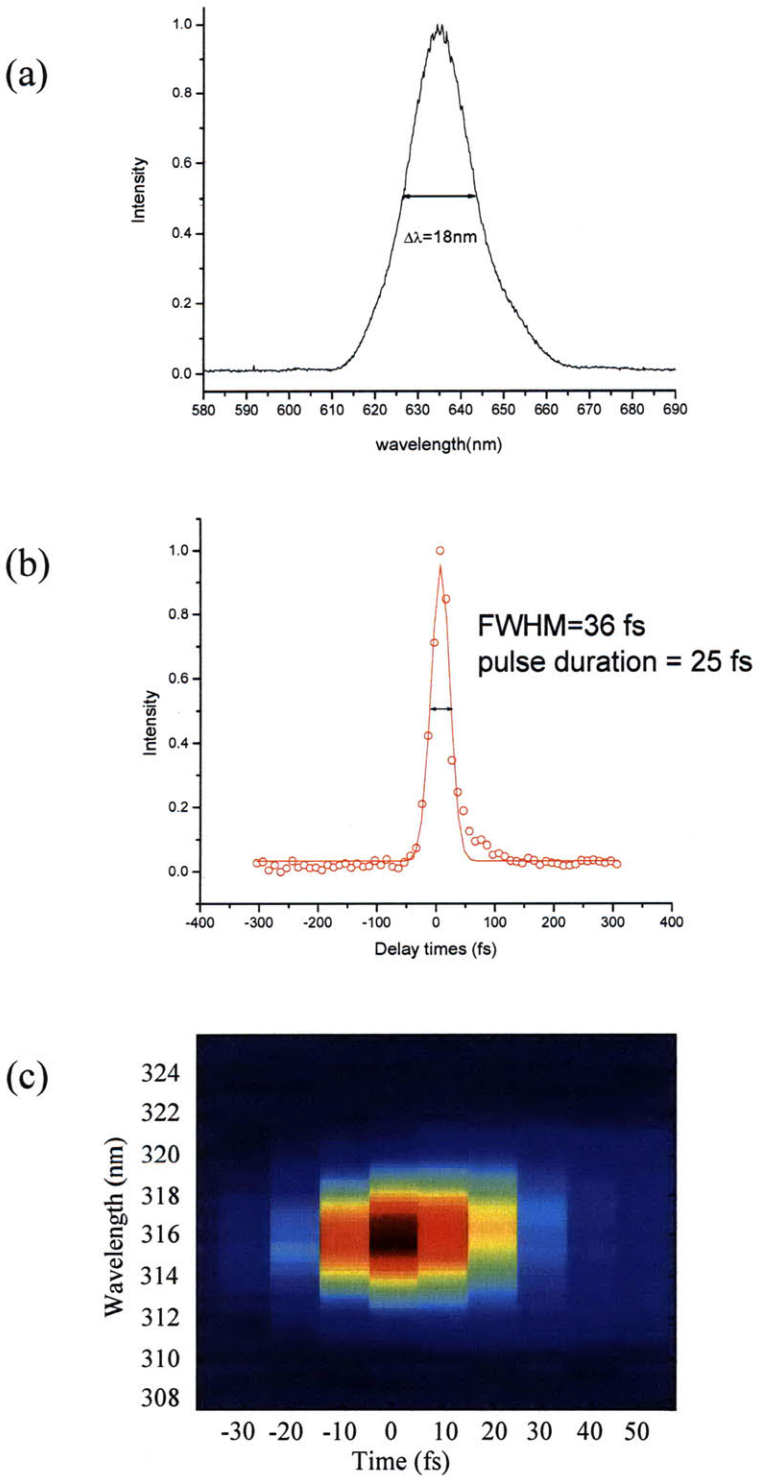

Figure 2-35: Characterization of the NOPA output. (a) shows the spectrum revealing a bandwidth of 18 nm at the central wavelength of 635 nm. (b) represents the intensity autocorrelation trace yielding a pulse duration of 25 fs. (c) is a frequency-resolved optical gating (FROG) trace.

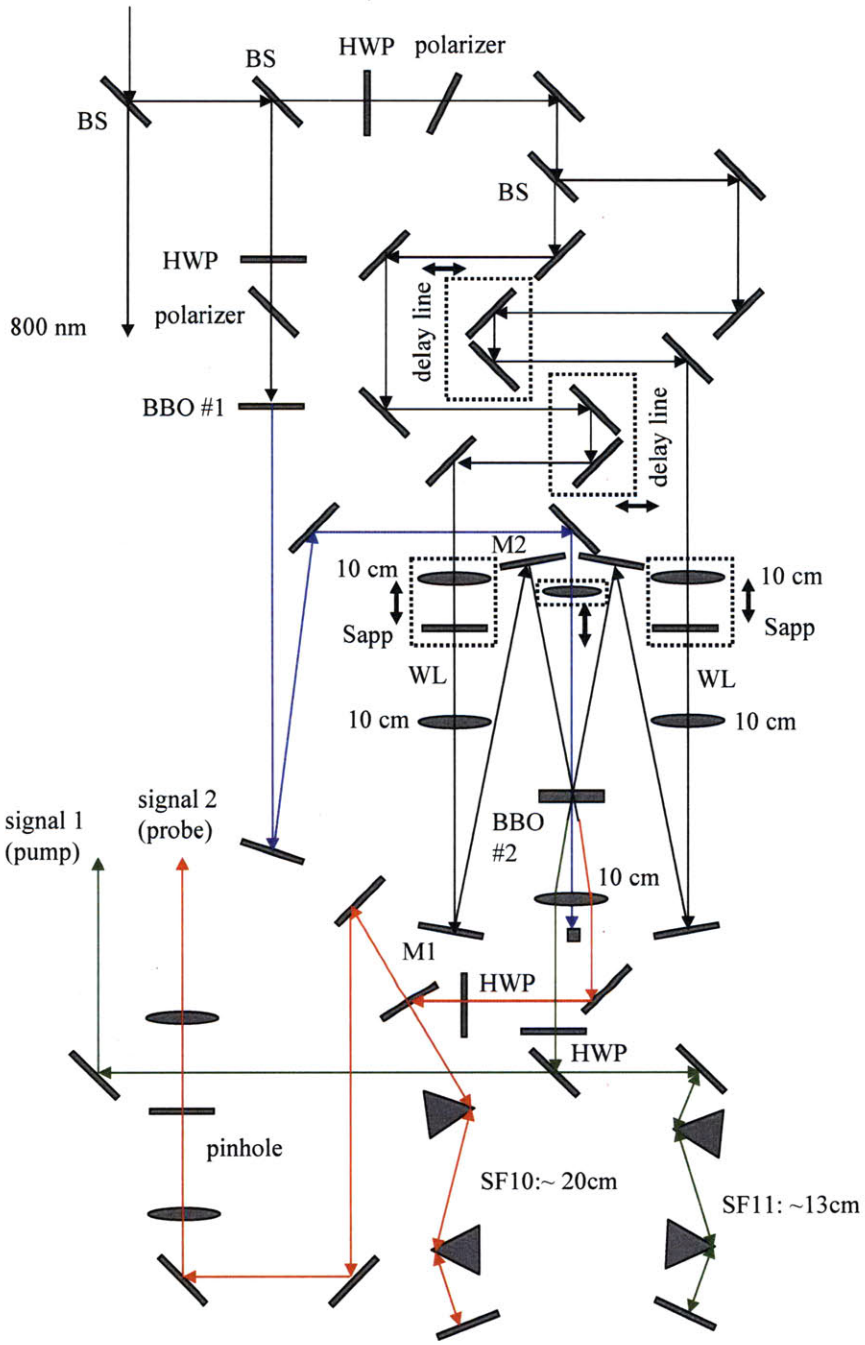

Figure 2-36: Schematic illustration of the dual beam single-shot NOPA. Two continuum generation stages are used to seed the NOPA on both sides of the pump beam, producing two independent tunable pulses. They are compressed by two separate prism compressors.

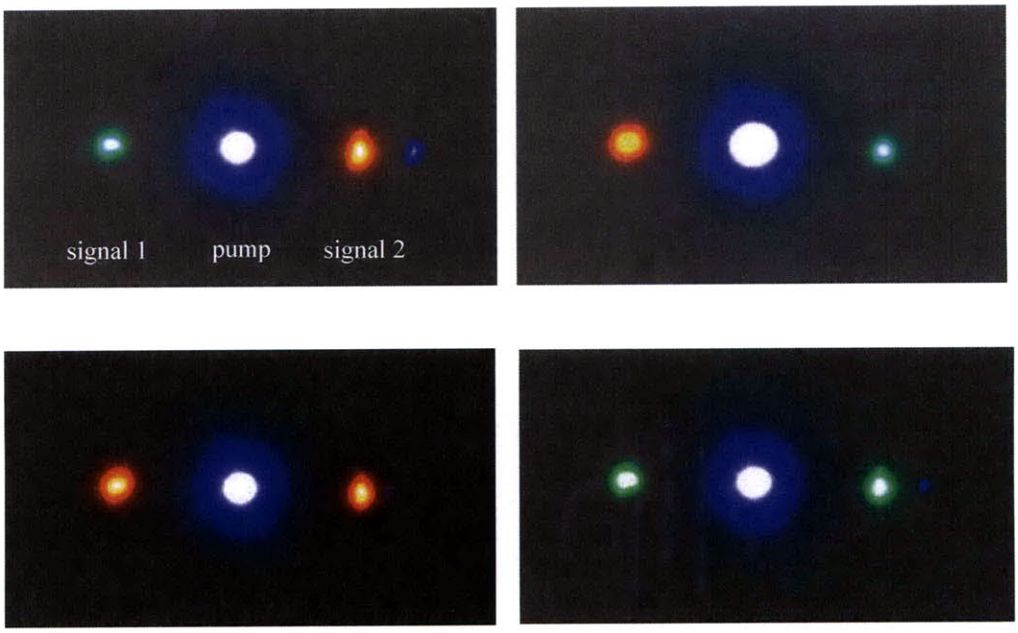

Figure 2-37: Two simultaneous outputs obtained from the NOPA. Two different colors are selected by adjusting the seed delay lines.

Chapter 3

Photoinduced Phase Transition in Bismuth

Bismuth has been studied extensively because of its strong optical phonon response and its unique electronic structure [ZVC+92, DRBM01, HMH+96, HKiNM02]. Recently, ultrafast diffraction measurements have been successfully applied to study the nonthermal melting process in bismuth [SBB+03, FRA+07, SHK+09]. However, no optical spectroscopy has been used to this end. In this chapter, we present experimental results for transient reflectivity of bismuth by varying film thickness and probe wavelength. The thickness-dependent response is discussed in terms of coherent phonons, bond softening, dephasing, and carrier dynamics. The electronic background reflectivity is influenced by film thickness and probe wavelength, which suggests electronic gap broadening with decreasing thickness. The single-shot optical pump-probe technique was employed to study the photoinduced phase transition in bismuth in real-time. Based on our thermal modeling and thin film measurements, it is revealed that the solid-to-liquid transition in bismuth involves both thermal and nonthermal effects.

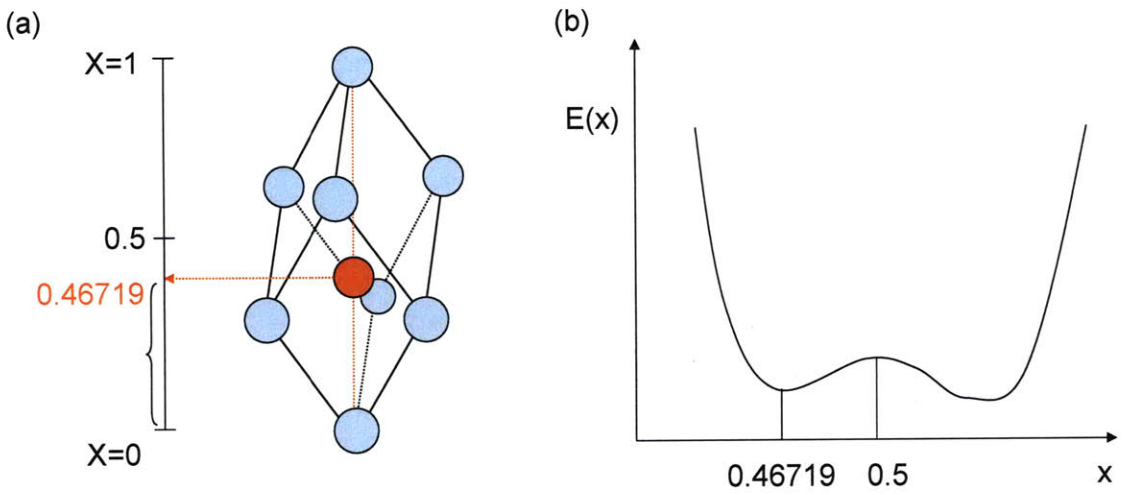

Figure 3-1: (a) illustrates the rhombohedral unit cell of bismuth. The crystal basis consists of two atoms. X represents a fractional lattice spacing and x = 1 corresponds to 1.18 nm. In the Peierls distorted structure, the red atom is not at the center along the diagonal direction. This introduces a double-well potential to the whole system as shown in (b).

3.1 Introduction

Bi, Sb, and As crystallize into an A7 structure with rhombohedral space group R$\bar{3}$m. There are two basis atoms per unit cell. The structure results from a Peierls distortion of a simple cubic structure, with alternating atoms spaced non-equidistantly along the body diagonal direction. A double-well potential results from the Peierls distortion. Figure 3-1 illustrates the unit cell and the potential energy surface.

The full representation of the A7 structure vibrational modes is given by

$$\Gamma_{tot} = A_{1g} + A_{1u} + E_g + E_u, \tag{3.1}$$

where the A_{1g} and E_g modes are Raman active but A_{1u} and E_u are acoustic modes. A_{1g} is a totally symmetric singlet mode and E_g a doubly degenerate mode. The frequencies of these modes have been observed experimentally via CW Raman scattering. They are 98 cm^{-1} for A_{1g} and 74 cm^{-1} for E_g [CotPoSgS71]. The scattering cross-sections for both symmetries have been measured. The cross-section is about 5 times larger for the A_{1g} mode than for E_g [RRCS73].

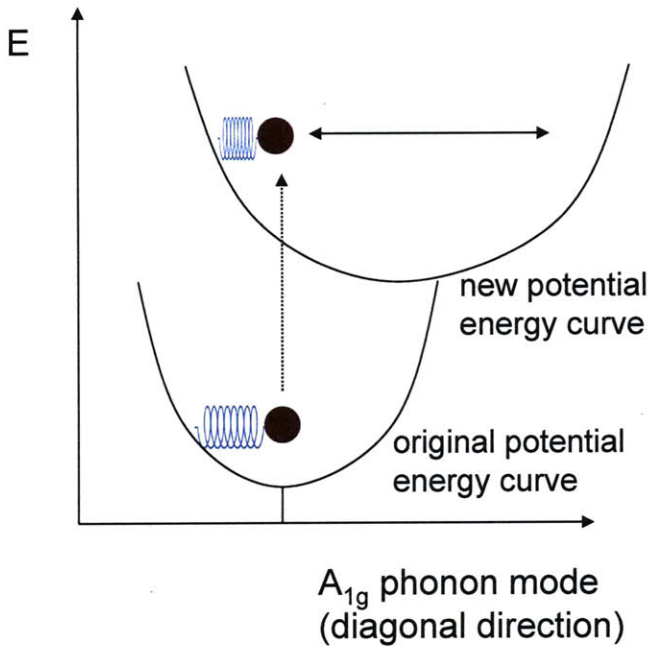

Figure 3-2: The population redistribution of valence electrons modifies the potential energy surface of the lattice. The potential deformation occurs instantaneously by impulsive laser excitation. Accordingly, atoms are initially located at the repulsive region of the new potential energy surface. The repulsive or restoring force drives the coherent lattice vibrations. This is referred as Displacive Excitation of Coherent Phonons (DECP).

Excitation of coherent lattice vibrations by impulsive absorption of electrons has previously been reported in semimetals including bismuth. Zeiger *et al.* observed strong oscillations in transient reflectivity with periods characteristic of semimetal lattice vibrations [ZVC+92]. They presented a classical theory for the oscillations and referred to the lattice vibration mechanism as displacive excitation of coherent phonons (DECP): The impulsive excitation of electrons from the valence to the conduction band by an ultrashort laser pulse leads to an instantaneous deformation of the potential energy surface. This takes place before atoms can be redistributed, so atoms are located at the repulsive region of the new potential energy surface at t=0. The restoring force launches the lattice vibrations along the diagonal direction as shown in figure 3-2.

Hase *et al.* observed that the frequency of the A_{1g} mode is red-shifted with increasing pump fluence and is chirped in time. They attributed the redshift to anhar-

monicity of the lattice potential based on the observed frequency dependence on the squared oscillation amplitude [HKiNM02]. Reis and coworkers simulated the pump-probe reflectivity oscillations in bismuth using a simple phenomenological model of the optical reflectivity in the presence of diffusion and recombination of the electron-hole plasma. They observed that the time variation of the coherent phonon frequency was determined by the decay of the plasma density at the surface due to diffusion of the plasma into the bulk. They also confirmed that the anharmonic contribution to the phonon period is negligible for an excitation of 1.25 % or less of the valence electrons, corresponding to electronic frequencies in the range of 2.9 to 2.3 THz [FR04, MFW$^+$05].

More recently, Fritz *et al.* used density functional calculations to generate the detailed mapping of the carrier density-dependent interatomic potential of bismuth which approaches a solid-solid phase transition [FRA$^+$07]. The calculations suggested that increasing carrier density in the conduction band reduces the Peierls distortion continuously and removes the distortion completely at about 2.7 % excitation of the valence electron population, meaning that bismuth undergoes a structural phase transition to a higher symmetry phase. It is not clear whether the higher symmetry phase is accessible without subsequent melting of the material initially at room temperature. There has been no experimental evidence for the higher symmetry phase so far. The DFT calculations are supported by ultrafast X-ray diffraction results which exhibit quasi-equilibrium lattice constant following along the potential energy minima with increasing carrier density. However, the measurements could not probe all the way to the high-symmetry phase because of sample damage upon such intense irradiation.

Sciaini and coworkers used a femtosecond electron diffraction technique to study the phase transition in bismuth [SHK$^+$09]. They found that the dynamics of the transition depend strongly on the excitation intensity, with melting occurring as quickly as 190 fs after the highest excitation (23 mJ/cm^2). They attributed the anomalous speed of the melting process to laser-induced changes in the potential energy surface of the lattice, which leads to strong acceleration of the atoms along the longitudinal direction of the lattice and efficient coupling of this motion to an unstable transverse

vibrational mode. That is, they showed that the atomic motions in crystalline bismuth can be electronically (nonthermally) accelerated so that the solid-to-liquid phase transition occurs significantly faster than it would be on a thermalization timescale of several picoseconds.

3.2 Coherent Phonon Generation at weak pump fluence: standard pump-probe measurements

Regular pump-probe spectroscopy was employed for the study of the A_{1g} mode coherent phonon launched by DECP. Time-dependent dynamics at longer delay times up to 100 ps are revealed in a single crystal as well as in thin films. Comparison between the bulk single crystal and thin films is made in terms of bond softening, chirping, dephasing, and longer time dynamics. The detailed experimental setup was described in section 2.5.1. The wavelength of both pump and probe were 800 nm and both were p-polarized.

3.2.1 Results in Bi Single Crystals

Figure 3-3 illustrates the transient reflectivity change of bulk bismuth as a function of pump fluence. Strong oscillations are observed. The oscillations are attributed to the A_{1g} coherent phonon mode. The mechanism launching the lattice vibrations is illustrated in figure 3-2. The population redistribution of valence and conduction electrons alters the original potential energy surface of the lattice. Since this process is impulsive, and atoms are heavy, atoms remain in the same locations along the new potential energy surface during the excitation pulse. Thus, they feel the repulsive force on the new potential energy surface at time zero. The repulsive force launches coherent lattice vibrations which modulate the transient reflectivity.

The reflectivity increases instantaneously during the pump pulse duration and then decays gradually. The damped oscillations are superimposed on the decaying background electronic signal. Increasing the pump fluence augments both the ampli-

tude of the oscillations and the initial electronic signal. Also, the oscillations exhibit red-shifting with increasing pump fluence. It is evident that more oscillations are observed between the first and second dotted lines at lower pump fluence in figure 3-3. This suggests that the A_{1g} mode undergoes bond softening or weakening with increasing carrier density in the conduction band, indicating a lower curvature of the new potential energy surface. It is not immediately obvious, but the phonon mode exhibits time-dependent frequency at a fixed pump fluence. It red-shifts at earlier times but blue-shifts as time goes on, which is in agreement with previous studies [HKiNM02, MFW$^+$05]. We attribute the change in phonon frequency to the time-dependent change in carrier distribution.

The reflectivity can be fitted with a functional form which includes the slowly decaying electronic background term and the fast oscillating term [ZVC$^+$92, HKiNM02]. In order to retrieve parameters which are only relevant to the phonon oscillations, the time derivative signal was used. The slowly decaying term is negligible after taking the time derivative:

$$\frac{\Delta R}{R} = A_1 \exp\left(-t/\tau\right) + A_2 \exp(-t/\tau_p)\cos[\omega t + \phi_0] \tag{3.2}$$

$$\frac{\mathrm{d}}{\mathrm{d}t}\frac{\Delta R}{R} \cong A \exp(-t/\tau_p)\cos[\omega t + \phi], \tag{3.3}$$

where

$$\omega = \omega_0 + \beta t. \tag{3.4}$$

In the above equation 3.3, τ_p represents the damping or dephasing time of the coherent phonons and ω indicates the instantaneous frequency of the oscillation. The frequency ω is assumed to be linearly chirped as shown in equation 3.4, where ω_0 and β represent its initial frequency and linear chirp rate, respectively. Figure 3-4 shows the result of fitting the time derivative of the signal at the highest pump fluence of figure 3-3 using equation 3.3. As shown, the fit is fairly satisfactory and is not affected by the background electronic reflectivity signal because of its very slow decay. Results of the

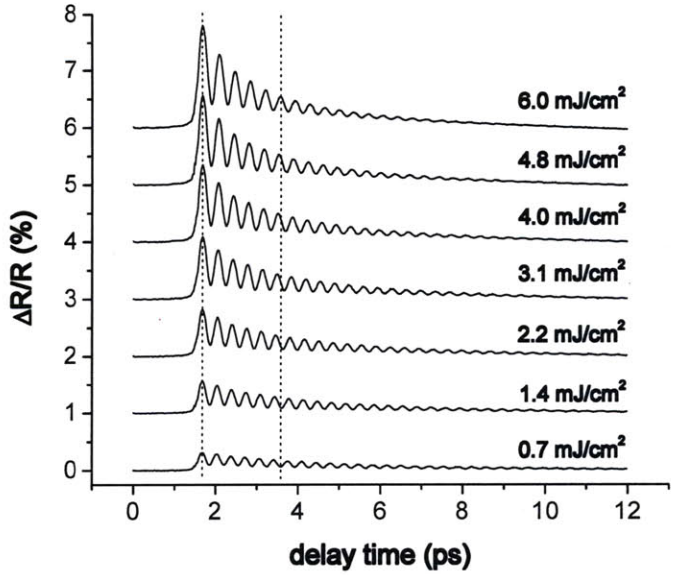

Figure 3-3: Time-dependent reflectivity change of bulk bimuth at different pump powers. The amplitude and electronic background increase with increasing pump power. The vertical dotted lines illustrate the relative phase change of coherent phonons and indicate that the oscillations are red-shifted with increasing pump power. Mild multi-shot damage was observed above 6.5 mJ/cm^2.

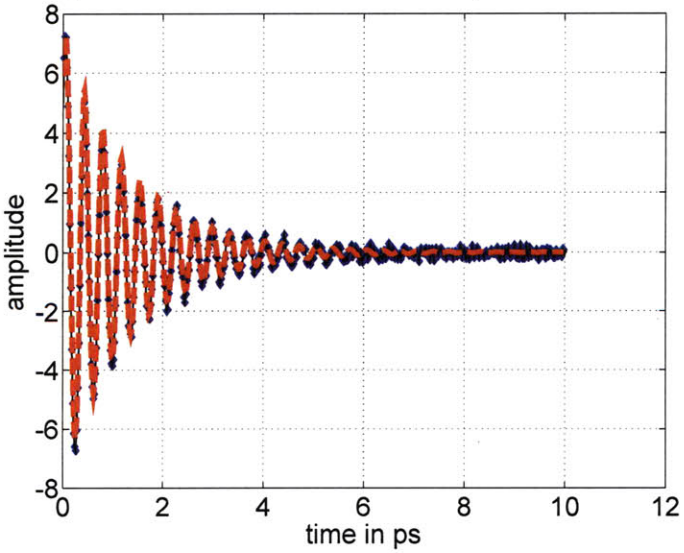

Figure 3-4: The blue dots represent the time derivative of the signal at 6.0 mJ/cm^2 in figure 3-3. The red shows the result of fitting the time derivative using equation 3.3. The slowly decaying background electronic signal is negligible so the parameters relevant to phonon oscillation are recovered well. Fitting yields an initial frequency of 2.64 THz, a dephasing time (τ_p) of 1.35 ps, and a chirp rate of 0.0303 THz/ps.

fitting analysis are displayed in figures 3-5 to 3-7.

Bond softening

The initial frequencies of the A_{1g} mode obtained from the fitting are shown in figure 3-5. They exhibit strong linear dependence on the pump fluence and small deviations become noticeable above 4 mJ/cm^2. The initial frequency, ranging from 2.90 to 2.64 THz, is red-shifted relative to that measured in continuous-wave Raman scattering experiments (2.93 THz) [HMH+98].

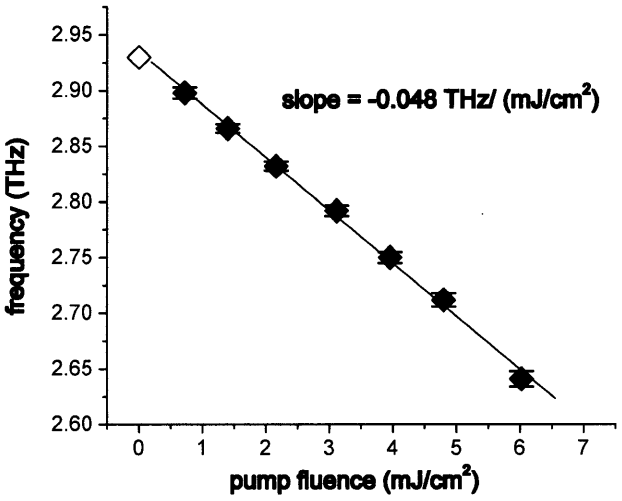

Figure 3-5: The initial frequency (solid squares) was obtained from the fit. The values show a strong linear dependence on the pump fluence, but small deviation begins to be observed at 4.0 mJ/cm^2. At room temperature, in the absence of photoexcitation, the frequency is 2.93 THz as shown by the open diamond.

Chirping

As mentioned, the frequency depends on the delay time as well. It is red-shifted at earlier times, but less so at later times. That is, the frequency is positively chirped. The assumption of linear chirp yields an excellent fit with small error at all pump fluences as shown in figure 3-6, suggesting that higher order chirp terms are negligible in this regime. The frequency is lower for higher pump fluences and correspondingly higher carrier density in the conduction band. Therefore, the instantaneous frequency

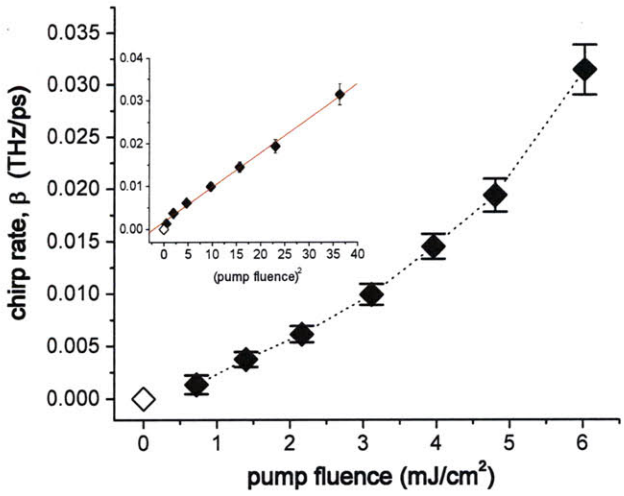

Figure 3-6: The frequency of the A_{1g} mode is chirped with time. The initial red-shift at early times diminishes at later times as hot carriers recombine. The chirp rate was obtained assuming that the frequency is linearly chirped with the delay time. The chirp rate increases nonlinearly with the pump fluence. The chirp rate is plotted with the square of the pump fluence in the inset. It exhibits a linear behavior, which might indicate second order recombination.

is indicative of conduction band carrier density. The positive chirp ($\beta > 0$) reveals that the carrier population in the conduction band decreases with the time via recombination or diffusion out of the probing region. The chirp rate increases nonlinearly with fluence.

The diffusion rate ($r_D = \mathrm{d}n/\mathrm{d}t = D\mathrm{d}^2n/\mathrm{d}z^2$) would increase with fluence because the density gradient increases. The increased diffusion rate may account for the blue-shifting with time. However, it has been reported that diffusivity is significantly lower at high densities of photoexcited carriers in bismuth [JBM+08], telluride [TF02], and Si [LSD97]. This diffusivity decrease results from increased carrier-carrier scattering. The lower diffusivity would produce a slower diffusion rate and counterbalance the increased density gradient at high carrier density. Accordingly, the net effect of the diffusion on the chirp rate is negligible.

The recombination rate was assumed to be proportional to the carrier density, following first order kinetics [ZVC+92]. According to kinetic theory, however, it is more likely that the recombination rate follows second order of carrier density because

$r_R = -\mathrm{d}[e^-]/\mathrm{d}t = k[e^-][h^+] \simeq k[e^-]^2$. If the recombination rate follows first order kinetics, it would yield a chirp rate increasing linearly with pump fluence (under the assumption of linear absorption—the carrier density proportional to the fluence up to 6 mJ/cm^2). However, the chirp rate increases nonlinearly with pump fluence as shown in figure 3-6. The nonlinearly growing chirp rate might originate from the second order recombination process. This is supported by the chirp rate's linear dependence on the square of the fluence (inset in figure 3-6).

Dephasing

The coherence dephasing process involves complex incoherent phonon-phonon and carrier-phonon scattering processes. It is observed that the dephasing time decreases exponentially with pump power (figure 3-7). Since the carrier density is elevated at higher fluence, more scattering events between carriers and phonons take place, introducing incoherence in the phonon oscillations. Higher carrier densities thus produce faster dephasing times. A precise and quantitative description of electron-phonon interactions is needed to explain the exponential decay in dephasing time..

Long time dynamics

Most spectroscopic studies of bismuth have focused on the coherent phonon response at early delay times. However, in order to understand carrier dynamics such as recombination and diffusion as well as thermal processes, longer time dynamics are also important. Figure 3-8 shows the time-dependent reflectivity of bismuth up to 100 ps. Following the fast rise at time zero, the background electronic signal continues to decay until the minimum level is reached at around 30 ps. The reflectivity crosses the zero level around 10 ps. It was observed that reflectivity crosses the zero level earlier with increasing pump fluence. After reaching the minimum value, the reflectivity continues to grow very slowly compared to the decay rate. It does not return to the original value within 100 ps at 6 mJ/cm^2.

The fast rise at time zero is attributed to the impulsive photoexcitation of carriers. In addition to thermalization between hot carriers and the lattice, carrier recombina-

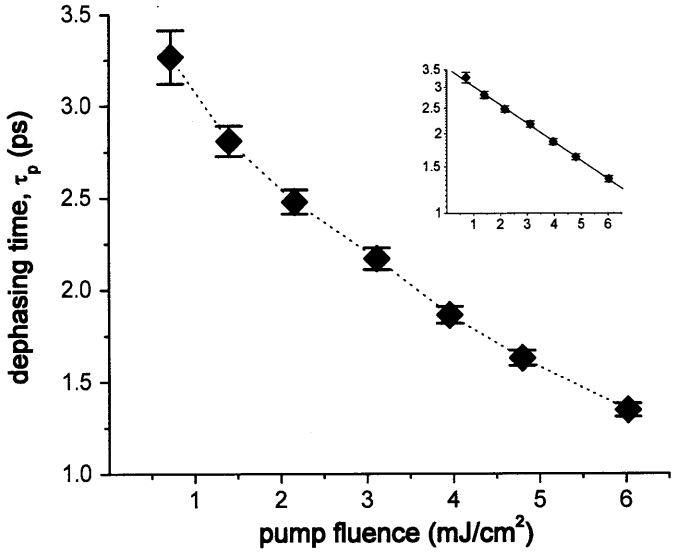

Figure 3-7: Phonon dephasing time as a function of pump fluence. The dephasing time decays exponentially with increasing pump fluence. The dephasing time vs. fluence is shown in logarithmic scale in the inset.

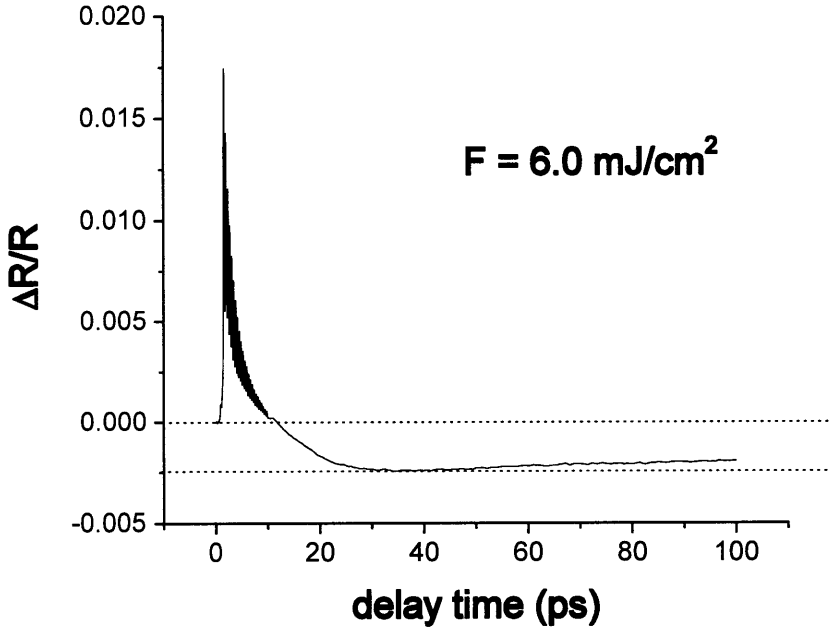

Figure 3-8: Time-dependent reflectivity at 800 nm up to 100 ps. The time step is 50 fs between 0 and 10 ps and afterwards the time step is 500 fs. The pump wavelength was 800 nm.

tion can contribute to lattice heating via non-radiative events. According to thermal analysis the decaying stage (up to ~30 ps) coincides with the heating of the bismuth lattice and the minimum reflectivity (at ~30 ps) represents the highest lattice temperature. Since diffusion and recombination reduce hot carrier density during the decaying stage, carriers are no longer available for heat conduction. Therefore, heat dissipation or cooling proceeds only through the lattice whose thermal diffusivity is much smaller than that of electrons. This can explain the slow recovery rate after ~30 ps.

Double pump experiments

Decamp *et al.* used two pump pulses to demonstrate coherent control of phonon modes. The arrival time of the second pump can be adjusted with respect to an initial first excitation such that the phonon amplitude is amplified or suppressed [DRBM01]. In addition to coherent control, excitation by the second pump can provide information on carrier density and lattice heating or cooling. The introduction of the second excitation to a nonequilibrium or highly excited state should exhibit a somewhat different response due to excited phonons, a higher population of carriers, or an elevated lattice temperature. In order to investigate carrier dynamics and lattice heating or cooling, double pump experiments were conducted. The interval time between the first and second pump was adjusted from 10 to 150 ps. Figure 3-9 shows the results of the double pump experiments in which the first pump fluence was varied. The second pump power is kept constant at 1.2 mJ/cm^2 and the inter-pump delay was fixed at 10 ps.

The amplitude of oscillations launched by the first pump grows with increasing fluence as seen previously. In addition, higher excitation causes more pronounced bond softening and shorter dephasing times. The effect of the first excitation on the second excitation seems subtle at first glance. By the time the second pump arrives, phonon launched by the first pump disappears almost completely, so there is little chance for phonon interaction. However, residual hot carriers and elevated lattice temperature may influence the response to the second perturbation.

Bond softening

The oscillatory parts in figure 3-9 were fitted using equation 3.3. Figure 3-10 shows the initial phonon frequency launched by the first excitation in red and by the second excitation in blue. Bond softening is observed with increasing pump power as shown by the red squares. In other words, the initial phonon frequency reduces monotonically with increasing excitation. Bond softening is also noticeable in the second response even though the second excitation is fixed. There are two major contributions to bond softening of the second oscillations: preexisting carriers and elevated lattice temperature.

Residual carriers which are generated by the first pump will maintain deformation in the potential energy surface, its smaller gradient softening the bond. Therefore, if significant amounts of carriers generated by the first pump can survive longer than the inter-pump delay 10 ps, they may soften phonon launched by the second excita-

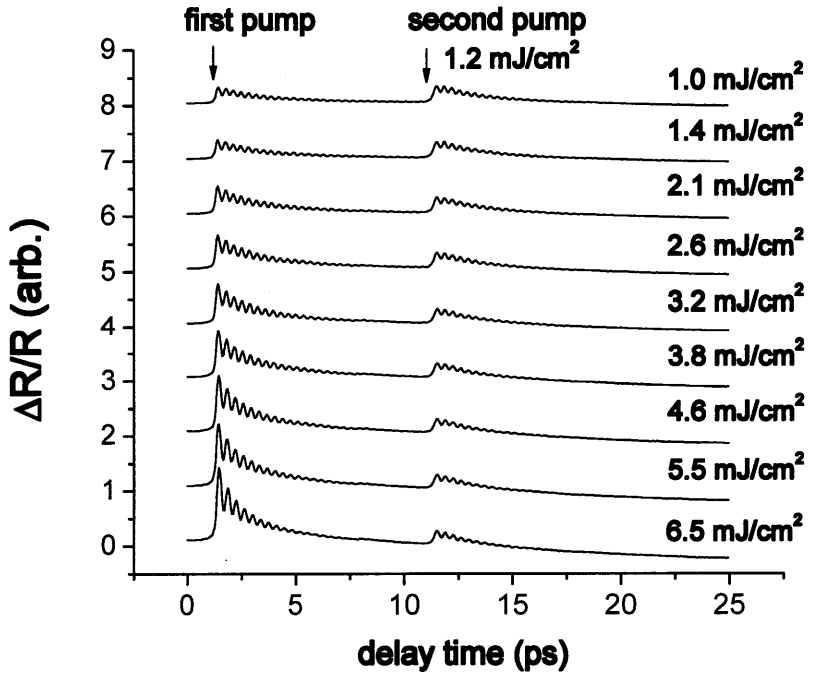

Figure 3-9: The reflectivity change under double excitation. The first pump power is varied from 1.0 to 6.5 mJ/cm^2, while the second pump is fixed at 1.2 mJ/cm^2. The inter-pump delay is 10 ps.

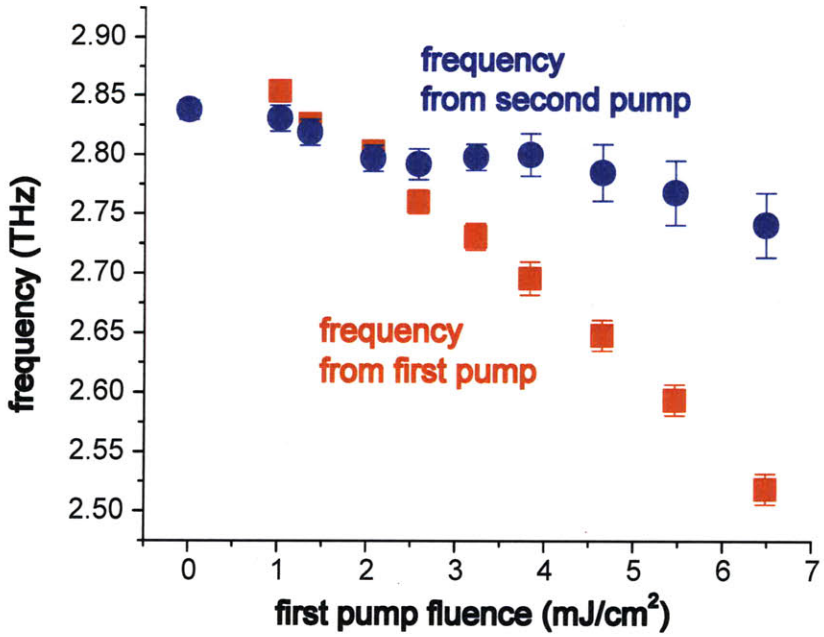

Figure 3-10: Initial frequency of the A_1g phonon mode as a function of the first excitation. Red squares represent the A_1g phonon frequency by the first excitation. The blue circles correspond to the phonon frequency launched by the second excitation. The second pump fluence is fixed at 1.2 mJ/cm^2 and the inter-pump delay time is 10 ps.

tion. There has been no direct evidence for the lifetime of carriers so far. Fahy and Reis suggested 5 ps as an electron-hole recombination time based on good agreement between their simulation results and experimental results in an effort to explain the dependence of phonon frequency on amplitude [FR04].

One way to measure the electron-hole recombination rate would be to measure the damping time of the coherent A_{1g} phonon under extremely low pump fluence at very low temperature. In this case, dephasing resulted from carrier-phonon scattering would be negligible due to the low carrier density. In addition, temperature effects such as enhanced phonon-phonon scattering would not affect the damping time. Accordingly, under the conditions, the damping is caused predominantly by electron-hole recombination which drives relaxation of the modified potential energy. Hase *et al.* measured the frequency and the damping time of the A_{1g} mode as a function of temperature in bismuth. At 10 K, the damping time was measured to

be 16 ps [HMH+98]. This can be considered as the approximate recombination time. Since the recombination time of 16 ps is longer than the inter-pump delay (10 ps), significant amount of carriers may survive until the second pump arrives. At 10 ps, more residual carriers are populated at higher excitation by the first pump. This higher density of carriers softens the bond further and causes lower initial frequency as shown by blue circles in figure 3-10.

It has been reported that the increased lattice temperature would affect the initial frequency. Hase *et al.* observed that the average frequency shifts from 101.5 cm^{-1} (3.045 THz) to 97.7 cm^{-1} (2.931 THz) when the temperature increases from 10 to 295 K [HMH+98]. Recently, Garl and coworkers also reported that the initial frequency changes from ~2.9 THz at 50 K to ~2.58 THz at 510 K [GGB+08]. Garl *et al.* attributed the high temperature bond softening to decreased binding energy and the increased interatomic distance due to thermal expansion from lattice anharmonicity.

Besides the anharmonicity, higher temperature increases thermal population of carriers in the conduction band and the high density of carriers can cause bond softening. A simple calculation using the Boltzmann distribution reveals that thermal population increases from 2.88×10^{17} cm^{-3} [Kit05] to $\sim1.00\times10^{19}$ cm^{-3} when the temperature increases from 300 K to 544 K (melting point of bismuth) under the assumption that the band gap is 0.2 eV. A carrier density of $\sim1.00\times10^{19}$ cm^{-3} corresponds to ~0.007% of valence electrons [MFW+05]. The contribution of this density to the bond softening is negligible [FRA+07]. If the band gap of 0.4 eV is used for the calculation, then 0.25% of valence electrons are promoted to the conduction band. Even this increased density cannot explain the large bond softening observed at 510 K in reference [GGB+08]. This leads to a conclusion that the temperature effects on bond softening originate from lattice anharmonicity, not from the increased carrier density. The photoexcitation (by the first pump) increases the lattice temperature as well as conduction band carrier density. The increased temperature by the first pump explains the bond softening observed in the second pump response as well.

To investigate whether residual carriers and increased lattice temperature has the

predominant effect, the inter-pump delay was adjusted from 10 to 150 ps. Results are presented in figure 3-11. For a given first excitation, the initial phonon frequency launched by the second excitation is plotted with respect to the inter-pump delay time. 6.5 mJ/cm^2 was used for the first excitation. If we assume that the electron-hole recombination time is ~15 ps, we can decouple the two effects. A thermal analysis indicates that the lattice temperature reaches its maximum around 20–30 ps rapidly but cools down very slowly afterwards. Therefore, we can assume that the lattice temperature is roughly constant from 30 to 150 ps. There is a noticeable change in the initial frequency between 150 ps and ∞ (when the lattice reaches room temperature), as shown in figure 3-11. This difference is attributed to a purely thermal effect such as thermal expansion (due to lattice anharmonicity) because the number of residual carriers at 150 ps are the same at ∞, but the lattice temperature at 150 ps is still high compared to that of ∞. By contrast, small variations in the

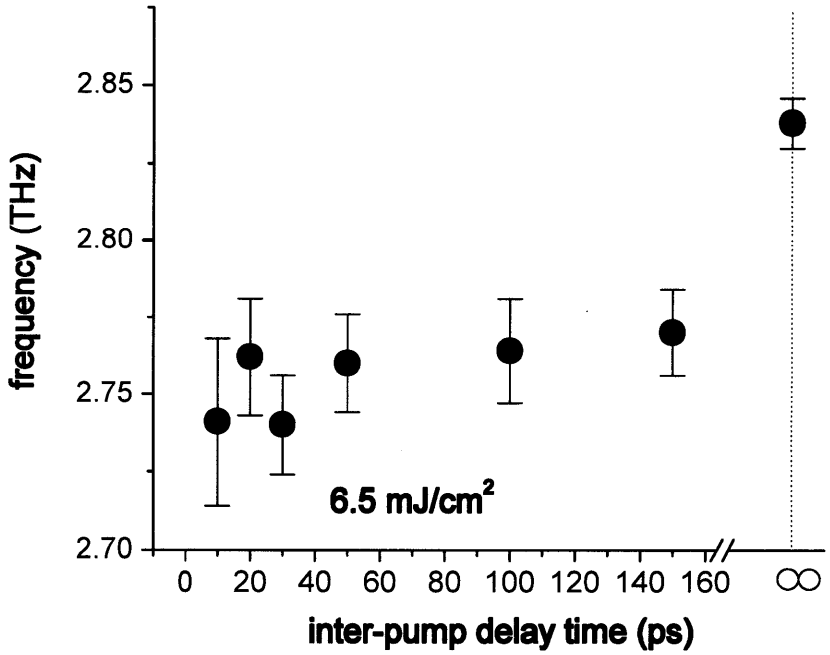

Figure 3-11: Initial frequency of the phonon generated by the second pump (1.2 mJ/cm^2) as a function of inter-pump delay time from 10 ps to 150 ps. The data were obtained under an initial excitation of 6.5 mJ/cm^2.

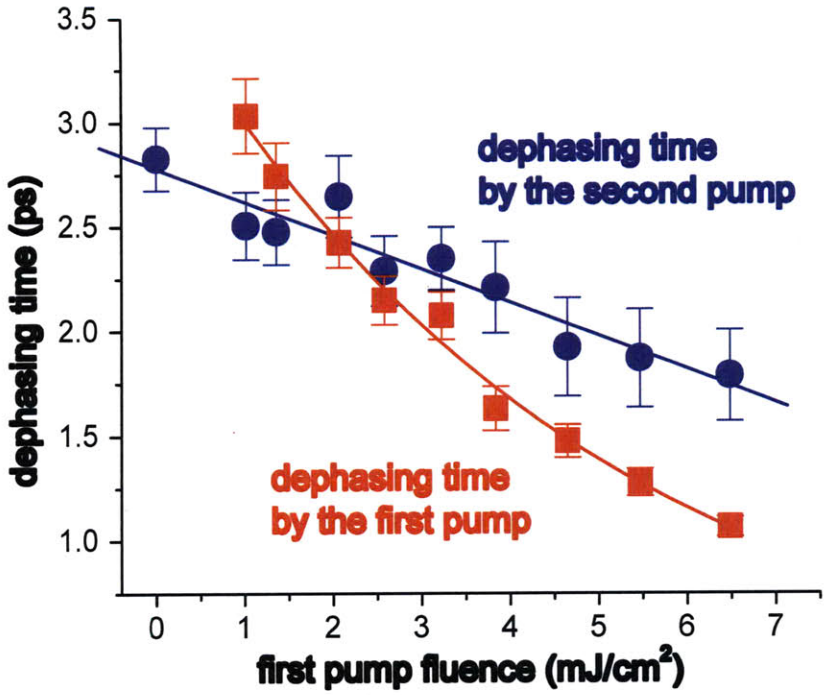

Figure 3-12: Dephasing time of the A_1g phonon mode as a function of the first excitation fluence. The red squares represent the phonon dephasing time for the first excitation. The blue circles correspond to the phonon dephasing time for the second excitation. The second pump fluence is fixed at 1.2 mJ/cm^2 and the inter-pump delay time is 10 ps.

initial frequency are observed from 10 to 150 ps. This small change results from both residual carriers and the increased temperature. According to thermal modeling which will be described later in this chapter, the lattice temperature at 10 ps is already significantly high. This means that the effect of the elevated temperature on the bond softening is already included at 10 ps. A small change from 10 to 50 ps is observed. This change is likely due to residual electron-hole recombination. From 50 to 150 ps, the initial frequency stays at the same level suggesting there is no significant change in both the carrier density and the lattice temperature.

Dephasing

Figure 3-12 illustrates the damping or dephasing time of the oscillations. The red squares represent the oscillation dephasing time caused by the first pump, revealing an exponential decay with increasing pump fluence as observed in figure 3-7. The blue circles illustrate the oscillation dephasing time caused by the second excitation at the inter-pump delay time of 10 ps. They show a linear decrease with increasing excitation even though the second pump is fixed. This reveals that the first excitation affects the second response at least until 10 ps, and stronger excitation by the first pump causes shorter damping time of phonon by the second excitation. This suggests that different mechanisms might exist between them. Dephasing involves complex carrier-phonon scattering and phonon-phonon scattering. As described, higher excitation leads to higher carrier density of carriers which introduces incoherence via electron-phonon scattering. In addition, high temperature effects such as increased phonon-phonon scattering or anharmonic phonon behavior can cause more rapid dephasing. Since the carrier density is appreciable and the lattice temperature is high at 10 ps, it is difficult to decouple the two effects. In an effort to decouple them, the dephasing time was measured while adjusting the inter-pump delay time from 10 to 150 ps. Results are presented in figure 3-13. The comparison of the dephasing time between 150 ps and ∞ reveals the role of temperature effects only because the excited carrier density is negligible (15 ps lifetime) and the lattice temperature is still high due to the slow cooling at this time. The difference in dephasing times between the two delay times (150 ps and ∞) is considerably large. On the contrary, there is a small increase in the dephasing time from 10 to 50 ps. The increase is ascribed to electron-hole recombination. From 50 to 150 ps, the dephasing time is constant because both the lattice temperature and the carrier density do not change within this time.

Hase *et al.* used the damped harmonic oscillator model to explain the temperature dependence of the dephasing time from 10 to 300 K and suggested that the dephasing of phonon is caused by anharmonic decay or energy relaxation [HMH+98]. They suggested that the possible decay channel of the A_{1g} mode is into two acoustic phonons

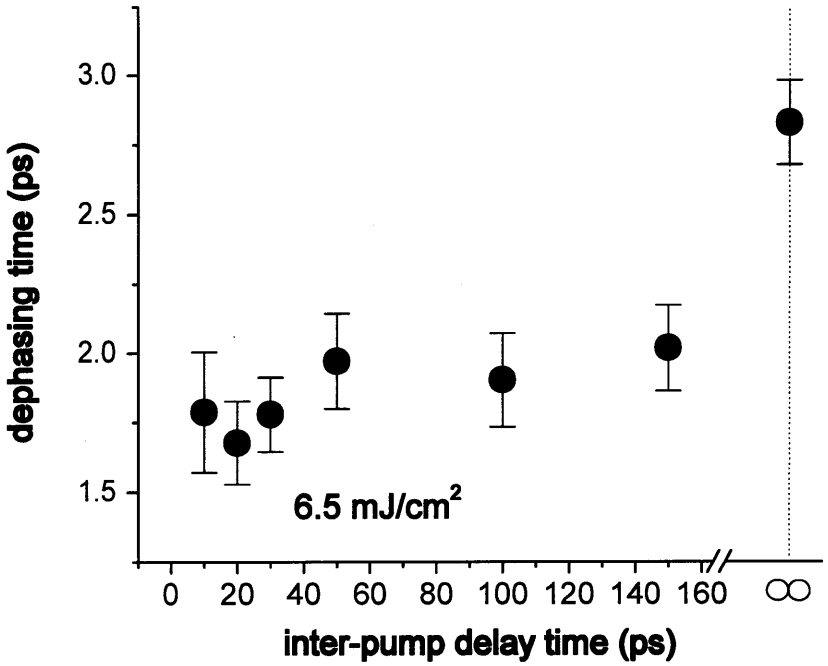

Figure 3-13: Dephasing time of the phonon generated by the second pump (1.2 mJ/cm^2) as a function of inter-pump delay time from 10 ps to 150 ps. The data were obtained under the first excitation of 6.5 mJ/cm^2.

at the L point whose frequency is half that of the A_{1g} mode [MFP$^+$07]. Garl *et al.* also attributed the dephasing of the A_{1g} mode to decay into two acoustic phonons which eventually leads to nonlinear chaotic motion of Bi atoms. The linear behavior represented by the blue circles in figure 3-12 agrees with the temperature-dependent dephasing observed in references [HMH$^+$98] and [GGB$^+$08]. If we assume that the lattice temperature is proportional to the first excitation used, the linear behavior might imply that the pure temperature dephasing effects win over residual carrier dephasing effects at 10 ps. By contrast, exponential decay is observed in the phonon caused by the first pump (the red squares in figure 3-12). In this case, the A_{1g} phonon and the carriers are generated at the same time and the high density carrier-phonon scattering would dominate dephasing effects over the elevated lattice temperature. It is probable that the exponential decay with the increasing excitation is due to the carrier-phonon scattering.

3.2.2 Single Crystal versus Thin Films

Hot carriers play an important role in ultrafast processes such as coherent optical or acoustic phonon generation, lattice heating, and phase transitions in solid-state materials [SM02]. Diffusion and recombination determine the spatial distribution of carriers which eventually governs their interaction with the lattice.

It is possible to confine the carriers and thus to alter the whole dynamics involving them by performing Bi thin film measurements. In thin films, carrier diffusion can be suppressed in a direction normal to the surface. Comparison between the bulk and thin film measurements may provide useful insight into carrier dynamics and their influence on other processes such as bond softening and phase transitions. In this section, experimental results from Bi thin films are presented and discussed in comparison with results from bulk Bi.

Thickness-dependent reflectivity

For the thin film measurements, four thin films were used. All of them were prepared by sputtering deposition. The thickness of thin films on glass substrate was estimated by measuring their absorption at 800 nm and using the absorption coefficient of Bi $\sim 6 \times 10^5$ cm^{-1} at 800 nm [WX07]. Since the absorption measurement was not viable for the opaque Si substrate, the thickness was determined by measuring the propagation time of acoustic waves through the thin layer. Figure 3-14 shows the reflectivities as a function of film thickness. All traces show oscillations resulting from the A_{1g} phonon mode launched via DECP. Another common feature is the decay of the background reflectivity, which is indicative of lattice heating by electron-phonon collisions or non-radiative electron-hole recombination. Other clear differences are observed between samples as well.

First of all, it is revealed that the absolute level of electronic background signal shows strong thickness dependence. For the bulk sample, the signal increases to a positive value instantaneously at the time origin and then decays with the delay time. A similar background signal is observed in the 300 nm thin film. However, for the

25 nm thin film, the signal is always negative. A thinner film yields a more negative change in the signal. This dependence implies that the electronic structure changes as a function of film thickness. The electronic structure of thin films still appears to develop towards that of the bulk sample. Considering that metals show fully developed electronic structure at the sub-nanometer scale, the present Bi thickness is unusually large. It is likely that the large thickness is ascribed to the large Fermi wavelength of Bi. The Fermi wavelength (λ_F), which is the de Broglie wavelength of electrons at the Fermi level, is as large as ~40 nm in bismuth, as compared to a few Å in most metals [GKS72]. Because of the large characteristic length, bismuth has been extensively studied for quantum transport and quantum size effects. For example, there have been many endeavors to elucidate the semimetal to semiconductor transition for very thin Bi films [Lut65, San67, HMB+93, RGN+03, RLD07]. However, the current optical studies do not provide crucial evidence to map the detailed thickness-dependent electronic structure.

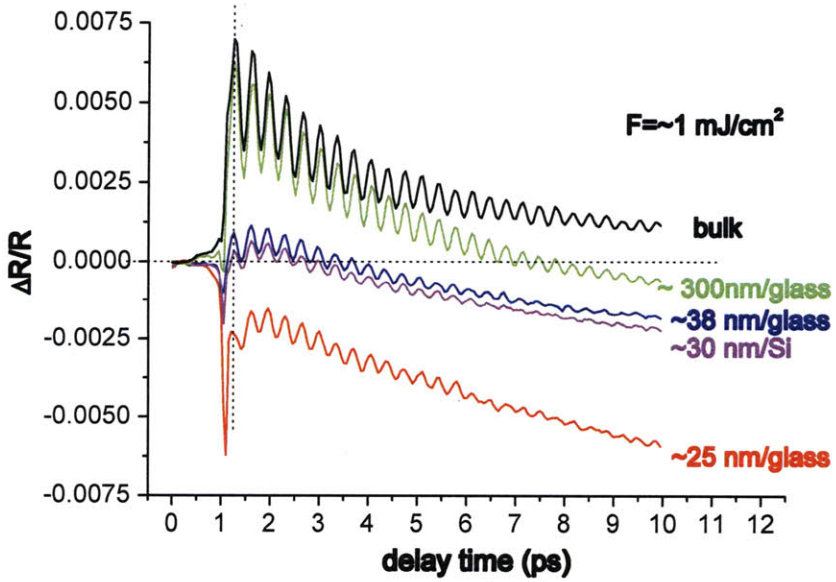

Figure 3-14: Thickness-dependent reflectivity. The electronic background signal in reflectivity exhibits strong dependence of the thickness. Also, the amplitude of the oscillations appears to decrease with decreasing thickness. The pump fluence is about ~1 mJ/cm^2.

The phonon amplitude is strongly influenced by the thickness. The amplitude is comparable to the electronic signal near the time origin for the bulk and 300 nm thin film. On the contrary, the amplitude is only ~10% of the background signal for the very thin films (25–40 nm). The strong dependence of the amplitude is quite interesting but difficult to interpret. It is likely that the probing depth in reflection measurements is constant for all samples, which is supported by the observation that the reflectivity is similar for all samples (~60–70% at 800 nm). This also implies that the probing depth is less than or comparable to the penetration depth because the thickness of all the samples are larger than the penetration depth (~16 nm). The number of phonons excited by the pump is approximately the same for the thin films as for the bulk because the thickness is larger than the penetration depth (this argument is applicable to the carrier density as well). Also, the number of phonons is expected to show roughly the same amplitude in reflectivity for all the samples because the probing depth is comparable to the penetration depth. However, the amplitude is much smaller in thin films than in the bulk sample. This reveals that the thickness-dependent amplitude might also result from thickness-dependent electronic structure, which affects electron-phonon coupling or the probe sensitivity to the phonons at a specific probe wavelength.

Another thickness-dependent feature is an initial drop below the unperturbed level at the time origin. It is more pronounced in the thin films and is very weak in the bulk sample. Boschetto *et al.* observed a large drop in the bulk sample using a 35 fs pulse [BGR+08]. They noticed that the drop is not produced by a longer 50 fs pulse. They established a relationship between forces exerted on atoms during laser-matter interaction, atomic motion, and optical parameters and suggested that the initial negative drop is related to a delicate coherent displacement of atoms by the polarization force during the pulse. However, their model can not explain the very strong drop observed in the thin film measurements presented here. In the model, the material parameters involved in the negative drop are the zero order polarizability, interatomic distance, and density. They are all unchanged for thin films. Based on the fast timescale of the initial drop, it may be due to fast carrier dynamics such

as carrier-carrier scattering or carrier-electric field interaction across the penetration depth rather than to coherent displacement of atoms. In reference [BGR+08], the depth of the drop grows with increasing pump power implying that a higher density of electrons causes a larger drop for a given pulse duration and bismuth sample. The density of electrons and holes are governed by diffusion and recombination. The long characteristic recombination time (~15 ps) cannot explain the fast timescale of the drop. The characteristic timescale for the diffusion reads $t_D = z^2/2D$, where z and D represent the propagation distance and diffusivity, respectively. The time required for electrons to cross the skin depth is $t_D = (15\text{ nm})^2/(2 \times 230\text{ nm}^2/\text{ps}) \approx 0.5$ ps [JBM+08]. This is also a longer timescale compared to the initial drop.

The only physical process that affects the density across the penetration depth on such a fast timescale is ballistic carrier transport. It is known that the carrier mean free path in bismuth can be as large as ~1 mm at 4.2 K, which means several orders of magnitude larger than in most metals [Ren58]. The large mean free path enables photoexcited electrons to propagate through the skin depth anomalously fast without scattering with other electrons or phonons, especially at low carrier density. Since the thickness of the thin films is smaller than the mean free path, the photoexcited electrons are confined within the Bi layer. The electron migration within the skin depth (or probing depth) may generate the initial drop. In addition, the intrinsic electronic structure cannot be ruled out in causing the huge difference of the fast initial drop as a function of film thickness. However, it is not trivial to unveil these effects.

Transient reflectivity of thin films is presented in figures 3-15 to 3-17. As the pump fluence increases, the negative change of the background electronic signal increases for all the films. The trend is most noticeable in 25 nm film. The change is about 0.5% at 4 mJ/cm^2 in the 38 nm film, while it is 3 % in the 25 nm film. Bond softening with increasing excitation is also observed for all the films. More cycles are contained between the two dotted lines at lower fluence in the figures.

The mathematical functional form of equation 3.2 which accurately fits the bulk reflectivity cannot accurately fit the thin film transient reflectivity. A more general

form is necessary to describe the reflectivity of thin films. However, the slowly-varying electronic background signal can be eliminated by differentiating the reflectivity with respect to delay time as before. Then equation 3.3 is used to fit the time-derivative signal in order to recover parameters for the oscillation parts. This fit is also used to investigate the effects of the thickness on bond softening, dephasing, and chirp rate.

Bond softening

Bond softening results from a smaller gradient of the potential energy surface at higher carrier densities or higher excitation fluence. Figure 3-18 shows the initial frequency of the A_{1g} mode with increasing pump fluence for the bulk and thin films.

The frequency shows a linear decay with the pump fluence in the bulk and thin films. The slope is steeper in thinner films, which indicates that the bond softening is more pronounced in thinner films. However, it appears that the intercepts of the lines converge on a constant value around 2.93 THz. This reveals that the interatomic force is the same in the unperturbed bismuth regardless of the thickness and that the

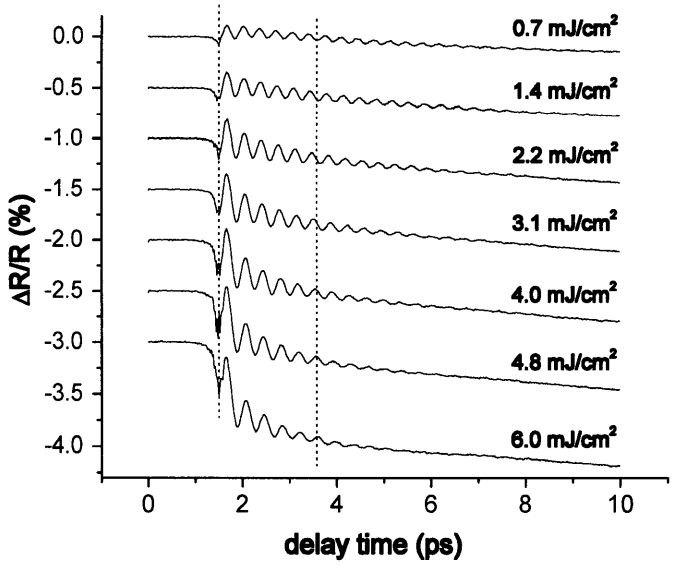

Figure 3-15: Transient reflectivity of 38 nm thin film on glass. The higher pump induces the bigger negative change in the background electronic signal. Bond softening is observed with increasing photoexcitation.

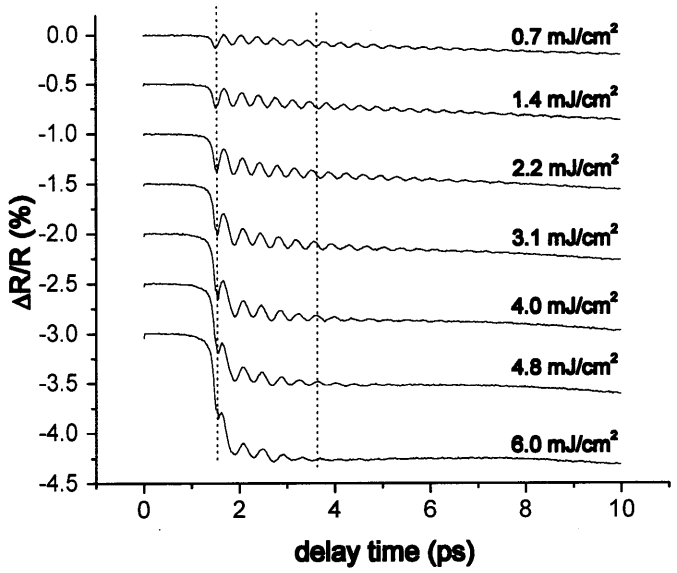

Figure 3-16: Transient reflectivity of 30 nm thin film on Si. The higher pump induces a larger negative change in the background electronic signal. Bond softening is observed with increasing photoexcitation.

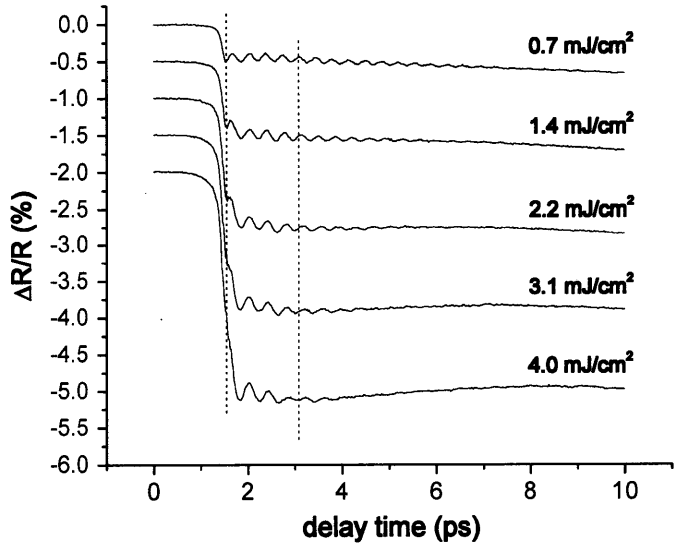

Figure 3-17: Transient reflectivity of 25 nm thin film on glass. The higher pump induces a larger negative change in the background electronic signal. Bond softening is observed with increasing photoexcitation. Mutlishot damage is noticeable above an excitation of 4 mJ/cm^2.

equilibrium potential energy is unchanged at least up to 25 nm thick. Since the thickness of all samples is more than the skin depth (~15 nm), photon absorption should be similar for all the samples. This suggests that the number of photogenerated carriers is also similar. Density functional calculations [MFW+05, FRA+07] have shown that the carrier density modifies the interatomic potential energy and softens the bond. Then, what causes bigger red-shifts of the frequency in thin films under the same excitation? The "initial" frequency is an instantaneous value at the time origin (t=0). Therefore, an extremely fast process should be involved, or intrinsic thickness-dependent properties such as electronic structure play a crucial role in the bond softening. Fast diffusion of carriers or ballistic transport may account for the considerable red-shift of the "initial" A_{1g} phonon frequency. As soon as carriers are generated impulsively, they can diffuse out of the skin depth due to the density gradient. The density can change significantly near the time origin if the diffusion rate is fast. A broad range of carrier diffusivities has been reported. A diffusion coefficient of 100 cm^2/s (= 10^4 nm^2/ps) was measured for the ground state of bismuth at room

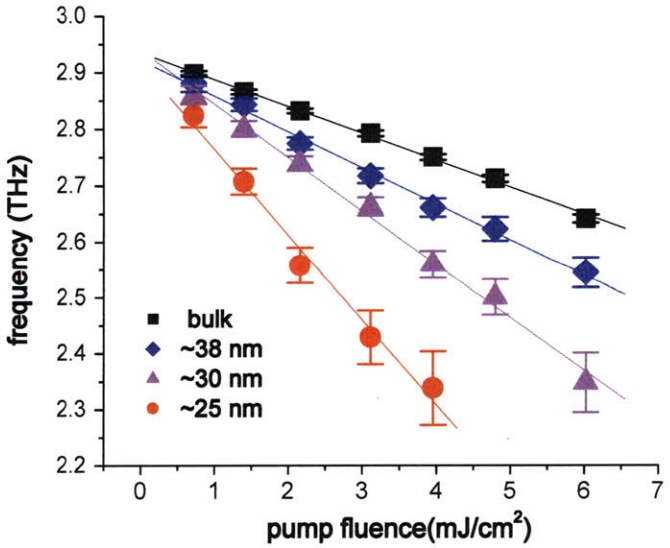

Figure 3-18: Red-shifting of the initial A_{1g} phonon frequency with increasing pump fluence as a function of film thickness. The bond softening becomes pronounced as the film thickness decreases, but the same ground state interatomic force or equilibrium potential energy is revealed regardless of the film thickness.

temperature [SS72]. A smaller diffusivity 2.3–5 cm^2/s (= 230–500 nm^2/ps) was also suggested. An approximate estimate can be made for the timescale on which carriers diffuse out of the skin depth. In the case of $D = 10^4$ nm^2/ps, the diffusion timescale is $t_D = (15\text{ nm})^2/(10^4\text{ nm}^2/\text{ps}) \approx 0.02$ ps. In this case, the timescale for diffusion is shorter than the pulse duration (~70 fs) and can be considered an impulsive process (A diffusion coefficient of $\sim 3 \times 10^3$ nm^2/ps yields a timescale comparable to the pulse duration). Given a large diffusion coefficient, carriers can diffuse out of the skin depth or probing depth near the time origin. This lowers the excited carrier density, eventually causing a small red-shift of the "initial" phonon frequency. This argument is applicable to the bulk sample. However, the diffusion of hot carriers is suppressed along the surface normal direction in thin films because of the large substrate bandgap (glass or silicon). The suppressed diffusion results in a higher carrier density within the skin or probing depth, which softens the bond more in thin films as shown in figure 3-18.

Amplitude

The power-dependent amplitude is illustrated in figure 3-19. For all pump fluences, the oscillation amplitude is significantly larger in the bulk than in the thin films, which was already illustrated in figure 3-14. As discussed earlier, the small amplitude may originate from the thickness-dependent electronic structure which affects the phonon sensitivity or couples to phonons at a probe specific wavelength. The amplitude increases gradually with increasing pump fluence and reaches a plateau in thin films. The saturation suggests less efficient absorption at high excitation. The earlier saturation in thin films might result from the higher carrier density confined within the skin depth which hampers further absorption of photons and further generation of carriers.

Dephasing

Shorter dephasing times are observed in thin films. Several complicated processes such as carrier-phonon scattering, phonon-phonon scattering, and anharmonicity account

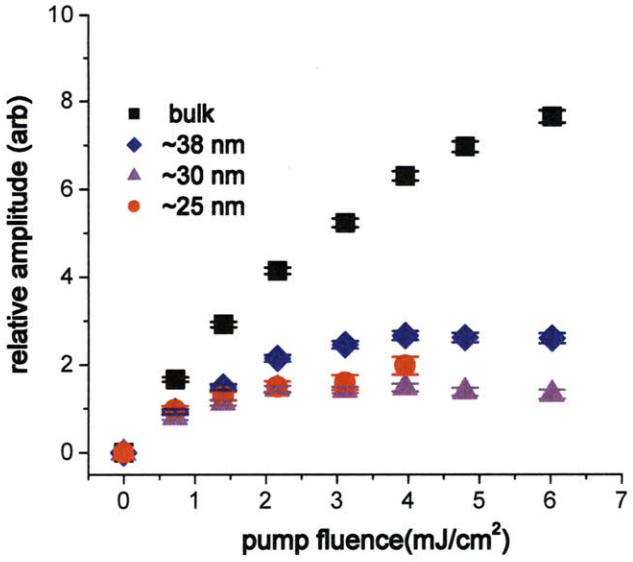

Figure 3-19: Amplitude of phonon oscillations with increasing pump fluence for multiple film thickness. Bulk bismuth exhibits a large phonon amplitude, while thin films show significantly smaller amplitudes. The amplitude increases gradually with increasing fluence and reaches a plateau in thin films.

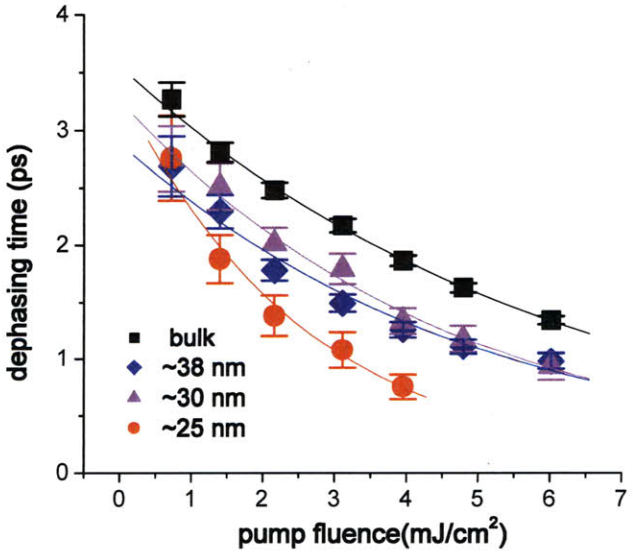

Figure 3-20: Coherence dephasing time with increasing pump fluence as a function of film thickness. It is revealed that the phonon coherence decays faster in thin films because of high carrier density in the probing depth.

for dephasing. The shorter dephasing time in thin films is mainly due to a high density of carriers confined within the thin layer. The lattice is likely heated more quickly in thin films through denser carrier-phonon coupling. The resulting high temperature reduces the dephasing time as discussed. All samples show an exponential decay with increasing pump fluence.

Long time dynamics and acoustic pulse generation

Long time dynamics up to 100 ps of Bi films are revealed in figure 3-21 to figure 3-23. Strong oscillations of the A_{1g} mode exist near the time zero, but they are not immediately visible due to the longer time range. For the 38 nm thin film in figure 3-21, the reflectivity decays quickly until 25 ps and then grows very slowly up to 100 ps.

During the decay up to 25 ps, thermalization between hot carriers and the lattice leads to lattice heating. Non-radiative recombination increases the lattice temperature as well. The decay reflects the fast timescale of the lattice heating via short electron-phonon coupling times and a fast recombination rate. After reaching the minimum, it changes direction and continues to grow slowly toward the pre-excitation level. This period corresponds to the lattice cooling. Since electron-hole pairs recombine earlier than 25 ps, they are not available for heat dissipation. Even if they are available, their diffusion perpendicular to the surface is suppressed at the interface so they rarely contribute to the lattice cooling. The heat conduction in the radial direction is insignificant because the beam diameters of pump and probe ($\sim$100 μm) are much larger than the skin depth. The resulting temperature gradient, the driving force for heat flow, is several orders of magnitude larger perpendicular to the surface than in the radial direction. Thin films cool through slow heat conduction perpendicular to the surface, mediated by lattice atoms in bismuth and the glass substrate. The equilibrium thermal conductivity of bismuth is 7.97 W/m/K. The thermal conductivity is dominated by the lattice part because photoexcited or thermally populated electrons in the conduction band are negligible. The growth rate of the reflectivity increases with increasing pump fluence because the larger temperature gradient at high pump fluence yields a faster cooling rate. At a given pump fluence, the growth

rate increases with decreasing film thickness.

Common dips are observed near 25 ps for all pump fluences in the 38 nm film, as shown in figure 3-21. Those dips are also observed around 20 ps in other films as shown in figures 3-22 and 3-23. The bulk bismuth did not exhibit such dips. The origin of the dips is acoustic phonon pulses generated in thin films. The general mechanism of the acoustic pulse generation in thin films is explained in reference [TM94, SMW03]. Figure 3-24 illustrates how the acoustic phonon pulse is generated in bismuth thin films. A strong pump pulse generates hot electrons in the conduction band and these hot electrons raise the lattice temperature quickly on a picosecond timescale. Accordingly, the lattice experiences a sudden thermal expansion, represented by a linear combination of many acoustic phonon modes or equivalently by an acoustic phonon pulse. The acoustic pulse generated at the surface can propagate through the thin layer and transmit across the bismuth-glass interface. The pulse is reflected from the interface as well, but reflectance of the acoustic pulse is low (~15%) because of similar acoustic impedances among bismuth (~17.5 g/cm^3·nm/ps), glass, and silicon

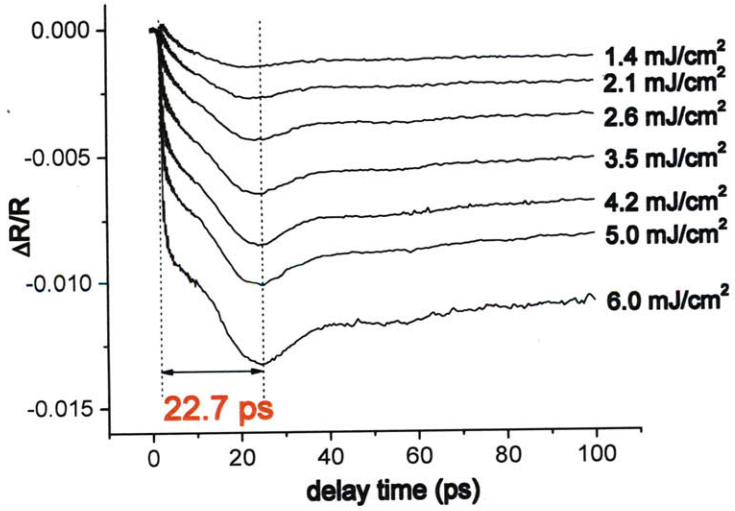

Figure 3-21: The long time dynamics of 38 nm thin film on glass are illustrated. Reflectivity decays quickly until ~25 ps and then increases very slowly up to 100 ps. For all pump fluences, common dips are observed, which are attributed to an acoustic phonon generated at the Bi-glass interface. The time of 22.7 ps represents the traveling time of the acoustic pulse from the interface to the surface.

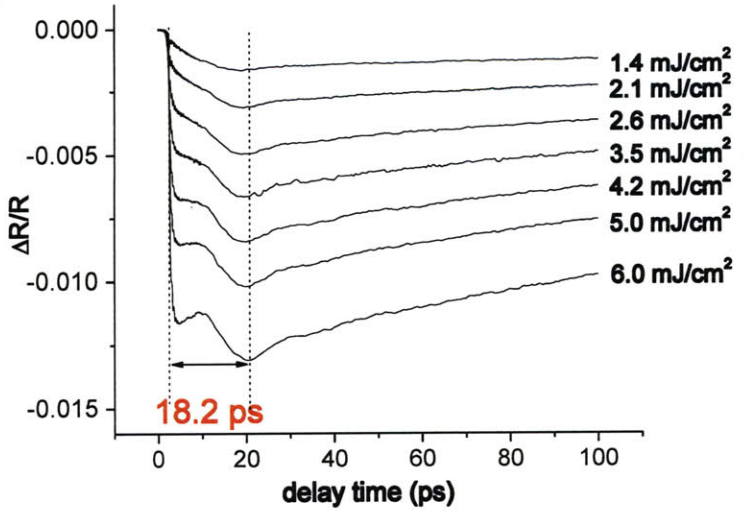

Figure 3-22: Long time dynamics of 30 nm thin film on silicon. Reflectivity decays quickly until 25 ps and then increases very slowly up to 100 ps. Common dips are observed for all pump fluences, which are attributed to acoustic phonons generated at the interface. The traveling time of the acoustic pulse from the interface to the surface is 18.2 ps.

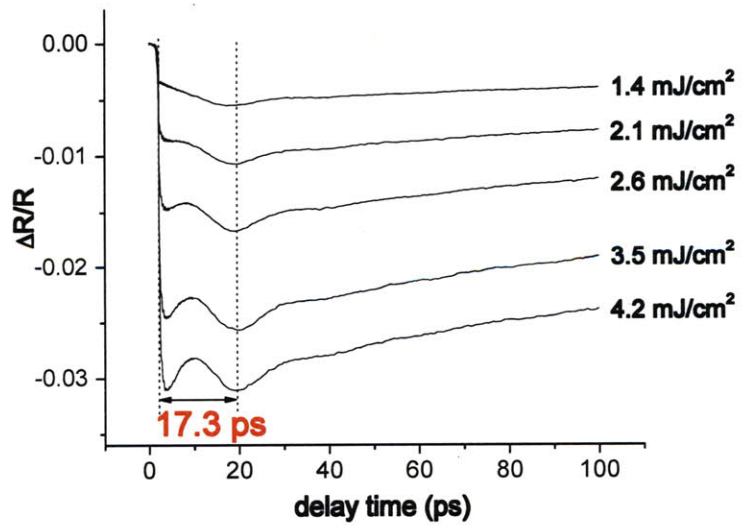

Figure 3-23: Long time dynamics of 25 nm thin film on glass. Reflectivity decays quickly until 25 ps and then increases very slowly up to 100 ps. Common dips are observed for all pump fluences, which are attributed to acoustic phonons generated at the interface. The traveling time of the acoustic pulse from the interface to the surface is 17.3 ps.

oxide (~13 g/cm^3·nm/ps). The acoustic pulse (~15%) reflected from the interface barely contributes to the optical reflectivity. The dip is more noticeable with higher excitation revealing that a higher amplitude acoustic pulse is launched by higher optical excitation.

The acoustic impedance is characteristic of materials and is given by the following equation:

$$Z = \rho \cdot c, \tag{3.5}$$

where ρ and c represent a material's density and speed of sound, respectively. At the interface between media 1 and 2, the reflection coefficient R is represented as follows:

$$R = \frac{Z_1 - Z_2}{Z_1 + Z_2}. \tag{3.6}$$

Hot electrons propagate through the thin Bi layer via diffusion or ballistic transport, but they cannot cross the interface. The hot carriers heat the lattice at the interface and lead to thermal expansion of the lattice. This generates another phonon pulse which can propagate in both directions. The phonon pulse moving toward the bismuth surface modulates the optical reflectivity and creates the dip. The film thickness can be estimated from the acoustic pulse traveling time from the interface to the surface and the speed of sound in Bi (1.79 nm/ps). The traveling time of hot carriers from the surface to the interface can be ignored for this estimation. There is good agreement between the thicknesses obtained by the optical absorption measurement and by the current acoustic measurement. In this thesis, the thickness of 38 nm and 25 nm film thickness on glass substrate are given by the optical absorption measurement, while the thickness of 30 nm film thickness on silicon substrate is provided by the acoustic measurement.

Interestingly, the arrival or traveling time of the acoustic pulse is dependent on the excitation. This difference is subtle, but it is evident between the lowest and highest excitations, as shown in figure 3-25. For ease of comparison, the reflectivity is enhanced by a factor of 8 in the lowest excitation. The acoustic pulse from the lowest excitation arrives at the surface ~3 ps earlier than that from the highest

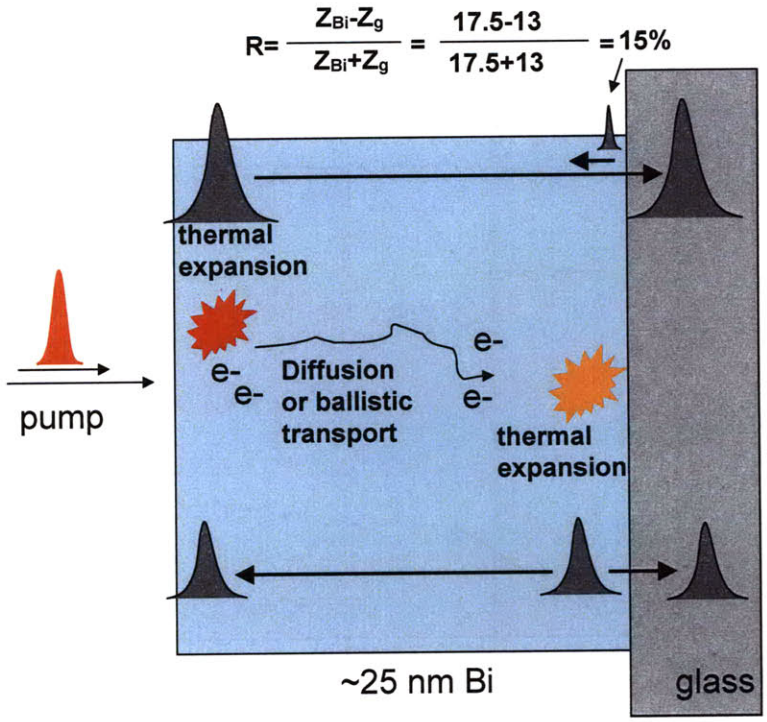

Figure 3-24: Schematic illustration of acoustic phonon pulse generation in bismuth thin films.

excitation. The time difference of 3 ps is significant at the given arrival time of 22.7 ps, corresponding to ~13%. Higher excitation yields a higher lattice temperature, which may be responsible for the time difference. The temperature effect on the speed of sound is obvious in the following equations and can be estimated for bismuth:

$$c = \sqrt{\frac{E}{\rho}}, \tag{3.7}$$

where E and ρ indicate Young's modulus and density, respectively. The density reduces with increasing temperature because the lattice expands with increasing temperature:

$$V = l^3 = [l_0(1+\alpha\Delta T)]^3 \simeq l_0^3(1+3\alpha\Delta T) = V_0(1+3\alpha\Delta T), \tag{3.8}$$

$$\rho = \frac{m}{V} \simeq \frac{m}{V_0(1+3\alpha\Delta T)} = \frac{\rho_0}{(1+3\alpha\Delta T)}, \tag{3.9}$$

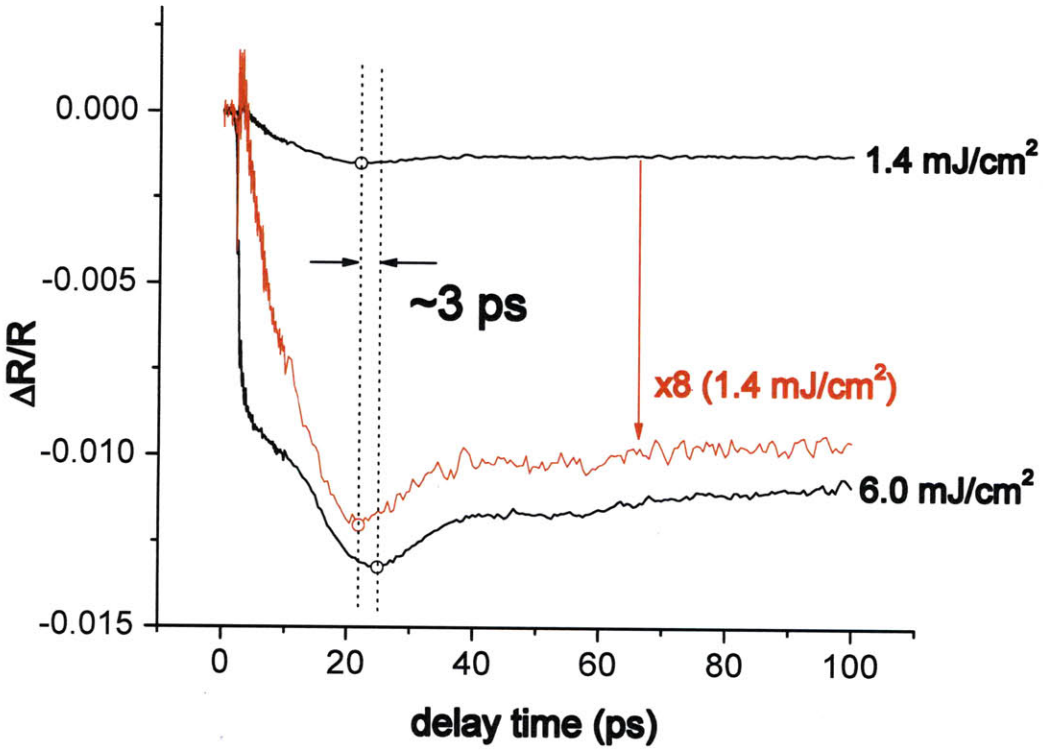

Figure 3-25: Comparison of arrival times of two acoustic pulses. One represents a strong pulse generated by 6.0 mJ/cm^2, while the other one represents a weak pulse generated by 1.4 mJ/cm^2. The weaker pulse is magnified by a factor of 8 for ease of comparison. A large change in the arrival time, ~3 ps, is observed.

$$c = \sqrt{\frac{E}{\rho}} \simeq \sqrt{\frac{E}{\rho_0}}\sqrt{(1+3\alpha\Delta T)} = c_0\sqrt{(1+3\alpha\Delta T)}, \tag{3.10}$$

$$\simeq c_0(1+\frac{1}{2}3\alpha\Delta T) = c_0(1+1.5\alpha\Delta T). \tag{3.11}$$

In the above equations, Young's modulus is assumed to be constant with changing temperature. α represents a linear thermal expansion coefficient whose value is +13.4 µm m^{-1}K^{-1} in bismuth. Therefore, equation 3.11 states that the speed of sound increases with increasing temperature or pump excitation. If we assume that ΔT is ~200 K from 1.4 mJ/cm^2 to 6.2 mJ/cm^2 excitation, the change in the speed of sound is only ~0.4%. However, the experimental results contradicts this estimate.

In reality, Young's modulus may not be constant with temperature. Young's modulus is defined as follows:

$$E = \frac{\text{tensile stress}}{\text{tensile strain}} = \frac{\sigma}{\varepsilon} = \frac{F/A_0}{\Delta L/L_0}. \tag{3.12}$$

Rearrangement of equation 3.17 yields Hooke's law and a relation between a spring constant and Young's modulus:

$$F = (\frac{EA_0}{L_0})\Delta L = kx, \tag{3.13}$$

$$k = \frac{EA_0}{L_0}. \tag{3.14}$$

Young's modulus is proportional to the force constant, as shown in equation equation 3.14. For simplicity, let's assume that the thin film grows such that the (111) crystal axis is identical to the surface normal direction. Then the displacement ΔL occurs along the A_{1g} phonon mode coordinate. In this case, k represents the Bi-Bi interatomic force constant of the A_{1g} phonon mode. Temperature affects the force constant through the lattice anharmonicity. The frequency of the A_{1g} phonon mode red-shifts from 2.95 to 2.58 THz when the temperature increases from 50 to 510 K [GGB$^+$08]. Using the relation $k = \sqrt{w/m}$, we estimate that the force constant k decreases by 6.5% from 50 to 510 K. If we assume that the temperature changes from 300 to 500 K when the pump fluence increases from 1.4 to 6.0 mJ/cm^2, the bond softens by $\sim$4%. Finally, equation 3.7 reveals that the speed of sound decreases by $\sim$2% through anharmonicity. This overwhelms the effect of the decreased density by thermal expansion and explains the reduced speed qualitatively, but there is still a large discrepancy.

It was observed that bond softening of the A_{1g} phonon mode is caused by excited carriers as well as by the elevated lattice temperature. Bond softening due to excited carries is more severe than that due to the elevated temperature. As shown in figure 3-18, higher excitation leads to a significant decrease in bond strength. Eventually, this

slows the speed of sound. Judging from the frequency, the speed of sound would decrease by ~5.4% when the fluence increases from 1.4 to 6.0 mJ/cm^2. The density of carriers decreases and the temperature increases while the acoustic phonon pulse propagates through the layer.

It is also likely that the acoustic phonon pulse is generated at different times depending on the pump fluence. This is supported by the observation that carrier density influences the diffusivity of hot electrons. Electron diffusivity can be reduced significantly with increasing excitation or increasing carrier density. For example, it has been reported that the diffusivity was estimated as 230 nm^2/s at high excitation. This is much lower in magnitude than the 10^4 nm^2/ps ground state ambipolar diffusivity estimated from room temperature carrier mobilities along the inward surface normal [JBM$^+$08, SS72]. The slower diffusion of hot electrons gives rise to a later phonon pulse at the interface, which may account for the delayed acoustic phonon pulse arrival time at high excitation. Let us assume that the arrival time difference, 3 ps, is attributed only to the decreased diffusivity of electrons and that the speed of sound is the same for both excitations. If we use the diffusivity of 230 nm^2/s at 1.4 mJ/cm^2, then the diffusivity is estimated at 120 nm^2/s at 6.0 mJ/cm^2.

For other thin films (25 nm and 30 nm), the acoustic phonon pulse also arrives at the surface ~1–2 ps later at higher excitation.

3.3 Probing Electronic Structures: 800 nm pump-continuum probe

We have observed large differences in transient reflectivity including background electronic signal, bond softening, coherence dephasing, and chirp between Bi bulk and thin films. Among them, the thickness-dependent background electronic signal is striking. For a 25 nm thin film, negative reflectivity at 800 nm is observed at all times regardless of pump excitation and delay time. By contrast, for the bulk, positive reflectivity is observed at early times. The reflectivity continues to decay and crosses

the unperturbed level at later times. The thickness-dependent behavior strongly suggests that the electronic structures are significantly different among samples. It appears that the electronic structure evolves with increasing thickness (25–40 nm) towards that of the bulk. It is surprising that even for a 38 nm thin film, the electronic structure is far from that of the bulk. This likely originates from quantum size effects or quantum confinement effects due to the long Fermi wavelength (~40 nm) [GKS72]. In an efforts to investigate the electronic structure of bismuth, we carried out 800 nm pump-continuum probe experiments where the probe wavelength is varied from 560 to 880 nm. Experimental details were described in section 2.5.1.

3.3.1 Results

Bulk single crystals

Figure 3-26 shows the transient reflectivity of bulk Bi as a function of probe wavelength. (a) and (b) show the dynamics up to 10 ps and 70 ps, respectively. For all wavelengths, strong oscillations due to the A_{1g} phonon mode are observed as shown in (a). The frequency and phase are the same regardless of probe wavelength. The amplitude is influenced by the probe wavelength, but it is not clear whether this is a real effect or an artifact originating from pulse duration.

For long wavelengths from 700 to 850 nm, the background electronic reflectivity increases initially near the time origin and proceeds to decay to its minimum around 25–30 ps. On the other hand, for short wavelengths from 600 to 640 nm, the reflectivity decreases to a negative value initially at the time origin and continues to decrease until 25–30 ps. Reflectivity at 680 nm shows the intermediate between the two regimes. In that case, the background level stays at zero shortly after the time origin and then shows a continuous decay. The absolute value of the minimum reflectivity continues to increase as the wavelength decreases from 850 to 640 nm, but it starts to decrease at shorter wavelength than 640 nm.

For all wavelengths, the background reflectivity exhibits common features. First, it decays until around 25 ps as shown in (b). It is likely that the decay corresponds to

lattice heating via inelastic electron-phonon scattering and nonradiative electron-hole pair recombination. The common minimum level near 25 ps coincides with the maximum temperature of the lattice which is revealed by the thermal model described in the next section. Second, following the minimum point, it increases towards the unperturbed level "slowly" which is due to slow lattice cooling through heat conduction. As previously discussed, the heat conduction involves lattice atoms only because the

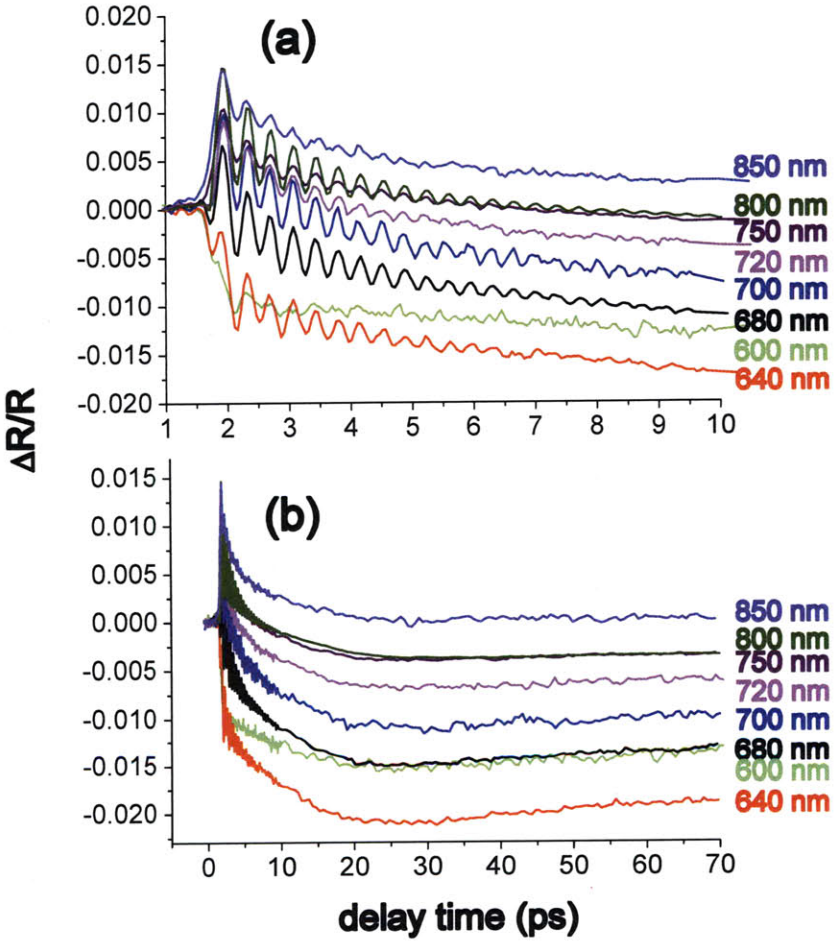

Figure 3-26: Wavelength-dependent reflectivity of bulk single crystal bismuth. A white light source was created by focusing a fundamental 800 nm pulse on a sapphire plate. The white light was focused on the sample which was excited by an 800 nm pulse. Each wavelength was selected using a bandpass filter in front of the photodiode. (a) shows the reflectivity change up to 10 ps where strong oscillations are observed. (b) reveals long time dynamics of bismuth up to 70 ps. The pump fluence was 6 mJ/cm^2.

majority of electron-hole pairs recombine and are unavailable for the heat conduction. In other words, carriers heat the lattice and disappear without cooling the system. The "slow" increase in reflectivity may support the idea that cooling proceeds only via lattice conduction as revealed by the thermal model in the next section. It is clear that the increasing rate changes depending on the wavelength. For example, the slope is steeper for 640 nm than 850 nm. The slope of a specific wavelength might be related to the relaxation rate of electrons which are thermally populated to a certain energy level. Electrons are thermally populated to higher energy levels and then relax with decreasing temperature obeying the Fermi-Dirac distribution. The temporal change or relaxation of the electron population may account for the reflectivity change in the reflectivity as the temperature decreases. The different slope could be attributed to different relaxation rate of the populated electrons. For instance, the electron population relaxes more rapidly, which involves the energy level of 640 nm than that of 850 nm.

Interestingly, similarities exist between the film thickness and wavelength dependences. We observed that decreasing film thickness causes a similar negative reflectivity change as shown in figure 3-14. This implies that increasingly thick Bi films evolve their electronic structures towards that of bulk bismuth.

Thin films

Figure 3-27 shows the probe wavelength-dependent reflectivity of 25 nm thin film on glass. The background reflectivity is always negative regardless of the probe wavelength. The (negative) change increases as the wavelength decreases from 880 to 640 nm, and it then decreases for wavelengths shorter than 640 nm. Even a 960 nm wavelength does not change the reflectivity sign to the positive level.

It is observed that the oscillation amplitudes exhibit strong wavelength dependence in (a) of figure 3-27. The amplitude of oscillations at 800 nm is typically 0.2% or less. The amplitude of the oscillations at 800 nm is smaller in figure 3-27 than in figure 3-14 due to a longer pulse duration. Even when the 800 nm pulse duration is ideally optimized to 60–70 fs, the amplitude is not larger than 0.2%. However,

the oscillation amplitude becomes significantly larger for wavelengths shorter than 680 nm. It is comparable to ~1%. This reveals that the oscillatory behavior is strongly coupled to electronic energy levels.

An acoustic phonon pulse is observed around 20 ps for almost all the wavelengths as shown in (b) of figure 3-27.

Similar to the bulk, the thin film reflectivity increases slowly after 20–30 ps, indicating that the lattice cools. Because of the broad acoustic phonon pulse, it is hard to

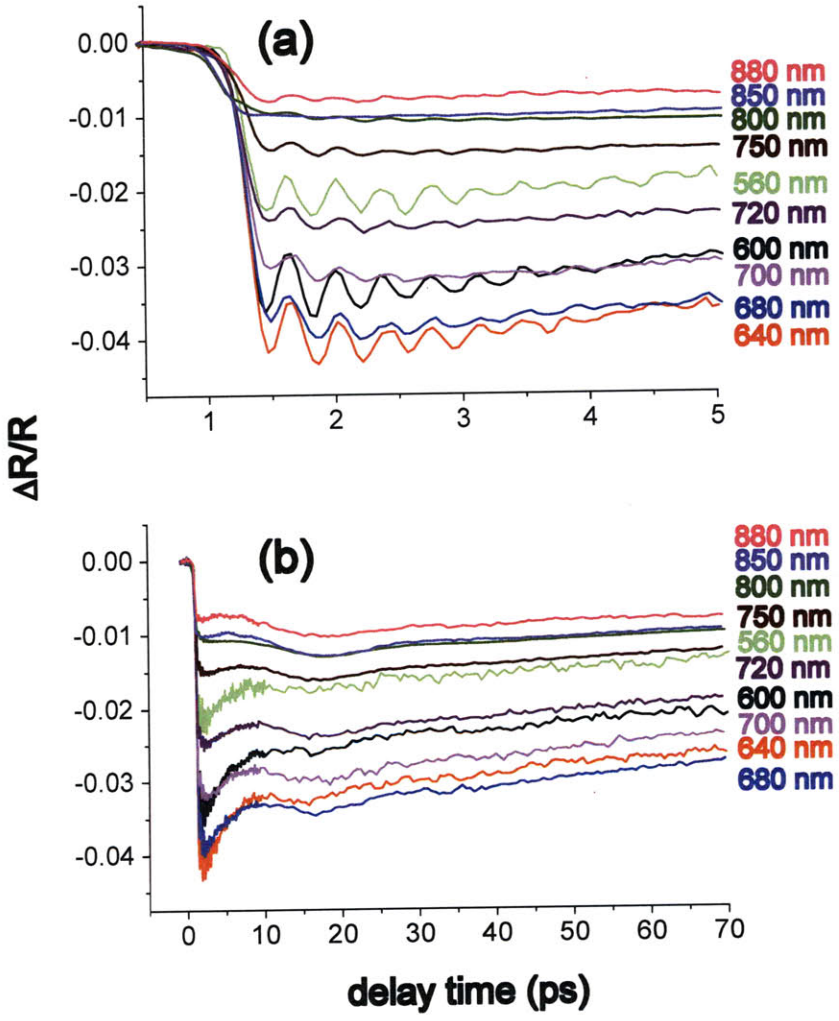

Figure 3-27: Wavelength-dependent reflectivity of the 25 nm thin film. The wavelength is varied from 560 to 880 nm. (a) shows the reflectivity change up to 10 ps where strong oscillations are observed. (b) reveals long time dynamics of bismuth up to 70 ps. The pump fluence was ~2.0 mJ/cm^2.

identify precisely when the lattice begins to cool. The increasing rate or slope in the reflectivity is wavelength-dependent, as was seen in the bulk (figure 3-26). For example, the reflectivity increases more rapidly at 680 nm than at 880 nm. As discussed in the bulk measurements, the varying slope is attributed to different relaxation rates of thermally populated electrons in certain energy levels which are associated with the probe wavelength.

Reflectivity up to ~10 ps is very sensitive to the probe wavelength. The change is moderate from 880 to 720 nm, while it is more significant from 700 to 560 nm. The change might be associated with the relaxation rate of nonequilibrium electrons, which may be affected by electron-occupied energy levels. Since electron-hole pairs recombine on this timescale, the change may reveal the recombination rate. The recombination can occur preferentially when electrons and holes stay at certain energy levels. This may explain the wavelength-dependent change.

3.3.2 Discussion

Our current transient reflectivity measurements may provide information about the electron or lattice temperature raised by optical excitation. This idea comes from traditional thermo-modulation spectroscopy where small thermal variations are introduced in a sample and the corresponding reflectivity change is measured [Sco67, RL72]. Several effects may cause the reflectivity change, including the smearing of electronic occupancy near the Fermi level, Fermi level shifting, lattice expansion, or electron-phonon coupling [SLFE87]. Differential reflectivity measurements have been used to investigate interband electronic transitions from the d bands to conduction band energies near the Fermi level in noble metals [SLFE87, Ees83, RL72, Sco67].

For photon energies near the interband transition, the major contribution to thermoreflectance is Fermi smearing caused by electron or lattice heating. An increase in temperature leads to increased electron populations above the Fermi energy and decreased populations below the Fermi energy. In noble metals such as Au and Cu, a simple model may be established considering interband transitions from flat d bands to states about the Fermi energy [RL72, SLFE87]. For a large temperature change,

the corresponding change in electron population is determined by the Fermi-Dirac distribution:

$$\Delta P = P(\hbar\omega, T_1) - P(\hbar\omega, T_0), \tag{3.15}$$

$$P(\hbar\omega, T) = \frac{1}{1 + \exp[\hbar\omega - (E_F - E_d)]/kT}. \tag{3.16}$$

where E_F is the Fermi energy and E_d is the d-band energy. Figure 3-28 shows the calculated change in electron population for a wide range range of energy levels when the lattice temperature is elevated from T_0 to T_1. The value for (E_F-E_d) is 2.38 eV for gold. As shown in figure 3-28, the elevated temperature leads to increased occupancy above the Fermi energy and decreased occupancy below the Fermi energy. This change may account for the wavelength-dependent thermoreflectance. The change in the electron population is achieved by optical heating as well. Pump-probe transient reflectivity measurements may make it possible to connect the temporal reflectivity change and electron population change by varying the probe wavelength. For small

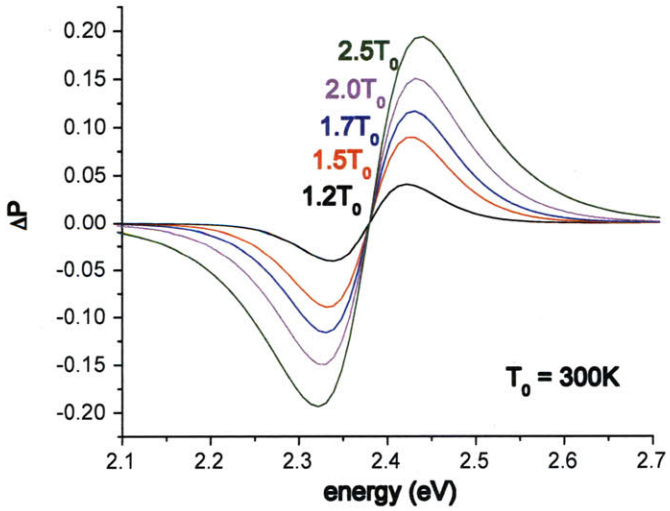

Figure 3-28: Calculated change in electron population at energy levels from 2.1 to 2.7 eV. The population difference is obtained using equation 3.15 and 3.16. (E_F-E_d) is set as 2.38 eV for gold. T_1 is varied from $1.2T_0$ to $2.5T_0$ where T_0 is 300 K. Values are taken from reference [SLFE87].

changes in optical constants, the differential reflectivity is linear in $\Delta\epsilon_1$ and $\Delta\epsilon_2$:

$$\frac{\Delta R}{R} = \frac{1}{R}\left[\frac{\partial R}{\partial \epsilon_1}\Delta\epsilon_1 + \frac{\partial R}{\partial \epsilon_2}\Delta\epsilon_2\right]. \tag{3.17}$$

Changes in the electron population give rise to changes in interband absorption. These are directly proportional to the change in the imaginary part of the dielectric constant, $\Delta\epsilon_2$. The corresponding change in the real part of the dielectric constant, $\Delta\epsilon_1$ can be obtained by the Kramers-Kronig relation.

Schoenlein *et al.* investigated thermal relaxation of the electronic distribution in gold through pump and continuum measurements of transient reflectivity [SLFE87]. Figure 3-29 shows their results. The probe energy-dependent reflectivity change is very similar to the change in the electron population caused by the elevated (electron) temperature as shown in figure 3-28. This reveals that the reflectivity results from the electronic occupancy change by the elevated temperature.

The same analysis will reveal the change in the Bi electron population through the 800 nm pump-continuum probe reflectivity measurements. There are two problems to be solved in terms of the electronic structure. First, the bandgap for the interband transition in bismuth is not presently known. Second, equation 3.15 is overly simpli-

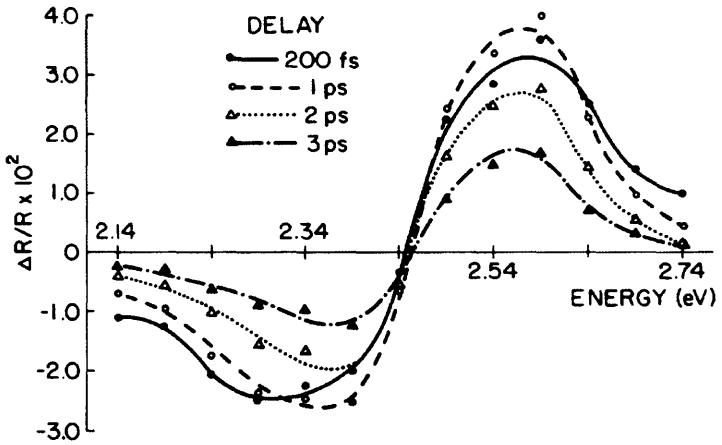

Figure 3-29: Transient-reflectivity measurements of gold as a function of probe-photon energy at various time delays from the heating pulse ([SLFE87]).

fied. It may work only for interband transitions where two parallel bands are involved such that the single-valued bandgap is justified. It needs to be modified to account for the band structure including curvature of the bands and density of states. In order to generalize the change in electron population, a certain bandgap range ΔE_g is assumed instead of a single value. A Gaussian weight function for the bandgap is introduced so that the probability of the interband transition is maximized at the center, and it diminishes as the bandgap value moves away from the center. The curvature of the bands and the density of states may be included in the Gaussian distribution of the bandgap. Equation 3.15 can be generalized:

$$\Delta P = \sum_{E_{g,i}} \mathrm{W}(E_{g,i})[P(E_{ph}, T_1) - P(E_{ph}, T_0)], \tag{3.18}$$

where

$$\mathrm{W}(E_{g,i}) = \exp[-\frac{(E_{g,i} - E_{g,0})^2}{2\sigma^2}], \tag{3.19}$$

and

$$P(E_{ph}, T) = \frac{1}{1 + \exp[E_{ph} - E_{g,i}]/kT}. \tag{3.20}$$

Equations from 3.18 to 3.20 can be used to fit the wavelength-dependent reflectivity change directly. The reflectivity data (of thin films and the bulk) were taken at a 10 ps delay time. The reflectivity change is normalized by its maximum. ΔP is also normalized by its maximum during the fitting procedure. The normalized shape of ΔP is not sensitive to the final temperature T_1 for the small range 300 to 500 K ($\mathrm{T_{melt}} = 544.7$ K). In fact, normalization of the curves by their maxima yields almost identical curves in figure 3-28. For the purpose of finding the center bandgap and the weight function, the normalization scheme works well by rendering the temperature insensitive. The final temperature is assumed to be 450 K.

Fitting results are shown in figures 3-30 to 3-35. In each figure, circles represent the reflectivity data at 10 ps and the curve indicates the change in the electron

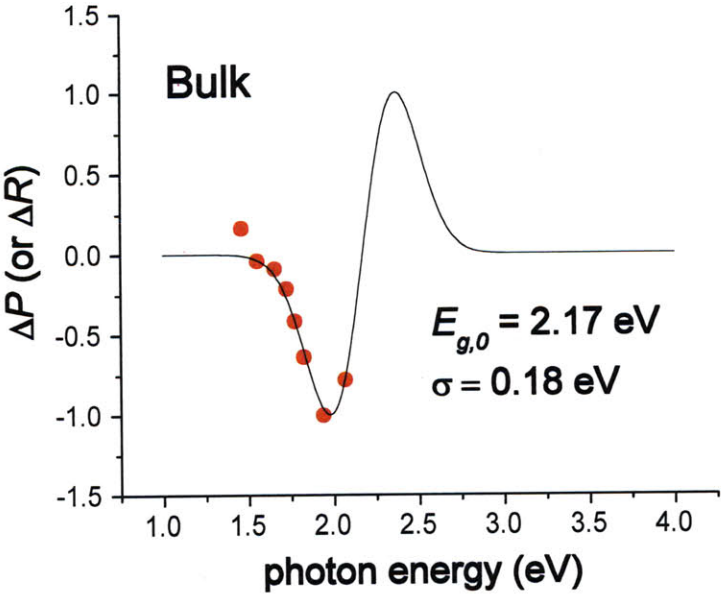

Figure 3-30: Fitting the wavelength-dependent reflectivity by the change in electron population. Circles represent the transient reflectivity of the bulk at 10 ps delay time. The center bandgap is estimated as 2.17 eV and the width as 0.18 eV.

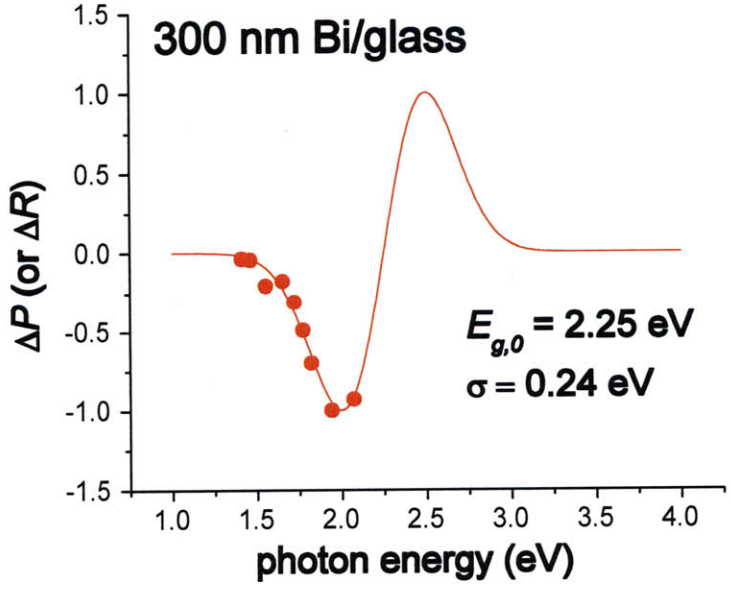

Figure 3-31: Fitting the wavelength-dependent reflectivity by the change in electron population. Circles represent the transient reflectivity of 300 nm Bi film at 10 ps delay time. The center bandgap is estimated as 2.25 eV and the width as 0.24 eV.

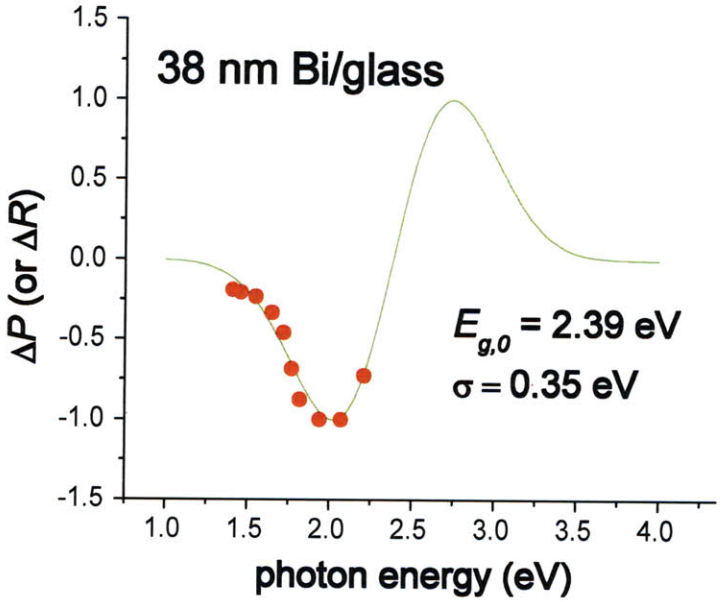

Figure 3-32: Fitting the wavelength-dependent reflectivity by the change in electron population. Circles represent the transient reflectivity of 38 nm Bi film at 10 ps delay time. The center bandgap is estimated as 2.39 eV and the width as 0.35 eV.

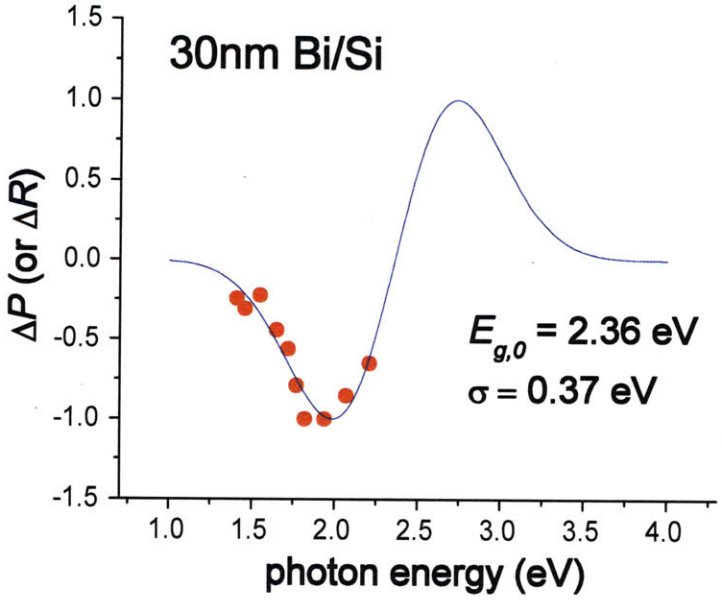

Figure 3-33: Fitting the wavelength-dependent reflectivity by the change in electron population. Circles represent the transient reflectivity of 30 nm Bi film at 10 ps delay time. The center bandgap is estimated as 2.38 eV and the width as 0.37 eV.

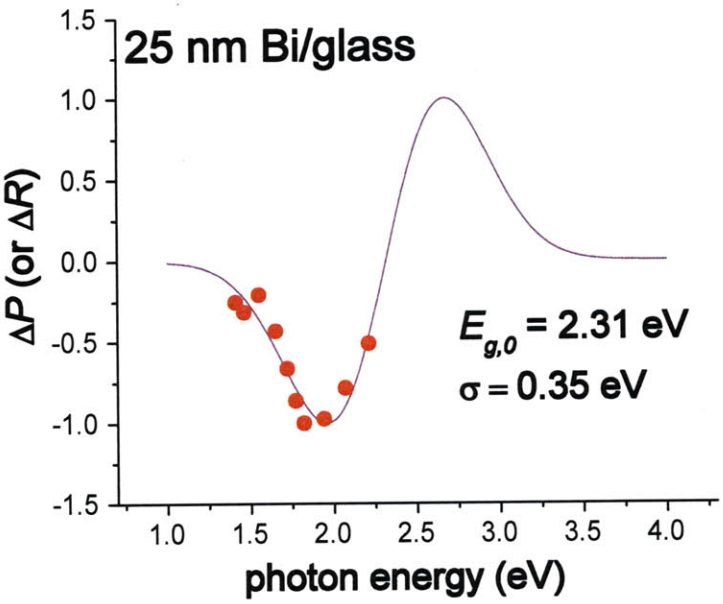

Figure 3-34: Fitting the wavelength-dependent reflectivity by the change in electron population. Circles represent the transient reflectivity of 25 nm Bi film at 10 ps delay time. The center bandgap is estimated as 2.31 eV and the width as 0.35 eV.

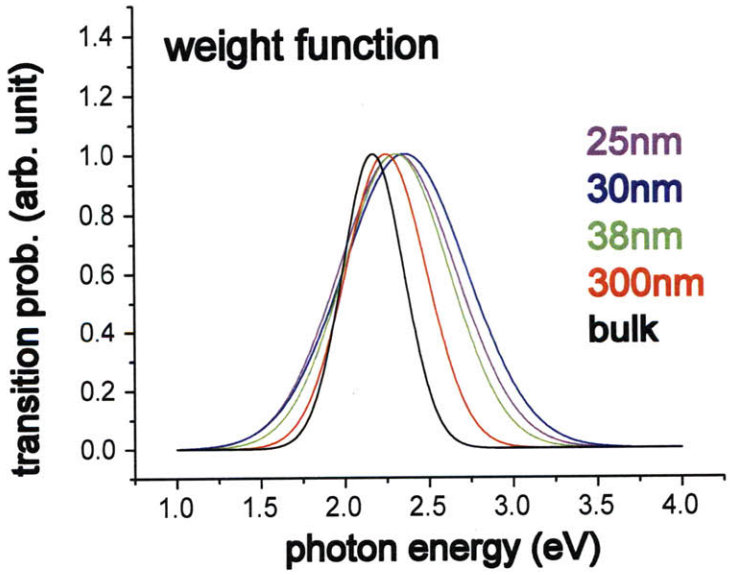

Figure 3-35: Gaussian weight function as a function of film thickness. The function was introduced in order to include the band curvature and density of states effectively. The function exhibits the blue-shifts of the center bandgap with decreasing film thickness.

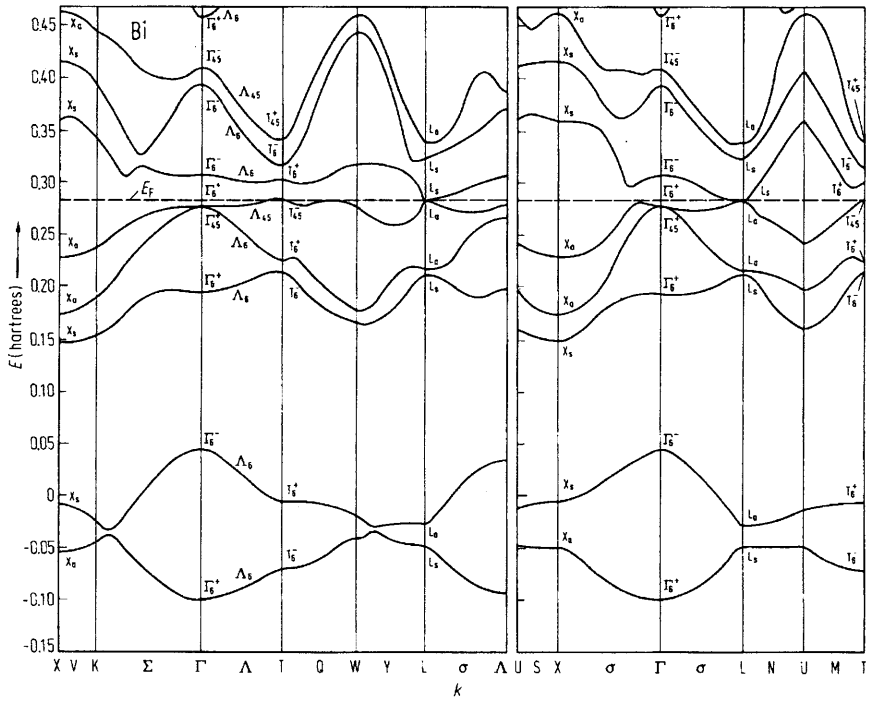

Figure 3-36: Band structure of bismuth obtained by pseudopotential calculations [Gol68]. The interband transition, 5→7 near $\sum$ accounts for the bandgap we obtained.

occupancy obtained by optimizing the parameters of the Gaussian weight function such as the center bandgap and the width. The fitted curves (changes in electron occupancy) are all in good agreement with the reflectivity data. The center bandgap is represented by the intercept that the fitted curves (or reflectivity data) cross at the unperturbed level. The center bandgap for the interband transition shows a blue-shift with decreasing thickness. The blue-shift may result from a quantum confinement effect which produces a larger energy gap between the valence and the conduction bands for a smaller particle size. It is also observed that the effective bandgap width increases with decreasing thickness. If two bands for the interband transition are perfectly parallel at any wave vectors, then the width is zero and the bandgap is single-valued. The width provides the relative band geometry. The resulting Gaussian functions for each sample are summarized in figure 3-35.

Wang *et al.* measured interband transitions of bismuth bulk single crystals using a modulated piezoreflectance method [WJ70]. They observed a variety of interband

transitions. Among them, a transition energy of 2.49 eV is close to the bandgap (2.17 eV) obtained here. The transition is supported by pseudopotential calculations, which indicate that the transition originates from 5→7 transition near $\sum$ as shown in figure 3-36 [Gol68]. The good agreement for the bandgap for the interband transition may support the bandgap Gaussian distribution.

Now that we know the center bandgap and the Gaussian distribution, it is possible to estimate the time evolution of the lattice temperature from the wavelength-dependent reflectivity. By using the known Gaussian weight function (equation 3.19) in equation 3.18 and by fitting the time- and wavelength-dependent reflectivity data while changing the final temperature T_1 as a fit parameter, we can estimate the lattice temperature (or even nonequilibrium electron temperature). In order to do so, we assume that electrons are thermally distributed and follow the Fermi-Dirac distribution. Resonant electronic excitation would fail the above analysis. For example, 800 nm (1.55 eV) optical excitation would excite electrons to specific energy levels preferentially because the transition probability($\sim$10%) is not negligible at 1.55 eV, especially for thin films (see figure 3-35).

3.4 Thermal Modeling: Modified Two-temperature Model

In this section, a thermal model is established to understand the ultrafast dynamics of bismuth. The two-temperature model has been used to describe the time evolution of the electron and lattice temperatures, especially in metals [FLIB84]. Nonequilibrium electrons can be created by ultrashort pulse excitation. Their initial temperature is much higher than that of the lattice because the heat capacity of electrons is significantly lower than that of the lattice. Thermalization between electrons and lattice is achieved several picoseconds after the excitation via electron-phonon scattering. The two-temperature model describes such processes well quantitatively. However, the model cannot directly describe the thermalization in bandgap materials for several

reasons. The density of hot electrons in the conduction band is not as constant as it is in metals. A time-varying density must be included. Also, recombination of electron-hole pairs can modify the energy flow. For example, radiative recombination deprives electrons of their energy and causes heat loss in the system. By contrast, nonradiative recombination contributes to lattice heating. The electron heat capacity, which is proportional to the electron temperature, must be treated differently when the density of electrons is very low in the conduction band.

The thermal model can offer good insight into the thermal behavior of bismuth. The main purpose of the model is to estimate the time evolution of the lattice temperature and highlight the effects of pump fluence, electron diffusivity, electron-phonon coupling, recombination rate, and film thickness. In this section, we extend the two temperature model, discuss computational results, and compare them with the experimental results in bismuth.

3.4.1 Derivation

Electronic heat equation

Let us consider heat transfer in which particles diffuse and carry their thermal energy from z to $z+\Delta z$ as illustrated in figure 3-37. j indicates particle flux which measures how many particles cross per unit area and unit time (#/cm^2/s). C represents the heat capacity of the particles which may be dependent on the temperature at z.

The heat accumulated at the control volume $A\Delta z$ (A: unit area) per unit time Δt is given by

$$\frac{\Delta Q}{\Delta t} A\Delta z = A(j_z C_z T_z - j_{z+\Delta z} C_{z+\Delta z} T_{z+\Delta z}), \tag{3.21}$$

where Q indicates heat density (energy per unit volume). As Δt and Δz approach zero, equation 3.21 is transformed into a differential equation:

$$\frac{\partial Q}{\partial t} = -CT\frac{\partial j}{\partial z} - jT\frac{\partial C}{\partial z} - jC\frac{\partial T}{\partial z}. \tag{3.22}$$

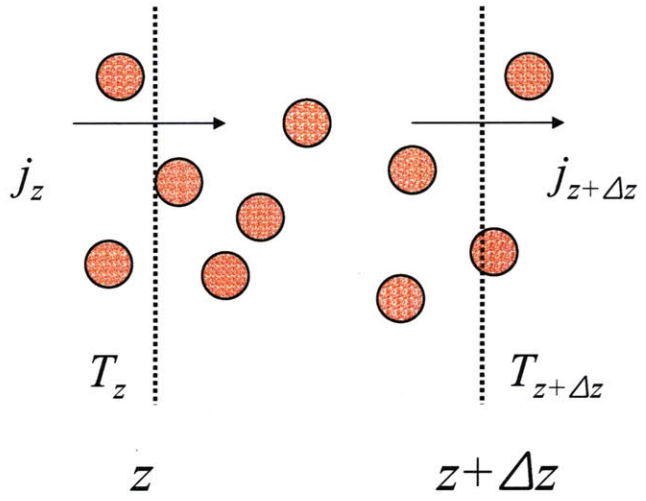

Figure 3-37: Heat transfer mediated by moving particles. Particles diffuse and carry thermal energy from z to $z + \Delta z$.

Using Fick's first law $j = -D\frac{\partial n}{\partial z}$, equation 3.22 is re-written as

$$\frac{\partial Q}{\partial t} = DCT\frac{\partial^2 n}{\partial z^2} + D\frac{\partial n}{\partial z}T\frac{\partial C}{\partial z} + D\frac{\partial n}{\partial z}C\frac{\partial T}{\partial z}, \tag{3.23}$$

where n denotes the density of particles ($\#/\text{cm}^3$) and D the diffusivity (cm^2/s). Equation 3.23 describes the heat flow which is driven by particle diffusion of part. Hereafter, particles represent the hot electrons photogenerated in the conduction band. Subscript e indicates the quantity of electrons:

$$\frac{\partial Q_e}{\partial t} = D_e C_e T_e \frac{\partial^2 n_e}{\partial z^2} + D_e \frac{\partial n_e}{\partial z} T_e \frac{\partial C_e}{\partial z} + D_e \frac{\partial n_e}{\partial z} C_e \frac{\partial T_e}{\partial z}. \tag{3.24}$$

If there is a heat source ($\dot{Q}_{e,+}$) and a heat sink ($\dot{Q}_{e,-}$), those are included as follows:

$$\frac{\partial Q_e}{\partial t} = D_e C_e T_e \nabla^2 n_e + D_e T_e \nabla n_e \nabla C_e + D_e C_e \nabla n_e \nabla T_e + \dot{Q}_{e,+} - \dot{Q}_{e,-}. \tag{3.25}$$

The heat source is the additional energy introduced to the electronic subsystem, including the energy deposited by the optical pump. The heat sink represents heat loss of the electronic subsystem by electron-phonon coupling or electron-hole recombina-

tion. Equation 3.25 is the generalized electronic heat equation.

Lattice heat equation

The heat flow in the lattice subsystem is simpler than the electronic subsystem because the diffusion of atoms is negligible. The conventional heat equation can describe the lattice subsystem:

$$\frac{\partial Q_i}{\partial t} = \frac{\partial [n_i C_i T_i]}{\partial t} = n_i C_i \frac{\partial T_i}{\partial t} = K_i \nabla^2 T_i + \dot{Q}_{i,+} - \dot{Q}_{i,-}, \tag{3.26}$$

where n_i and C_i represent the density of lattice atoms and the heat capacity of the lattice, respectively. Both are independent of space and time coordinates. K_i is the thermal conductivity of the lattice. Both the heat source and heat sink in the lattice subsystem are included as $\dot{Q}_{i,+}$ and $\dot{Q}_{i,-}$, respectively. Energy flow from the electronic subsystem to the lattice subsystem via electron-phonon coupling and nonradiative recombination becomes the heat source term.

Electron diffusion and recombination

Spatial and temporal distribution of electrons is determined by diffusion and recombination processes:

$$\frac{\partial n_e}{\partial t} = D_e \nabla^2 n_e - k n_e, \tag{3.27}$$

where the first term represents the diffusion process and the second term describes the first-order recombination process. k represents the first-order rate constant, and $1/k = \tau$ indicates the lifetime of an electron or hole.

Coupled equations

Equation 3.25 can be simplified by several steps. Since $Q = nCT$,

$$\frac{\partial Q_e}{\partial t} = \frac{\partial [n_e C_e T_e]}{\partial t} \tag{3.28}$$

$$= n_e C_e \frac{\partial T_e}{\partial t} + n_e T_e \frac{\partial C_e}{\partial t} + C_e T_e \frac{\partial n_e}{\partial t} \tag{3.29}$$

$$= n_e C_e \frac{\partial T_e}{\partial t} + n_e T_e \frac{\partial C_e}{\partial t} + C_e T_e D_e \nabla^2 n_e - k n_e C_e T_e. \tag{3.30}$$

Equation 3.27 was used when propagating equation 3.29 to equation 3.30. Comparison between equations 3.25 and 3.30 yields

$$n_e C_e \frac{\partial T_e}{\partial t} + n_e T_e \frac{\partial C_e}{\partial t} - k n_e C_e T_e = D_e T_e \nabla n_e \nabla C_e + D_e C_e \nabla n_e \nabla T_e + \dot{Q}_{e,+} - \dot{Q}_{e,-}. \tag{3.31}$$

Although the electronic heat capacity is proportional to the electron temperature in the free electron model, let us assume that the heat capacity is constant in equation 3.31. This assumption will be discussed shortly. Then equation 3.31 becomes

$$n_e C_e \frac{\partial T_e}{\partial t} - k n_e C_e T_e = D_e C_e \nabla n_e \nabla T_e + \dot{Q}_{e,+} - \dot{Q}_{e,-}. \tag{3.32}$$

As mentioned earlier, the energy loss term $\dot{Q}_{e,-}$ contains energy loss via electron-phonon coupling and the recombination process:

$$\dot{Q}_{e,-} = g(T_e - T_i) + k n_e C_e T_e, \tag{3.33}$$

where g is the electron-phonon coupling constant. Plugging equation 3.33 into equation 3.32 leads to

$$n_e C_e \frac{\partial T_e}{\partial t} = D_e C_e \nabla n_e \nabla T_e - g(T_e - T_i) + \dot{Q}_{e,+}. \tag{3.34}$$

The lattice heat equation 3.26 can be re-written by putting the energy gain terms in $\dot{Q}_{i,+}$. The energy loss in the electronic subsystem may become the energy gain in the lattice subsystem. It is evident that $g(T_e - T_i)$ raises the thermal energy of the lattice. However, electron-hole recombination can increase the lattice thermal energy only when it is nonradiative. Radiative recombination will lead to energy loss of the whole system (electron and lattice) to the environment. If we denote the ratio of

the nonradiative process to all processes (nonradiative and radiative) by ξ, then the energy gain in the lattice subsystem is

$$\dot{Q}_{i,+} = g(T_e - T_i) + \xi k n_e C_e T_e. \tag{3.35}$$

Substitution of equation 3.35 yields

$$n_i C_i \frac{\partial T_i}{\partial t} = K_i \nabla^2 T_i + g(T_e - T_i) + \xi k n_e C_e T_e. \tag{3.36}$$

The energy loss term $\dot{Q}_{i,-}$ was ignored in equation 3.36 because nonradiative phonon emission (which is a main channel to loss) is negligible.

Three equations, 3.27, 3.34, and 3.36 describe the temporal evolution of electron temperature, lattice temperature, and electron density in three-dimensional space. Fortunately, 3-D spatial problems can be reduced to 1-D problems because the penetration depth (~15 nm) is several orders of magnitude smaller than the diameter of the pump and probe (~100–200 μm). Thus, heat flow and electron diffusion occur dominantly perpendicular to the surface where there are large temperature and density gradients along the direction.

The remaining task is to solve the coupled equations numerically by setting up proper initial and boundary conditions.

3.4.2 Physical constants

Electronic heat capacity (C_e)

Classical statistical mechanics predicts that the heat capacity of a free particle should be $\frac{3}{2}k_B$, where k_B is the Boltzmann constant. If there are N electrons in the conduction band and they can move freely, then the electronic contribution to the heat capacity should be $\frac{3}{2}Nk_B$, just as for a monoatomic ideal gas. However, the observed electronic heat capacity at room temperature is usually less than 1% of this value. The discrepancy can be explained by the Pauli exclusion principle and the Fermi distribution function.

When the metal is heated, not every electron gains thermal energy $\sim k_B T$ as expected classically. Only those electrons in orbitals within an energy range $k_B T$ are excited thermally. This fact gives an approximate solution for the electronic heat capacity. If there are N electrons in total in the conduction band, a small fraction T/T_F can contribute to the total electronic thermal energy among N electrons:

$$U_e \simeq N\frac{T}{T_F}k_B T. \tag{3.37}$$

Accordingly, the electronic heat capacity is given by

$$C_e = \partial U_e/\partial T \simeq Nk_B(T/T_F). \tag{3.38}$$

The electronic heat capacity is proportional to T. At room temperature, C_e is much smaller than the classically expected value $\frac{3}{2}Nk_B T$ by a factor on the order of 0.01 or less because of the high Fermi energy energy or Fermi temperature, T_F. It is typically $\sim 5 \times 10^4$ K. A more precise heat capacity can be derived using the Fermi distribution function and is given by

$$C_e = \frac{1}{2}\pi^2 Nk_B T/T_F. \tag{3.39}$$

In bandgap materials, what is the heat capacity of N electrons photoexcited in the conduction band? If a large number of electrons are excited in the conduction band so that T/T_F' is much smaller than 1, then the heat capacity would be given by equation 3.39. Here, T_F' denotes the new Fermi temperature defined by the excited electrons in the conduction band. If a small number of electrons are excited to the conduction band, then T/T_F' can be comparable to 1. In this case, almost every electron in the conduction band can be considered as a classical free particle and each of N electrons contributes to the thermal energy $\frac{3}{2}k_B T$. Accordingly, the total electronic thermal energy is given by $\frac{3}{2}Nk_B T$, and the resulting heat capacity is $\frac{3}{2}Nk_B$. Besides the low electron density, the high electron temperature can also verify the classical limit of the heat capacity. When the bandgap is small compared to the

photon energy, then excess energy is consumed to increase the thermal energy of electrons in the conduction band. In this case, T/T_F' can be larger than 1.

In bismuth, the density of electrons excited in the conduction band is low. For example, only ~1.3% of the valence electrons are excited to the conduction band by a pump fluence of 7.7 mJ/cm^2 [FRA$^+$07, MFW$^+$05]. Moreover, since the bandgap of bismuth is considerably low (~0.2 eV) compared to the photon energy (~1.55 eV at 800 nm), the thermal energy of every electron would be very high. This would yield the classical heat capacity even at a high density of electrons in the conduction band. Those two effects support an electronic heat capacity of $\frac{3}{2}Nk_B$ for electrons excited in the conduction band in bismuth. There is no temperature dependence in the heat capacity, which supports the transformation of equation 3.31 into equation 3.32.

Electronic diffusivity (D_e)

Electron diffusivity plays a critical role in heat exchange between hot electrons and the cold lattice. For example, if hot electrons are immobile, then thermalization between the hot electrons and the lattice would occur within the skin depth. Since thermalization is achieved within the narrow skin depth, the local lattice temperature may be raised to a high value. Slow heat flow from the skin depth to the deeper region is expected because only lattice atoms (phonons) participate in the heat flow via heat conduction. This is usually inefficient compared to electronic heat conduction. On the contrary, if hot electrons can move very quickly, they distribute the initial electronic thermal energy over a large volume. Accordingly, if the thermalization process occurs over the large volume, the lattice temperature would be relatively low. It has been reported that the diffusivity is as high as 100 cm^2/s (= 10^4 nm^2/ps) for the ground state of bismuth at room temperature [SS72]. A smaller diffusivity 2.3–5 cm^2/s (= 230–500 nm^2/ps) was also suggested [RGN$^+$03, FR04, JBM$^+$08]. These reported values are large enough that a considerable fraction of photogenerated hot electrons move out of the skin depth within 1 ps. This implies that the time evolution of the lattice temperature may be significantly different between the bulk and thin films whose thicknesses are comparable to the skin depth. Since the diffusion

of hot electrons is suppressed in thin films, the lattice temperature may be raised effectively.

Electron-phonon coupling constant (g)

Inelastic scattering of hot electrons by phonons is responsible for lattice heating. This is the only mechanism for lattice heating in metals. The electron-phonon coupling constant g is expressed by

$$g \simeq \frac{\pi^2 m_e n_e v_s^2}{6\tau_{ep} T_i}, \tag{3.40}$$

where m_e is the electron mass, n_e the electron density, v_s the speed of sound, and τ_{ep} the electron-phonon collision time [FLIB84, AKP75, KLT57]. Since $\tau_{ep} \sim 1/T_i$, g is a constant independent of temperature. It is assumed that the collision time is 50 fs at 290 K. The free electron mass was used for m_e. The speed of sound v_s is 1.79 nm/ps in bismuth. Substitution of those values yields

$$g \simeq 3.3 \times 10^{-25} n_e \quad [\text{in J/K/ps}], \tag{3.41}$$

where n_e is the density of electrons excited in the conduction band in $\#/\text{nm}^3$. The same calculation using equation 3.40 yielded good agreement in aluminum [TM94].

Lattice heat capacity (C_i) and thermal conductivity (K_i)

The specific heat capacity of bismuth is 25.52 J/mol/K at room temperature, which is close to the classical limit of the heat capacity of solids, 3R. This results from the low Debye temperature of 86.5–112 K [Gop75, FSS78]. 3R is used as the lattice heat capacity, C_i.

The thermal conductivity of bismuth is 8.0 W/m/K. Since the electron density in the conduction band is low, the electronic contribution to the conductivity is negligible. The value 8.0 W/m/K is used for the lattice conductivity, K_i. The corresponding thermal diffusivity D_i ($= K_i/n_i C_i$) is 6.7 nm^2/ps. This is very small compared to the electronic diffusivity D_e ($\simeq$ 200 nm^2/ps), discussed above.

3.4.3 Initial and Boundary Conditions

Initial lattice temperature

In equations 3.34 and 3.36, T_e and T_i can represent the absolute temperature or the temperature change with respect to an initial reference temperature. Here, the initial conditions are such that T_e and T_i represent the change. The initial condition for the lattice temperature is

$$T_i(z, t = 0) = 0. \tag{3.42}$$

Initial electron density

The optical pump pulse is treated as a delta function instead of a Gaussian function with a finite width. Equivalently, it can be assumed that electrons are excited to the conduction band impulsively. This is a good approximation because our main concern is to examine the thermalization and lattice cooling which occur after the pulse duration. The thermalization occurs in the first several picoseconds and the lattice cooling proceeds slowly afterwards.

The initial condition for electron density in the conduction band is given by

$$n_e(z, t = 0) = \frac{e}{e-1} n_0 \frac{F}{F_0} \exp(-z/\sigma). \tag{3.43}$$

F is the pump fluence and σ is the penetration depth (=15 nm). n_0 and F_0 are reference values which are provided from previous experiments and DFT calculations in which ~1.3% of the valence electrons are excited to the conduction band by the excitation fluence of ~7.7 mJ/cm^2 [FRA+07]. The initial condition 3.43 was set such that the average electron density from $z = 0$ to $z = 15$ nm is n_0= 1.86 electrons/nm^3 under the fluence F_0=7.7 mJ/cm^2. 1.3% of the valence electrons corresponds to n_0= 1.86 electrons/nm^3. The initial density of electrons is assumed to be proportional to the maximum fluence up to 30 mJ/cm^2.

Initial electron temperature

Under the same approximation that the optical pump is represented by a delta function, the initial electron temperature can be obtained from the initial electron density given by equation 3.43. Like the density, it is assumed that the initial electron temperature profile is represented by an exponential decay:

$$T_e(z, t = 0) = T_{e,0}\exp(-z/\sigma). \tag{3.44}$$

In fact, this assumption is not realistic because every single electron which is excited by a photon ($h\nu$) should have the same kinetic or thermal energy ($E_k = h\nu - E_g$) no matter its location. That is, the temperature of the excited electrons should be same regardless of the depth, z. However, it is not trivial to treat such a temperature profile mathematically.

$T_{e,0}$ in equation 3.44 can be determined from energy conservation. It is assumed that all of the pump energy absorbed by bismuth increases the electron density only without increasing the electron temperature (and lattice temperature). This assumption is justified because the same kinetic energy of electrons should be produced by the same photon energy independently of the photon flux ($E_k = h\nu - E_g$) as discussed before. The impulsively deposited energy (at $t = 0$) is given by

$$E_{abs} = F(1 - R)A \tag{3.45}$$

R is the reflectivity of bismuth which is 0.7 at 800 nm light, while A is the excited area. However, not all the deposited energy contributes to the kinetic energy of the excited electrons. Some is consumed to overcome the bandgap and only the remainder contributes to the thermal energy of electrons:

$$E_{kin} = E_{abs}[1 - \frac{E_g}{h\nu}] = F(1 - R)A[1 - \frac{E_g}{h\nu}], \tag{3.46}$$

where $h\nu$ is the photon energy (1.55 eV = 800 nm) and E_g the average bandgap (0.2 eV). The pump excitation produces electrons in the conduction band whose

density is given by equation 3.43. The energy conservation law says:

$$\begin{aligned} E_{kin} &= F(1-R)A[1-\frac{E_g}{h\nu}] \\ &= \int_0^\infty (Adz) n_e(z,t=0) C_e T_e(z,t=0) \\ &= \int_0^\infty (Adz)[\frac{e}{e-1} n_0 \frac{F}{F_0} \exp(-z/\sigma)][T_{e,0}\exp(-z/\sigma)] \\ &= \frac{e}{e-1}\frac{F}{F_0}\frac{\sigma}{2} A n_0 C_e T_{e,0} \end{aligned} \tag{3.47}$$

Rearrangement of equation 3.47 yields

$$T_{e,0} = 2\frac{e-1}{e}\frac{(1-R)F_0}{\sigma n_0 C_e}[1-\frac{E_g}{h\nu}]. \tag{3.48}$$

It should be noted that $T_{e,0}$ is not influenced by pump fluence. That is, the initial temperature profile, $T_e(z, t = 0)$, is always the same regardless of pump fluence. Instead, a higher pump fluence gives rise to more electrons in the conduction band. The effect of higher pump fluence is to raise the lattice temperature by increasing the number of hot electrons, not by elevating the temperature of electrons.

Six boundary conditions

In order to solve three (coupled) second-order differential equations, six boundary conditions are needed in addition to the three initial conditions. The boundary conditions are given by

$$\frac{\partial T_e}{\partial z}|_{z=0} = 0, \qquad T_e(z=z_L) = 0, \tag{3.49}$$

$$\frac{\partial T_i}{\partial z}|_{z=0} = 0, \qquad T_i(z=z_L) = 0, \tag{3.50}$$

$$\frac{\partial n_e}{\partial z}|_{z=0} = 0, \qquad n_e(z = z_L) = n_{e,0}, \tag{3.51}$$

where $z = 0$ corresponds to the surface of bismuth. Three Neumann boundary conditions at $z = 0$ are introduced. z_L indicates the thickness of bismuth used for numerical calculations. For the modeling, 300 nm is used for z_L. In boundary condition 3.51, $n_{e,0}$ denotes the equilibrium density of the electrons in the conduction band at room temperature. The value is $\sim 10^{-3}$ electrons/nm^3.

3.4.4 Numerical Results

Lattice temperature

The coupled heat and diffusion equations are solved numerically using a Matlab code. Figure 3-38 shows the simulated lattice temperature as a function of depth to the surface normal. Physical parameters used for the analysis are listed inside the figure. The maximum temperature at $z = 0$ is reached at 23 ps and deeper regions show a maximum temperature at later times. At deeper regions, the lattice heating by hot electrons through electron-phonon coupling and recombination is less significant because hot electrons disappear due to recombination with in a characteristic time of 15 ps. The lattice heating is caused mainly by the (slow) lattice conduction channel at deeper regions. This is supported by the observation that the time for maximum temperature increases rapidly with increasing depth. For example, the maximum temperature is delayed by only 8 ps (= 31 ps - 23 ps) from $z = 0$ to $z = 15$ nm, while it is delayed by 80 ps (= 130 ps - 50 ps) from $z = 30$ to $z = 50$ nm. Under the parameters used, the fluence of 10 mJ/cm^2 raises the lattice temperature higher than its melting point. This suggests that the disordering of Bi atoms is significant at this fluence. However, a temperature higher than the melting point does not necessarily imply melting because the enthalpy of melting is not considered in this model. The time (23–31 ps) for the maximum temperature within the skin depth (0–15 ps) coincides with the time for the minimum reflectivity observed in figure 3-8 and 3-26. In addition, the reflectivity changes rapidly before its minimum but slowly

after its minimum, as does the lattice temperature before and after the maximum temperature. This strongly suggests that the minimum reflectivity corresponds to the maximum temperature. It suggests further that the more negative reflectivity originates from the higher lattice temperature.

Figure 3-39 shows the time evolution of the total lattice and electron energy integrated over the entire thickness. Their sum is represented by the blue line as well. As shown, the lattice energy increases with time while the electron energy decreases. The characteristic time for the energy exchange is about 12 ps which is determined by the electron coupling constant and the recombination rate. The total energy of the system decays with time indicating that there is energy loss to the environment. The loss is attributed to radiative recombination. It was assumed that the nonradiative process (which contributes to lattice heating) is responsible for 50% of the whole process ($\xi = 0.5$). It was confirmed that the total energy is conserved when $\xi = 1.0$.

Electron density

Figure 3-40 shows the total density of electrons integrated over the entire thickness. It decreases with time because of recombination. The lifetime of carriers, assumed to be 15 ps, determines the characteristic decay time. Figure 3-41 shows the time evolution of electron density as a function of depth.

Electron temperature and energy

Figure 3-42 exhibits the electron temperature as a function of depth. Since the photon energy of 800 nm light is 1.55 eV and the bandgap is 0.2 eV, 1.35 eV can be imparted to increase the kinetic energy initially. We can estimate the initial electron temperature approximately as follows:

$$T_e \simeq \frac{(1.55 - 0.2)\text{ eV}}{0.025\text{ eV}}(300\text{ K}) = 16,200\text{ K}$$

In reality, electron temperature in figure 3-42 is three times higher than this value. It

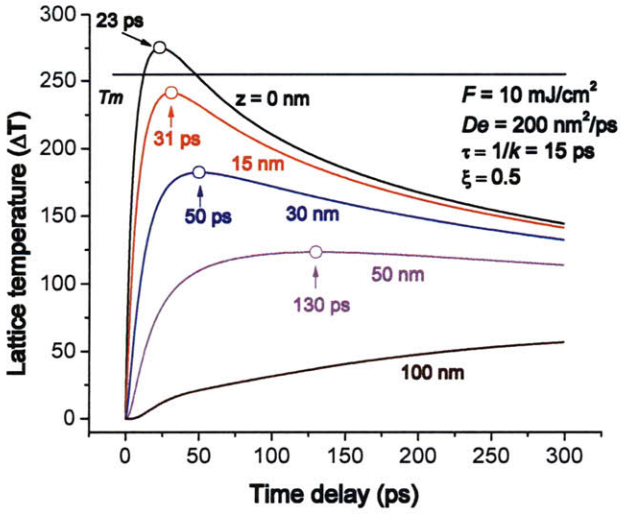

Figure 3-38: Time evolution of lattice temperature as a function of depth. The maximum temperature is reached at about 20–30 ps in the skin depth through electron-phonon coupling and non-radiative recombination. The pump fluence (F) was fixed to 10 mJ/cm^2, diffusivity (D_e) to 200 nm^2/ps, the lifetime of carriers (τ) to 15 ps, and the ratio of non-radiative recombination (ξ) to 0.5.

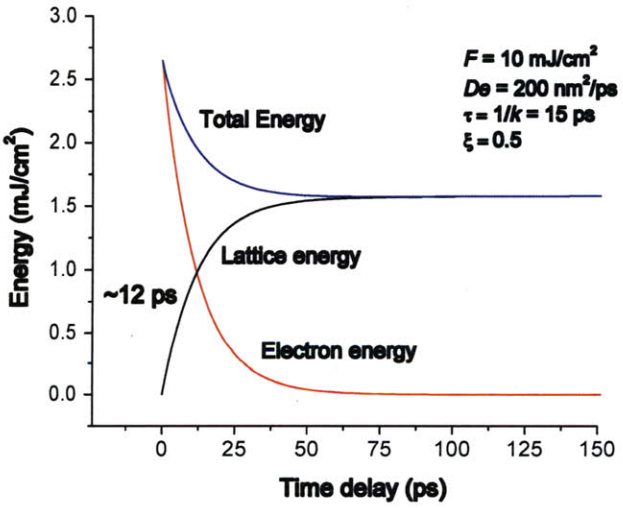

Figure 3-39: Energy exchange between electrons and lattice. The characteristic time for the exchange is about ~12 ps. It is assumed that total energy loss results from radiative recombination. The pump fluence (F) was fixed to 10 mJ/cm^2, diffusivity (D_e) to 200 nm^2/ps, the lifetime of carriers (τ) to 15 ps, and the ratio of non-radiative recombination (ξ) to 0.5.

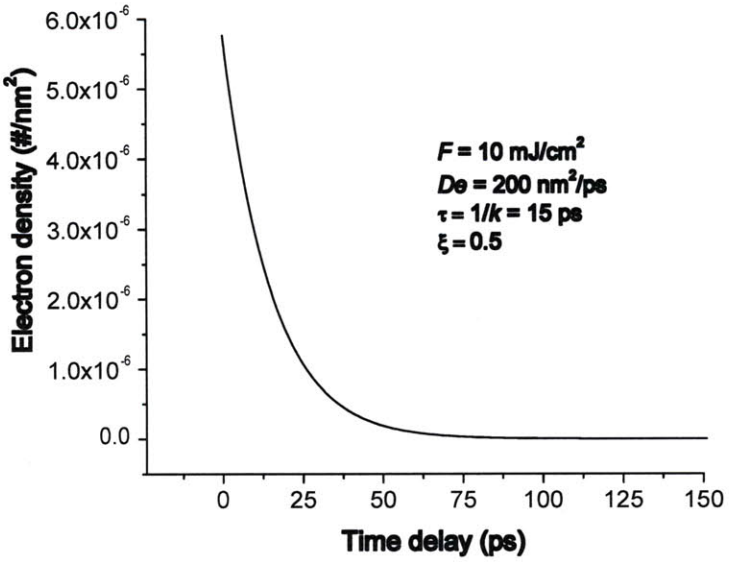

Figure 3-40: Time evolution of total electron density. Electrons disappear due to electron-hole pair recombination. The pump fluence (F) was fixed to 10 mJ/cm^2, diffusivity (D_e) to 200 nm^2/ps, the lifetime of carriers (τ) to 15 ps, and the ratio of non-radiative recombination (ξ) to 0.5.

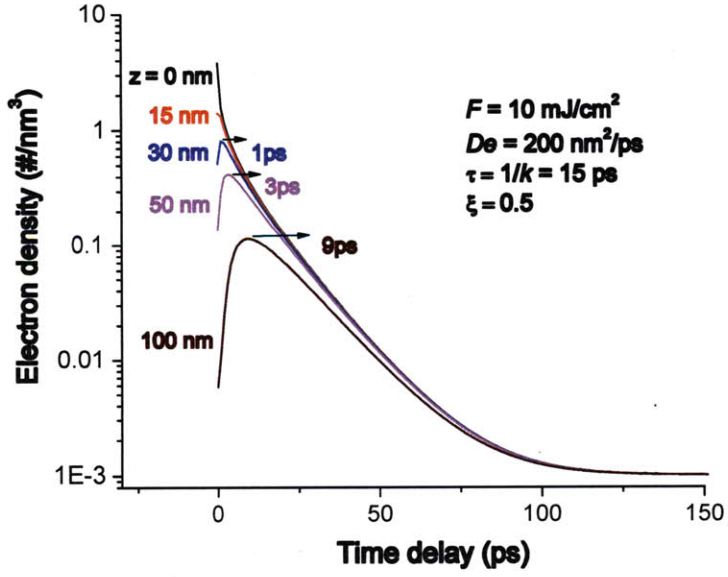

Figure 3-41: Spatial and temporal variation of electron density. The pump fluence (F) was fixed to 10 mJ/cm^2, diffusivity (D_e) to 200 nm^2/ps, the lifetime of carriers (τ) to 15 ps, and the ratio of non-radiative recombination (ξ) to 0.5.

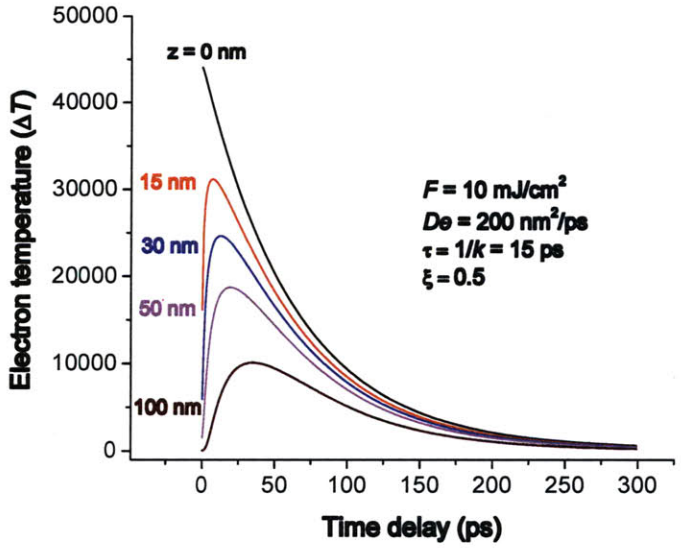

Figure 3-42: Time evolution of electron temperature as a function of depth. The temperature stays very high because of the density-dependent electron-phonon coupling constant. The pump fluence (F) was fixed to 10 mJ/cm^2, diffusivity (D_e) to 200 nm^2/ps, the lifetime of carriers (τ) to 15 ps, and the ratio of non-radiative recombination (ξ) to 0.5.

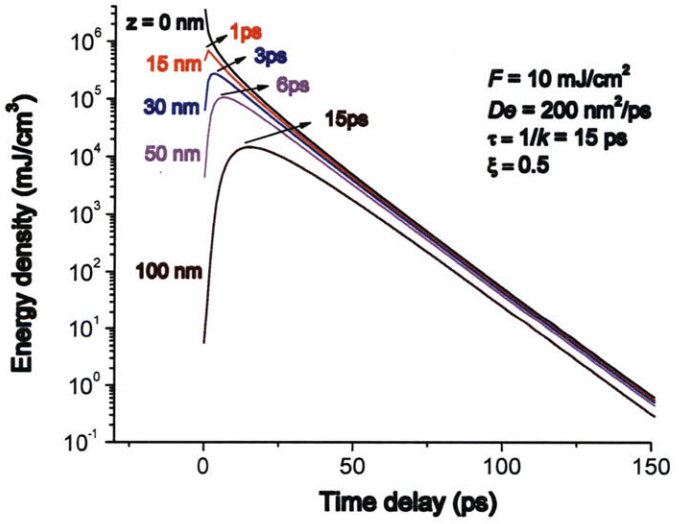

Figure 3-43: Spatial and temporal variation of local electron energy. This is a more adequate quantity than electron temperature for describing the energy transfer from electron to lattice. The pump fluence (F) was fixed to 10 mJ/cm^2, diffusivity (D_e) to 200 nm^2/ps, the lifetime of carriers (τ) to 15 ps, and the ratio of non-radiative recombination (ξ) to 0.5.

was observed that the characteristic time for the energy exchange between the electrons and lattice is about 25 ps from figure 3-39. Therefore, it is expected that the temperature of electrons and lattice are similar to each other at ~20-30 ps. However, the temperature of electrons is substantially higher than that of the lattice even at 100 ps. This discrepancy results from the density-dependent electron-phonon coupling constant as shown in equation 3.41. As the density decreases due to recombination, the electron-phonon coupling term from equation 3.40 becomes insignificant. Equation 3.40 is not a good approximation in this limit. However, the electron density becomes significantly lower at longer delay times, at which the high temperature does not affect the lattice temperature significantly. The electron energy (figure 3-43) is more adequate to describe the electronic part because it includes both the temperature and the density.

Effects of pump fluence

Figure 3-44 shows the effect of pump fluence on the lattice temperature. The lattice temperature is exactly proportional to the fluence. As discussed, the pump fluence increases the initial number of hot electrons excited in the conduction band without raising the electron temperature. The higher density of electrons contributes to lattice heating more by augmenting the electron-phonon coupling constant and the heat released from nonradiative recombination. Both the electron-phonon coupling constant and recombination rate are proportional to the local electron density. These quantities raise the lattice temperature linearly as shown in equation 3.36.

We can estimate the threshold pump fluence to induce the melting of bismuth at the surface under the assumption that 100% of the deposited energy goes to the lattice without being partitioned into the electronic part. This underestimates the melting threshold.

$$\frac{F(1-R)}{\sigma}\left(\frac{h\nu - E_g}{h\nu}\right) = \rho C_i \Delta T \; + \; \Delta H, \tag{3.52}$$

where ΔH is the enthalpy of melting (~557 J/cm^3), σ the skin depth(15 nm), and

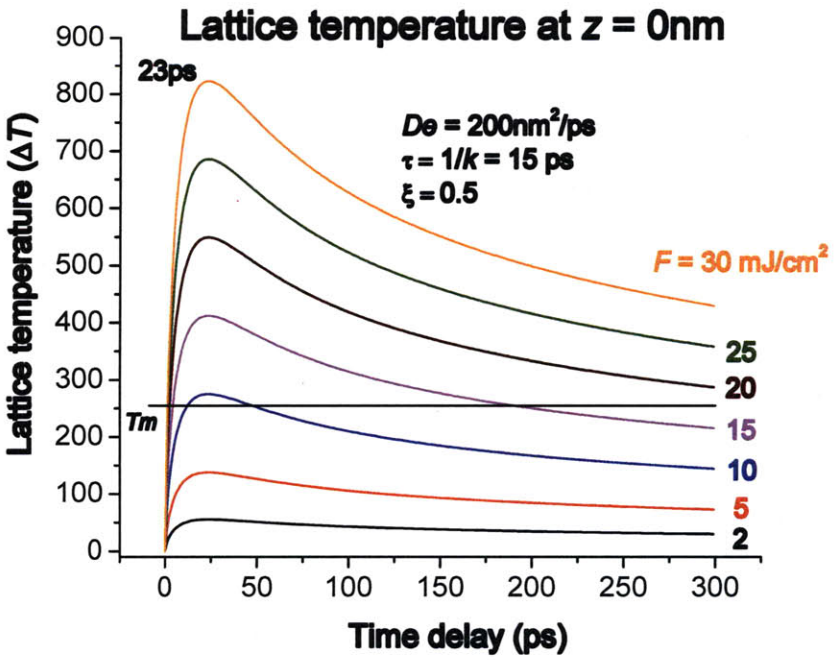

Figure 3-44: Effects of pump fluence on the lattice temperature. The pump fluence (F) was varied from 2 to 30 mJ/cm^2. The electron diffusivity (D_e) was set to 200 nm^2/ps, the lifetime of carriers (τ) to 15 ps, and the ratio of nonradiative recombination (ξ) to 0.5.

ρ the density of bismuth (~10 g/cm^3). After substituting parameters, the left side becomes ~174×F (J/cm^3) in which F denotes the pump fluence in mJ/cm^2. To prepare solid bismuth at its melting point (ΔT= 545 - 300 K),

$$\begin{aligned} \frac{F(1-R)}{\sigma}\left(\frac{h\nu - E_g}{h\nu}\right) &= \rho C_i \Delta T \\ 174 \times F &= 10\ (\mathrm{g/cm^3}) \times 0.125\ (\mathrm{J/g/K}) \times (545\ \mathrm{K} - 300\ \mathrm{K}) \\ F &\simeq 1.8\ \mathrm{mJ/cm^2}. \end{aligned}$$

In order to transform the phase from solid to liquid at its melting point, 545 K, we need a larger pump fluence,

$$\begin{aligned} \frac{F(1-R)}{\sigma}\left(\frac{h\nu - E_g}{h\nu}\right) &= \Delta H \\ 174 \times F &= 557\ (\mathrm{J/cm^3}) \end{aligned}$$

$$F \simeq 3.2 \text{ mJ/cm}^2.$$

According to numerical results in figure 3-44, at least $\sim$10 mJ/cm^2 is necessary to reach the melting point. The large discrepancy (between 1.8 and 10 mJ/cm^2) originates from the assumption that the pump energy is deposited only into the lattice without being partitioned into electrons. In reality, all of the deposited energy is consumed to raise the density of hot electrons in the conduction band at the time origin and then the hot electrons heat the lattice via electron-phonon coupling and non-radiative recombination. If electrons are confined within a very narrow region such as the skin layer, the discrepancy would be small because all of the initial electron energy would be transferred to the lattice eventually within the region. The discrepancy is attributed mainly to electron diffusion. We will discuss the effects of electron diffusivity on the lattice heating shortly.

As we noticed, a larger pump fluence is needed to transform the phase at its melting point than needed to raise the lattice from room temperature to its melting point. According to the simulations, 10 mJ/cm^2 is required to increase the lattice temperature from 300 to 545 K (melting point) as shown in figure 3-44, then $\sim$18 mJ/cm^2 ($\simeq$ 10 mJ/cm^2 $\times$ $\frac{3.2 \text{ mJ/cm}^2}{1.8 \text{ mJ/cm}^2}$) would be needed to convert the phase from solid to liquid at 545 K. Accordingly, in total $\sim$28 mJ/cm^2 is needed to melt bismuth at room temperature.

Another noticeable feature is the cooling rate. The rate increases after the maximum temperature is reached at $\sim$23 ps as the pump fluence increases. This is because a larger temperature gradient is created at higher pump fluences. The higher cooling rate or steeper slope coincides with the observation that the reflectivity relaxes at a higher rate at high pump fluences as illustrated in figures 3-21, 3-22, and 3-23.

Effects of recombination

Together with thermalization through electron-phonon coupling, non-radiative recombination also plays an important role in contributing to lattice heating. The lattice temperature would be higher as the ratio of nonradiative recombination, ξ, increases

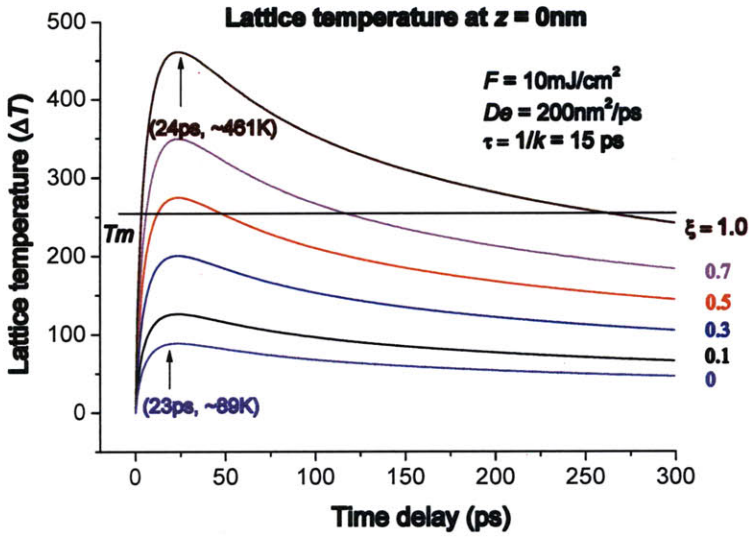

Figure 3-45: Effects of nonradiative recombination on the lattice temperature. The ratio(ξ) is varied from 0 to 1. The electron diffusivity (D_e) was set to 200 nm^2/ps, the pump fluence (F) to 10 mJ/cm^2, and the lifetime of carriers (τ) to 15 ps.

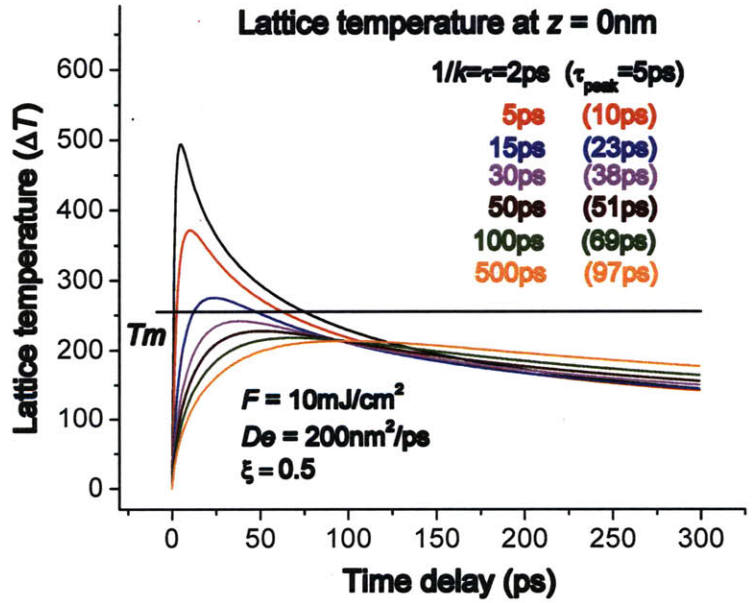

Figure 3-46: Effects of nonradiative recombination rate on the lattice temperature. The lifetime (τ=1/k) was varied from 2 to 500 ps. The electron diffusivity (D_e) was set to 200 nm^2/ps, the pump fluence (F) to 10 mJ/cm^2, and the ratio of non-radiative recombination (ξ) to 0.5.

as shown in figure 3-45. As mentioned earlier, ξ is defined as

$$\xi = \frac{r_{non}}{r_{non} + r_{rad}}, \tag{3.53}$$

where r_{non} represents the rate of nonradiative recombination and r_{rad} the rate of radiative recombination. Radiative recombination would lead to energy loss to the environment, while the nonradiative process can contribute to lattice heating in equation 3.36. Therefore, the higher ξ causes higher lattice temperatures as observed in figure 3-45. If all carriers undergo the radiative process so that they do not contribute to lattice heating, the lattice temperature is significantly lower. In this case (ξ=0), the maximum temperature change is 90 K at 23 ps. Hot electrons raise the lattice temperature only via the electron-phonon scattering process. On the contrary, if all carriers recombine nonradiatively, they heat the lattice. Then the maximum lattice temperature change is as high as 460 K at 23 ps. The contribution of nonradiative recombination is significant compared to that of the electron-phonon coupling term. The contribution to lattice heating by inelastic electron-phonon scattering corresponds to only 20% of that by nonradiative recombination. It should be also noted that the characteristic timescale for electron-phonon thermalization via inelastic electron-phonon scattering coincides with the timescale for nonradiative recombination. The maximum temperature is observed at 23 ps when $\xi = 0$ and $\xi = 1$.

Since nonradiative recombination is significant in energy transfer, its rate affects the lattice temperature substantially. Figure 3-46 shows the effects of the recombination rate or carrier lifetime on the lattice temperature. At short carrier lifetimes such as 2 ps, the maximum temperature change of ~492 K is observed as early as 5 ps. After reaching the maximum temperature, the lattice cools quickly because fast energy transfer results in a large temperature gradient. By contrast, when τ is 100 ps, the maximum temperature change of ~216 K is achieved at 69 ps. Since the heating occurs slowly, the resulting cooling rate is also slow. There have been no direct data for the lifetime of carriers in bismuth. However, based on the dephasing time obtained by low excitation fluence at low temperature [HMH+98], the lifetime

of carriers is estimated to be ~15 ps. The same value is used here. This results in the coincidence between the times when the minimum reflectivity (figure 3-26) and the maximum temperature (figure 3-45) are observed, which supports the carrier lifetime of 15 ps.

Effects of diffusivity

Electron diffusivity is responsible for the high thermal conductivity of metals. However, in equilibrium at room temperature, heat conduction by electrons would be negligible in bismuth because of a low population of electrons in the conduction band. In the bismuth experiments described here, hot electrons are created impulsively in the conduction band and carry thermal energy initially while the lattice stays cold. Accordingly, the diffusion of hot electrons could influence energy transfer to the lattice considerably. Figure 3-47 shows the effects of electron diffusivity on the lattice temperature. At the lowest diffusivity, the peak temperature(ΔT) is as high as 540 K at 19 ps. On the contrary, at the highest diffusivity, it becomes ~274 K at 23 ps which is significantly lower. This can be easily understood. When hot electrons move very slowly, they interact locally with the lattice within a narrow region before they lose their thermal energy. Accordingly, only a small number of lattice atoms within the narrow volume take the initial thermal energy of hot electrons. As a result, a large temperature gradient is created by this effect. The rapid heating and cooling at D_e=1 nm^2/ps are explained well. By contrast, when hot electrons move very quickly, they distribute their thermal energy over a broad region rapidly before cooling. As a consequence, the initial thermal energy of hot electrons is shared with more lattice atoms over the large volume, which results in a lower lattice temperature and a smaller temperature gradient. This accounts for the slower lattice heating and cooling at D_e=200 nm^2/ps.

As observed in figure 3-47, the peak temperature appears to converge to a certain value asymptotically as diffusivity increases from 1 to 200 nm^2/ps. However, diffusivity cannot be increased higher than 200 nm^2/ps for the simulation because of the small thickness of sample used. The thickness (z_L) used for the current analysis

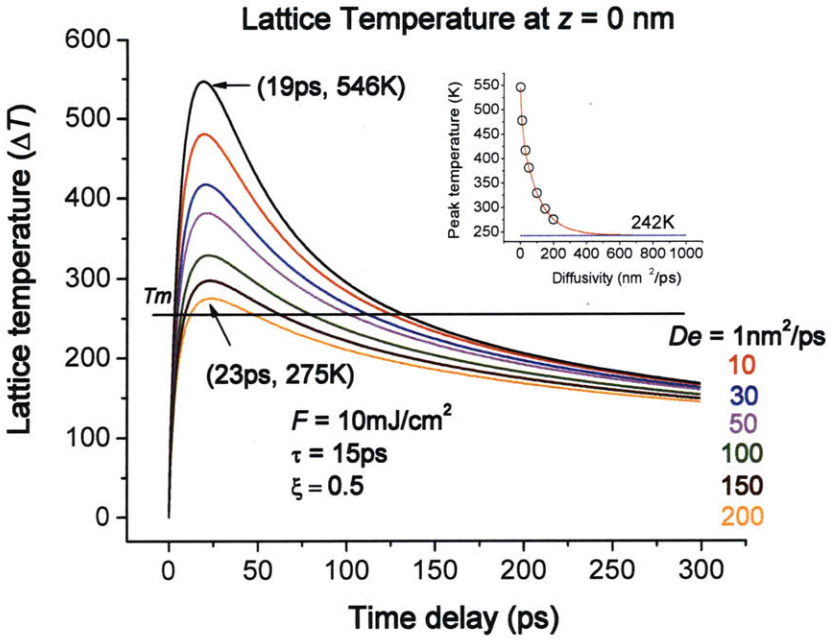

Figure 3-47: Effects of the electron diffusivity on the lattice temperature. The electron diffusivity (D_e) is changed from 1 to 200 nm^2/ps. The pump fluence (F) was set to 10 mJ/cm^2, and the lifetime of carriers (τ) to 15 ps. The ratio of nonradiative recombination (ξ) was set to 0.5. In the inset, the peak temperature is fitted as a function of the diffusivity. The fitting yields the peak temperature change of 242 K at $D_e = \infty$.

is 300 nm which limits the maximum diffusivity. Considerable amounts of hot electrons diffuse out of the finite sample size on the timescale under investigation. This leads to a violation of energy conservation. Instead of putting higher values into the simulation directly, the peak temperature is fitted as a function of the diffusivity up to 200 nm^2/ps and extrapolated to a higher diffusivity using a bi-exponential decay function as shown in the inset of figure 3-47. At present, it is not clear why the bi-exponential decay function fits the data well but it is obvious that the peak temperature approaches 242 K at a infinitely large diffusivity. The source of this high temperature is unclear. The peak temperature might be ascribed to lattice heating due to nonradiative recombination. The infinitely large diffusivity minimizes lattice heating because of the large region in which energy is distributed and because in the calculation equation 3.40 suggests incorrectly that there is an infinitely small

cross-section for inelastic electron-phonon scattering.

The effects of the electronic diffusivity imply that there may be a substantial difference between the bulk and thin film measurements. In the bulk sample, hot electrons diffuse quickly to the deeper region distributing their thermal energy over a large volume. However, the diffusion of hot electrons is suppressed at the bismuth-substrate interface in films because they cannot overcome the bandgap of the insulating substrate. The suppression drives the efficient energy transfer from hot electrons to lattice within a small volume, resulting in a higher lattice temperature in thin films than in bulk. In that sense, the smaller diffusivity in figure 3-47 may simulate the lattice temperature in thin films.

Effect of electron-phonon coupling

The electron-phonon coupling constant is given by equations 3.40 and 3.41. Larger values suggest more efficient inelastic electron-phonon scattering, producing a high lattice temperature. There is some uncertainty originating from the electron effective mass, m_e and the electron-phonon collision time, τ_{ep}, in evaluating the electron-phonon coupling constant in equation 3.40. In order to examine the effects of the electron-phonon coupling constant, g, its proportionality constant in equation 3.41 is varied from 0 to 3.3×10^{-24}. $g = 0$ means that the inelastic electron-phonon scattering does not contribute to lattice heating. The only channel leading to lattice heating is nonradiative heating.

Figure 3-48 shows the results. As the proportionality constant increases, the lattice temperature increases and the peak temperature appears earlier. For example, when the proportionality constant increases from $g = 0$ to $g = 10\ g_0$, the peak temperature (ΔT) increases from 209 K to 588 K. In addition, the peak temperature time is shifted from 29 ps to 10 ps. Faster and more efficient lattice heating is observed. A proportionality constant of $\sim 3.3 \times 10^{-25}$ yields the best agreement with experimental results where the minimum reflectivity appears around 20–30 ps. When $g = 0$, thermalization between hot electrons and phonons by electron-phonon coupling does not occur. The lattice temperature is raised only by nonradiative recombination. Under

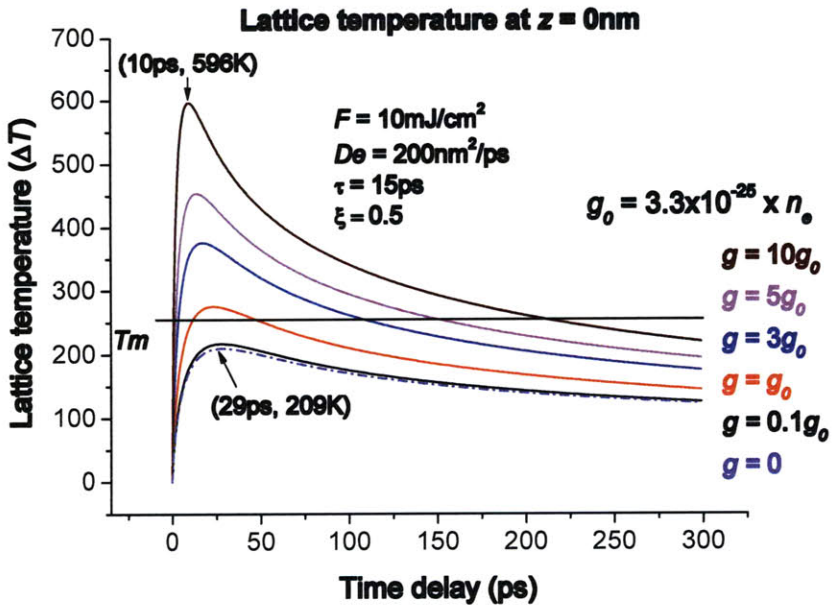

Figure 3-48: Effects of the electron-phonon coupling constant on the lattice temperature. The proportionality of the coupling constant is changed from 0 to 3.3×10^{-24}. The pump fluence (F) was set to 10 mJ/cm^2, the electron diffusivity (D_e) to 200 nm^2/ps, and the lifetime of carriers (τ) to 15 ps. The ratio of nonradiative recombination (ξ) was set to 0.5.

the above conditions, it appears that lattice heating by nonradiative recombination ($\xi = 0.5$) is more significant than that by thermalization through electron-phonon coupling ($g = 3.3 \times 10^{-25} n_e$).

3.5 Toward a phase transition: Single-shot measurements

We have examined coherent lattice vibrations, bond softening, vibrational dephasing, and lattice heating in various thicknesses of bismuth samples. The conventional pump-probe technique was used for study described above because optical excitation was below the material damage threshold. In this section, single-shot measurements were conducted for study described above of phase transitions in bismuth under high fluence excitation.

3.5.1 Single Crystal

Short delay time dynamics

Figures 3-49 and 3-50 show the transient reflectivity of bulk single crystalline bismuth as a function of pump fluence obtained from single-shot measurements. Both wavelengths for pump and probe were 800 nm. Mild multishot damage was observed above $\sim$6.5 mJ/cm^2 in the conventional pump-probe measurements in which data scans are carried over at least 1-2 minutes at 1 kHz repetition rate. Multishot damage prevents extension of the conventional pump-probe method to the study of phase transitions. Single-shot pump-probe spectroscopy enables us to investigate phase transitions by eliminating the limitations of conventional pump-probe spectroscopy. In order to increase the signal-to-noise level, each time trace in figures 3-49 and 3-50 was obtained averaging over $\sim$10–30 shots depending on the fluence. Very mild single-shot damage was observed above $\sim$20–30 mJ/cm^2, but low multishot average did not change the overall temporal signal.

The electronic background reflectivity rises positively and then decays below the zero level as observed previously. It crosses the zero level increasingly early with increasing pump fluence. For example, at 10 mJ/cm^2, it crosses the unperturbed level at $\sim$4 ps. Above $\sim$30 mJ/cm^2, the reflectivity decays below the zero level immediately after the first vibrational oscillation. The earlier negative reflectivity may suggest disordering of the lattice atoms.

The oscillations are observed at low pump fluence and they continue to grow. The dephasing time decreases as the pump excitation increases. This is mainly due to carrier-phonon scattering. The elevated lattice temperature can also contribute to dephasing as discussed previously. Above $\sim$12 mJ/cm^2, the oscillations continue to diminish, disappearing around 20 mJ/cm^2 within the vibrational period ($\sim$500 fs). This may suggest a solid to liquid phase transition, i.e., melting. Since the vibrations are fingerprints of the crystalline solid, and disordering of atoms does not support the lattice vibrations, the disappearance of them may be indicative of melting. The disappearance of oscillations can also indicate a transition to a higher symmetry phase

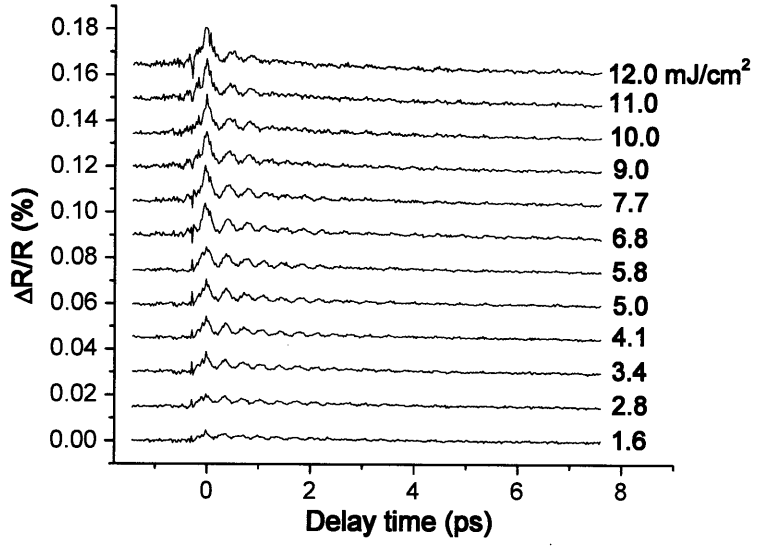

Figure 3-49: Single-shot measurements of transient reflectivity of Bi bulk single crystal. Each data trace was obtained by taking an average over 30 shots. The wavelength for pump and probe was 800 nm. An offset was added for each time trace for clarity. The A_{1g} phonon oscillations are observed from 1.6 to 12.0 mJ/cm^2.

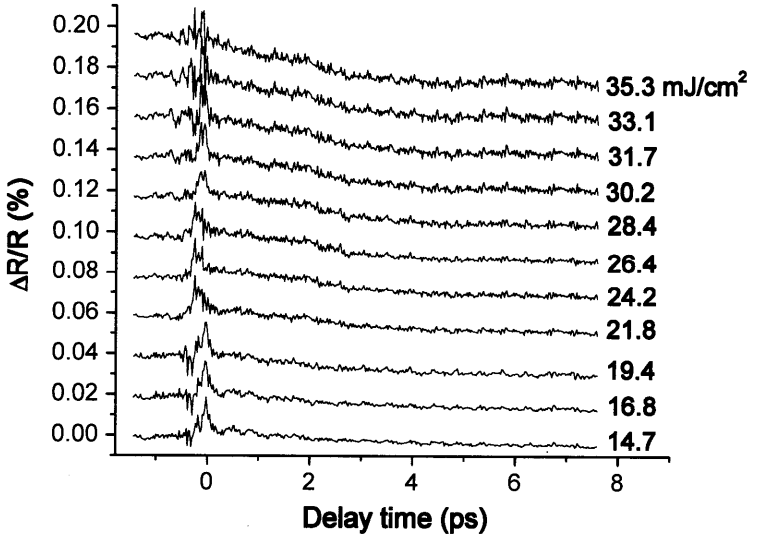

Figure 3-50: Single-shot measurements of transient reflectivity of Bi bulk single crystal. Each data trace was obtained by taking an average over 10–30 shots. An offset was added for each time trace. The A_{1g} phonon oscillations become weaker with increasing pump fluence. They disappear completely around 20 mJ/cm^2.

as suggested by earlier DFT calculations [FRA+07, MFW+05]. The DFT calculations showed that a high excitation of carriers reduces the Peierls distortion, and a higher symmetry state is achieved at a carrier density of ~2.7%. In the high symmetry phase, the red atom in figure 3-1 is located exactly at the center along the diagonal direction in the unit cell. The A_{1g} phonon is not Raman active and would not produce signal by high symmetry solid phase.

It is experimentally challenging to distinguish whether melting or the higher symmetry crystalline phase is responsible for the disappearance of the oscillations. A high density of electrons (~2.7%) may result in the high symmetry phase, while the resulting hot electrons can also melt the lattice simultaneously. It is also difficult to decouple pure electronic and thermal effects. It would be possible to decouple these effects by generating "cold electrons" with a lower photon energy. The present photon energy (1.55 eV) is significantly higher than the bandgap (~0.2 eV). The resulting excess energy of 1.35 eV is converted into the kinetic energy of an electron in the conduction band. This then can heat the lattice. However, if we lower the photon energy significantly such that it is comparable to the bandgap, then electrons in the conduction band are thermally cold and can not heat the lattice except through nonradiative recombination. In this case, only the electronic effect would come into play.

In addition to thermal melting by hot electrons, nonthermal melting is also possible. Nonthermal melting is a purely electronic effect. It has been observed that a high density of the excited electrons collapses the structure of a parent solid phase such as Al, Ge, GaAs, and GeSb [GRLT00, Sid99, SWS+91, SSB+98]. Nonthermal melting in bismuth is strongly associated with the transition to the high symmetry crystalline phase which also results from the same electronic effect. The distinction between nonthermal melting and the transition to a high symmetry phase can be made by considering energetic atomic motions due to ultrafast excitation. DFT calculations predict the high symmetry phase [FRA+07, MFW+05], but they do not consider the dynamical nature of atomic motions. The impulsive absorption by electrons leads to the energization of atoms. The atoms are instantaneously located on the repulsive

region of the new potential energy surface which may represent the high symmetry phase. If the kinetic energy of atoms due to the repulsive force is not high enough, then the atoms are trapped on the new potential energy at least transiently. In this case, the lattice would show the high symmetry structure. However, if the atoms gain kinetic energy high enough to overcome the new potential barrier, then the lattice structure would collapse (or melt) without holding the high lattice symmetry. This is nonthermal melting. Recently, Sciaini *et al.* showed that the accelerated atomic motion along the diagonal (longitudinal) direction may be coupled to a transverse acoustic mode as a consequence of anharmonic coupling, which produces an isotropic liquid phase anomalously fast. They showed that nonthermal melting can occur as quickly as 190 fs at high pump fluence [SHK+09].

Ultrafast phase transitions of bismuth are very complex involving three possibilities—thermal melting, a nonthermal transition to the high symmetry phase, and nonthermal melting. Each potential transition has its own characteristic timescale. It is likely that thermal melting occurs around 20–30 ps through inelastic electron-phonon coupling and nonradiative recombination. The minimum reflectivity is reached at 25-30 ps, which coincides with the maximum lattice temperature in the thermal model. In addition, Garl *et al.* obtained numerical solutions of coupled electron and lattice energy equations. These results showed that the maximum lattice temperature is reached after thermal equilibration of electrons and the lattice, after ~20 ps [GGB+08]. On the other hand, ultrafast electron diffraction showed that bismuth thin films melt nonthermally in as quickly as 190 fs at 23 mJ/cm^2 [SHK+09]. Femtosecond X-ray measurements revealed that bismuth thin films undergo nonthermal melting within several picoseconds [SBB+03].

Long delay time dynamics: double pump measurements

It is essential to investigate the disappearance of the oscillations in order to understand the nature of the phase transition. To this end, double pump measurements were conducted. The schematic diagram for the measurements is illustrated in figure 3-51. The first pump pulse is usually strong enough to induce the phase transition.

The second pump pulse, however, is too weak to significantly perturb the sample area excited by the first. It is only strong enough to launch the phonon oscillations if bismuth is in its original crystalline phase. The time interval between the first and second pump pulses can be varied between 0 and 100 ps. The probe train was time-delayed so that it could detect the transient reflectivity induced by the second pump. The two pumps were created by the optical scheme illustrated in (b). The same scheme was used for the double pump measurements using the standard pump-probe method. The power of the first pump is controlled by the half-wave plate-polarizer pair, and that of the second pump by the quarter-wave plate-polarizer pair. After being time-delayed by separate delay lines, they are incorporated back at the second beam splitter and then propagate co-linearly.

Figures 3-52 to 3-55 show the results from the double pump measurements. When running the experiment twice, once with the first and second pump pulses and once with just the first pump pulse, in each case probing the same temporal range, and arrives 5 to 100 ps after the strong first pump. The series of time-dependent responses in figure 3-52 were recovered by subtracting the response after the first from the combined response after the first and second pumps. Therefore, each time trace represents the response to the second pump only. The second pump launches weak but clear oscillations. They dephase rapidly mainly due to the elevated lattice temperature. The appearance of oscillations from the second pump reveals that bismuth never melted at any time. The fast dephasing of the oscillations (from the first pump) is due to carrier-phonon scattering, not due to a phase transition. As discussed earlier, the maximum lattice temperature is reached around 20–30 ps. It could be imagined that bismuth undergoes thermal melting around 20–30 ps or prior, resulting in the gradual disappearance of lattice vibrations. However, the presence of the oscillations at 30 ps reveals that thermal melting does not occur. Oscillations do not grow or reduce when the second pump delay time is varied from 5 to 100 ps. There is no significant change. After a long delay time (∞), the oscillations grow completely to the original level due to lattice cooling. According to thermal analysis, the lattice requires several nanoseconds to reach room temperature.

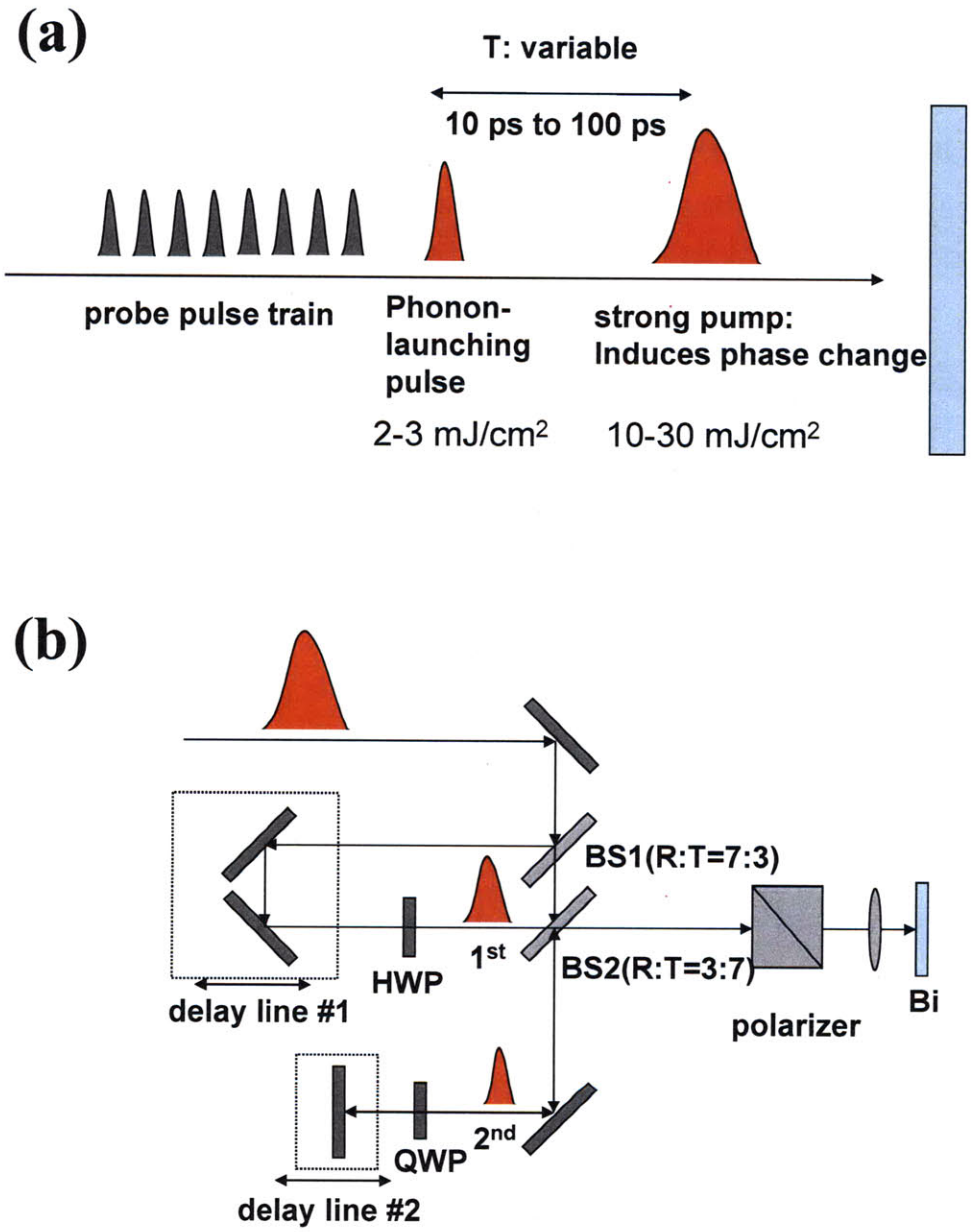

Figure 3-51: Schematic illustration of double pump measurements. (a) shows the scheme for double pump measurements. A strong pump pulse comes earlier and induces the phase transition. A second pump follows the first strong pump pulse and launches phonon oscillations. Finally, the probe array measures the time-dependent reflectivity. (b) illustrates the optical setup for generating the two pumps. A pulse is divided by the first beamsplitter into two pieces. One is reflected and delayed by delay line #1. The half-waveplate (HWP)-polarizer pair controls the power of the first, strong pump. The other pump is transmitted through both the first and second beamsplitter and delayed by delay line #2. The quarter-waveplate (QWP)-polarizer pair controls the power of the second, weak pump.

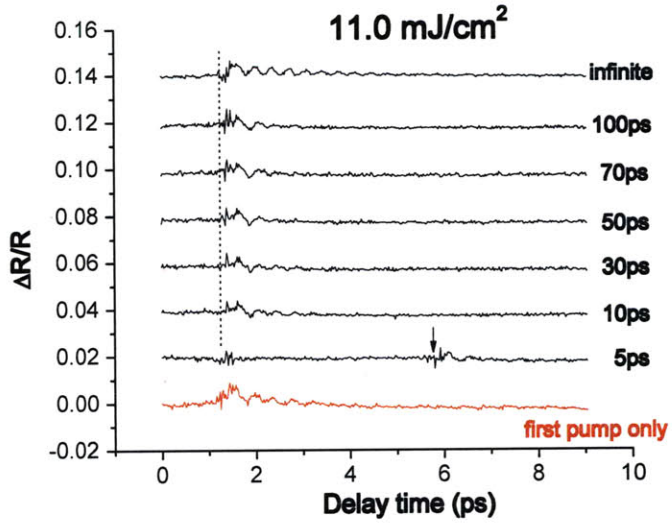

Figure 3-52: Double pump measurements in bulk bismuth. Oscillations are observed due to the first pump excitation (11 mJ/cm^2). A weak second pump (3 mJ/cm^2) arrives 5 to 100 ps after the first excitation. The oscillations from the second pump are visible at all times. The time-dependent signal from the second pump was obtained by subtracting the first pump response from that of both pumps.

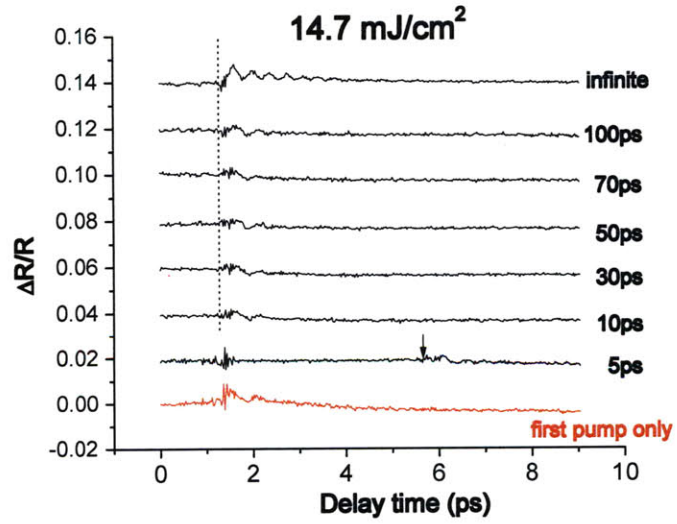

Figure 3-53: Double pump measurements in bulk bismuth. A few cycles of oscillations are induced by the first pump excitation (14.7 mJ/cm^2). A weak second pump (3 mJ/cm^2) arrives 5 to 100 ps after the first excitation. The oscillations from the second second are very weak but visible at all times.

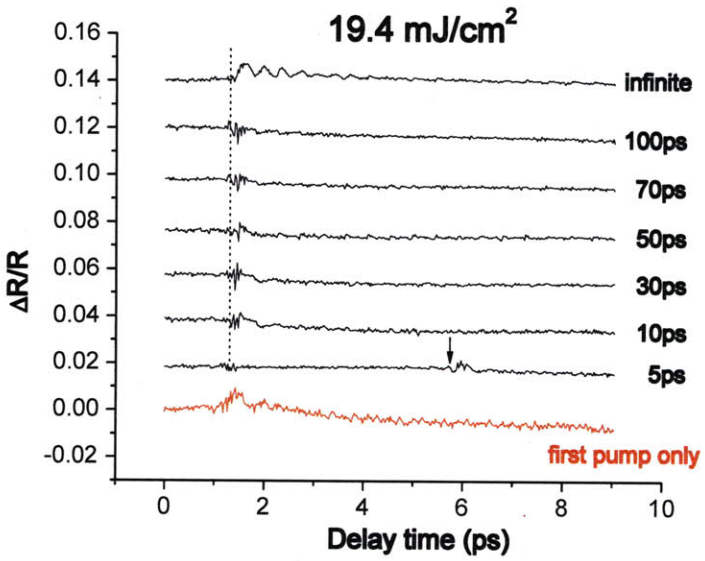

Figure 3-54: Double pump measurements in bulk bismuth. A few cycles of oscillations are generated by the first pump (19.4 mJ/cm^2). A weak second pump (3 mJ/cm^2) arrives 5 to 100 ps after the first excitation. The oscillations from the second pump are extremely small at all times.

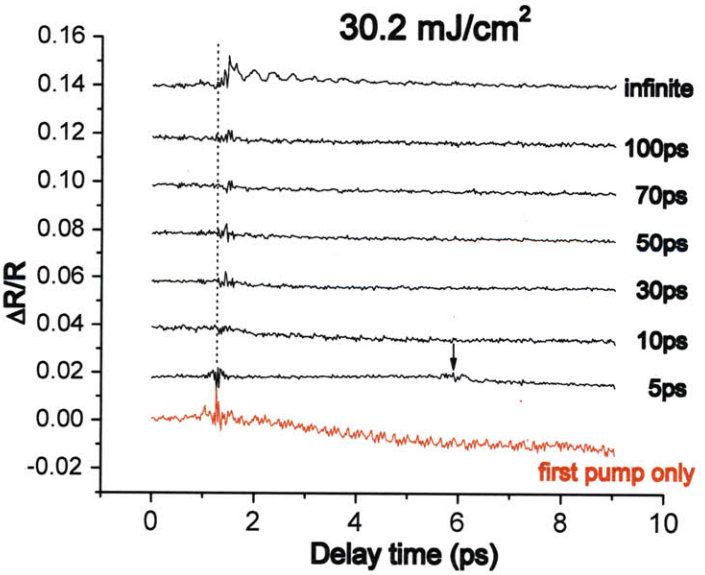

Figure 3-55: Double pump measurements in bulk bismuth. Phonon oscillations disappear very quickly after the first pump (30.2 mJ/cm^2). A weak second pump (3 mJ/cm^2) arrives 5 to 100 ps after the first excitation. No oscillations by the second pump are observed at any time.

At a fluence of 14.7 mJ/cm^2 (figure 3-53), the oscillations from the first strong pump disappear within a few vibrational cycles (~1 ps), but reappear after the second pump at 5–10 ps delay. This suggests that the oscillation disappearance (from the first pump) is due to simple fast dephasing caused by a high frequency of carrier-phonon collisions. Based on the presence of the oscillations at 10-30 ps, it is clear that thermal melting does not occur. The disappearance of oscillations might also suggest a transition to the higher symmetry (the reverse Peierls transition). Since the lifetime of hot carriers is about 15 ps, the oscillation amplitude should grow gradually until 15 ps because the stability of the higher symmetry phase is supported only by the high density of carriers [FRA$^+$07, MFW$^+$05]. However, the amplitude stays constant. Therefore, the transition to the higher symmetry phase is unlikely.

Above 19.4 mJ/cm^2 (figure 3-54), oscillations disappear within a few vibrational cycles as well. The oscillations launched by the second pump are extremely small or invisible. The oscillations do not grow until the characteristic recombination time (~ 15 ps). This rules out the phase transition to the higher symmetry phase. The absence of the oscillations or extremely weak oscillations for 10–100 ps strongly suggest the onset of the liquid phase. But is melting driven electronically or thermally? Thermal modeling cannot account for the disappearance of oscillations at early as 1–5 ps. According to the thermal modeling, a significant part of the energy from the laser pulse is stored in electrons on this timescale. This reveals that the melting is initiated nonthermally or electronically. Nonthermal melting is supported by a recent ultrafast X-ray diffraction study [SBB$^+$03] where the vibrational atomic motions were found to disappear immediately after optical excitation. More recently, Sciaini *et al.* observed the structure of bismuth collapse as quickly as 190 fs after optical excitation using ultrafast electron diffraction measurements [SHK$^+$09]. Based on the fast timescale, it is likely that the melting of bismuth is driven nonthermally. But the thermal contribution to lattice heating should not be ignored. Even though the melting seems to be initiated electronically, the lattice temperature continues to rise until ~20–30 ps via inelastic electron-phonon coupling and nonradiative recombination. Every lattice atom gains higher kinetic energy due to thermal processes. The thermal lattice

heating by hot carriers prolongs lattice cooling. At 30.2 mJ/cm^2 (figure 3-55), no oscillations are observed at any time suggesting that the bismuth melts completely.

Bismuth may melt thermally under certain excitation levels. In this case, the vibrational signature should decrease and disappear before 20–30 ps when the highest lattice temperature is achieved. The second pump could not then generate lattice vibrations at 20–30 ps. In our double pump measurements, however, this was not observed. It appears that the high carrier density drives melting electronically near time zero before bismuth undergoes thermal melting around 20–30 ps.

3.5.2 300 nm Thin Film

Short delay time dynamics

Figures 3-56 and 3-57 show the transient reflectivity of a 300 nm thin film as a function of pump fluence obtained from single-shot measurements. Each time trace was typically averaged over 10–30 shots. The reflectivity rises positively initially and then decays to a negative value as in bulk crystals. The decay rate and the negative value increase with increasing pump fluence. Oscillations are observed until ~15 mJ/cm^2, but they disappear or dephase rapidly around 15–20 mJ/cm^2. Generally, ultrafast dynamics of the 300 nm film are very similar to those of the bulk sample.

In addition to the present single-shot studies, conventional pump-probe measurements also showed that the 300 nm thin film exhibits ultrafast dynamics similar to those of bulk crystals at low pump fluence. For example, the transient reflectivity of a 300 nm thin film is much closer to that of the bulk sample than to thinner films as shown in figure 3-14. It is also inferred from figure 3-18 that the extent of bond softening in the 300 nm thin film and in the bulk are almost the same. These are probably because the electronic structure of bismuth is almost fully developed in 300 nm thickness and because the carrier dynamics should be similar in both cases. The thickness of 300 nm is enough that the diffusion timescale across a 300 nm thin layer is much longer than the recombination time ($t_D = (300\text{ nm})^2/(2 \times 200\text{ nm}^2/\text{ps}) \simeq 200\text{ ps} \gg 15\text{ ps}$). This indicates that carri-

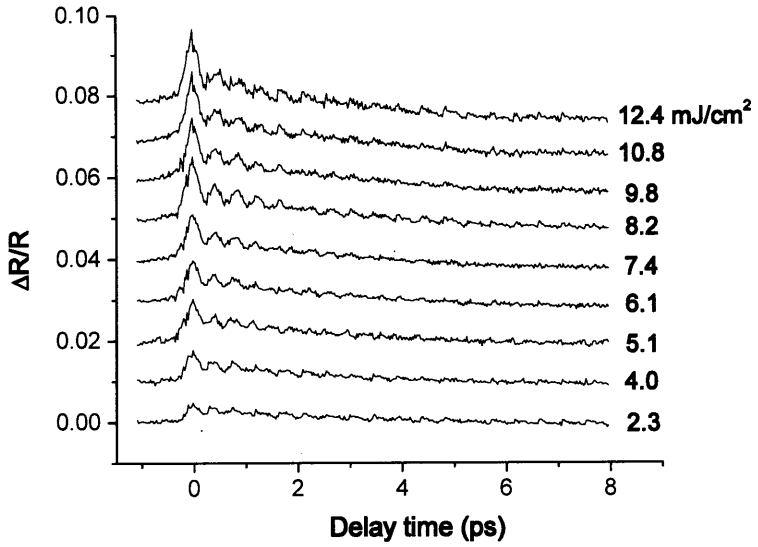

Figure 3-56: Single-shot measurements of the transient reflectivity of 300 nm thin film. Each data trace was obtained by taking an average over 30 shots. The wavelength for pump and probe was 800 nm. An offset was added for each time trace for clarity. The A_{1g} phonon oscillations are observed for pump fluence from 2.3 to 12.4 mJ/cm^2.

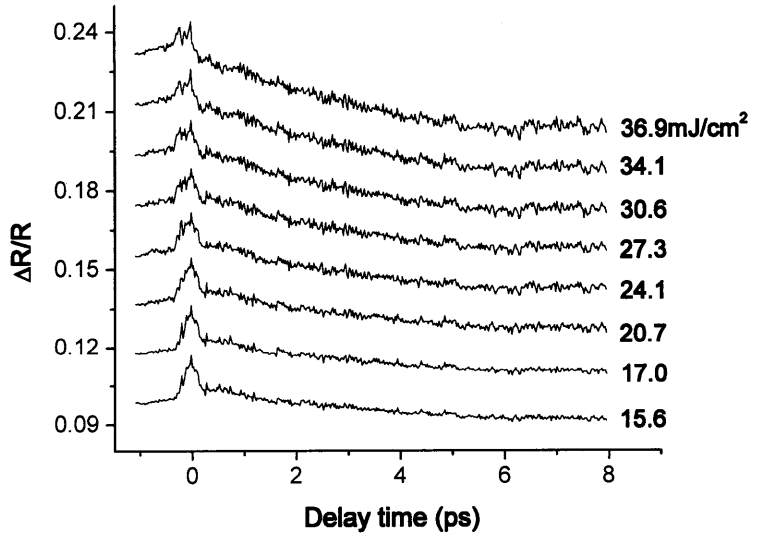

Figure 3-57: Single-shot measurements of transient reflectivity of 300 nm thin film. Each data trace was obtained by taking an average over 10-30 shots depending on the fluence. An offset was added for each time trace for clarity. The A_{1g} phonon oscillations disappear almost completely around 15–17 mJ/cm^2.

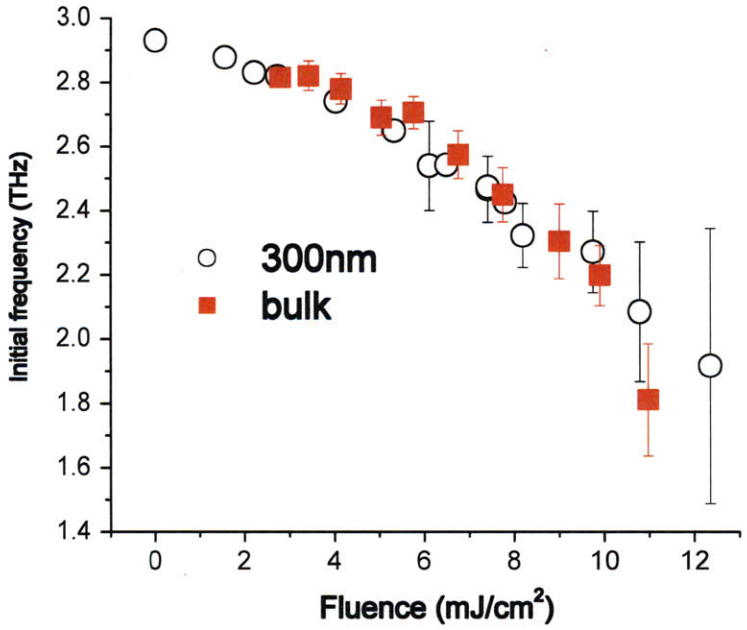

Figure 3-58: Bond softening in 300 nm thin film and bulk crystals. The initial phonon frequency red-shifts with increasing pump fluence. The film and the bulk crystal undergo bond softening to almost the same extent. Initial frequencies were recovered from curve fitting. The curve fitting yields large errors above ~10 mJ/cm^2 because of the small number of oscillations, or fast dephasing.

ers do not distinguish between the 300 nm thin film and bulk crystals. Figure 3-58 compares the bond softening in 300 nm thin film and bulk crystals. Initial frequency shows red-shifting up to ~10 mJ/cm^2 with increasing pump fluence. It appears that the extent of bond softening is almost the same in both samples. At high pump fluences, large errors are produced because of only a few cycles of oscillations and the fast dephasing.

Long delay time dynamics: double pump measurements

As shown in figure 3-57, oscillations disappear or dephase rapidly at 15–20 mJ/cm^2. Based on the bulk sample measurements, this suggests nonthermal melting or simple fast dephasing. Double pump measurements were made to distinguish between the two possibilities as in the bulk sample.

At 10.8 mJ/cm^2, it is evident that bismuth does not undergo thermal or nonther-

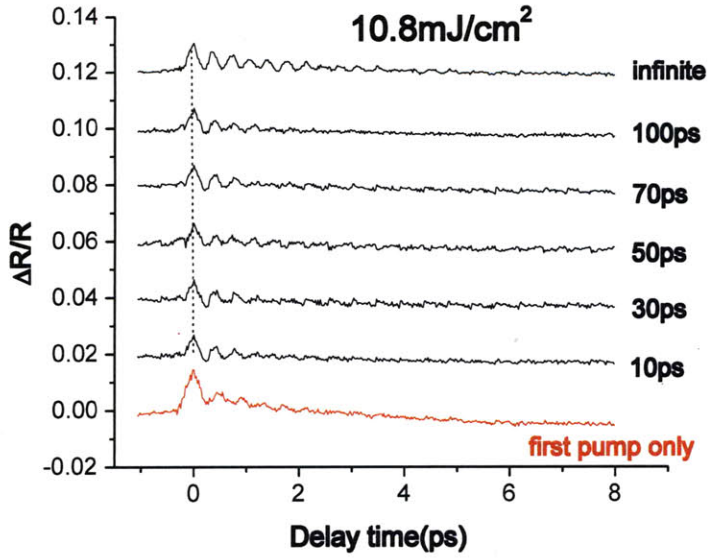

Figure 3-59: Double pump measurements in 300 nm Bi thin film. Oscillations are launched by the first pump excitation (10.8 mJ/cm^2). A weak second pump (3 mJ/cm^2) arrives 10 to 100 ps after the first excitation. The oscillations from the second pump are observed at all times.

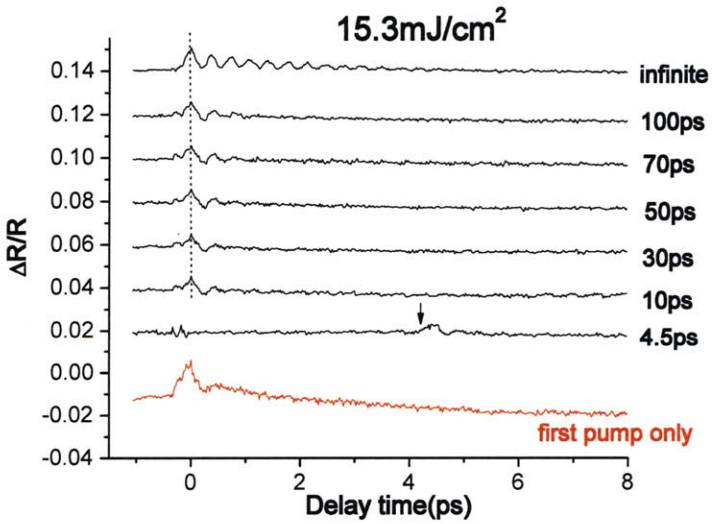

Figure 3-60: Double pump measurements in 300 nm Bi thin film. Oscillations by the first pump excitation (15.3 mJ/cm^2) dephase rapidly. A weak second pump (3 mJ/cm^2) arrives 4.5 to 100 ps after the first excitation. The oscillations from the second pump are weak but apparent at all times.

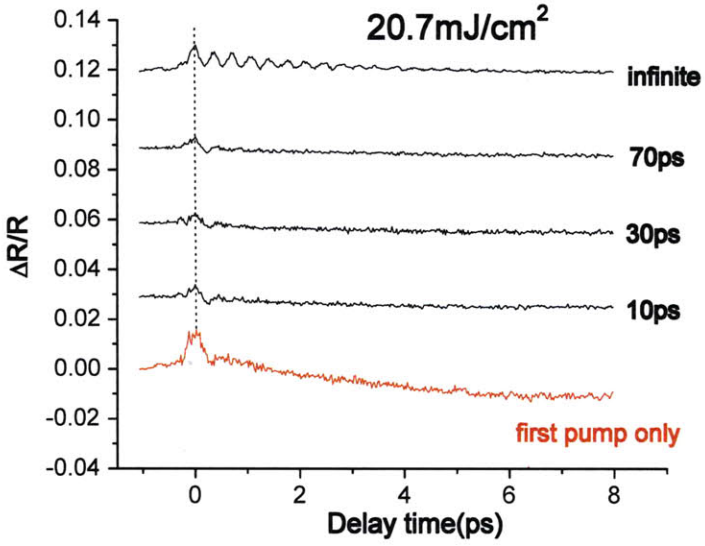

Figure 3-61: Double pump measurements in 300 nm Bi thin film. Oscillations from the first pump excitation (20.7 mJ/cm^2) dephase very quickly. A weak second pump (3 mJ/cm^2) arrives 10 to 70 ps after the first excitation. Oscillations from the second pump are extremely weak at all times, suggesting the onset of the liquid phase.

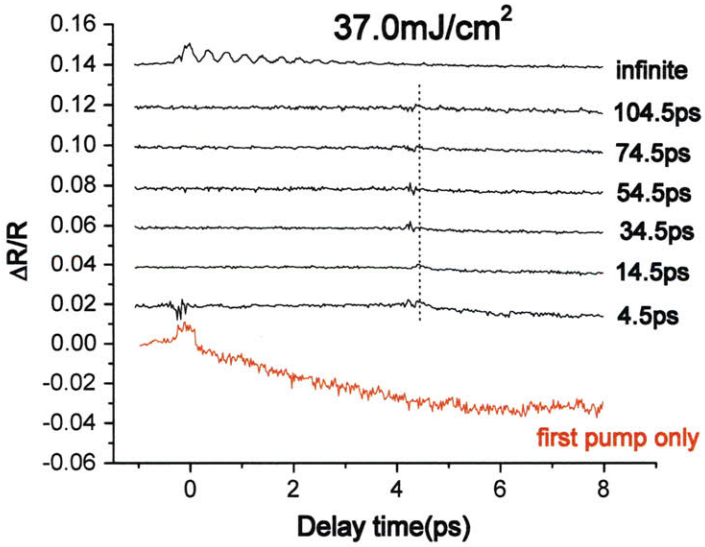

Figure 3-62: Double pump measurements in 300 nm Bi thin film. Oscillations from the first pump excitation (37.0 mJ/cm^2) dephase very quickly. A weak second pump (3 mJ/cm^2) arrives 4.5 to 104.5 ps after the first excitation. No oscillations are observed at any time, suggesting a complete transition to liquid.

mal melting based on the existence of the oscillations at all times. Bismuth stays in its original crystalline phase. At 15.3 mJ/cm^2, the oscillations disappear within 1 or 2 vibrational cycles. This is ascribed simply to fast dephasing supported by the induced oscillations at 4.5–10 ps. Observation of oscillations at the maximum lattice temperature at 20–30 ps further indicates the crystalline phase. At 20.7 mJ/cm^2, oscillations from the second pump are extremely weak or almost invisible. This suggests the onset of the liquid phase. At 37 mJ/cm^2, bismuth melts completely before 4.5 ps by the nonthermal mechanism. Disordering of atoms should proceed further via thermal effects including hot electron-phonon scattering and nonradiative recombination.

3.5.3 25 nm Thin Film

Short delay time dynamics

Very thin Bi films show unusually large bond softening as shown in figure 3-18. A small decrease in thickness causes further bond softening. Bond softening differences at the same pump fluence are more pronounced when the thickness decreases from 38 nm to 30 nm than when the thickness decreases from ∞ (bulk) to 38 nm. A further decrease in thickness from 30 nm to 25 nm results in significantly more severe bond softening. As discussed before, the dependence of the initial phonon oscillation frequency on the thickness may involve ultrafast carrier dynamics such as fast diffusion or intrinsic electronic band structure. This thickness-dependent bond softening suggests that a thinner film may undergo a phase transition at a lower threshold fluence.

Figures 3-63 and 3-64 exhibit transient reflectivity of 25 nm thin films. Each time signal was obtained by taking an average over 10–30 shots. Mild single-shot damage was observed above 5–6 mJ/cm^2, but the number of shots for averaging is small enough not to change the time-dependent signal. 600 nm probe wavelength was used for better sensitivity (figure 3-27). As observed in the conventional pump-probe measurements, the film shows a negative change in reflectivity and relaxes towards the unperturbed level. A_{1g} phonon oscillations are observed at low fluence up to

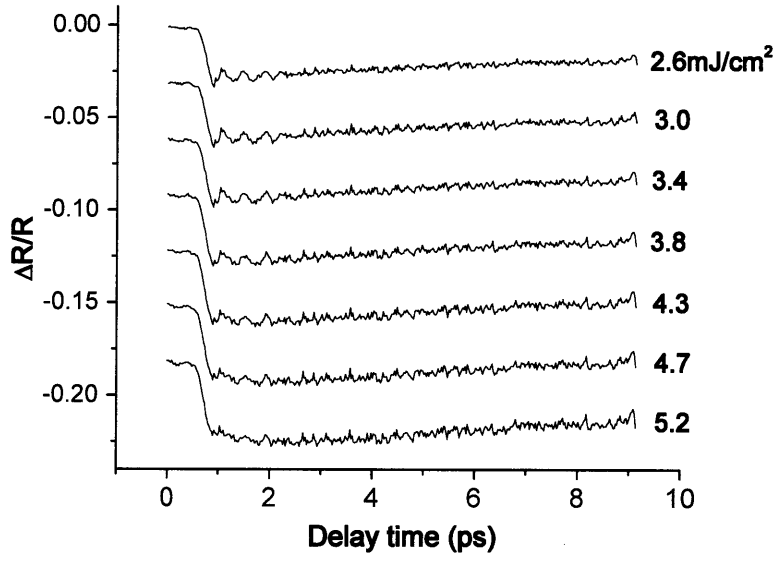

Figure 3-63: Single-shot measurements of transient reflectivity of 25 nm Bi thin film. Each data trace was obtained by taking an average over 30 shots. The wavelengths for pump and probe were 800 nm and 600 nm, respectively. An offset was added for each time trace for clarity. The A_{1g} phonon oscillations are observed from 2.6 to 4.7 mJ/cm^2, but they weaken by 5.2 mJ/cm^2.

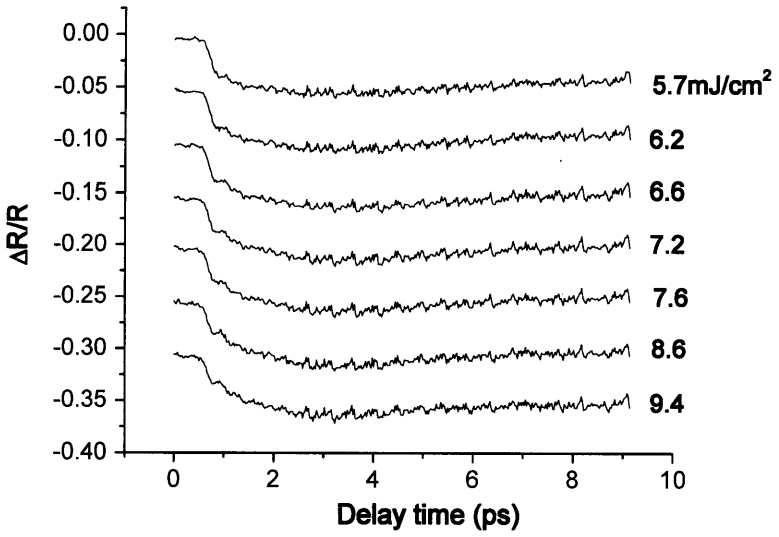

Figure 3-64: Single-shot measurements of transient reflectivity of 25 nm Bi thin film. Each data trace was obtained by taking an average over 10-30 shots. An offset was added for each time trace. No oscillations are observed from 5.7 to 9.4 mJ/cm^2.

4.7 mJ/cm^2. Excitation fluences of 5.2–5.7 mJ/cm^2 lead to the disappearance of the phonon oscillations. It should be noted that this fluence is significantly lower than that of bulk crystals or 300 nm thin film. This lower threshold fluence may be the same reason for the more pronounced bond softening in 25 nm thin film. Fast carrier dynamics or different electronic structure are factors that may contribute.

Long delay time dynamics: double pump measurements

The same double pump measurements were made in the 25 nm thin film to examine the origin of the oscillation disappearance. Figures 3-65 to 3-68 show the results. At 3.0 mJ/cm^2, oscillations from the first pump are visible and reappear as early as 10 ps as shown in figure 3-65. It appears that the oscillations are weakest around 5 ps. This might be due to fast dephasing caused by electron-phonon scattering. At 20–30 ps, when the highest lattice temperature is expected, oscillations are observed. This indicates that the thin film still exists in the crystalline phase. The oscillations become much smaller or dephase more rapidly at the higher pump fluence of 4.3 mJ/cm^2 in figure 3-66. Oscillations are produced by the second pump after 10 ps, revealing that the film did not melt. The oscillations are extremely small or invisible at 5.3 mJ/cm^2 in figure 3-67. The second pump launches barely visible oscillations, suggesting the onset of the liquid phase. No oscillations are observed under the fluence of 6.6 mJ/cm^2. They do not reappear within 100 ps. Complete melting is evident. The melting occurs earlier than 5 ps, resulting from the nonthermal mechanism. It should be noted that the threshold fluence for melting is significantly lower than that of bulk crystals or 300 nm thin films. The threshold for nonthermal melting in bulk crystals and 300 nm film was measured to be 20–25 mJ/cm^2 from the double pump measurements.

The lower threshold fluence for the melting transition may be associated with severe bond softening in the thin films. As we observed earlier, the initial frequency at $t = 0$ is much lower in 25 nm thin film than in bulk crystals under the same optical excitation fluence (figure 3-18). The almost identical frequencies at very low pump fluences indicate that the interatomic force constant is the same at equilibrium inde-

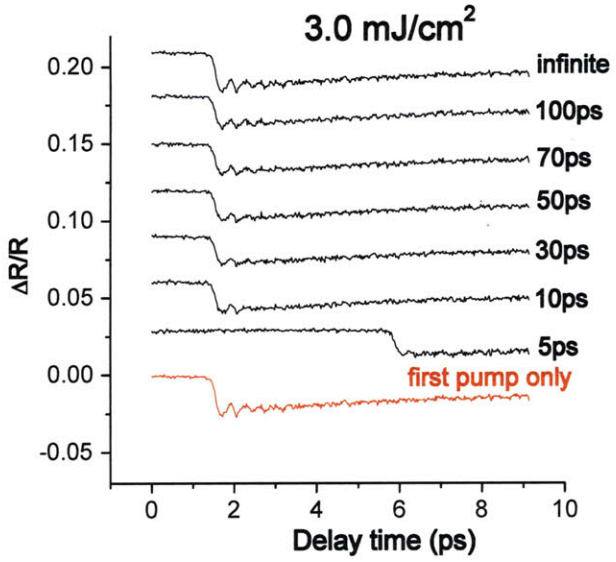

Figure 3-65: Double pump measurements in 25 nm Bi thin film. Oscillations are launched by the first pump excitation (3 mJ/cm^2). A weak second pump (1.9 mJ/cm^2) arrives 5 to 100 ps after the first excitation. The oscillations from the second pump are observed at all times.

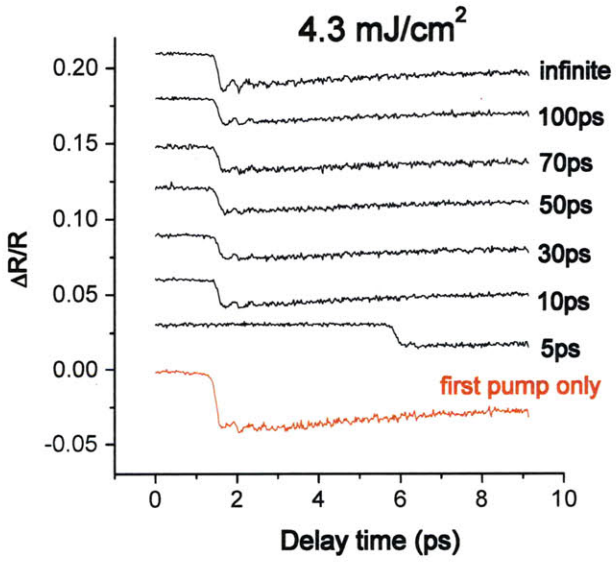

Figure 3-66: Double pump measurements in 25 nm Bi thin film. Very weak oscillations are launched by the first pump excitation (4.3 mJ/cm^2). A weak second pump (1.9 mJ/cm^2) arrives 5 to 100 ps after the first excitation. Oscillations from the second pump are weak, but they are clear at all times.

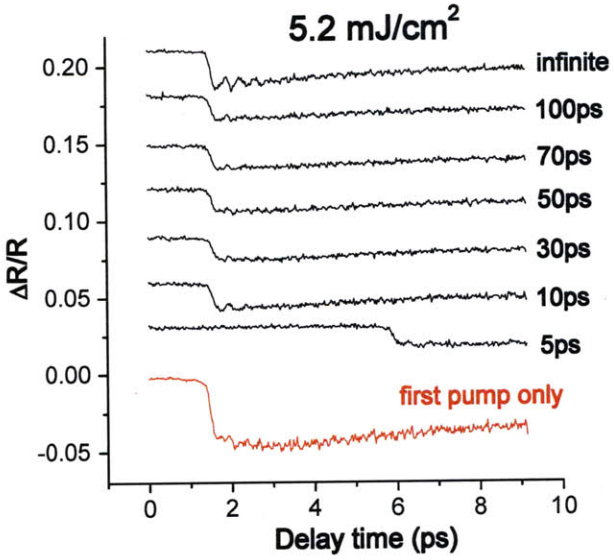

Figure 3-67: Double pump measurements in 25 nm Bi thin film. No oscillations are launched by the first pump excitation (5.2 mJ/cm^2). A weak second pump (1.9 mJ/cm^2) arrives 10 to 100 ps after the first excitation. Oscillations from the second pump are extremely weak at all times.

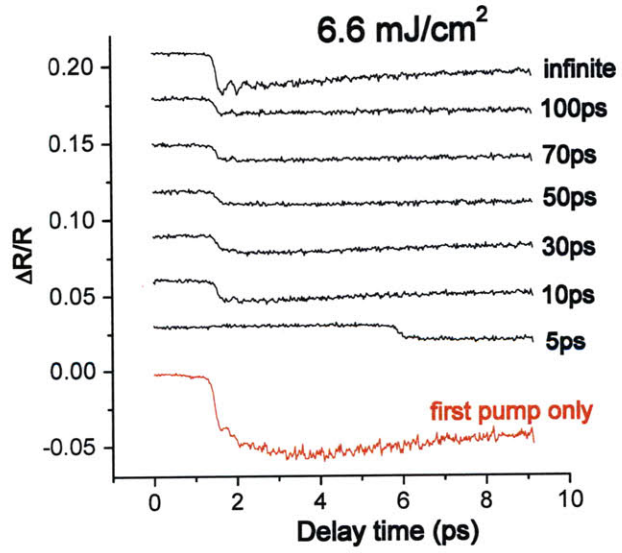

Figure 3-68: Double pump measurements in 25 nm Bi thin film. No oscillations from the first pump excitation (6.6 mJ/cm^2) are observed. A weak second pump (1.9 mJ/cm^2) arrives 10 to 100 ps after the first excitation. No oscillations from the second are observed at any time, suggesting a transition to the liquid phase.

pendent of the thickness. Therefore, the dependence of the instantaneous frequency (at $t = 0$) on the thickness can be explained by impulsive or ultrafast processes of carriers upon impulsive excitation. For example, ballistic transport of hot electrons may account for the thickness-dependent bond softening based on timescale. However, it is not known how many carriers can transport ballistically, $D_e \gg 200$ nm^2/ps, or conventionally, $D_e \sim 200$ nm^2/ps. If it is assumed that a significant portion of carriers transport ballistically, then free carriers should deplete in the probing depth instantaneously at $t = 0$. The resulting lower density of carriers can maintain equilibrium frequency by hampering bond softening in bulk [FRA$^+$07, MFW$^+$05]. In thin films, ballistic transport of free carriers along the surface normal direction is suppressed because they cannot proceed across the interface by overcoming the large substrate bandgap. The resulting higher carrier density can lead to more pronounced bond softening at $t = 0$.

Whether hot carriers move ballistically or conventionally, their diffusion should affect the thermalization process between hot carriers and the cold lattice. For example, since free hot carriers are confined in thin films, their thermal energy should be transferred to the lattice only within the thin layer. This results in efficient lattice heating near the surface. By contrast, since free hot carriers can diffuse out of the skin depth in bulk crystals or thicker films, their thermal energy is distributed over a broader region. This leads to a less effective heating and a lower lattice temperature near the surface.

The effects of diffusivity on the lattice heating at $z = 0$ were estimated in figure 3-47. A small value of diffusivity ($D_e = 1$ nm^2/ps) simulates the suppressed diffusion of hot carriers in thin films. A higher lattice temperature results from the suppressed diffusion in thin films. The change in lattice temperature is twice as high at $D_e = 1$ nm^2/ps than at $D_e = 200$ nm^2/ps. It should be noted that the effects of diffusivity are strictly thermal in the model. Because of this, the maximum lattice temperature is achieved on a similar timescale (around 20 ps) in both cases. The maximum lattice temperature is observed at 19 ps when $D_e = 1$ nm^2/ps (simulating thin films). The maximum temperature is reached at 23 ps when $D_e = 200$ nm^2/ps

(simulating a bulk crystal). This time difference is negligible, implying that thermal effects originating from the suppressed diffusion of hot carriers in thin films are significant until 20 ps as in bulk samples. However, since melting occurs prior to at least 5 ps in bismuth, the enhanced thermal heating (due to suppressed diffusion) can not explain the significantly lower threshold fluence for ultrafast melting of the thin film. The enhanced thermal heating can explain lower damage threshold fluence than in bulk crystals.

The accumulated high density of free carriers may account for the low melting threshold for the thin film, as it accounts for the more pronounced bond softening in thin films at $t = 0$. A high density of excited carriers within the skin depth alters the original potential energy surface [FRA+07, MFW+05]. In bulk samples, the excited carriers diffuse out of the skin depth and the original potential energy surface would be recovered quickly. By contrast, excited free carriers are confined within the skin depth in thin films so the excited potential energy surface can relax only via electron-hole recombination. Due to the slower rate of the recombination compared to diffusion, the excited potential energy will relax more slowly in thin films than in bulk. In this fashion, a threshold potential energy surface which eventually leads to nonthermal melting is achieved under lower excitation fluence in thin films. These are nonthermal effects. Hot carriers do not heat the lattice significantly on this timescale.

For a better understanding of phase transitions in bismuth, it is necessary to decouple the thermal and nonthermal effects in photoinduced phase transitions. As mentioned earlier, optical excitation with a photon energy comparable to the bandgap (0.2 eV) would generate "free cold electrons" in the conduction band. This would eliminate thermal effects such as thermalization between hot electrons and lattice, and enable us to examine purely electronic effects on lattice melting in bismuth.

3.6 Summary

In this chapter, we examined ultrafast dynamics in bismuth under highly nonequilibrium conditions by measuring transient reflectivity. The ultrafast dynamics in-

clude coherent phonons, vibrational dephasing, bond softening, hot carrier dynamics, electron-phonon interactions, and nonthermal melting. Those dynamics are strongly influenced by film thickness.

Bond softening is most pronounced in thin films. Ballistic carrier transport and conventional diffusion reduce the carrier density greatly in the skin depth in bulk crystals. On the contrary, ballistic transport and diffusion are suppressed in thin films. A higher density of carriers is sustained in thin films. The potential energy surface is very sensitive to carrier density and accounts for more pronounced bond softening in thin films.

Thickness-dependent reflectivities were interpreted using the Fermi-Dirac distribution function. A larger bandgap for interband transitions was observed in thinner films. This may result from quantum confinement effects in thin Bi films.

A thermal model was proposed for ultrafast dynamics in bismuth. This model is applicable to other bandgap materials. The model includes the electron and lattice heat equations, diffusion equation, and electron-hole recombination kinetics. Using proper parameters such as electron diffusivity, the model predicts that the maximum lattice temperature is reached after 20–30 ps via inelastic electron-phonon coupling and nonradiative recombination. The maximum temperature coincides with the minimum reflectivity at 20–30 ps, which may verify the thermal modeling.

Disappearance of phonon oscillations was observed under strong excitation. This can be attributed to the fast dephasing or phase transitions. Together with thermal modeling and double pump measurements, the disappearance reveals that bismuth undergoes nonthermal melting within 5 ps. The melting threshold is significantly lower in thin films than in bulk samples. This may result from the suppressed transport of hot carriers in thin films.

Chapter 4

Photoinduced Phase Transition of a Quasi-one-dimensional Platinum Iodide Complex

In this chapter we examine the ultrafast optical response in a quasi-one-dimensional halogen-bridged mixed valence metal complex $[Pt(en)_2][Pt(en)_2I_2](ClO_4)_4$, where en denotes ethylenediamine. We observed oscillatory modulations in the time-resolved reflectivity, which is ascribed to wave packet motion in a self-trapped exciton state. Higher excitation leads to the disappearance of the oscillations. We suggest the disappearance of the oscillations as evidence for a phase transition from a charge density wave state to a Mott-Hubbard phase. Using double pump measurements, we measured the recovery time of the oscillations. An extremely short lifetime of the Mott-Hubbard phase is revealed.

4.1 Introduction

Halogen(X)-bridged metal(M) complexes have been studied because of electronic properties originating from their one dimensional structures [OY98]. The complexes are represented as $[MA_2]$-$[MA_2X_2]Y_4$, where A and Y indicate a ligand and the counter anion, respectively. The interesting feature of these complexes is their one-

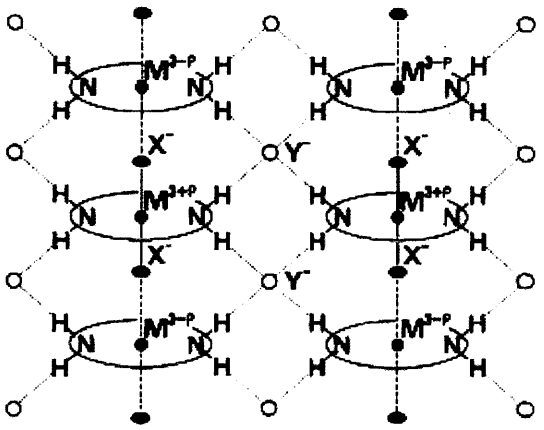

Figure 4-1: One-dimensional structure of the halogen-bridged metal compound. Ligand molecules are represented by ovals. Hydrogen bonds are illustrated by the dotted lines. Taken from [OY98].

dimensional structure as shown in figure 4-1. The $[MA_2]$ moieties are bridged by the halogen ions (X), and the hydrogen bonds between the ligand (A) and the counter-anions (Y) constitutes the one-dimensional structure. The outstanding feature of the complexes is the tunability of the electronic ground states [OY98]. The amplitude of the charge density wave (CDW) and the optical gap energy can be controlled by varying the metals (M=Pt, Pd, and Ni), the bridging halogen ions (X=Cl, Br, and I), the ligand species, and the counter anions.

In the MX complexes, the one-dimensional electronic state consists of metal d_{z^2} orbitals and p_z orbitals of the bridging halogens. z is the direction parallel to the one-dimensional chain. The ground state of the complexes is the monovalent state or the mixed valence state as illustrated in figure 4-2. The upper structure describes the monovalent state (3+) or equivalently, the Mott-Hubbard state insulator. By contrast, the bottom ostructure represents the Peierls distorted, mixed valence state, where the valence alternates between 4+ and 2+. The ground state is determined by two competing energy terms. One is the stabilization energy (E_s) of the d_{z^2} electrons due to the distortion of the bridging halogens. The other is the Coulomb repulsion energy (U) on the metal site [Nas83, Nas84]. For example, when the stabilization energy (E_s) is larger than the Coulomb repulsion energy (U), the mixed valence state is favorable as the ground state. The Ni compounds favor the monovalent ground

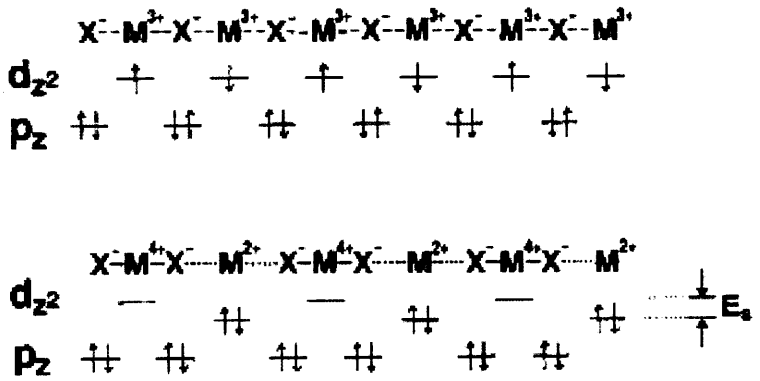

Figure 4-2: Schematic electronic structures of the MX chain. The upper represents the mono-valence symmetric state (Mott-Hubbard phase), while the bottom illustrates the mixed valence state or charge density wave state (CDW). Taken from [OY98].

state [TWM+89], while the Pt and Pd compounds favor the mixed valence state [WMYK85].

The MX complexes have been studied using femtosecond pump-probe spectroscopy. Dexheimer *et al.* observed the lattice motions associated with formation of the self-trapped exciton in $[Pt(en)_2][Pt(en)_2Br_2](PF_6)_4$ (en = ethylene-diamine) using femtosecond impulsive excitation techniques [DPBS00]. Wave packets at $\sim$110 cm^{-1} were produced due to formation of the self-trapped exciton (STE) on a $\sim$200 fs timescale following excitation of the intervalence charge transfer transition (figure 4-5). Sugita *et al.* examined $[Pt(en)_2][Pt(en)_2I_2](ClO_4)_4$ by measuring femtosecond time-resolved reflectivity. There, wave packet motions both in the ground (124 cm^{-1}) and self-trapped exciton (110 cm^{-1}) states are observed as oscillatory modulations [SSK+01]. Self-trapped exciton dynamics of $[Pt(en)_2][Pt(en)_2Cl_2](ClO_4)_4$ were investigated by femtosecond time-resolved luminescence spectroscopy [TNS+98]. In these measurements, a fast rise and decay were observed in the low and high energy tail of the luminescence band, while a slow rise of about 500 fs was seen near the luminescence peak energy. Sugita *et al.* explained these behaviors as a result of the prethermalized STE cooling. The STE state lifetime in $[Pt(en)_2][Pt(en)_2Cl_2](ClO_4)_4$ was measured to be about 30 ps. On the contrary, time-resolved luminescence measurements of

$[Pt(en)_2][Pt(en)_2Br_2](ClO_4)_4$ revealed that the STE state annihilates as quickly as ~5.5 ps. The authors attributed the short lifetime to nonradiative relaxation of the STE through conversion into a soliton or polaron, as suggested by previous studies [OMTY92, OY98].

Recently, Kimura *et al.* reported that a similar Pt complex $[Pt(chxn)_2]I_2$ undergoes a photoinduced phase transition from the CDW phase to the Mott-Hubbard (MH) phase. This observation was based on the spectral change using femtosecond pump-probe reflection spectroscopy [KMT+09]. They suggested further phase conversion from the MH phase to a metallic state evidenced by the low-energy spectral weight in the reflectivity response.

Among the MX complexes, we focus only on the $[Pt(en)_2][Pt(en)_2I_2](ClO_4)_4$, which is abbreviated as PtI in this chapter. The ground state of the PtI complex is Peierls distorted, i.e., the mixed valence state (CDW). The distance between Pt^{4+} and Pt^{2+} atoms is 5.820Å. The bond length between Pt^{4+} and I^- atoms is 2.726Å, and that between Pt^{2+} and I^- atoms is 3.093Å [EKM+79]. The maximum absorption energy is observed at 1.38 eV, which is responsible for the charge transfer from Pt^{2+} to Pt^{4+} [OY98]. The luminescence peaks at 0.60 eV [WMYK85].

4.2 Wave Packet Dynamics in the Self-Trapped Exciton State

4.2.1 Experimental

A standard pump-probe technique was employed in order to investigate the ultrafast dynamics of the wave packets of the self-trapped exciton state. The polarizations of pump and probe were both parallel to the orientation of the 1-D chain. Photon energy for the excitation was 1.55 eV (800 nm) which is slightly higher than the optical gap energy 1.38 eV. The probe wavelength was varied from 520 nm to 960 nm using the continuum generation source from a sapphire plate. More experimental details were described in chapter 2.

4.2.2 Results and discussion

Time-resolved reflectivity at 800 nm (1.55 eV) is presented in figure 4-3-(a). A negative reflectivity change is observed, and an oscillatory component is superimposed on it. The electronic background reflectivity continues to decrease until its minimum at ~2 ps after the excitation. It then increases toward the unperturbed level. To highlight the oscillatory components, the reflectivity signal was differentiated twice with respect to the delay time. The resulting signal is shown in figure 4-3-(b). The amplitude of the oscillations decays rapidly. Fast Fourier transformation (FFT) of the signal yields the frequency of 116 cm^{-1} as shown in the inset.

Figure 4-4-(a) shows the transient reflectivity change at 520 nm (2.38 eV). A faster decay is observed as compared to the reflectivity at 800 nm. The decay time is estimated approximately to be 150–200 fs and the minimum value is reached at about 500 fs after the excitation. The FFT spectrum yields a frequency of 110 cm^{-1} in Figure 4-4-(b). The linewidth at 520 nm becomes significantly broader than at 800 nm, revealing a faster dephasing rate at 520 nm.

The two frequencies 116 cm^{-1} and 110 cm^{-1} are substantially lower than the frequency of the symmetric stretching mode (I^-–Pt^{4+}–I^-) at 122.6 cm^{-1} observed in resonant Raman spectra [CK81]. Sugita *et al.* measured time-resolved reflectivity and observed 107 cm^{-1} at 2.00 eV and 110 cm^{-1} at 1.77 eV, respectively [SSK+01]. They suggested that both frequencies originate from the wave packet motion in the electronic excited state. They also observed the frequency of 124 cm^{-1} at 2.00 eV, which is attributed to the wave packet motion in the electronic ground state launched by an impulsive stimulated Raman scattering (ISRS) mechanism. However, the frequency of 124 cm^{-1} was not obtained in our measurements. Based on the assignment by Sugita *et al.*, both two frequencies 116 cm^{-1} and 110 cm^{-1} are ascribed to the oscillatory wave packet motion in the electronic excited state or the self-trapped exciton state even though 116 cm^{-1} seems higher.

Figure 4-5 describes the dynamics of the wave packets on potential energy surfaces. The initial photoexcited state is the free exciton (FE) state, and the exciton is

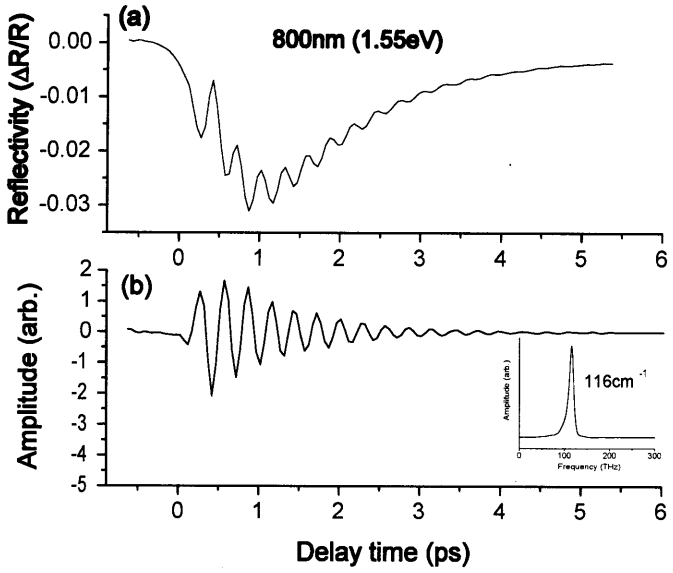

Figure 4-3: (a) Time-resolved reflectivity of the PtI complex at the probe energy 1.55 eV (800 nm). (b) The oscillatory signal is recovered by differentiating the temporal signal twice. The inset shows the Fourier-transformed spectrum of the time-derivative signal. The frequency of the oscillations is 116 cm^{-1}.

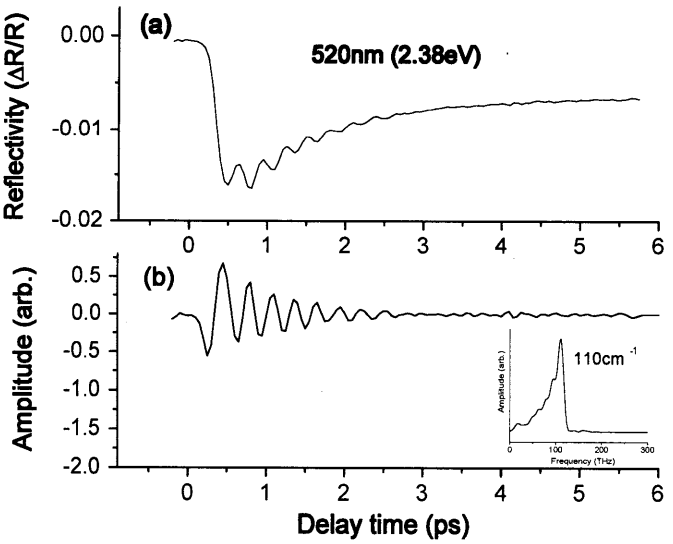

Figure 4-4: (a) Time-resolved reflectivity of the PtI complex at the probe energy 2.38 eV (520 nm). (b) The oscillatory signal is obtained by differentiating the temporal signal twice. The inset shows the Fourier-transformed spectrum of the time-derivative signal. The frequency of the oscillations is 110 cm^{-1}.

considered to be delocalized over many lattice sites. The free exciton potential and self-trapped exciton (STE) potential surfaces are expected to be continuous. There is no potential barrier between FE and STE potential surfaces as a characteristic of the 1D–exciton system [TS80, SSK+01]. As a result, the lattice relaxation from the FE to STE states occurs spontaneously just after FE formation. The excitation energy (1.55 eV) used in this study is higher than the optical gap (or the peak of the FE band) by 0.17 eV. Accordingly, thermalization within the band might take place. Once the exciton is trapped by the STE potential, the wave packets oscillate between the inner and outer turning points. This vibrating motion modulates the reflectivity as shown in figures 4-3-(a) and 4-4-(a).

Figure 4-6 illustrates the transient reflectivity as a function of probe wavelength or energy from 520 nm to 960 nm. At all wavelengths, the electronic background

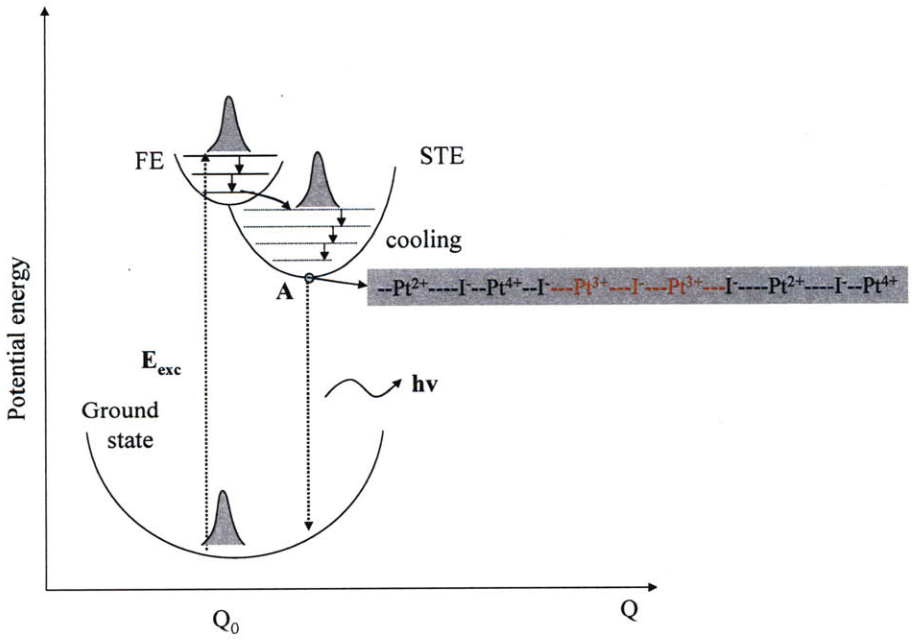

Figure 4-5: Generation and relaxation dynamics of the wave packet on the potential energy surfaces in the PtI complex. After being photoexcited, the nonequilibrium wave packet undergoes the thermalization process in the free exciton (FE) band. The lattice relaxes from the free exciton to the self-trapped exciton (STE) state. The equivalent charge distribution of the STE state is shown. The self-trapped exciton is annihilated via radiative or nonradiative relaxation such as conversion into a soliton or polaron. Modified from [SSK+01].

reflectivity continues to decrease until its minimum value around 1 ps after the excitation, and then increases toward zero. However, the decreasing and increasing rates differ depending on the wavelength. At all wavelengths, oscillations of the wave packet are observed. Since the pulse was not compressed after white light generation, it is not always possible to compare the amplitude of the oscillations. However, the pulse duration is short enough to resolve the ~350 fs vibrational period vibration for each wavelength. FFT reveals the frequency of the oscillation depending on the probe energy as shown in figure 4-7. Four different frequencies are observed—107, 110, 113, and 116 cm^{-1}. Since the resolution of the FFT spectrum is typically better than ± 2 cm^{-1} and the frequencies are distinctively distributed near those values, the distinct frequencies appear to be real. All frequencies are associated with the STE

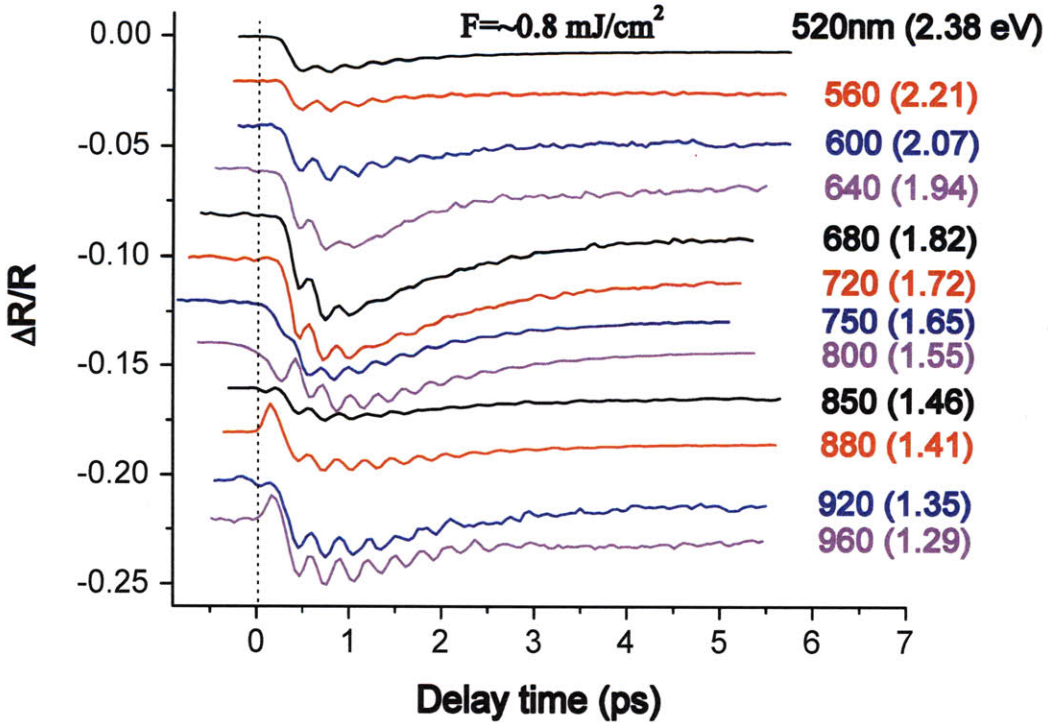

Figure 4-6: Probe wavelength dependent reflectivity of the PtI complex. The pump wavelength is fixed at 800 nm. The probe wavelength varies from 520 nm to 960 nm. The time origin for each wavelength was adjusted using the instantaneous electronic signal of glass and the impulsive absorption signal of thin Bi films.

state. The frequency of the symmetric stretching mode (I^-–Pt^{4+}–I^-) at 122.6 cm^{-1} was not produced at any probe wavelength.

Interestingly, very similar frequencies such as 107, 109, 114, and 115 cm^{-1} were observed in the time-resolved absorption experiment of $[Pt(en)_2][Pt(en)_2Br_2](PF_6)_4$ [DPBS00]. In the experiment, a frequency of ~175 cm^{-1} was observed, which originates from the symmetric stretching mode (Br^-–Pt^{4+}–Br^-) identified by resonant Raman spectroscopy [DPBS00]. The very similar frequencies between the PtI and PtBr complexes suggest that the halogen ions are not involved in the vibrational modes. This is plausible if we consider two symmetric stretching modes, Pt^{3+}–I^-–Pt^{3+} and Pt^{3+}–Br^-–Pt^{3+}. Since the I^- and Br^- ions are stationary at the center during the symmetric stretching motion and only two Pt^{3+} ions are oscillating out of phase, the frequency of the modes would be almost identical. The small variations of the frequency of this mode are not well-understood.

Figure 4-8 shows the wavelength-dependent change in reflectivity as a function of the delay time. The reflectivity near 1.82 eV (680 nm) changes most dramatically over the delay time. On the contrary, it varies only slightly at a probe energy higher

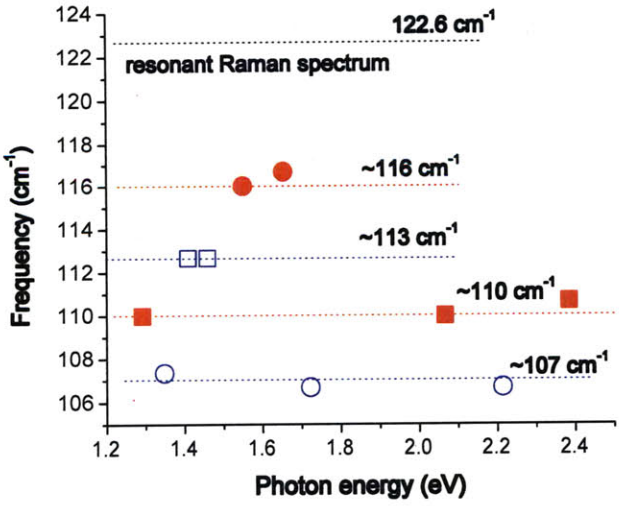

Figure 4-7: Frequencies revealed by FFT analysis. Four different frequencies are identified. They are attributed to the excited electronic state (STE state). The frequency of the symmetric stretching mode (I^-–Pt^{4+}–I^-) is presented at 122.6 cm^{-1}.

than 2.21 eV (560 nm) or lower than 1.45 eV (850 nm). The temporal evolution of the wavelength-dependent reflectivity suggests two consecutive events—vibrational cooling of the wave packets on the STE potential energy surface and annihilation of the STE state.

The temporal change up to ~0.8 ps is reminiscent of the vibrational relaxation of the wave packets in small molecules such as I_2^- [KV96]. The wave packets just after the localization are in the excited vibrational states on the STE potential surface as shown in figure 4-5. They will undergo vibrational relaxation until reaching the minimum of the potential well. If there are higher electronic states over the STE state such that the transient absorption by the probe light is possible from the STE potential to the higher states, then the probe wavelength-dependent absorption will reflect the vibrational cooling with the delay time. That is, when vibrational cooling proceeds, only the absorption will increase from the bottom of the potential well to the upper electronic state. The absorption process will change the transient reflectivity which might reveal vibrational cooling as well. Preferential decrease in reflectivity

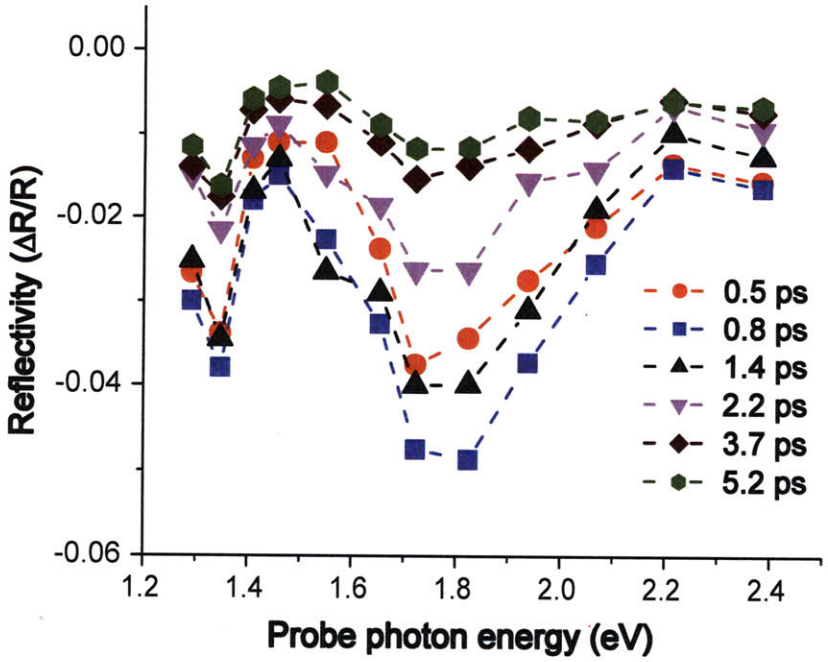

Figure 4-8: Temporal evolution of the probe energy dependent reflectivity.

(up to ~0.8 ps) at 1.82 eV (680 nm) is observed in figure 4-8. By contrast, the reflectivity change is small at both wings near 1.45 eV (850 nm) and 2.21 eV (560 nm). This implies that a probe energy of 1.82 eV (680 nm) is associated with the bottom of the STE potential energy surface, and vibrational cooling towards the bottom takes place. Sugita *et al.* observed that the dephasing rate depends on the probe energy, and it increases gradually from 1.77 to ~2.14 eV [SSK+01]. They interpreted the probe energy dependence to be due to the thermalization process in the STE potential. Since their probe energy from 1.77 to ~2.14 eV corresponds to the right side of the probe energy in figure 4-8, their interpretation agrees with vibrational cooling observed here. Tomimoto *et al.* also observed the vibrational relaxation in $[Pt(en)_2][Pt(en)_2Br_2](ClO_4)_4$ while measuring time-resolved luminescence [TSS+99].

After 0.8 ps, the reflectivity near 1.82 eV (680 nm) increases more quickly compared to other probe energies. This suggests that the STE relaxes at the bottom of the STE potential simultaneously as the vibrational cooling takes place. If the lifetime of the STE is much longer than several picoseconds, then the population of the STE at the bottom of the potential would accumulate as a consequence of vibrational cooling. Therefore, the reflectivity at 1.82 eV (680 nm) would decrease further and the linewidth of the reflectivity spectrum would become narrower until vibrational relaxation is complete. However, this is not the case. It appears that the STE stays at the bottom of the potential very shortly. The relaxation rate of the STE seems comparable to the vibrational cooling rate. In other words, $k_i \simeq ka_i$ in the following equation 4.1. The decay rate of the STE at the i^{th} vibrational level can be expressed by

$$\frac{\mathrm{d}}{\mathrm{d}t}[\mathrm{STE}]_i = k_{i+1}[\mathrm{STE}]_{i+1} - k_i[\mathrm{STE}]_i - ka_i[\mathrm{STE}]_i, \tag{4.1}$$

where k_i and k_{i+1} denote rate constants for vibrational relaxation of the STE at the i^{th} and $(i+1)^{th}$ vibrational levels, respectively. ka_i denotes the rate constant for relaxation of the STE at the i^{th} level. The STE can relax by emitting light (a radiative process) or by creating a soliton or polaron (nonradiative processes). The STE lifetime in $[Pt(en)_2][Pt(en)_2Cl_2](ClO_4)_4$ was measured to be 25 ps in time-resolved lumines-

cence [TNS+98]. By contrast, the lifetime of the STE in $[Pt(en)_2][Pt(en)_2Br_2](ClO_4)_4$ was measured to be 5.5 ps. This is a substantial decrease. It appears that the lifetime of the STE is about 2 ps based on the decay time of the reflectivity in figures 4-6 and 4-8. It was revealed that the intensity of the luminescence decreases with decreasing optical gap energy (E_{CT}), which is responsible for the charge transfer [OY98]. For example, the intensity of the luminescence in the PtI complex (E_{CT}=1.38 eV) was observed to be 5 orders of magnitude weaker than that of $[Pt(en)_2][Pt(en)_2Cl_2](ClO_4)_4$ (E_{CT}=2.73 eV). This indicates that the STE in the PtI complex annihilates mainly through a nonradiative process such as the conversion into soliton or polaron [OY98]. The nonradiative relaxation of the STE would lead to lattice heating. The weaker intensity of luminescence at a lower E_{CT} coincides with the shorter lifetime of the STE at a lower E_{CT}. This implies that the nonradiative process occurs considerably faster than does the radiative process.

4.3 Phase Conversion from Charge Density Wave state (CDW) to Mott-Hubbard Phase

We have examined the wave packet dynamics in the self-trapped states of the PtI complex. The pump fluence was low and the corresponding density of the self-trapped exciton was also low. As pump excitation is increased, the self-trapped exciton, or equivalently, a symmetrically charged state, $-Pt^{3+}-I^{-}-Pt^{3+}-$ will spread over broader lattice sites. What happens when we increase the pump excitation continuously? Is it possible to achieve a completely monovalent and highly symmetric state before the PtI complex decomposes or melts? In this section, we present experimental results obtained under high excitation and discuss the possibility of phase transitions from the original mixed valence CDW state to a highly symmetric monovalent Mott-Hubbard phase.

4.3.1 Pump fluence dependence

In order to examine the phase transition of the PtI compound, the pump power dependence of the transient reflectivity was investigated using standard pump-probe spectroscopy. Both pump and probe wavelengths were 800 nm and their polarizations parallel to the 1-D chain.

Low pump fluence

Figure 4-9 shows the transient reflectivity change of the PtI complex at low pump fluence. As the pump fluence increases, the background electronic reflectivity change becomes more negative and the oscillation amplitude increases. These indicate that higher pump fluences give rise to an increased population of the self-trapped exciton state (STE), i.e., the monovalent symmetric species $-Pt^{3+}-I^{-}-Pt^{3+}-$ along 1-D chains. No sample damage was observed below 1.6 mJ/cm^2.

Figure 4-10 shows the FFT power spectrum of the second-derivative signal of the transient reflectivity change. The oscillatory motion of the wave packets at 116 cm^{-1} is

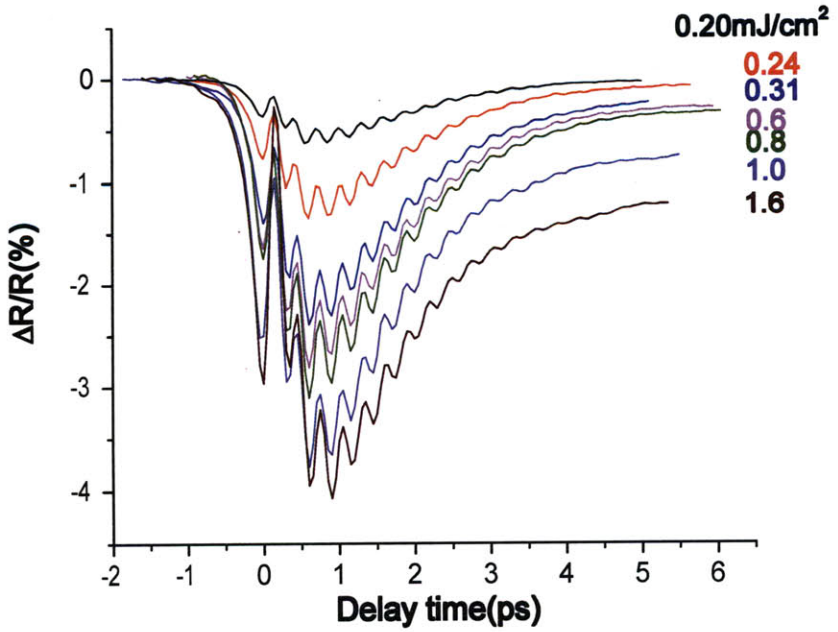

Figure 4-9: Transient reflectivity of the PtI complex as a function of pump fluence.

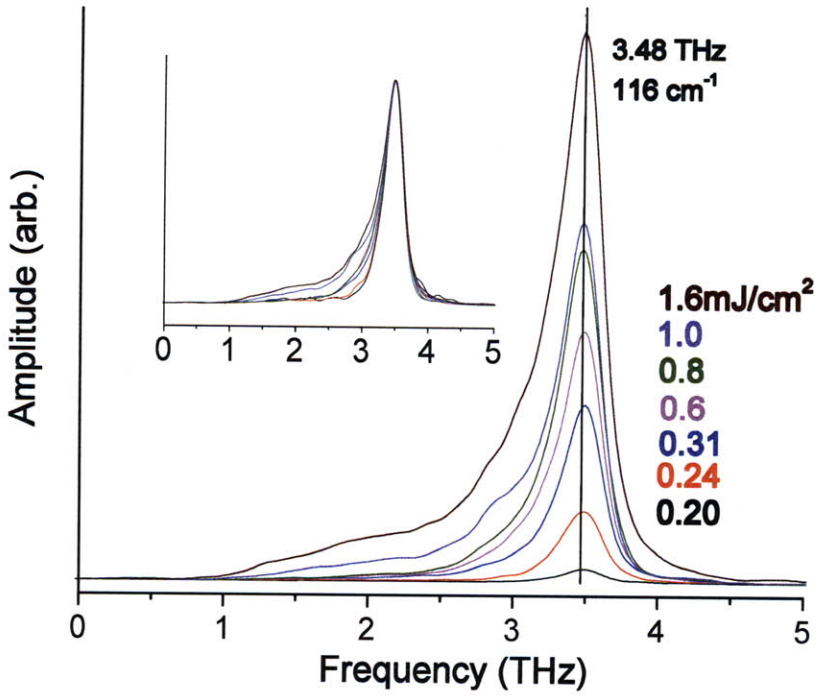

Figure 4-10: FFT spectrum of the second-derivative of the time-resolved reflectivity change in figure 4-9. The inset shows the normalized spectrum at all pump fluences for ease of comparison.

revealed, and the amplitude increases with increasing pump fluence up to 1.6 mJ/cm^2. The lineshape of the spectrum is symmetric at lower pump fluence, but it becomes asymmetric under stronger excitation. The inset was obtained by normalizing every spectrum at all pump fluences, revealing that the linewidth increases slightly with increasing excitation. This suggests that the dephasing rate of the oscillations is affected only slightly by increasing excitation or increasing population of the STE state. The origin of the asymmetric behavior at higher fluences is not clear. It appears that the asymmetric spectrum is resolved into two components. One component is centered at 116 cm^{-1}, and the other is centered at about 110 cm^{-1}. However, the presence of the frequency at $\sim$110 cm^{-1} is unclear. A frequency shift or bond softening is not observed in the PtI. This implies that the potential energy surface of the self-trapped state is not influenced by the high population of the state. This may result from the local nature of the self-trapped exciton state.

High pump fluence

Now let us increase the pump fluence further. Figure 4-11 shows the time-resolved reflectivity change as a function of increasing pump fluence. The background electronic signal becomes less negative with increasing pump fluence. Following the initial negative response, a strong positive rise appears and decays at higher pump fluences. At the same time, the oscillation amplitude becomes considerably weaker. The oscillations disappear above ~7–8 mJ/cm^2.

Unfortunately, the PtI crystal undergoes damage over multishots above ~2.4 mJ/cm^2. In order to check sample damage by high excitation in reflectivity measurements, the same reflectivity measurement was performed on the same spot using a weak pump fluence (below damage threshold). The result is illustrated in figure 4-12. If the sample spot was not damaged by high excitation, the same time trace should be reproduced. However, the transient reflectivity changes over high excitation measurements, indicating that the sample undergoes damage above 2.4 mJ/cm^2. The damage might originate from the accumulated thermal energy (thermal degradation

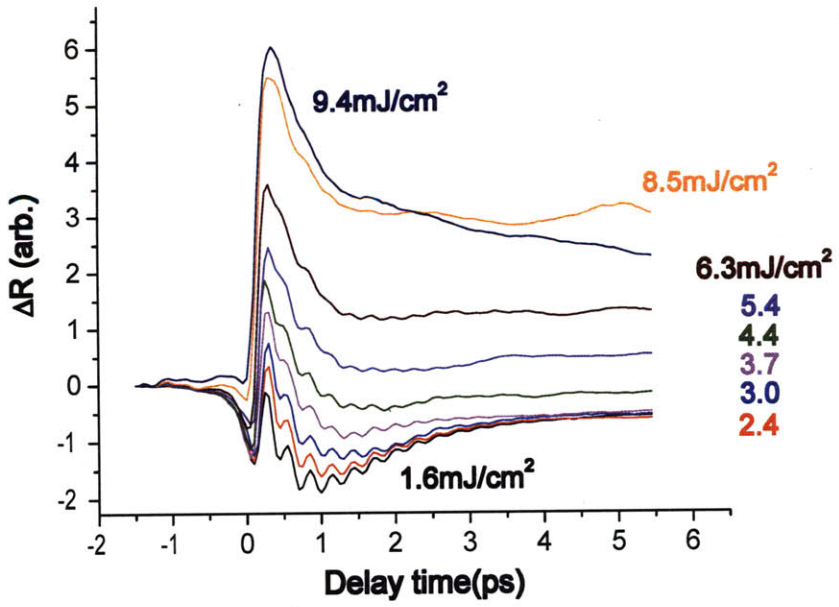

Figure 4-11: Transient reflectivity of the PtI complex at high pump fluence.

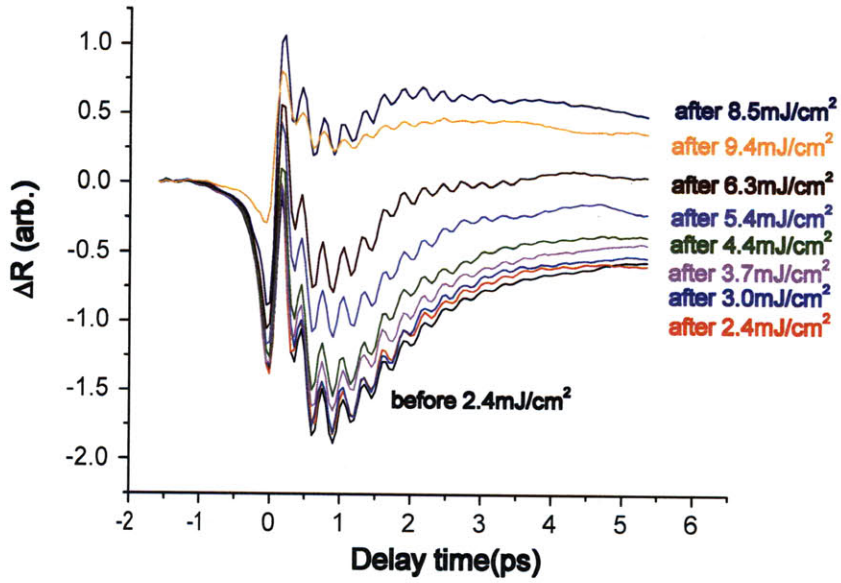

Figure 4-12: Transient reflectivity measurement to check sample damage at high pump fluence. Each time trace was obtained using weak pump fluence (1.6 mJ/cm^2) after reflectivity measurements at high pump fluence.

or from a high density of electronic excited states). Lattice fatigue by repetitive atomic motion due to the charge transfer may account for the damage.

It should be noted that only the background electronic component changes and the oscillation amplitude is almost constant even though the spot is damaged after high excitation measurement (figure 4-12). This strongly implies that the absence of oscillations above ~7–8 mJ/cm^2 is real, and not simply due to sample damage (figure 4-11). The disappearance of the oscillations must then be due to a phase transition to the high symmetry monovalent, Mott-Hubbard phase which does not show the oscillations: As the pump fluence increases, the population of the STE state (–Pt^{3+}–I^{-}–Pt^{3+}–) increases over the 1-D chain. Further excitation eventually leads to the complete replacement of mixed valence units by monovalent units. That is, a photoinduced phase conversion takes place from the charge density wave state to the Mott-Hubbard phase. The oscillation amplitude will begin to decrease as the monovalent units replace approximately more than half of the mixed valence units along the 1-D chain. Finally, the complete phase transition results in the disappearance of

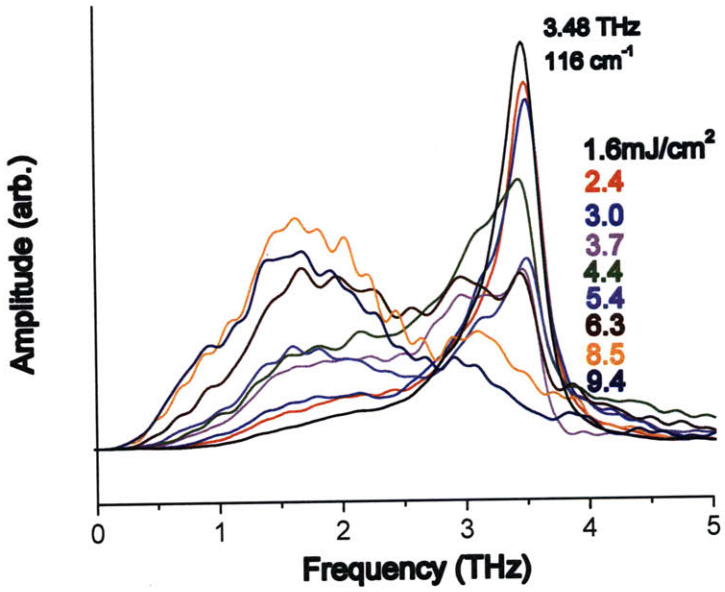

Figure 4-13: FFT spectrum of the second-derivative of the time-resolved reflectivity change in figure 4-11.

the oscillations.

Figure 4-13 exhibits the FFT power spectrum of the second derivative of the reflectivity at high pump fluence (figure 4-11). The maximum amplitude of the oscillation at 116 cm^{-1} is observed near 1.6 mJ/cm^2. This fluence might cause a phase in which there is maximum population of $-Pt^{3+}-I^{-}-Pt^{3+}-$ behaving like an isolated species. Above this fluence, however, the population of $-Pt^{3+}-I^{-}-Pt^{3+}-$ increases and the chance increases that at least more than two $-Pt^{3+}-I^{-}-Pt^{3+}-$ units are in contact with each other. Therefore, further excitation will reduce the amplitude continuously and removes the oscillations completely at 8.5 mJ/cm^2. The broad peak at ~1.5 THz becomes more pronounced at higher pump fluences, but this is just due to the fast response (its second derivative) near the time origin.

4.3.2 Single-shot Measurements

Conventional pump-probe spectroscopy suggested the phase transition of the PtI complex from the charge density wave state to the Mott-Hubbard insulating phase.

High excitation, however, induces sample damage and thus conventional pump-probe spectroscopy imposes ambiguity on high excitation measurements. To eliminate ambiguity resulting from multishot damage, single-shot femtosecond spectroscopy was employed. The same 800 nm wavelength was used to induce the phase transition of the PtI. Both the pump and probe polarizations were parallel to the orientation of the 1-D chain. Since the optical quality of the PtI sample is poor, some pump light was directed into the CCD generating systematic noise. To spectrally separate the scattered light, a probe wavelength other than 800 nm was selected and the NOPA setup was used to vary the probe wavelength. In order to enhance the signal to noise level, the time-resolved reflectivity was averaged over about 100 shots.

Short delay time dynamics

Figure 4-14 illustrates the transient reflectivity of the PtI complex obtained using the single-shot instrument. The probe wavelength is 600 nm. The temporal signal is very similar to that of the standard pump-probe experimental results as shown in figure 4-6. Optical excitation decreases the reflectivity. The oscillations due to the wave packet motion of the STE state are clearly observed up to 2.5 mJ/cm^2. Oscillations show significantly smaller amplitudes at 4.5 mJ/cm^2 and they disappear completely at 12.0 mJ/cm^2, suggesting a phase transition to the high symmetry Mott-Hubbard phase. Fast dephasing due to free carrier-phonon scattering is unlikely because free carrier density is negligible.

As previously discussed, the oscillation amplitude increases initially with increasing pump fluence as the population of the STE state (–Pt^{3+}–I^{-}–Pt^{3+}–) increases. However, as the population of –Pt^{3+}–I^{-}–Pt^{3+}– units increases further, units can be connected together to form a longer linear chain. As a consequence, the number of Raman active, symmetric stretching modes of isolated –Pt^{3+}–I^{-}–Pt^{3+}– units at ~110 cm decreases. This leads to a decrease in the oscillation amplitude. When the phase transition to the Mott-Hubbard phase is complete, the symmetric stretching mode is no longer available and the oscillations disappear accordingly. This series of events is in good agreement with what is observed in figure 4-14 in terms of oscilla-

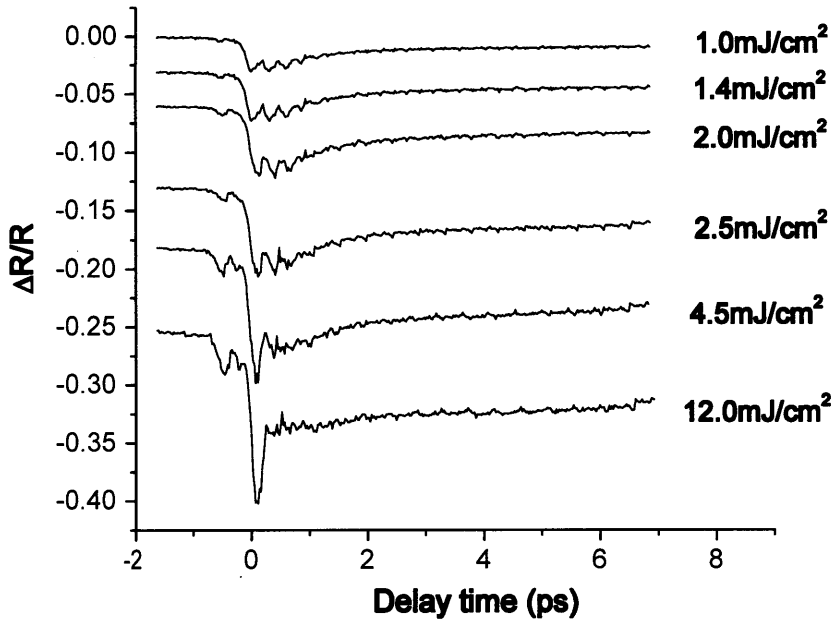

Figure 4-14: Time-resolved reflectivity change of the PtI obtained using single-shot femtosecond spectroscopic method. The pump and probe wavelengths are 800 nm and 600 nm, respectively. Pump fluence varied from 1.0 to 12.0 mJ/cm^2. The temporal signal was averaged over 100 shots.

tion amplitude. The oscillation amplitude increases until 2.0–2.5 mJ/cm^2 and then becomes smaller at 4.5 mJ/cm^2. No oscillations are observed at 12.0 mJ/cm^2.

Long delay time dynamics

The phase transition of the PtI from the CDW to the Mott-Hubbard state is evident at high pump fluence. The transition takes place within 1 ps which is determined by the timescale on which the wave packet transfers from the potential energy surface of the FE state to that of the STE state in figure 4-5. How long does the Mott-Hubbard phase exist once the photoinduced phase transition is complete? We may answer this question by using the double pump experiments as described in figure 3-51 of chapter 3.

The experimental results are illustrated in figures 4-15 to 4-17. In each figure, the bottom red curve represents the transient reflectivity change induced by the first pump pulse. The above blue signal contains the response by both the first and second

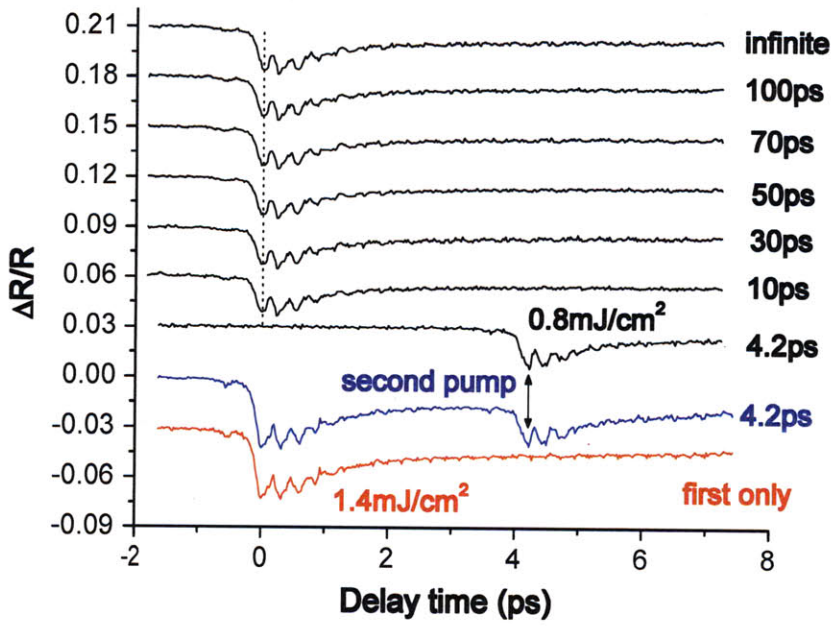

Figure 4-15: Double pump measurements of the PtI complex. Oscillations from the first pump excitation (1.4 mJ/cm^2) are observed. A weak second pump (0.8 mJ/cm^2) arrives 4.2 to 100 ps after the first excitation. The oscillation amplitude from the second pump stays constant from 10 to 100 ps. The bottom red curve shows the time-dependent signal from the first pump only. The above blue curve represents the response by the first and second pumps at 4.2 ps. The time-dependent signal from the second pump (black curves) was obtained by subtracting the the first pump response from that of both pumps.

pumps. The above black curves were obtained by subtracting the first pump response from that of both pumps.

In figure 4-15, the first pump fluence is 1.4 mJ/cm^2. The weaker second pump follows 4.2 to 100 ps after the first pump. Both the first and second pump fluences lie in the regime in which the oscillation amplitude increases with increasing pump fluence (figures 4-9 and 4-14). Oscillations from the first pump are easily visible and those from the second pump are also observed at all times (4.2 to 100 ps). The temporal response from the second pump is unchanged after 10 ps., because is because the wave packets of the STE state relax as quickly as $\sim$2 ps. At 4.2 ps, the amplitude is slightly smaller compared to other delay times because a relatively high population of the STE state does not relax until 4.2 ps.

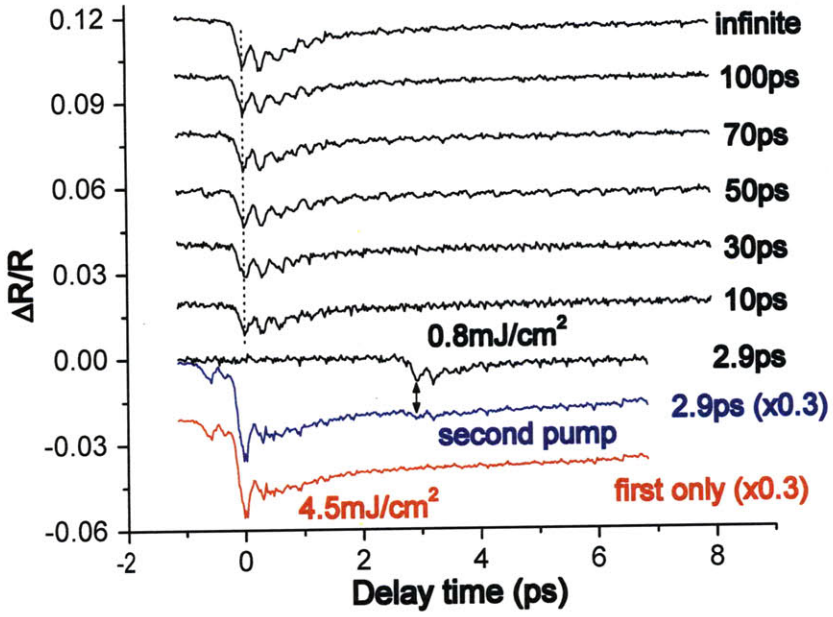

Figure 4-16: Double pump measurements in the PtI complex. Oscillations from the first pump excitation (4.5 mJ/cm^2) are weak but clearly visible. A weak second pump (0.8 mJ/cm^2) arrives 2.9 to 100 ps after the first excitation. The oscillation amplitude increases until about ~10 ps.

In figure 4-16, the first pump fluence is 4.5 mJ/cm^2. Oscillations from the first pump are substantially smaller indicating a significantly higher population of the STE state. A high population of the STE state (–Pt^{3+}–I^-–Pt^{3+}–) is formed approaching the Mott-Hubbard phase. Weaker but still visible oscillations reappear after 2.9 ps due to fast relaxation of the STE state. The oscillation amplitude grows quickly and becomes unchanged at ~10 ps.

Figure 4-17 illustrates the transient reflectivity change under high excitation. No oscillations are observed, suggesting the phase transition to the Mott-Hubbard phase. However, oscillations reappear as quickly as 2.9 ps. The oscillations are very weak but clearly visible. This reveals that the reverse phase transition from the Mott-Hubbard phase to the original CDW phase takes place in as quickly as 2.9 ps. As the reverse phase transition proceeds, the separate and isolated species (–Pt^{3+}–I^-–Pt^{3+}–) should increase in number. The increased number of the species enhances the amplitude of

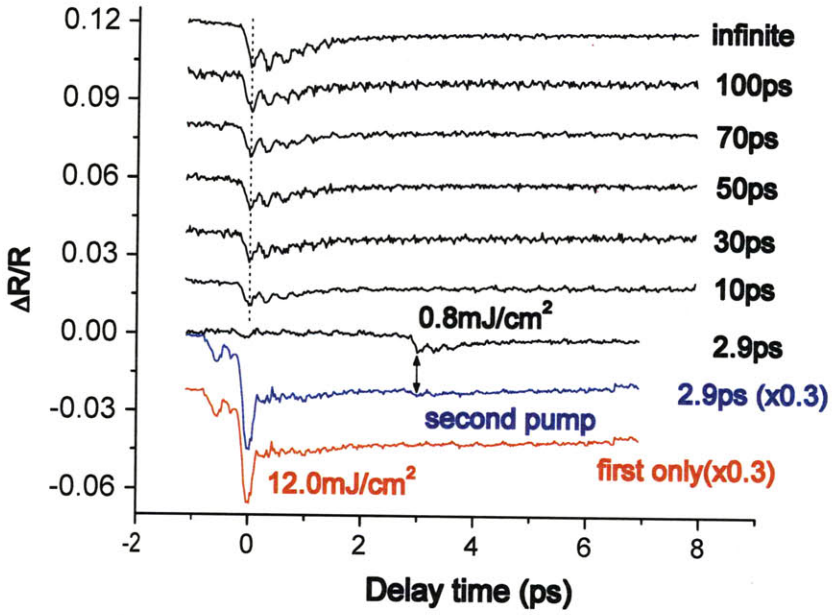

Figure 4-17: Double pump measurements in the PtI complex. No Oscillations from the first pump excitation (12.0 mJ/cm^2) are observed. A weak second pump (0.8 mJ/cm^2) follows 2.9 to 100 ps after the first excitation. Oscillations reappear as early as 2.9 ps and the amplitude grows until about ~30 ps.

the oscillations at ~110 cm^{-1}. The amplitude continues to grow approximately until ~30 ps and then becomes constant.

Due to the Peierls instability, the reverse phase transition to the original CDW state takes place immediately after the complete phase transition to the Mott-Hubbard phase is achieved. The lifetime of the Mott-Hubbard phase is extremely short. It appears that there are no favorable collective effects supporting the Mott-Hubbard phase. In other words, the single monovalent state (–Pt^{3+}–I^-–Pt^{3+}–) relaxes to the mixed valence state (–Pt^{4+}-I^-—Pt^{2+}–) at the same rate independently of the density of the monovalent states. Accordingly, the rate of the reverse phase transition is determined by the relaxation rate of the STE state.

The lifetime of the STE state in the PtI complex is measured to be as short as 2 ps. The STE state in the PtI complex relaxes mainly via the nonradiative process, producing little luminescence peaked at ~0.6 eV. This will increase the lattice temperature in the PtI crystal. The smaller electronic response at the time origin

might reflect a higher lattice temperature at earlier delay times. As observed in figure 4-17, the initial electronic drop becomes bigger from 2.9 to 100 ps, and it recovers to its original level after an infinite time, likely indicating that the lattice cools over time. The same behavior is observed in figure 4-16.

Unlike the short lifetimes of the STE state in the PtI and PtBr complexes, it was observed that the PtCl complex exhibits a much slower decay rate of the self-trapped exciton state. Time-resolved luminescence studies showed that the STE state in the PtCl complex annihilates on the timescale of 30 ps [TNS+98]. In this complex, the Mott-Hubbard phase would last as long as ~25 ps if the photoinduced phase transition takes place.

4.4 Summary

In this chapter, we studied ultrafast dynamics in a quasi-one-dimensional platinum iodide complex using conventional and single-shot pump-probe spectroscopy.

The oscillatory wave packet motions on the STE potential energy surface were observed. The wavelength dependence of the transient reflectivity reveals that the ultrafast vibrational cooling of the wave packets and relaxation of the STE state occur simultaneously. The STE state relaxes on a timescale of about 2 ps through a nonradiative process.

At higher pump fluences, oscillations of the wave packets disappeared. This results from the phase transition from the charge density wave (CDW) state to the Mott-Hubbard state. Double pump measurements showed that the Mott-Hubbard phase exists for an extremely short time due to the Peierls instability and the reverse phase transition to the CDW state occurs as quickly as 2.9 ps.

Chapter 5

Conclusions and Future Work

Conclusions

In order to overcome the limitations of conventional pump-probe spectroscopy and to investigate irreversible ultrafast dynamics in solid-state materials, we have developed dual-echelon single-shot femtosecond spectroscopy. In this thesis, we have discussed the development and application of single-shot femtosecond spectroscopy. Despite the nature of the single-shot measurement, a high signal-to-noise level was achieved using background and reference calibration schemes. The signal-to-noise level can be enhanced further by averaging over multiple shots. In addition to random noise due to shot-to-shot fluctuations of the laser, several factors introduce systematic and periodic noise. These factors include the location of the sample relative to the probe focal plane, a small pump spot size, a nonlinear response at higher excitation, and aberration of the focusing lens. Much caution is necessary to eliminate the systematic noise resulting from the above artifacts. A standard pump-probe instrument and non-collinear optical parametric amplifier were incorporated into the single-shot instrument for versatility.

Ultrafast dynamics of bismuth have been examined by varying film thickness and probe wavelength. Strong lattice vibrations are launched via displacive excitation of coherent phonons (DECP). Film thickness influences bond softening and the transient reflectivity. Bond softening is more pronounced in thinner films. Ultrafast carrier

dynamics such as ballistic carrier diffusion may account for more severe bond softening in thinner films. In addition, electronic structures are involved in the softening. Dependence of the electronic background reflectivity on the film thickness may be understood in terms of different electronic structures with different film thickness. Through wavelength-dependent reflectivity measurements and the Fermi distribution analysis, a larger energy gap for the interband transition is observed in thinner films. The larger gap might result from quantum confinement effects of the thin bismuth film.

A thermal model has been established to investigate thermal behaviors in bismuth. The model includes electronic and lattice heat equations, as well as diffusion and recombination kinetic equations. Three coupled equations are numerically solved. The model predicts that bismuth reaches its highest lattice temperature around 20–30 ps via inelastic electron-phonon scattering and nonradiative recombination. Afterwards, the lattice temperature decreases slowly via slow lattice heat conduction. The effects of pump fluence, electron diffusivity, nonradiative recombination rate, and inelastic electron-phonon scattering rate were investigated.

Photoinduced phase transitions of bismuth has been examined through single-shot reflectivity measurements. Disappearance of lattice vibrations within a few vibrational cycles at high pump fluence suggests three possibilities—a phase transition to liquid, a phase transition to a high symmetry phase, or simple fast dephasing due to electron-phonon scattering in the crystalline phase. The thermal model and double pump measurements reveal that bismuth undergoes nonthermal melting. Melting is initiated nonthermally but afterwards the lattice temperature increases by thermal effects such as inelastic electron-phonon coupling and nonradiative recombination.

Thin films exhibit a significantly lower melting threshold as compared to thicker films or bulk crystals. Disappearance of lattice vibrations within a few vibrational cycles suggests nonthermal melting as well. Suppressed carrier diffusion increases the carrier density effectively within the skin depth leading to severe bond weakening, acceleration of atoms along the phonon mode, and finally collapse of the lattice structure via coupling into transverse acoustic modes. By contrast, ballistic transport is

allowed in bulk, lowering the carrier density effectively and leading to less pronounced bond weakening and thus higher nonthermal melting threshold. In addition to the above nonthermal effects originating from diffusion, the lattice temperature would be higher in thin films because of the larger thermal effects due to a higher frequency of carrier-phonon scattering and nonradiative recombination. This thermal heating continues until ~20-30 ps.

For the present double pump measurements, the time delay between the first and second pump extends only up to 100 ps. In order to examine the cooling timescales between the bulk and thin films, the delay time should be spanned up to a few nanoseconds. The different recovery time of the oscillations between the bulk and thin films would reveal thermal effects originating from suppressed diffusion of hot carriers.

It would be interesting to decouple the nonthermal and thermal effects by exciting bismuth with a lower photon energy which exceeds the bandgap (~0.2 eV) only slightly. In this case, the thermal energy of free carriers would be very low and only the electronic effects would come into play. By using a frequency difference technique and subsequent amplification, it may be possible to generate high pump powers.

We have studied the ultrafast dynamics of wave packets and phase transitions in a quasi-one-dimensional platinum iodide complex. We observed oscillatory motions of wave packets on the self-trapped exciton (STE) potential energy surface. The STE state undergoes vibrational cooling and annihilation simultaneously on the timescale of 2 ps. Above a certain excitation level, higher excitation leads to a smaller amplitude of the oscillations indicating the formation of longer chains consisting of the monovalent species $-Pt^{3+}-I^{-}-Pt^{3+}-$. Further excitation finally induces the phase transition from the charge density wave (CDW) state to the Mott-Hubbard phase transition. Double pump measurements reveal that the Mott-Hubbard phase is very short-lived. It begins to return to the original CDW phase as quickly as 2.9 ps due to the Peierls instability.

It is known that the PtCl compound exhibits a longer decay time of the STE state than does the PtI complex. This implies that the lifetime of the Mott-Hubbard phase

may be longer. Double pump measurements would yield a later recovery time of the oscillations.

Future work

Among many irreversible processes, we have studied phase transitions of bismuth, phase transition of the PtI compound, and irreversible photochemistry of triiodide crystals [Pou06]. These are just a very small fraction of the possible systems to study using the dual-echelon single-shot technique. Femtosecond irreversible dynamics in solid-state materials is largely an unexplored field.

Among the possible systems, let us consider photoinduced solid-state polymerization of diacetylene. No one has tried to examine the ultrafast dynamics of polymerization despite its important application to conducting polymers. Diacetylene monomer crystals [R_1-C≡C-C≡C-R_2] may undergo polymerization depending on their topological structure. It would be interesting to look into the effects of the lattice structures on polymerization on an ultrafast timescale. Also, it would be valuable to examine the time evolution of electronic structure towards a metallic polymer in real-time as polymerization occurs.

GST ($Ge_2Sb_2Te_5$) exhibits a dramatic change in reflectivity between its amorphous and crystalline phases. Because of the high contrast, it has drawn much attention owing to its application to optical data storage. However, the exact mechanism for the photoinduced phase transition between its two phases is not yet well-understood. In particular, it would be important to understand whether the phase transition mechanism is thermal or nonthermal.

In addition, single-shot spectroscopy enables us to examine the photochemistry and photophysics of solid-state materials under shock-loading. We can examine photoinduced phase transitions of materials under shock-loading. For example, it would be possible to investigate how shock-loading facilitates the phase transition in bismuth thin films. It is known that an ultrathin Bi film acts as a semiconductor rather than a semimetal. The shock may induce metallization of the semiconducting bismuth thin film. This can be examined by dual-echelon single-shot femtosecond spectroscopy.

As a promising and powerful means, dual-echelon femtosecond single-shot spectroscopy can be applied to study solid-state materials far from equilibrium, and can provide a deep understanding of highly nonequilibrium ultrafast dynamics.

Bibliography

[AKP75] S. I. Anisimov, B. L. Kapeliovich, and T. L. Perel'man. *Sov. Phys. JETP*, 39:375, 1975.

[BGR+08] D. Boschetto, E. Gamaly, A. Rode, B. Luther-Davies, D. Glijer, T. Garl, O. Albert, A. Rousse, and J. Etchepare. Small atomic displacements recorded in bismuth by the optical reflectivity of femtosecond Laser-Pulse excitations. *Physical Review Letters*, 100(2), 2008.

[CK81] Robin J. H. Clark and Mohamedally Kurmoo. Electronic, infrared, and resonance-Raman spectra of mixed-valence iodide-bridged linear-chain complexes of platinum. *Journal of the Chemical Society, Dalton Transactions*, (2):524, 1981.

[CNS97] Giulio Cerullo, Mauro Nisoli, and Sandro De Silvestri. Generation of 11 fs pulses tunable across the visible by optical parametric amplification. *Applied Physics Letters*, 71(25):3616, 1997.

[CNS+99] G. Cerullo, M. Nisoli, S. Stagira, S. De Silvestri, G. Tempea, F. Krausz, and K. Ferencz. Mirror-dispersion-controlled sub-10-fs optical parametric amplifier in the visible. *Optics Letters*, 24(21):1529, 1999.

[CNSS98] G. Cerullo, M. Nisoli, S. Stagira, and S. De Silvestri. Sub-8-fs pulses from an ultrabroadband optical parametric amplifier in the visible. *Optics Letters*, 23(16):1283, 1998.

[CotPoSgS71] D Carter, Conference on the Physics of Semimetals, and Narrow gap Semiconductors. *The physics of semimetals and narrow-gap semiconductors proceedings*. Pergamon Press, Oxford ;New York, [1st ed.]. edition, 1971.

[CS03] Giulio Cerullo and Sandro De Silvestri. Ultrafast optical parametric amplifiers. *Review of Scientific Instruments*, 74(1):1, 2003.

[DFN94] Lisa Dhar, John T. Fourkas, and Keith A. Nelson. Pulse-length-limited ultrafast pump-probe spectroscopy in a single laser shot. *Optics Letters*, 19(9):643, 1994.

[DPBS00] S. Dexheimer, A. Van Pelt, J. Brozik, and B. Swanson. Femtosecond vibrational dynamics of Self-Trapping in a Quasi-One-Dimensional system. *Physical Review Letters*, 84(19):4425–4428, 2000.

[DRBM01] M. DeCamp, D. Reis, P. Bucksbaum, and R. Merlin. Dynamics and coherent control of high-amplitude optical phonons in bismuth. *Physical Review B*, 64(9), 2001.

[Ees83] G. Eesley. Observation of nonequilibrium electron heating in copper. *Physical Review Letters*, 51(23):2140–2143, 1983.

[EKM+79] H. Endres, H. J. Keller, R. Martin, Hae Nam Gung, and J. Traeger. The structure of the linear chain bis(1,2-diaminoethane)platinum(II) bis(1,2-diaminoethane)diiodoplatinum(IV)tetraperchlorate. *Acta Crystallographica Section B Structural Crystallography and Crystal Chemistry*, 35(8):1885–1887, 1979.

[FDNT95] John T. Fourkas, Lisa Dhar, Keith A. Nelson, and Rick Trebino. Spatially encoded, single-shot ultrafast spectroscopies. *Journal of the Optical Society of America B*, 12(1):155, 1995.

[FLIB84] J. Fujimoto, J. Liu, E. Ippen, and N. Bloembergen. Femtosecond laser interaction with metallic tungsten and nonequilibrium electron and lattice temperatures. *Physical Review Letters*, 53(19):1837–1840, 1984.

[Fow89] Grant Fowles. *Introduction to modern optics.* Dover Publications, New York, 2nd ed., dover ed. edition, 1989.

[FR04] S. Fahy and D. Reis. Coherent phonons: Electronic softening or anharmonicity? *Physical Review Letters*, 93(10), 2004.

[FRA+07] D. M. Fritz, D. A. Reis, B. Adams, R. A. Akre, J. Arthur, C. Blome, P. H. Bucksbaum, A. L. Cavalieri, S. Engemann, S. Fahy, R. W. Falcone, P. H. Fuoss, K. J. Gaffney, M. J. George, J. Hajdu, M. P. Hertlein, P. B. Hillyard, M. Horn von Hoegen, M. Kammler, J. Kaspar, R. Kienberger, P. Krejcik, S. H. Lee, A. M. Lindenberg, B. McFarland, D. Meyer, T. Montagne, E. D. Murray, A. J. Nelson, M. Nicoul, R. Pahl, J. Rudati, H. Schlarb, D. P. Siddons, K. Sokolowski-Tinten, Th. Tschentscher, D. von der Linde, and J. B. Hastings. Ultrafast bond softening in bismuth: Mapping a solid's interatomic potential with x-rays. *Science*, 315(5812):633–636, 2007.

[FSS78] P Fischer, I Sosnowska, and M Szymanski. Deby-Waller factor and thermal expansion of arsenic, antimony and bismuth. *J. Phys. C: Solid State Phys*, 11:1943, 1978.

[GCH98] G. M. Gale, M. Cavallari, and F. Hache. Femtosecond visible optical parametric oscillator. *Journal of the Optical Society of America B*, 15(2):702, 1998.

[GGB+08] T. Garl, E. Gamaly, D. Boschetto, A. Rode, B. Luther-Davies, and A. Rousse. Birth and decay of coherent optical phonons in femtosecond-laser-excited bismuth. *Physical Review B*, 78(13), 2008.

[GKS72] N. Garcia, Y. Kao, and Myron Strongin. Galvanomagnetic studies of bismuth films in the Quantum-Size-Effect region. *Physical Review B*, 5(6):2029–2039, 1972.

[Gol68] Stuart Golin. Band structure of bismuth: Pseudopotential approach. *Physical Review*, 166(3):643–651, 1968.

[Gop75] K Gopinathan. Ultrasonic studies on bismuth single crystals. *Solid State Communications*, 16(6):817–821, 1975.

[GRLT00] C. Guo, G. Rodriguez, A. Lobad, and A. Taylor. Structural phase transition of aluminum induced by electronic excitation. *Physical Review Letters*, 84(19):4493–4496, 2000.

[Hau84] Hermann Haus. *Waves and fields in optoelectronics.* Prentice-Hall, Englewood Cliffs NJ, 1984.

[Hec02] Eugene Hecht. *Optics.* Addison-Wesley, Reading Mass., 4th ed. edition, 2002.

[HKiNM02] Muneaki Hase, Masahiro Kitajima, Shin ichi Nakashima, and Kohji Mizoguchi. Dynamics of coherent anharmonic phonons in bismuth using high density photoexcitation. *Physical Review Letters*, 88(6), 2002.

[HMB+93] C. Hoffman, J. Meyer, F. Bartoli, A. Di Venere, X. Yi, C. Hou, H. Wang, J. Ketterson, and G. Wong. Semimetal-to-semiconductor transition in bismuth thin films. *Physical Review B*, 48(15):11431–11434, 1993.

[HMH+96] M. Hase, K. Mizoguchi, H. Harima, S. Nakashima, M. Tani, K. Sakai, and M. Hangyo. Optical control of coherent optical phonons in bismuth films. *Applied Physics Letters*, 69(17):2474, 1996.

[HMH+98] Muneaki Hase, Kohji Mizoguchi, Hiroshi Harima, Shin ichi Nakashima, and Kiyomi Sakai. Dynamics of coherent phonons in bismuth generated by ultrashort laser pulses. *Physical Review B*, 58(9):5448–5452, 1998.

[JBM+08] S. Johnson, P. Beaud, C. Milne, F. Krasniqi, E. Zijlstra, M. Garcia, M. Kaiser, D. Grolimund, R. Abela, and G. Ingold. Nanoscale Depth-Resolved coherent femtosecond motion in Laser-Excited bismuth. *Physical Review Letters*, 100(15), 2008.

[Kit05] Charles Kittel. *Introduction to solid state physics.* Wiley, Hoboken NJ, 8th ed. edition, 2005.

[KLT57] M. I. Kaganov, I. M. Lifshitz, and L. V. Tanatarov. *Sov. Phys. JETP*, 4:173, 1957.

[KMT+09] K. Kimura, H. Matsuzaki, S. Takaishi, M. Yamashita, and H. Okamoto. Ultrafast photoinduced transitions in charge density wave, mott insulator, and metallic phases of an iodine-bridged platinum compound. *Physical Review B*, 79(7), 2009.

[KV96] Thomas Kuhne and Peter Vohringer. Vibrational relaxation and geminate recombination in the femtosecond-photodissociation of triiodide in solution. *The Journal of Chemical Physics*, 105(24):10788, 1996.

[LM02] Tobias Lang and Marcus Motzkus. Single-shot femtosecond coherent anti-Stokes raman-scattering thermometry. *Journal of the Optical Society of America B*, 19(2):340, 2002.

[LSD97] Chun-Mao Li, Theodore Sjodin, and Hai-Lung Dai. Photoexcited carrier diffusion near a si(111) surface:non-negligible consequence of carrier-carrier scattering. *Physical Review B*, 56(23):15252–15255, 1997.

[Lut65] V.N. Lutskii. *Sov. Phys. JETP Lett.*, 2:245, 1965.

[MFIT06] Yoshinori Makishima, Naoki Furukawa, Akihiro Ishida, and Jun Takeda. Femtosecond Real-Time Pump-Probe imaging spectroscopy implemented on a single shot basis. *Japanese Journal of Applied Physics*, 45(No. 7):5986–5989, 2006.

[MFP+07] . Murray, S. Fahy, D. Prendergast, T. Ogitsu, D. Fritz, and D. Reis. Phonon dispersion relations and softening in photoexcited bismuth from first principles. *Physical Review B*, 75(18), 2007.

[MFW+05] . Murray, D. Fritz, J. Wahlstrand, S. Fahy, and D. Reis. Effect of lattice anharmonicity on high-amplitude phonon dynamics in photoexcited bismuth. *Physical Review B*, 72(6), 2005.

[Nas83] Keiichiro Nasu. Extended Peierls-Hubbard model for One-Dimensional N-Sites N-Electrons system. i. phase diagram by mean field theory. *Journal of the Physics Society Japan*, 52(11):3865–3873, 1983.

[Nas84] Keiichiro Nasu. Extended Peierls-Hubbard model for One-Dimensional N-Sites N-Electrons system. II. effect of fluctuation, optical and magnetic excitations. *Journal of the Physics Society Japan*, 53(1):302–311, 1984.

[OMTY92] H Okamoto, T Mitani, K Toriumi, and M Yamashita. Control of CDW state in halogen-bridged metal complexes. *Materials Science and Engineering: B*, 13(4):L9–L14, 1992.

[OY98] Hiroshi Okamoto and Masahiro Yamashita. Solitons, polarons, and excitons in Quasi-One-Dimensional Halogen-Bridged transition metal compounds. *Bulletin of the Chemical Society of Japan*, 71(9):2023–2039, 1998.

[PBR00] J. Piel, M. Beutter, and E. Riedle. 2050-fs pulses tunable across the near infrared from a blue-pumped noncollinear parametric amplifier. *Optics Letters*, 25(3):180, 2000.

[Pou05] P.R. Poulin. *Coherent Lattice and Molecular Dynamics in Ultrafast Single-Shot Spectroscopy.* PhD thesis, Massachusetts Institute of Technology, 2005.

[Pou06] P. R. Poulin. Irreversible organic crystalline chemistry monitored in real time. *Science*, 313(5794):1756–1760, 2006.

[Ren58] D. Reneker. New oscillatory absorption of ultrasonic waves in bismuth in a magnetic field. *Physical Review Letters*, 1(12):440–442, 1958.

[RGN+03] E. I. Rogacheva, S. N. Grigorov, O. N. Nashchekina, S. Lyubchenko, and M. S. Dresselhaus. Quantum-size effects in n-type bismuth thin films. *Applied Physics Letters*, 82(16):2628, 2003.

[RL72] R. Rosei and D. Lynch. Thermomodulation spectra of al, au, and cu. *Physical Review B*, 5(10):3883–3894, 1972.

[RLD07] E Rogacheva, S Lyubchenko, and M Dresselhaus. Semimetalsemiconductor transition in thin bi films. *Thin Solid Films*, 2007.

[RRCS73] J. B. Renucci, W. Richter, M. Cardona, and E. Schstherr. Resonance raman scattering in group vb semimetals: As, sb, and bi. *Physica Status Solidi (b)*, 60(1):299–308, 1973.

[Rul05] Claude Rulliere. *Femtosecond laser pulses : principles and experiments.* Springer, New York, 2nd ed. edition, 2005.

[San67] V.B. Sandomirskii. *Sov. Phys. JETP*, 25:101, 1967.

[SBB+03] Klaus Sokolowski-Tinten, Christian Blome, Juris Blums, Andrea Cavalleri, Clemens Dietrich, Alexander Tarasevitch, Ingo Uschmann, Eckhard Frster, Martin Kammler, Michael Horn-von-Hoegen, and Dietrich von der Linde. Femtosecond x-ray measurement of coherent lattice vibrations near the lindemann stability limit. *Nature*, 422(6929):287–289, 2003.

[Sco67] W. Scouler. Temperature-Modulated reflectance of gold from 2 to 10 eV. *Physical Review Letters*, 18(12):445–448, 1967.

[SHK+09] Germn Sciaini, Maher Harb, Sergei G. Kruglik, Thomas Payer, Christoph T. Hebeisen, Frank-J. Meyer zu Heringdorf, Mariko Yamaguchi, Michael Horn von Hoegen, Ralph Ernstorfer, and R. J. Dwayne Miller. Electronic acceleration of atomic motions and disordering in bismuth. *Nature*, 458(7234):56–59, 2009.

[Sid99] C. W. Siders. Detection of nonthermal melting by ultrafast x-ray diffraction. *Science*, 286(5443):1340–1342, 1999.

[SK98] Akira Shirakawa and Takayoshi Kobayashi. Noncollinearly phase-matched femtosecond optical parametric amplification with a 2000cm[sup 1] bandwidth. *Applied Physics Letters*, 72(2):147, 1998.

[SLFE87] R. Schoenlein, W. Lin, J. Fujimoto, and G. Eesley. Femtosecond studies of nonequilibrium electronic processes in metals. *Physical Review Letters*, 58(16):1680–1683, 1987.

[SM02] S. K. Sundaram and E. Mazur. Inducing and probing non-thermal transitions in semiconductors using femtosecond laser pulses. *Nature Materials*, 1(4):217–224, 2002.

[SMW03] T. Saito, O. Matsuda, and O. Wright. Picosecond acoustic phonon pulse generation in nickel and chromium. *Physical Review B*, 67(20), 2003.

[SS72] G. A. Saunders and Z. Sumengen. Frozen-In defects in bismuth in relation to its magnetoresistivity and thermoelectric power. *Proceedings of the Royal Society A: Mathematical, Physical and Engineering Sciences*, 329(1579):453–466, 1972.

[SSB+98] K. Sokolowski-Tinten, J. Solis, J. Bialkowski, J. Siegel, C. Afonso, and D. von der Linde. Dynamics of ultrafast phase changes in amorphous GeSb films. *Physical Review Letters*, 81(17):3679–3682, 1998.

[SSK+01] A. Sugita, T. Saito, H. Kano, M. Yamashita, and T. Kobayashi. Wave packet dynamics in a Quasi-One-Dimensional Metal-Halogen complex studied by ultrafast Time-Resolved spectroscopy. *Physical Review Letters*, 86(10):2158–2161, 2001.

[SSTK99] A. Shirakawa, I. Sakane, M. Takasaka, and T. Kobayashi. Sub-5-fs visible pulse generation by pulse-front-matched noncollinear optical parametric amplification. *Applied Physics Letters*, 74(16):2268, 1999.

[SWS+91] P. Saeta, J.-K. Wang, Y. Siegal, N. Bloembergen, and E. Mazur. Ultrafast electronic disordering during femtosecond laser melting of GaAs. *Physical Review Letters*, 67(8):1023–1026, 1991.

[TF02] P. Tangney and S. Fahy. Density-functional theory approach to ultrafast laser excitation of semiconductors: Application to the a1 phonon in tellurium. *Physical Review B*, 65(5), 2002.

[TM94] Guray Tas and Humphrey Maris. Electron diffusion in metals studied by picosecond ultrasonics. *Physical Review B*, 49(21):15046–15054, 1994.

[TNS+98] S. Tomimoto, H. Nansei, S. Saito, T. Suemoto, J. Takeda, and S. Kurita. Femtosecond dynamics of the exciton Self-Trapping process in a Quasi-One-Dimensional Halogen-Bridged platinum complex. *Physical Review Letters*, 81(2):417–420, 1998.

[TO75] Michael R. Topp and Gail C. Orner. Group dispersion effects in picosecond spectroscopy: Frequency dispersion. *Chemical Physics Letters*, 32(3):407–413, 1975.

[TRJ71] M.R. Topp, P.M. Rentzepis, and R.P. Jones. Time resolved picosecond emission spectroscopy of organic dye lasers. *Chemical Physics Letters*, 9(1):1–5, 1971.

[TS80] Yutaka Toyozawa and Yuzo Shinozuka. Stability of an electron in deformable lattice Force range, dimensionality and potential barrier. *Journal of the Physical Society of Japan*, 48(2):472–478, 1980.

[TSS+99] S. Tomimoto, S. Saito, T. Suemoto, K. Sakata, J. Takeda, and S. Kurita. Observation of the wave-packet oscillation during the exciton self-trapping process in a quasi-one-dimensional halogen-bridged pt complex. *Physical Review B*, 60(11):7961–7965, 1999.

[TWM+89] Koshiro Toriumi, Yoshiki Wada, Tadaoki Mitani, Shunji Bandow, Masahiro Yamashita, and Yuki Fujii. Synthesis and crystal structure of a novel one-dimensional halogen-bridged nickel(III)-X-nickel(III) compound, [Ni(R,R-chxn)2Br]Br2.infin. *Journal of the American Chemical Society*, 111(6):2341–2342, 1989.

[Wak01] G.P. Wakeham. *Dual-Echelon Single-Shot Femtosecond Spectroscopy.* PhD thesis, Massachusetts Institute of Technology, 2001.

[WJ70] P. Wang and A. Jain. Modulated piezoreflectance in bismuth. *Physical Review B*, 2(8):2978–2983, 1970.

[WLGS97] R. Weinkauf, L. Lehr, D. Georgiev, and E.W. Schlag. Time multiplexing: a new single shot femtosecond pump-probe technique. *Applied Physics B: Lasers and Optics*, 64(5):515–519, 1997.

[WMYK85] Yoshiki Wada, Tadaoki Mitani, Masahiro Yamashita, and Takao Koda. Charge transfer exciton in Halogen-Bridged Mixed-Valent pt and pd

complexes: Analysis based on the Peierls-Hubbard model. *Journal of the Physics Society Japan*, 54(8):3143–3153, 1985.

[WPR97] T. Wilhelm, J. Piel, and E. Riedle. Sub-20-fs pulses tunable across the visible from a blue-pumped single-pass noncollinear parametric converter. *Optics Letters*, 22(19):1494, 1997.

[WX07] A Wu and X Xu. Coherent phonon excitation in bismuth. *Applied Surface Science*, 253(15):6301–6304, 2007.

[ZVC+92] H. Zeiger, J. Vidal, T. Cheng, E. Ippen, G. Dresselhaus, and M. Dresselhaus. Theory for displacive excitation of coherent phonons. *Physical Review B*, 45(2):768–778, 1992.